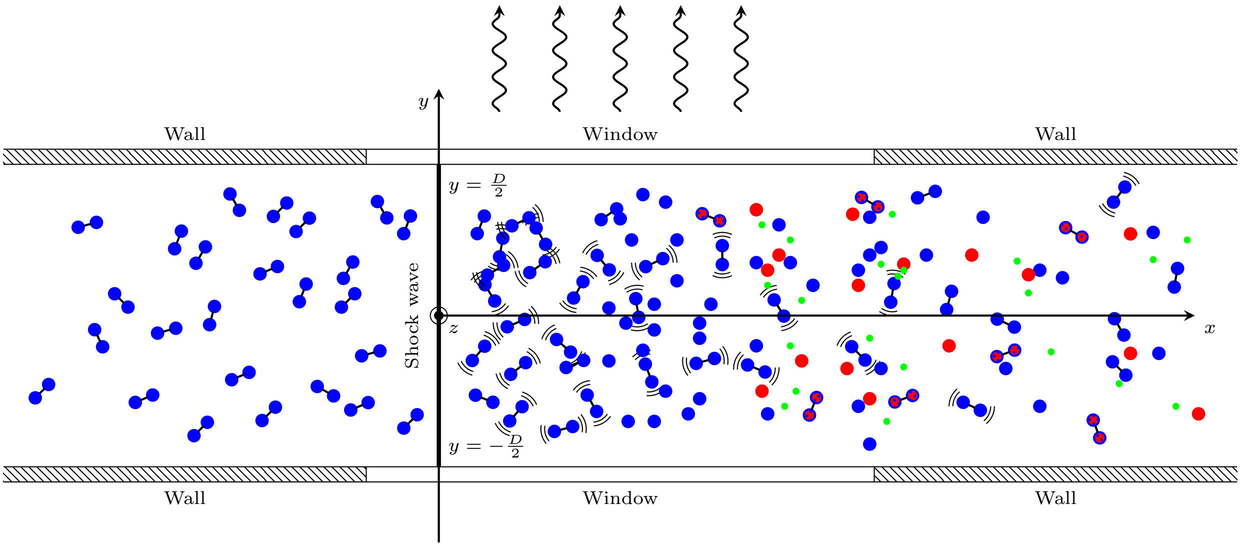

High-temperature kinetic and thermodynamic models for nitrogen plasmas

Élio Cordeiro Pereira

Thesis to obtain the Master of Science Degree in

Aerospace Engineering

Supervisor: Prof. Mário António Prazeres Lino da Silva

Examination Committee

Chairperson: Prof. Full Name
Supervisor: Prof. Mário António Prazeres Lino da Silva
Member of the Committee: Prof. Full Name 3

Month Year

Aos meus pais e irmãos,
que estiveram sempre ao meu lado.

Acknowledgments

I definitely would like to express gratitude to my supervisor Prof. Mário Lino da Silva, for giving me the opportunity of grasping one of the most beautiful and interesting topics of Aerospace Engineering that is currently in development. The area of Aerothermodynamics isn't for sure a common subject to be heard about in the quotidian. Probably, it will take many years to be absorbed by our culture, and I feel lucky to still find in this country some people who try doing something about it. I also have to thank him for granting me an investigation scholarship when I mostly needed it.

I do have to thank the help of Prof. Jorge Loureiro from IPFN group for introducing me to the Landau-Zener and Rosen-Zener-Demkov models. I did also enjoy and found myself fortunate to have the opportunity of hearing his remarkable thoughts on some of the philosophical aspects about the scientific research which was done in the old days and the one which is being done in the new days. The acknowledgement extends itself to Prof. Vasco Guerra from the same group, for enlighten me about particular aspects of the Schrödinger equation, and suggesting me the articles of Donald Rapp which were crucial for my understanding about vibrational transitions of heavy particles in collisions.

With respect to the process of putting thoughts into practice, I cannot forget the aid of the students under the APPLAuSE PhD program Duarte Gonçalves, João Vargas and Ricardo Ferreira, as well as the help of Dr. Bruno Lopez at the University of Illinois Urbana-Champaign, who provided me technical support for the SPARK code. Their patience and serenity were overwhelming.

I also want to thank Dr. Annarita Laricchiuta from the National Research Council of Italy, for her clarifications and providing me her values for the branching ratios associated to the process of non-dissociative ionisation of nitrogen molecules by electron impact, as well as the used database for the vibrational energies of the nitrogen molecule in its ground electronic state. I thank Dr. Steven Guberman from the Institute for Scientific Research for his noteworthy discussion about the valid temperature range for which his numerical data may be used in the modelling of rates of dissociative recombination of molecular nitrogen ions. I thank the courtesy of Dr. Brett A. Cruden and Dr. Aaron Brandis from the NASA Ames Research Center, who shared with me their obtained data regarding the test 62 of the EAST shock tube. I acknowledge the clarifications provided by Dr. Julien Annaloro from the National Centre for Space Studies about the lumping procedure with respect to the electronic levels and Einstein coefficients for spontaneous emission issued by NIST (which he had recently done in one of his works). I thank Dr. Dan Potter from CSIRO in Australia for sharing with me his knowledge about the line-broadening mechanisms regarded in his PhD thesis.

I thank all my friends that supported me and made my free time much more pleasant, in lunches, dinners, day and night outs. Their camaraderie will never be forgotten. A special acknowledgement should be attributed to my lab colleagues Luís Fernandes and Marília Matos who shared with me an important part of this challenging adventure in a very humble and honest manner.

Finally, to be fair, I want to give the most of the gratitude to my family, who always cared and loved me. I value them more and more each day goes by, and I should apologise to them for the time I could not reciprocate. The least I can do is to dedicate this work to them.

Resumo

As condições de não-equilíbrio térmico, químico e radiativo que se obtêm ao sujeitar-se um gás de N_2 puro a uma forte onda de choque foram quantificadas usando modelos estado-para-estado específicos quanto aos níveis de energia vibrónica. O modelo do Oscilador Harmónico Forçado (FHO) foi implementado no cálculo de taxas de transição vibracional e dissociação de N_2 e N_2^+ por impacto com espécies pesadas. Taxas de dissociação termal de $N_2(X^1\Sigma_g^+)$ por impacto com N_2 e N foram obtidas e comparadas com os mais recentes resultados experimentais, mostrando uma concordância entre -59.9 e $8.9\,\%$, e entre -80.9 e $-36.1\,\%$ para os dois casos, respetivamente. Constatou-se impraticável uma extensão dos modelos de Landau-Zener e Rosen-Zener-Demkov para transições vibrónicas de partículas moleculares por impacto com espécies pesadas, preferindo-se uma lei do tipo "exponencial de hiato energético". Ajustando-se a curva que representa esta lei aos valores obtidos experimentalmente para as taxas de várias transições vibrónicas de N_2, foram obtidas discrepâncias de até uma ordem de grandeza, revelando alguma ineficácia do modelo. Os disparos 19, 20 e 40 da campanha nº 62 do Tubo de Choque de Arco Eléctrico em Ames (EAST), foram simulados numericamente usando o código SPARK. Constatou-se que os valores de pico da intensidade radiativa obtidos através de uma simulação de escoamento unidimensional do tipo Euler corresponderam entre o dobro e o quintúplo daqueles obtidos através de uma simulação de relaxação temporal, mostrando-se inválida a hipótese de transferência de momento ser negligenciável (sendo esta considerada na última). Os valores obtidos experimentalmente para as variáveis que descrevem a radiação foram subestimados por uma a duas ordens de grandeza. Testes de sensibilidade quanto às taxas cinéticas simuladas mostraram ser ineficazes na obtenção de uma concordância razoável entre os resultados numéricos e os experimentais. As simulações permitiram descrever corretamente a forma dos perfis de intensidade radiativa obtidos no disparo de reduzida velocidade, mas não a dos obtidos nos de moderada e elevada velocidades, pois estes revelaram patamares procedendo ou coalescendo com picos que não foram reproduzidos numericamente. Encontrou-se uma forte evidência das discrepâncias terem resultado da não modelação da transferência de calor por radiação no interior do gás-teste, e possivelmente, entre o gás de alta pressão (assim como o arco eléctrico do tubo de choque) e o gás-teste.

Palavras-chave: Entrada atmosférica, Aerotermodinâmica, Plasma de azoto, Estado-para-estado, Radiação, Tubo de choque

Abstract

The conditions of thermal, chemical and radiative non-equilibrium attained in a pure N_2 gas subjected to a strong shock wave were quantified using vibronic-specific state-to-state models. The Forced-Harmonic-Oscillator model (FHO) was employed in the computation of rate coefficients for vibrational transition and dissociation of N_2 and N_2^+ by heavy particle impact. Thermal dissociation rate coefficients of $N_2(X^1\Sigma_g^+)$ by collisions with N_2 and N were obtained and compared with state-of-the-art experimental results, showing an agreeability between -59.9 and $8.9\,\%$, and between -80.9 and $-36.1\,\%$ for the former and latter interactions, respectively. An extension of the Landau-Zener and Rosen-Zener-Demkov models to vibronic transitions of molecular particles by heavy particle impact was found to be impractical, and an exponential gap law was ultimately preferred. By fitting the curve that represents the law to experimentally obtained values for rate coefficients values of several vibronic transitions of N_2 reported in the literature, discrepancies of as much as one order magnitude were obtained, showing some crudeness of the model. Shots 19, 20 and 40 of the test 62 of the Ames Electric Arc Shock Tube (EAST) were simulated using the SPARK code. The peak values of radiative intensity obtained from a Euler one-dimensional simulation were found to be between the double and the quintuple of the ones obtained from a zero-dimensional simulation, showing the hypothesis of the momentum transfer being negligible (which is taken by the latter) to be invalid. The experimental radiation variables were underestimated by one to two orders of magnitude, and sensibility tests performed on the rate coefficients weren't successful in getting a reasonable agreeability. The shape of the radiative intensities profiles of the low speed shot was correctly predicted, but not the ones of the medium and high speed shots which revealed non-null plateaus proceeding or coalescing with peaks. These plateaus weren't predicted at all. Strong evidence was found for such discrepancies resulting from the non-modelling of heat transfer by radiation within the test gas, and possibly, between the driver gas (as well as the driver arc of the shock tube) and the test gas.

Keywords: Atmospheric entry, Aerothermodynamics, Nitrogen plasma, State-to-state, Radiation, Shock tube

Contents

List of Tables

List of Figures

Nomenclature

Physical constants

Å	Angstrom.	1×10^{-10} m
a_0	Bohr radius.	$\varepsilon_0 h^2/(\pi m_\mathrm{e} \mathrm{e}^2) = 0.529\,177\,210\,67 \times 10^{-10}$ m
atm	Standard atmosphere.	101 325 Pa
c	Speed of light.	299 792 458 m/s
“cm^{-1}”	Reciprocal “centimeter”.	$\mathrm{cm}^{-1} \cdot (h \cdot c) = 1.986\,445\,824 \times 10^{-23}$ J
h	Plank constant.	$6.626\,070\,040 \times 10^{-34}$ J·s
$\hbar$	Reduced Plank constant.	$h/(2\pi) = 1.054\,571\,800 \times 10^{-34}$ J·s
k_B	Boltzmann constant.	$1.380\,648\,52 \times 10^{-23}$ J/K
m_e	Electron mass.	$9.109\,383\,56 \times 10^{-31}$ kg
$\mathscr{N}_A$	Avogadro constant.	$(\mathrm{g/u}) \cdot \mathrm{mol}^{-1} = 6.022\,140\,857 \times 10^{23}\ \mathrm{mol}^{-1}$
Ry	Rydberg unit of energy.	$m_\mathrm{e} \mathrm{e}^4/(8\varepsilon_0^2 h^2) = 2.179\,872\,325 \times 10^{-18}$ J
$\mathscr{R}$	Molar gas constant.	$k_B \mathscr{N}_A = 8.314\,459\,8\ \mathrm{J/(mol \cdot K)}$
Torr	Torricelli unit of pressure.	1/760 atm= 133.322 368 4 Pa
u	Atomic mass unit.	$1.660\,539\,040 \times 10^{-27}$ kg
ε_0	Vacuum permittivity.	$8.854\,187\,817 \times 10^{-12}$ F/m
π	Pi number.	3.141 592 653 589 793 ...

Roman symbols

A	Chemical symbol of the first collision partner (regarding binary collisions); or nucleus A (regarding the FHO model).
AB	Molecular particle AB (regarding the FHO model).
A	Pre-exponential factor of the repulsive exponential potential (regarding the FHO model).

$A_{s,e,v}^{e',v'}$	Einstein coefficient associated to spontaneous emission.
B	Chemical symbol of the second collision partner (regarding binary collisions); or nucleus B (regarding the FHO model).
B_v	Spectroscopic rotational function associated to the v-th vibrational and e-th electronic levels.
B_e	Spectroscopic rotational constant associated to the e-th electronic level.
$B_{s,e,v}^{e',v'}$	Einstein coefficient associated to induced emission, if $T_{e'v'} < T_{ev}$ or absorption if $T_{e'v'} > T_{ev}$.
C	Nucleus C (regarding the FHO model).
CD	Molecular particle CD (regarding the FHO model).
C_V	Mixture specific heat at constant volume.
$C_{V,s}$	s-Th species specific heat at constant volume.
$C_{V,s,i}$	s-Th species specific heat at constant volume associated to the i-th energy mode.
C_p	Mixture specific heat at constant pressure.
$C_{p,s}$	s-Th species specific heat at constant pressure.
$C_{p,s,i}$	s-Th species specific heat at constant pressure associated to the i-th energy mode.
c_s	Mass fraction of the s-th species.
D	Nucleus D (regarding the FHO model).
D_0	Dissociation energy.
D_e	Potential well depth.
d_{AB}	Distance between the centres of two collision partners when in contact with each other (regarding the billiard balls model).
E	Relative kinetic energy (regarding binary collisions).
E_a	Activation energy.
E_0	Initial relative kinetic energy of the collision partners (regarding the FHO model); or characteristic energy (regarding the energy gap law).
E_{M}	Morse potential well (regarding the FHO model).
E_n	n-Th eigenenergy of the quantum free harmonic oscillator (regarding the FHO model).
e	e-Th electronic energy level; or initial electronic level; or higher electronic level; or mass-specific internal energy of the flow associated to the mixture.
e'	Final electronic level; or lower electronic level.

$e^\dagger$	$e^\dagger$-Th electronic level which regards fine structure.
e_s	Mass-specific internal energy of the flow associated to the s-th species.
$e_{s,\mathrm{tr}}$	Contribution of the translation energy mode to the mass-specific internal energy of the flow associated to the s-th species.
$e_{s,\mathrm{tr_h}}$	Contribution of the heavy particle translation energy mode to the mass-specific internal energy of the flow associated to the s-th species.
$e_{s,\mathrm{tr_e}}$	Contribution of the free electron translation energy mode to the mass-specific internal energy of the flow associated to the s-th species.
$e_{s,\mathrm{rot}}$	Contribution of the rotational energy mode to the mass-specific internal energy of the flow associated to the s-th species.
$e_{s,\mathrm{vib}}$	Contribution of the vibrational energy mode to the mass-specific internal energy of the flow associated to the s-th species.
$e_{s,\mathrm{el}}$	Contribution of the electronic energy mode to the mass-specific internal energy of the flow associated to the s-th species.
$e_{s,0}$	Contribution of the ground level energy to the mass-specific internal energy of the flow associated to the s-th species.
F_{vJ}	Particle rotational energy associated to the v-th vibrational, J-th rotational and e-th electronic levels.
f	Distribution of relative speeds (regarding binary collisions); or force constant of the quantum harmonic oscillator that represents the molecular particle (regarding the FHO model).
$\tilde{f}$	Normalised distribution of relative speeds (regarding binary collisions).
G	Gaussian function.
G_v	Particle vibrational energy associated to the v-th vibrational and e-th electronic levels.
g	Degree of degeneracy of the energy level.
$\mathscr{H}_n$	n-Th order physicists' Hermite polynomial (regarding the FHO model).
H_n	n-Th eigenfunction of the quantum free harmonic oscillator (regarding the FHO model).
h_s	Mass-specific enthalpy associated to the s-th species.
I_λ	Specific radiant intensity.
$\hat{I}$	Instrumentally resolved radiative intensity.
$\hat{I}_\lambda$	Instrumentally resolved specific radiative intensity.

$\hat{I}_{\lambda}^{\mathrm{ne}}$	instrumentally resolved non-equilibrium metric.
J	Rotational quantum number.
j_{λ}	Emission coefficient.
K_c	Concentration-wise equilibrium constant.
k_{λ}	Absorption coefficient.
k_f	Forward process rate coefficient.
k_b	Backward process rate coefficient.
$k_{v_1,v_2}^{v_1',v_2'}$	V-V-T rate coefficient associated to a transition from the vibrational quantum numbers v_1 and v_2 to v_1' and v_2' (regarding the FHO model).
$k_v^{v'}$	V-T rate coefficient associated to a transition from the vibrational quantum number v to v'; or V-V-T rate coefficient associated to a transition of a molecular particle from the vibrational quantum number v to v' which accounts all possible transitions of the other molecular particle (regarding the FHO model).
k_v^D	V-D rate coefficient associated to dissociation from the vibrational quantum number v; or V-D rate coefficient associated to dissociation of a molecular particle from the vibrational quantum number v which accounts all possible transitions of the other molecular particle (regarding the FHO model).
L	Lorentzian function.
M	Chemical symbol of a collision partner (regarding binary collisions).
Ma	Mach number.
M	Mass of the mixture particles inside a space in the fluid.
$\tilde{M}$	Sum of the collision partners masses (regarding the FHO model).
M_s	Mass of s-th species particles inside a space in the fluid.
$\tilde{m}$	Reduced mass of the collision partners (regarding the FHO model).
m_s	Mass of a s-th species particle.
m_{A}	Mass of the first collision partner (regarding binary collisions); or mass of nucleus A (regarding the FHO model).
m_{B}	Mass of the second collision partner (regarding binary collisions); or mass of nucleus B (regarding the FHO model).
m_{C}	Mass of nucleus C (regarding the FHO model).

N	Number of particles.
N_S	Number of species.
N_R	Number of processes.
N_s	Number of s-th species particles.
$N_{s,j}$	Number of s-th species particles in the j-th total energy level.
n	Number density (or amount concentration) of the mixture particles inside a space in the fluid.
n_s	Number density (or amount concentration) of s-th species particles inside a space in the fluid.
P	Process probability.
$P_{v_1,v_2}^{v_1',v_2'}$	V-V-T transition probability from the vibrational quantum numbers v_1 and v_2 to v_1' and v_2' (regarding the FHO model).
$P_v^{v'}$	V-T transition probability from the vibrational quantum number v to v' (regarding the FHO model).
P_v^D	Dissociation probability from the vibrational quantum number v (regarding the FHO model).
p	Pressure.
p_s	s-Th species partial pressure.
Q	Partition function.
R_s	Mass-specific gas constant associated to the s-th species.
r_A	Radius of the first collision partner (regarding the billiard balls model).
r_B	Radius of the second collision partner(regarding the billiard balls model).
r	Internuclear distance (regarding the RKR method).
r_e	Equilibrium internuclear distance.
S	Quantum number for the total electronic spin of the diatomic molecular particle.
T	Thermal equilibrium temperature.
T_e	Particle electronic energy associated to the e-th electronic level.
T_{ev}	Particle vibronic energy associated to the e-th electronic and v-th vibrational levels.
T_{vJ}	Particle rovibrational energy associated to the v-th vibrational and J-th rotational levels.
T_{evJ}	Particle rovibronic energy associated to the e-th electronic, v-th vibrational and J-th rotational levels.

T_i	i-Th energy mode temperature.
$T_{\mathrm{tr_h}}$	Heavy particle translational temperature.
T_{rot}	Rotational temperature.
T_{vib}	Vibrational temperature.
T_{el}	Electronic temperature.
$T_{\mathrm{tr_e}}$	Free electron translational temperature.
$T_{\mathrm{tr_h\text{-}rot}}$	Heavy particle translational-rotational temperature.
$T_{\mathrm{el\text{-}tr_e}}$	Electronic-free electron translational temperature.
$T_{\mathrm{vib\text{-}el\text{-}tr_e}}$	Vibrational-electronic-free electron translational temperature.
T_{c}	Controlling temperature.
t	Instant of time.
$\vec{u}$	Mixture flow velocity vector.
u	x-Component of the flow velocity vector.
$\vec{u}_s$	s-Th species flow velocity vector.
$\mathscr{V}$	Space in the fluid.
$\mathscr{V}_s$	Space in the fluid whose boundary moves with the s-th species particles.
V	Volume of a space in the fluid; or global potential energy of the collision partners (regarding the FHO model); or non-centrifugally corrected internuclear potential (regarding the RKR method); or Voigt function.
V_{sr}	Short-range part of the non-centrifugally corrected internuclear potential.
V_{lr}	Long-range part of the non-centrifugally corrected internuclear potential.
V_{RKR}	Non-centrifugally corrected internuclear potential obtained through the RKR method.
V_{HH}	Hulburt-Hirschfelder potential.
V_{ER}	Extended Rydberg potential.
V'	Interaction potential energy between the collision partners (regarding the FHO model).
V'_{M}	Morse potential (regarding the FHO model).
$\vec{v}$	Relative velocity vector (regarding binary collisions).

v	Relative velocity speed (regarding binary collisions); or relative speed of the collision partners at the pseudo-crossing or crossing point (regarding the Landau-Zener model); or initial relative speed of the collision partners (regarding the Rosen-Zener-Demkov model); or v-th vibrational quantum number; or initial vibrational quantum number.
v_0	Initial relative speed of the collision partners (regarding the FHO model).
v_1	Initial vibrational quantum number of the molecular particle AB (regarding the FHO model).
v_2	Initial vibrational quantum number of the molecular particle CD (regarding the FHO model).
v_D	Vibrational quantum number associated to the dissociation limit (regarding the FHO model).
$v_{\max}$	Maximum vibrational quantum number for which the respective Dunham expansion is valid.
v'	Final vibrational quantum number.
v'_1	Final vibrational quantum number of the molecular particle AB (regarding the FHO model).
v'_2	Final vibrational quantum number of the molecular particle CD (regarding the FHO model).
w	Half-width at half-maximum of the symmetric function.
X_s	s-Th species chemical symbol.
$[\mathrm{X}_s]$	s-Th species amount concentration (number of s-th species particles per unit volume).
$\tilde{X}$	Difference between $\tilde{x}$ and $\tilde{x}_t$ (regarding the FHO model).
$\tilde{x}$	Difference between the centres of mass positions of the collision partners (regarding the FHO model).
$\tilde{x}_t$	Classical turning point of the trajectory (regarding the FHO model).
$\tilde{x}_\mathrm{A}$	Position of nucleus A (regarding the FHO model).
$\tilde{x}_\mathrm{B}$	Position of nucleus B (regarding the FHO model).
$\tilde{x}_\mathrm{C}$	Position of nucleus C (regarding the FHO model).
$\tilde{x}_R$	Centre of mass of the two collision partners (regarding the FHO model).
Y_{ij}	(i, j)-Th Dunham parameter.
$\tilde{Y}$	Difference between $\tilde{y}$ and $\tilde{y}_0$ (regarding the FHO model).
$\tilde{y}$	Difference between the positions of the molecular particle nuclei (regarding the FHO model).
$\tilde{y}_1$	Difference between the positions of the molecular particle AB nuclei (regarding the FHO model).
$\tilde{y}_2$	Difference between the positions of the molecular particle CD nuclei (regarding the FHO model).

$\tilde{y}_0$	Equilibrium difference between the positions of the molecular particle nuclei (regarding the FHO model).
Z	Specific collisional frequency (regarding binary collisions).
$\tilde{z}$	Difference between the positions of two interacting particles (regarding the FHO model).
$\tilde{z}_0$	Equilibrium difference between the positions of two interacting particles (regarding the FHO model).

Greek symbols

α	Inverse length parameter of the repulsive exponential potential; or inverse length parameter of the Morse potential (regarding the FHO model).
α_e	Spectroscopic rotational constant associated to the e-th electronic level.
γ	Ratio of specific heats; or mass factor associated to the molecular particle (regarding the FHO model).
$\Delta\epsilon_0$	Difference between the sum of the products ground level energies and the one associated to the reactants of the chemical equation.
ΔE	Energy defect (regarding the energy gap law).
ϵ	Particle sensible energy.
ϵ'	Particle absolute energy.
ϵ_i	Particle sensible energy associated to the i-th energy mode.
ϵ_{tr}	Particle sensible translational energy.
ϵ_{int}	Particle sensible internal energy.
ϵ_{rot}	Particle sensible rotational energy.
ϵ_{vib}	Particle sensible vibrational energy.
ϵ_{el}	Particle sensible electronic energy.
ϵ_{sp}	Particle sensible spin energy.
ϵ_s	s-Th species particle sensible energy.
ϵ_{m}	Molecular particle sensible energy.
ϵ_{a}	Atomic particle sensible energy.
ϵ_{e}	Free electron sensible energy.
$\epsilon_{i,j}$	Particle sensible energy associated to the j-th level of the i-th energy mode.

$\epsilon_{i,0}$	Particle ground-level energy associated to i-th energy mode.
$\epsilon_{s,j}$	s-Th species particle sensible energy associated to the j-th total energy level.
ϵ_s^+	Ionisation energy of a s-th species particle.
η_0	V-T transition probability parameter: ratio between the energy of a classical free harmonic oscillator and the quantum energy $\hbar\omega$ (regarding the FHO model).
θ	Polar angle.
$\Lambda_{s,e,v}^{e',v'}$	Escape factor with respect to the vibronic levels (e, v) and (e', v').
Λ	Quantum number for the projection of the total electronic orbital angular momentum vector on the internuclear axis of the diatomic molecular particle.
λ	Photon wavelength.
λ_0	Centre of the wavelength-specific symmetric function.
μ	Reduced mass of collision partners (regarding binary collisions); or reduced mass of the diatomic molecular particle (regarding the FHO model).
ν	Photon frequency.
ν_s	s-Th species stoichiometric coefficient in the reactants side of the chemical equation.
ν_s'	s-Th species stoichiometric coefficient in the products side of the chemical equation.
ν_0	Centre of the frequency-specific symmetric function.
ρ	Mass density of the mixture particles inside a space in the fluid.
ρ_s	Mass density of s-th species particles inside a space in the fluid.
σ	Collisional cross section.
σ_s	Symmetry factor of the diatomic particle nuclei.
σ_{av}	Average collisional cross section.
σ_p	Process cross section.
$\sigma_{p,\mathrm{av}}$	Average process cross section.
σ_0	Characteristic cross section (regarding the energy gap law).
$\phi_{\lambda,s,e,v}^{e',v'}$	Wavelength-specific line-shape factor associated to the set of vibronic levels (e,v) and (e',v') of the s-th species.
$\phi_{\nu,s,e,v}^{e',v'}$	Frequency-specific line-shape factor associated to the set of vibronic levels (e,v) and (e',v') of the s-th species.

$\hat{\phi}^{\mathrm{spe}}$	Instrument line-shape factor.
$\hat{\phi}^{\mathrm{spa}}$	Spatial resolution function.
φ	Azimuthal angle.
Ψ	Global wave function (regarding the FHO model).
ψ	Wave function associated to the vibration of the collision partners (regarding the FHO model).
Ω	Solid angle.
$\dot{\Omega}^{\mathrm{int}}_{s,\mathrm{e}}$	Energy transferred per unit of time per unit of volume from the inner s-th species particles to the inner free electrons.
$\dot{\Omega}_{\mathrm{rad}}$	Variation in time of the mixture energy density due to radiative processes.
ω	Natural angular frequency of the quantum harmonic oscillator that represents the molecular particle (regarding the FHO model).
ω_e	Spectroscopic vibrational constant associated to the e-th electronic level.
$\dot{\omega}_s$	Variation of mass of the s-th species particles per unit of time and per unit of volume due to chemical reactions.
$\dot{\omega}_{s,v}$	Variation of mass of the s-th species particles at the vibrational level v per unit of time and per unit of volume due to collisional and radiative processes.
$\dot{\omega}_{s,e}$	Variation of mass of the s-th species particles at the electronic level e per unit of time and per unit of volume due to collisional and radiative processes.
$\dot{\omega}_{s,e,v}$	Variation of mass of the s-th species particles at the electronic level e and vibrational level v per unit of time and per unit of volume due to collisional and radiative processes.

Subscripts

0	Ground-level.
∞	Flow upstream of the shock wave.
1	Molecular particle AB (regarding the FHO model).
2	Flow immediately downstream of the shock wave; or molecular particle CD (regarding the FHO model).
a	Atomic particle.
b	Backward direction of the process.
col	Collisional broadening.
D	Doppler broadening.

e	Free electron.
e	e-Th electronic energy level; or initial electronic level; or electronic level of the higher vibronic level.
el	Electronic energy mode.
$\mathrm{el\text{-}tr_e}$	Electronic-free electron translational energy mode.
e'	Electronic level of the lower vibronic level.
f	Forward direction of the process.
G	Gaussian function.
int	Internal energy mode.
i	i-Th energy mode.
J	Rotational quantum number.
j	j-Th total energy level; or j-th energy level of some energy mode.
k	k-Th translational energy level.
l	l-Th rotational energy level.
L	Lorentzian function.
m	Molecular particle.
m	m-Th vibrational energy level.
n	n-Th electronic energy level.
p	p-Th process.
q	q-Th species.
rot	Rotational energy mode.
r	r-Th reaction.
res	Resonance broadening.
S	Stark broadening.
sp	Spin energy mode.
s	s-Th species.
tr	Translational energy mode.
$\mathrm{tr_h}$	Heavy particle translational energy mode.

$\mathrm{tr_e}$	Free electron translational energy mode.
tr-rot	Heavy particle translational-rotational energy mode.
V	Voigt function.
vib	Vibrational energy mode.
$\mathrm{vib\text{-}el\text{-}tr_e}$	Vibrational-electronic-free electron translational energy mode.
v	v-Th vibrational quantum number; or initial vibrational quantum number; or vibrational quantum number of the higher vibronic level.
v'	Vibrational quantum number of the lower vibronic level.

Superscripts

$*$	Thermodynamic equilibrium condition.
Blue	"Blue" radiation.
D	Dissociation.
e	Electronic level of the higher vibronic level.
e'	Final electronic level; or electronic level of the lower vibronic level.
ie	Induced emission.
IR	Infra-red radiation.
l	l-Th wavelength interval.
Red	"Red" radiation.
se	Spontaneous emission.
s	s-Th species.
VUV	Vacuum ultra-violet radiation.
v	Vibrational quantum number of the higher vibronic level.
v'	Final vibrational quantum number; or vibrational quantum number of the lower vibronic level.

Mathematical entities

$\cdot$	Product.
$[\,]^*$	Complex conjugate (being "[ ]" the operand).
$\dot{[\,]}$	Time derivative (being "[ ]" the operand).
$\ddot{[\,]}$	Double time derivative (being "[ ]" the operand).

$\mathrm{H}(x)$	Heaviside function of argument x.
i	Unit imaginary number.
δ_{ij}	Kronecker delta.

Acronyms

ADV	Adaption in respect of the Database for the Vibrational energy levels.
CFD	Computational Fluid Dynamics.
EAST	Electric Arc Shock Tube.
FGH	Fourier Grid Hamiltonian method.
FHO	Forced Harmonic Oscillator model.
FOPT	First Order Perturbation Theory.
IPFN	Instituto de Plasmas e Fusão Nuclear (or in english, Institute for Plasmas and Nuclear Fusion).
IR	Infra-Red radiation.
IST	Instituto Superior Técnico.
JAXA-HIEST	Japan Aerospace Exploration Agency's High-Enthalpy Shock Tunnel.
NASA	National Aeronautics and Space Administration.
NIST	National Institute of Standards and Technology.
QCT	Quasi-Classical Trajectory model.
RKR	Rydberg-Klein-Rees method.
SPARK	Software Package for Aerothermodynamics, Radiation and Kinetics.
SSH	Schwartz-Slawsky-Herzfeld model.
V-D	Vibrational-Dissociation process.
V-T	Vibrational-Translational process.
V-V-T	Vibrational-Vibrational-Translational process.
VRP	Vibrational Redistribution Procedure.
VUV	Vacuum Ultra-Violet radiation.

Glossary

Boltzmann distribution	The Boltzmann distribution associated to an energy mode of the particles, corresponds to the population distribution of these particles with respect to the different energy levels of this energy mode, if its self-equilibrium was reached.
CFD	Computational Fluid Dynamics (CFD) is a branch of Fluid Mechanics that uses numerical methods and algorithms to solve problems involving fluid flows.
Chemical equilibrium	Chemical equilibrium with respect to the interior of an element of matter corresponds to a condition in which there's no change of its chemical composition.
Chemical kinetics	The chemical kinetics of a system correspond to the rates of the chemical reactions that occur in them.

Energy mode self-equilibrium	An energy mode of particles that compose an element of matter is said to be in self-equilibrium, or in equilibrium with itself, if the energy (associated to that energy mode) transferred between the particles, due to interactions, is such, that no heat transfer (associated to that energy mode) occurs inside the element of matter. For instance, if a body, with a sufficiently higher dimension than the typical one of the particles, was present in the element of matter when the energy mode self-equilibrium was reached, no energy from that energy mode would be transferred to the body. If this condition is satisfied, a temperature specific to that energy mode can be attributed to the element of matter.
Excitation kinetics	The excitation kinetics of a system correspond to the rates of the excitation and de-excitation processes that occur in them.
Mechanical equilibrium	Mechanical equilibrium with respect to the interior of an element of matter corresponds to a condition in which the transfer of momentum between its particles, due to interactions, is such, that the produced internal forces are balanced. For instance, if a body, with a sufficiently higher dimension than the typical one of the particles, was present in the element of matter when the mechanical equilibrium was reached, the sum of all interaction forces that act on it would be null. If this condition is satisfied, a pressure can be attributed to the element of matter.

Multi-temperature model	A multi-temperature model is a thermodynamic model which assumes that all energy modes of the particles are in self-equilibrium or even in equilibrium with some other. Multiple temperatures should therefore be assigned to the system, each one associated to a single or combination of energy modes.
Plasma	Plasma is one of the known four states of the matter, being the other three the solid, liquid and gas. A plasma has charges (ions and free electrons) in its composition, meaning that such matter can conduct electricity, produce magnetic fields, and respond strongly to electromagnetic forces.
Radiative equilibrium	Radiative equilibrium with respect to the interior of an element of matter corresponds to a condition in which the absorption and emission of radiation by the particles is balanced (both in intensity and energy).
SPARK	Software Package for Aerothermodynamics, Radiation and Kinetics (SPARK) is a code for the numerical simulation of hypersonic non-equilibrium flows, developed by Lopez et al. and being maintained at the University of Illinois at Urbana-Champaign (UIUC) and at the research unit Instituto de Plasmas e Fusão Nuclear (IPFN) of Instituto Superior Técnico (IST).
Shock tube	A shock tube is a ground-based test facility used for the study of the chemical and excitation kinetics, as well as heat transfer on a post-shock flow. In a shock tube, a shock wave is generated by the rupture of a diaphragm that separates two sections of the tube: one containing a gas at very high pressure and the other containing a gas at low pressure. The low pressure gas is the one being tested, which is subjected to post-shock high temperature phenonema for a very brief period of time.

Single-temperature model	A single-temperature model is a thermodynamic model which assumes thermal equilibrium, i.e. all energy modes of the particles are considered to be in equilibrium with each other. These energy modes are described by a single temperature.
State-to-state model	A state-to-state model is a thermodynamic model which assumes that some energy modes of the particle are not in self-equilibrium, and therefore the respective energy levels need to be dealt one by one.
Thermal equilibrium	Thermal equilibrium with respect to the interior of an element of matter corresponds to a condition in which all their energy modes are in self-equilibrium and the respective temperatures are identical - therefore, a single temperature is enough to describe all of the particles energy modes. One can also say that in thermal equilibrium, the energy modes are in equilibrium with each other, besides themselves.
Thermochemistry	The thermochemistry of a system corresponds to the heat energy associated to the chemical reactions and physical transformations occurring in them.
Thermodynamic equilibrium	Thermodynamic equilibrium is a condition of both mechanical, thermal, chemical and radiative equilibrium.

Chapter 1

Introduction

> "If you want to learn about nature, to appreciate nature, it is necessary to understand the language that she speaks in."
>
> — Richard P. Feynman

1.1 A synopsis on atmospheric entry flows

When a body from the outer space enters the atmosphere of a planet, a speed higher than the speed of sound (a *supersonic speed*) is reached, producing a *shock wave*. This corresponds to a propagating disturbance that causes an abrupt increase in temperature, pressure and density of the gas. Let's assume here that the atmosphere is solely composed by heavy particles[1]. The above-mentioned temperature is associated to the *translational energy mode* of the particles, being called *heavy particle translational temperature*, T_{tr_h}. The fast collisions between the gas particles induce a very rapid redistribution of their translational energy - the new distribution can be proved to be a *Boltzmann distribution* - and *translational equilibrium* is said to occur [1]. Only in these conditions a translational temperature can be attributed to the gas.

In the flowfield between the shock wave and the body - termed *shock layer* - a lot of physical phenomena occur besides the abrupt change in the translational mode of the particles. The increase of the translational temperature is associated to an increase of the relative speed between the colliding particles as well as an increase of the number of collisions per unit of time. Collisions in these circumstances induce an excitation of the rotational and vibrational modes of the molecular particles, with the cost of some of the translational energy being transformed into rotational and vibrational ones, which in its turn reduces the translational temperature [1]. The rotational excitation occurs almost as fast as the translational one (except for cases in which the gas is composed by molecular hydrogen [1]) and, therefore, a *rotational temperature* T_{rot} being equal to the translational temperature T_{tr_h} can almost immediately be defined. This equality means that a designation for the combination of both temperatures may be employed: the *heavy particle translational-rotational temperature* $T_{\text{tr}_\text{h}\text{-rot}} = T_{\text{tr}_\text{h}} = T_{\text{rot}}$. Translational

---

[1] A heavy particle corresponds to a particle with a mass equal or greater than the mass of the proton. A heavy particle then needs to be an atomic or a molecular particle.

and rotational excitations are much more faster than vibrational excitation (except, again, for cases in which the gas is composed by molecular hydrogen [1]), and translational-rotational equilibrium can be assumed to occur even before the commence of the vibrational excitation. With the excitation of the rotational and vibrational modes, comes the dissociation of the molecular particles, occurring through overstretching of the vibrational stroke or centrifugal tearing, by collisions with other particles [1]. Such processes produce atomic particles. The higher the rotational or vibrational energy of the molecular particle, the higher the probability of the particle to suffer dissociation (since less energy is required to cause the dissociation). Therefore, the dissociation process is preferential to the highly rotationally and vibrationally excited molecular particles, meaning an aftermath reduction of the number of these particles in the gas. Also, dissociation requires energy, which is supplied by the translational energy of the colliding particles, reducing even more the translational temperature. Since dissociation is preceded by excitation of the molecular particles, an interval of time called *incubation period* can be defined, corresponding to the period in which rotational and vibrational excitation occur without dissociation. With the presence of atomic particles in the flow, comes the possibility of occurring *associative ionisation reactions* in which the atomic particles associate, creating excited molecular particles, that spontaneously ionise, producing ionic molecular particles and free electrons. The produced ions and free electrons may conduct electricity, produce magnetic fields, and respond strongly to electromagnetic forces - the medium is then termed a *plasma* (plasma is one of the known four states of the matter, being the other three the solid, liquid and gas). Collisions between the free electrons and atomic particles will excite and ionise them, freeing even more electrons. Similarly, collisions between free electrons and molecular particles will excite and ionise them, and may even cause their dissociation. The electronic excitation of heavy particles (i.e. excitation of the bound electrons of heavy particles) by electron impact is much more efficient than by heavy particle impact [1], and therefore, the electronic excitation process has its major importance in the region of the flow where free electrons are present.

Excited particles may de-excite by a process termed *spontaneous emission*, which consists in the emission of a *photon* without any kind of external stimulus (therefore in a “spontaneous” way), lowering the *particle internal energy*. A *radiation field* is then created, inducing the emission of even more photons (by a process called *induced emission*). Some of the emitted photons are absorbed by the particles in the plasma and in the body, causing their excitation. The body is then subjected to *radiative heating*. Also, the emitted photons may even dissociate or ionise the particles [2].

After a considerable amount of collisions, the plasma begins a process of *relaxation*, i.e. it initiates an evolution to *thermodynamic equilibrium*. However, equilibrium may not be reached since as the flow gets closer and closer to the body, new interactions between the two start to occur. The density of the plasma increases due to compressibility effects, and a *boundary layer* is formed, in which the viscosity effects are significant (due to a coexistence of a flow and a stationary wall), decelerating the flow - some of the *flow translational kinetic energy* is converted to *thermal energy*. Also, due to the temperature of the particles in the boundary layer being much higher than the one of the particles in the surface of the body, there’s a transfer of energy, by the name of *convective heating*, from the former to the latter. The plasma temperature therefore decreases in the boundary layer, with the possibility of occurring atomic particles association, and recombination of ionic particles with electrons [3].

This whole wording is just a small introduction to the relevant phenomenology that occurs in atmospheric entry flows. Such introduction is necessary to properly define *hypersonic flows* - the flow upstream of a shock wave is said to be hypersonic if the herein described physical phenomena (with less or more accentuation) are present in the flow downstream of the wave, being the upstream *Mach number*[2] much greater than unity, i.e $\mathrm{Ma}_\infty \gg 1$.

1.2 Numerical models

1.2.1 Thermodynamic models

The term "non-equilibrium" may seem too vague when heard for the first time. There are a lot of different types of non-equilibrium that may occur in the flow: *mechanical non-equilibrium*, *chemical non-equilibrium*, *radiative non-equilibrium*, *thermal non-equilibrium* and *energy mode self-non-equilibrium.* And from these five terms, even more complicated ones can be built to represent a simultaneity of different types of non-equilibrium, as is example the *thermochemical non-equilibrium*, corresponding to a condition of both thermal and chemical non-equilibria.

A mechanical equilibrium with respect to the interior of an element of fluid corresponds to a condition in which the transfer of momentum between its particles, due to interactions, is such, that the produced internal forces are balanced. For instance, if a body, with a sufficiently higher dimension than the typical one of the particles, was present in the element of fluid when the mechanical equilibrium was reached, the sum of all interaction forces that act on it would be null. If this condition is satisfied, a pressure p can be attributed to the element of fluid.

The interior of an element of fluid is in chemical equilibrium if there's no tendency for a change in its chemical composition. As referred in Section §1.1, there is a cascade of physical phenomena in the post-shock flows which changes its chemical composition as an aftermath, and therefore one shouldn't assume that chemical equilibrium is reached in those cases.

Radiative equilibrium with respect to the interior of an element of fluid corresponds to a condition in which the internal absorption and emission of radiation by the particles is balanced (both in intensity and energy). Such condition is not observed in post-shock flows, and therefore, radiative equilibrium shouldn't be assumed [2].

Thermal equilibrium occurs if the energy transferred between the particles, due to interactions, is such, that no heat transfer occurs inside the element of fluid. For instance, if a body, with a sufficiently higher dimension than the typical one of the particles, was present in the element of fluid when the thermal equilibrium was reached, no heat would be transferred to the body. If this condition is satisfied, a temperature T can be attributed to the element of fluid, and the population of the particles energy levels would follow a Boltzmann distribution, with the temperature T as parameter.

An energy mode of the particles that constitute some element of fluid is in self-equilibrium if the

---

[2] The Mach number of a flow in a point corresponds to the ratio between the flow and sound speeds evaluated at that same point.

conditions said above about thermal equilibrium were true for that energy mode in particular. Therefore, if the i-th energy mode associated to the particles of the s-th species is in self-equilibrium, a temperature $T_{s,i}$ can be assigned. The population of the particles energy levels in that energy mode would follow a Boltzmann distribution, with the temperature $T_{s,i}$ as parameter. The term "self-equilibrium" is used to emphasize the fact that the mode is in equilibrium with itself but not with the others. Thermodynamic models which account the possibility of energy modes to be in self-equilibrium correspond to the so-called *multi-temperature models*. Well known examples of multiple-temperature models are the *Lee's three-temperature model* [4] and the *Park's two-temperature model* [5]. In both models it's assumed that all heavy species have the same temperature values for the same type of energy modes. Lee and Park consider other two common assumptions. The first one regards the tendency that the rotational mode has to very quickly equilibrate with the heavy particles translational mode - a heavy particle translational-rotational temperature, $T_{\mathrm{tr_h\text{-}rot}} = T_{\mathrm{tr_h}} = T_{\mathrm{rot}}$, is then defined. The second assumption regards the strong dependency that the electronic excitation of particles have on the translation of free electrons - this proposition is particular true for the low laying electronic levels of the particles. Park considers one more assumption than Lee, corresponding to a fast energy transfer between the translational mode of free electrons and the vibrational mode of molecular particles - which is particularly true for the case of molecular nitrogen N_2 [5]. Therefore Lee considers two temperatures besides the heavy particle translational-rotational one - the vibrational temperature T_{vib} and the electronic-free electron translational temperature $T_{\mathrm{el\text{-}tr_e}} = T_{\mathrm{el}} = T_{\mathrm{tr_e}}$ - and Park considers one - the vibrational-electronic-free electron translational temperature $T_{\mathrm{vib\text{-}el\text{-}tr_e}} = T_{\mathrm{vib}} = T_{\mathrm{el}} = T_{\mathrm{tr_e}}$.

As pointed out by Park [6], numerical results obtained through multi-temperature models are significantly more agreeable with the accurate experimental ones for the post-shock conditions than the *single-temperature models*, which assume thermal equilibrium. Several works such as the ones of Candler [7], Hornung [8] and Lobb [9] evidenced that the single-temperature model predicts the flow to be closer to thermodynamic equilibrium than it actually is. The use of the single-temperature model may then lead for incorrect predictions for the aerodynanamic characteristics of a hypersonic vehicle. And as Park [6] said "[b]ecause of this mistake, most people thought that the flight regime of the most hypersonic vehicles would be in the equilibrium regime, while, in reality, they would be in the nonequilibrium regime. The mistake is caused by using the one-temperature model".

There is the possibilty of the particles vibrational energy mode not being in self-equilibrium in some post-shock flows, as shown by Candler et al. [10], which means that a vibrational temperature T_{vib} can't even be assigned, and that the population of the vibrational energy levels doesn't follow a Boltzmann distribution. Since the distribution of the vibrational energy levels is unknown in such cases, there is no chance to treat all the vibrational levels as a group. Each vibrational energy level does need to be treated individually. The electronic energy mode and even the rotational energy mode may also not be in self-equilibrium, as referred by Munafó et al. [11], and a similar procedure with respect to the rotational and electronic energy levels would be needed. Such procedures require models which are specific to the internal energy levels of the involved particles - the so-called *state-to-state models* (or *collisional-radiative models*) [12]. Dealing with internal levels introduces an extensive set of variables to the problem, requiring much more computational resources than for the case of the multi-temperature models. The higher the number of specified internal energy modes the higher the associated computational costs. Therefore, the simultaneous assumption of self-equilibrium with respect to the fastest equilibrating energy modes, such as the rotational one, may be convenient if not necessary. And in fact, this approach is commonly taken: the most part of the existing state-to-state models aren't rotational-specific [12]. In this work a vibronic[3]-specific state-to-state model was considered.

1.2.2 Kinetic models

Models for the plasma kinetics, i.e. the chemical and excitation processes, are required to properly describe the phenomenology in post-shock flows. These models may be purely theoretical, semi-empirical (with a theoretical form, calibrated by experimental results) or purely empirical (solely described by experimental results). Both valid theoretical and semi-empirical models should agree with the experimental results. However, a significant part of the experimental data is obtained at room temperature (around 300 K), without specificity of the internal energy levels of the particles. Therefore, the validity of some of the theoretical and semi-empirical models may be only assured for the low temperature regime, and not for each internal energy level but for the overall contribution of the set. When the process isn't reasonably well understood, there's no option but to consider some crude assumptions for the dependencies on the temperature and internal levels, such as the *vibrational redistribution* procedure employed by João Vargas [13], and by Julien Annaloro [14] in their thesis, the latter in a more sophisticated form.

One important excitation process that will be further addressed in this work is the vibrational excitation of molecular particles by heavy particle impact. Adamovich et al. [15–17] did a good job reviewing the currently available models that can describe this particular process. One of the simplest models is the *Schwartz—Slawsky—Herzfeld model* (SSH) [18]. This is a *semiclassical model*[4] derived under a *first-order perturbation theory* (FOPT) approach, assuming collinearity of the collision (all nuclei and the collision velocity vector are disposed in a single line), harmonicity of the molecular particles (internuclear forces follow Hooke's law), and an exponential repulsive interaction potential. Due to the first-order perturbation theory approach, only single vibrational energy level jumps are regarded to occur in the excitation or de-excitation process, which is solely true for cases of small collision speeds. The model shouldn't therefore be employed in numerical simulations of entry post-shock flows, due to the very high heavy particle translational temperatures that occur in those conditions. The most precise models include the exact *quantum mechanical models*, like the one suggested by Secrest and Johnson [19], and semiclassical models like the one developed by Billing [20]. The latter, which corresponds to a *Quasi-Classical Trajectory* model (QCT) [21], considers three-dimensional collisions, and a more reallistic interaction potential. Both the model of Secrest and Johnson, and the one of Billing, require a considerable amount of computational resources, limiting their applicability. An alternative model which is much more accurate than the SSH model, and at the same time more practical than the two above mentioned, is the *Forced Harmonic Oscillator model* (FHO) [17]. It was originally conceived by Kerner

---

[3] The term vibronic is an agglutination of two other terms: **vib**rational and elect**ronic**.

[4] In semiclassical models both *Quantum Mechanics* and *Classical Mechanics* laws are taken into consideration.

[22] and Treanor [23], being only applicable for the case of a molecular particle-atomic particle collision. It consisted of a non-perturbative semiclassical model, assuming collinearity of the collision, harmonicity of the molecular particle and an exponential repulsive interaction potential. It was then generalised by Zelechow et al. [24] for the case of molecular particle-molecular particle collisions. At last, Adamovich et al. [15–17] applied corrections in the model to account the anharmonicity of the molecular particles, the attractive long-range part of the interaction potential, the possible non-collinearity of the collision, the case in which the molecular particles are non-identical, and energy conservation. The resultant model was shown to agree considerably well with the results obtained through the state-of-the-art Billing's model [20]. The work of M. Lino da Silva et al. [25], which considers the model of Adamovich et al. additionally regarding a more accurate method for computing the energies of the vibrational levels of the colliding particles, endorses this agreeability.

Other important excitation processes that should be accounted are the vibronic transitions of molecular particles by heavy particle impact. There are two well-known theoretical models which deal with the homologous processes for the case of atomic particles - the electronic transitions of atomic particles by atomic particle impact: the *Landau-Zener model* [26, 27] and *Rosen-Zener-Demkov* model [28, 29]. In this work, the possibility of these models being extended to the case of vibronic transitions of molecular particles by heavy particles will be studied. Empirical models may be used alternatively, such as the *exponential gap law* considered in the works of Bachmann et al. [30, 31], and a different kind of exponential gap law regarded in the works of Katayama et al. [32–34]. In the latter, the so-called *Franck-Condon factors* are employed. Katayama et al. [35] even suggests a different model, which takes into account the intermolecular potential well depth of the interaction.

1.3 The case of Earth atmospheric entries

When considering Earth atmospheric entries, one needs to deal with air. It is only below the *Kármán line* ($\sim$ 100 km) that air is dense enough to interact strongly with an spacecraft or meteor in its entry, being the chemical composition of the air almost constant in that layer of the atmosphere. The air components in such conditions are molecular nitrogen N_2, with a *mole fraction* of $x_{N_2} := N_{N_2}/N = 78.08$ %, molecular oxygen O_2 with $x_{O_2} = 20.95$ %, water H_2O with $x_{H_2O} \sim 2 \times 10^{-6}$ - 3×10^{-2} %, argon Ar with $x_{Ar} = 9.34 \times 10^{-3}$ %, and some others whose mole fractions are negligible [36]. However, it is important to add that the water mole fraction is only relevant below the *tropopause* ($\sim$ 11 km), and since the body should suffer most of the entry effects above that limit, one can disregard water in the entry environment. As referred in the Section §1.1, a lot of physical phenomena occurs downstream of the entry shock wave, causing a change in the chemical composition of the medium. By neglecting the small mole fraction of argon and the other trace chemical species, one can expect at least eleven species in the post-shock flow - N, O, N_2, O_2, NO, O^+, N^+, N_2^+, O_2^+, NO^+ and e^- - resultant from the two ones in the unperturbed flow - N_2 and O_2 [1]. There are therefore a lot of chemical species to take into account in an Earth atmospheric entry, which complicates the job of creating a reliable model that replicates all the inherent physical phenomena in the post-shock flow. One smart move is to start by building a less extensive model dedicated to hypothetical entry flows composed by solely one chemical species upstream of the shock wave, N_2 or O_2. This work will only deal with pure nitrogen hypersonic flows, and therefore, only five post-shock chemical species were considered - N, N_2, N^+, N_2^+ and e^-. Also, this work will be restricted to *zero-dimensional* and *one-dimensional* simulations, being these used to describe the physical phenomena obtained in *shock tube* tests. Figure 1.1 tries to depict such phenomena. A zero-dimensional simulation is particularly useful for a focused study on the chemical and excitation kinetics of the plasma from some initial conditions, disregarding fluid flow effects [37]. It runs faster than a one-dimensional simulation since it considers the momentum transfer between elements of fluid to be negligible, solving one less differential equation.

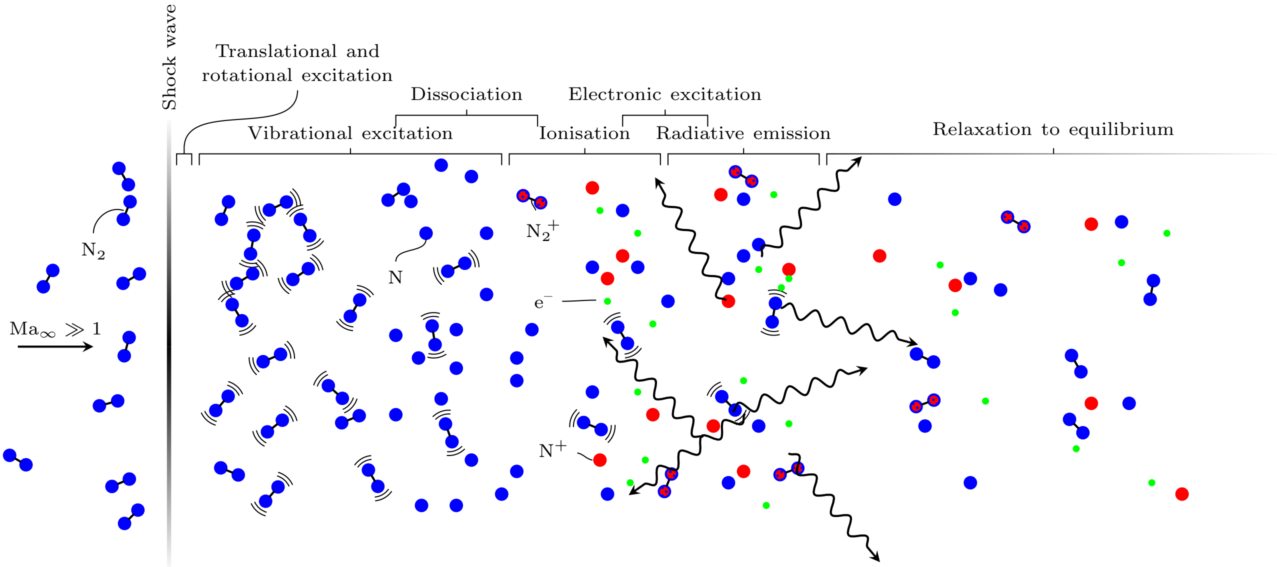

Figure 1.1: Representation of the post-shock physical phenomena that occur in a pure nitrogen hypersonic flow, inside a shock tube.

1.4 Objectives

The main objective of this study is to create a database of chemical and excitation rates, as well as a full set of vibrational and electronic energy levels of the species involved in a pure nitrogen post-shock flow. This can only be achieved by accomplishing a set of smaller objectives:

- Computation of the *internuclear potential curves* associated to N_2 and N_2^+, by employing the *Rydberg–Klein–Rees method* allied with an extrapolation procedure for the short and long-range parts. Computation of the vibrational energy values by applying the *Fourier Grid Hamiltonian method* and using the previously obtained internuclear potential curves;
- Computation of rates for vibrational transition and dissociation of N_2 and N_2^+ by collisions with the heavy particles (N, N_2, N^+ and N_2^+), using the Forced Harmonic Oscillator model. Computation of the respective thermal rates of dissociation (the dissociation rates of the involved molecular particles, at thermal equilibrium) and their comparison with numerically and experimentally determined values taken from the literature;

- Study of the possibility of computation of rate coefficients for transitions between vibronic levels of N_2 by collisions with heavy particles, through the Landau-Zener model and the Rosen-Zener-Demkov model;
- Zero and Euler one-dimensional numerical simulations, regarding vibronic-specific state-to-state approaches, of the high-temperature phenomena that occur in pure nitrogen post-shock flows, employing the conceived database in the SPARK code [38]. Calibration and validation of the database by comparison of the radiative field obtained in the simulations with the radiative field measured in the test 62 of the EAST shock tube in 2018 [39].

By reaching this milestone, the reader should now be able to decipher the title of the thesis: "High-temperature kinetic and thermodynamic models for nitrogen plasmas". The term "high-temperature" is with respect to the high temperatures that entry post-shock flows can achieve, "kinetic" is with respect to the modelling of chemical and excitation kinetics that occur in those conditions, "thermodynamic models" is with respect to the modelling of the thermodynamic variables (temperatures, enthalpies, internal energies, etc.), and "nitrogen plasmas" is with respect to the state of the matter in the post-shock flow, which, upstream of the shock wave, corresponds to gaseous nitrogen.

1.5 Thesis Outline

This work is divided into five parts:

- Chapter 1 (the present one), which acquaints the reader to the the post-shock physical phenomena that typically occur in atmospheric entries, the state-of-the-art of the models used in the numerical simulations of such entries, the objectives of this thesis and its outline;
- Chapter 2, that provides the mathematical formulation of the models introduced in Chapter 1, and enunciates relations for the involved physical variables and their dynamics;
- Chapter 3, which presents the application of the theory reported in Chapter 2 to the computation of rate coefficients values of the processes regarded in the kinetic database, and the way that the governing equations were adapted for the simulation of post-shock flows generated by a shock tube;
- Chapter 4, that reports the results of the zero and one-dimensional SPARK simulations of three benchmark shots executed in the EAST 62$^{\text{nd}}$ campaign, and presents the obtained values for the radiation variables, mole fractions, temperatures and evolution to equilibrium. A discussion on the discrepancies from the experimental results is made, possible causes for them are enunciated, and sensibility tests on the simulation parameters are reported;
- Chapter 5, which presents the conclusions of this work, its achievements, and modifications that may be tried in a near future in order to achieve better results.

Chapter 2

Background

2.1 Energy modes of a particle

The energy of a particle measured relatively to some point in space is a result of the motion of all its parts: nuclei and electrons. The motion can be described as a combination of two other: the motion of the *centre of mass* of the particle and the motion of its parts relatively to it. Therefore, the energy of the particle corresponds to $\epsilon' = \epsilon'_{\mathrm{tr}} + \epsilon'_{\mathrm{int}}$, where ϵ'_{tr} is the translational kinetic energy of its centre of mass and ϵ'_{int} the particle internal energy, i.e. the energy associated to the motion of the nuclei and electrons relatively to the centre of mass [2]. Due to the fact of the electrons having a much lower mass than the nuclei, they move much faster, and, therefore, the motion of the electrons and the motion of the nuclei can be considered to be independent from each other - this is the so-called *Born–Oppenheimer approximation* [40]. On the other hand, the motion of the nuclei relatively to the centre of mass corresponds to a combination of rotation, vibration and *spin* (rotation upon themselves). Nuclear spin can be neglected since it doesn't play any role in the chemical and excitation processes [2]. Although rotation and vibration are in some way coupled, for most engineering purposes this coupling can be disregarded [2]. The internal energy of the particle is then a sum of the contributions of each energy mode, i.e. $\epsilon'_{\mathrm{int}} = \epsilon'_{\mathrm{rot}} + \epsilon'_{\mathrm{vib}} + \epsilon'_{\mathrm{el}}$.

In the above paragraph it was assumed that the depicted particle was a molecular one, therefore, having multiple nuclei and electrons in their internal structure. Some particles can't express some of the stated energy modes: atomic particles are constituted by a single nucleus, and no rotation or vibration can be associated to them, and free electrons can only translate and spin[1]. Mathematically, the energies of a molecular particle, atomic particle and free electron are given by

$$\epsilon'_{\mathrm{m}} = \epsilon'_{\mathrm{tr}} + \epsilon'_{\mathrm{rot}} + \epsilon'_{\mathrm{vib}} + \epsilon'_{\mathrm{el}} \ , \quad (2.1) \qquad \epsilon'_{\mathrm{a}} = \epsilon'_{\mathrm{tr}} + \epsilon'_{\mathrm{el}} \ , \quad (2.2) \qquad \epsilon'_{\mathrm{e}} = \epsilon'_{\mathrm{tr}} + \epsilon'_{\mathrm{sp}} \ , \quad (2.3)$$

respectively. The translational, rotational, and vibrational energy modes of a diatomic molecular particle, and the electronic energy mode of an atomic particle are depicted by Figures 2.1, 2.2, 2.3 and 2.4.

---

[1] Spin is the only form of internal energy of the free electron, meaning that $\epsilon'_{\mathrm{e,int}} = \epsilon'_{\mathrm{sp}}$.

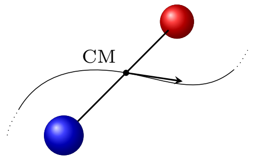

Figure 2.1: Representation of the translational energy mode of a diatomic molecular particle.

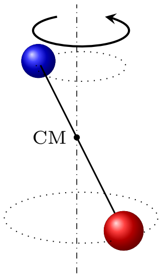

Figure 2.2: Representation of the rotational energy mode of a diatomic molecular particle.

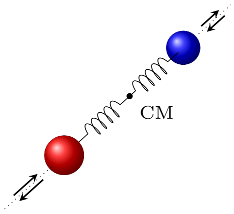

Figure 2.3: Representation of the vibrational energy mode of a diatomic molecular particle.

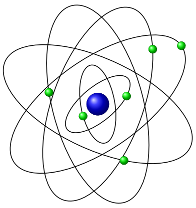

Figure 2.4: Representation of the electronic energy mode of an atomic particle.

It's well known that particles follow the laws of *Quantum Mechanics*. According to the theory of Quantum Mechanics, the motion of the particles and their internal structure agree with restrictedly defined directions and intensities being these discrete, or in other words, *quantised*. The combinations of directions and intensities are termed *energy states*, or simply *states* of the particle [2]. Due to the fact that motion has an energy associated to it, the quantisation of the former leads to the quantisation of the latter, and therefore, the energy values of a particle are also discrete, being termed *energy levels*. An energy level may assume multiple energy states, being said to be *degenerate* and having a *degree of degeneracy* g equal to the number of such states. For each energy mode there's an energy level whose value is the lowest of them all - the *ground energy level*. Let $\epsilon'_{i,j}$ be the energy associated to the j-th level of the i-th mode, and $\epsilon_{i,0}$ the energy of the ground level. From these two the so-called *sensible energy* may be defined, $\epsilon_{i,j} = \epsilon'_{i,j} - \epsilon_{i,0}$. To better differentiate the nomenclature in respect of the energy ϵ' and the sensible energy ϵ of a particle, the former will be for now on termed *absolute energy*. Since the energies of all modes are quantised, the sum of them is also quantised, which gives the opportunity of defining a *total energy level*. The sensible energy of the j-th total energy level of a molecular particle corresponds to the sum of the sensible energies of the respective k-th translational level, l-th rotational level, m-th vibrational level and n-th electronic level, $\epsilon_{\mathrm{m},j} = \epsilon_{\mathrm{m},k,l,m,n} = \epsilon_{\mathrm{tr},k} + \epsilon_{\mathrm{rot},l} + \epsilon_{\mathrm{vib},m} + \epsilon_{\mathrm{el},n}$. And the total degree of degeneracy is given by the multiplication between the degrees of degeneracy of the levels, $g_{\mathrm{m},j} = g_{\mathrm{m},k,l,m,n} = g_{\mathrm{tr},k} \cdot g_{\mathrm{rot},l} \cdot g_{\mathrm{vib},m} \cdot g_{\mathrm{el},n}$. Although decoupling of the energy modes was assumed (leading to relations (2.1), (2.2) and (2.3)) it's possible to account, in an approximate way, the coupling by applying corrections on the constants that describe each motion [40]. As result, a set of vibrational levels is defined for each electronic level, and a set of rotational levels is defined for each vibrational level (see Appendix A). The vibrational sensible energy and its degree of degeneracy should now take into account the label for the respective electronic level, and the rotational sensible energy and its degree of degeneracy should take into account the labels for the respective vibrational and electronic levels. For the case of a molecular particle one has then

$$\epsilon_{\mathrm{m},j} = \epsilon_{\mathrm{tr},k} + \epsilon_{\mathrm{rot},n,m,l} + \epsilon_{\mathrm{vib},n,m} + \epsilon_{\mathrm{el},n} \ , \quad (2.4) \qquad g_{\mathrm{m},j} = g_{\mathrm{tr},k} \cdot g_{\mathrm{rot},n,m,l} \cdot g_{\mathrm{vib},n,m} \cdot g_{\mathrm{el},n} \ . \quad (2.5)$$

2.2 The distribution of the particles in their energy levels

2.2.1 The case of the single-temperature model

If the system has reached thermal equilibrium, it's possible to show that the number of particles of the s-th species (let's assume that it is molecular) which are in the j-th total energy level is given by the so-called Boltzmann distribution [2]

$$N_{s,j} = N_s \frac{g_{s,j}\, e^{-\frac{\epsilon_{s,j}}{k_B T}}}{Q_s} = N_s \frac{g_{s,\mathrm{tr},k} \cdot g_{s,\mathrm{rot},n,m,l} \cdot g_{s,\mathrm{vib},n,m} \cdot g_{s,\mathrm{el},n}\, e^{-\frac{\epsilon_{s,\mathrm{tr},k}+\epsilon_{s,\mathrm{rot},n,m,l}+\epsilon_{s,\mathrm{vib},n,m}+\epsilon_{s,\mathrm{el},n}}{k_B T}}}{Q_s} = N_{s,k,l,m,n} \ , \tag{2.6}$$

in which k_B is the *Boltzmann constant*, T is the temperature of the system, N_s is the number of s-th species particles, and Q_s is their *partition function*. The partition function corresponds to

$$Q_s = \sum_j g_{s,j}\, e^{-\frac{\epsilon_{s,j}}{k_B T}} = \underbrace{\left(\sum_k g_{s,\mathrm{tr},k}\, e^{-\frac{\epsilon_{s,\mathrm{tr},k}}{k_B T}} \right)}_{:=Q_{\mathrm{s,tr}}} \cdot \underbrace{\left\{ \sum_n g_{s,\mathrm{el},n}\, e^{-\frac{\epsilon_{s,\mathrm{el},n}}{k_B T}} \overbrace{\left[\sum_m g_{s,\mathrm{vib},n,m}\, e^{-\frac{\epsilon_{s,\mathrm{vib},n,m}}{k_B T}} \underbrace{\left(\sum_l g_{s,\mathrm{rot},n,m,l}\, e^{-\frac{\epsilon_{s,\mathrm{rot},n,m,l}}{k_B T}} \right)}_{:=Q_{s,\mathrm{rot},n,m}} \right]}^{:=Q_{s,\text{vib-rot},n}} \right\}}_{:=Q_{\mathrm{s,int}}} \ , \tag{2.7}$$

being $Q_{s,\mathrm{tr}}$ the *translational partition function*, and $Q_{s,\mathrm{int}}$ the *internal partition function.* This latter quantity may be expressed through sums with respect to n and m involving the *vibrational-rotational partition functions* $Q_{s,\text{vib-rot},n}$ and the *rotational partition functions* $Q_{s,\mathrm{rot},m,n}$.

The reader should be warned about the very particular nomenclature that is being employed in this section. The label j represents a total energy level, and the labels k, l, m and n represent the respective energy levels of the translational, rotational, vibrational and electronic modes. The subscripted labels in the symbol for the number of particles N define the specificity of the quantity with respect to the energy modes. For example, $N_{s,k,m,n}$ is the number of s-th species particles that are in the k-th translational, m-th vibrational and n-th electronic levels, and $N_{s,k,m} = \sum_n N_{s,k,m,n}$ is the number of s-th species particles that are in the k-th translational and m-th vibrational levels.

2.2.2 The case of the multi-temperature model

If the system is described by a temperature for each energy mode, $T_{\mathrm{tr_h}}$, T_{rot}, T_{vib}, T_{el} and $T_{\mathrm{tr_e}}$, the number of particles of the s-th species (let's assume that it is molecular) in the j-th total energy level is

$$N_{s,k,l,m,n} = N_s \frac{g_{s,\mathrm{tr},k} \cdot g_{s,\mathrm{rot},n,m,l} \cdot g_{s,\mathrm{vib},n,m} \cdot g_{s,\mathrm{el},n}\, e^{-\left(\frac{\epsilon_{s,\mathrm{tr},k}}{k_B T_{\mathrm{tr_h}}} + \frac{\epsilon_{s,\mathrm{rot},n,m,l}}{k_B T_{\mathrm{rot}}} + \frac{\epsilon_{s,\mathrm{vib},n,m}}{k_B T_{\mathrm{vib}}} + \frac{\epsilon_{s,\mathrm{el},n}}{k_B T_{\mathrm{el}}} \right)}}{Q_s} \ . \tag{2.8}$$

In this model, the partition functions to deal with are the ones stated in §2.2.1 with T substituted by the temperature of the energy mode which they refer to. It's worthy to mention here two convenient models for the translational and rotational partition functions. The former can be obtained by solving the *Schrödinger equation*[2] for a free particle[3] of the s-th species with a mass m_s, inside a rectangular rigid box of volume V [2]. And the latter can be obtained by solving the Schrödinger equation for a *rigid rotor* (or *dumb-bell*) with a constant moment of inertia $I_{s,n,m}$ [2]. These are given by

$$Q_{s,\mathrm{tr}}(T_{\mathrm{tr}_s}, V) = V\left(\frac{2\pi m_s k_B T_{\mathrm{tr}_s}}{h^2}\right)^{\frac{3}{2}} \ , \qquad (2.9) \qquad\qquad Q_{s,\mathrm{rot},n,m}(T_{\mathrm{rot}}) = \frac{k_B T_{\mathrm{rot}}}{\sigma_s B_{s,n,m}} \ , \qquad (2.10)$$

respectively, being $T_{\mathrm{tr}_s} = T_{\mathrm{tr_h}}$ if the s-th species particle corresponds to a heavy particle, or $T_{\mathrm{tr}_s} = T_{\mathrm{tr_e}}$ if it corresponds to a free electron. The term $B_{s,n,m} = h^2/8\pi^2 I_{s,n,m}$ is the rotational function B_v (given by (A.4)) associated to the n-th electronic and m-th vibrational levels, being h the *Planck constant.* And the constant σ_s corresponds to the *nuclei symmetry factor*, giving 1 if the s-th species is heteronuclear or 2 if it is homonuclear. One should also comment here about the spin partition function of the free electrons. This corresponds to $Q_{\mathrm{e,sp}} = 2$ due to the fact of the spin energy mode expressing itself through a sole energy level and two energy states.

2.2.3 The case of the vibronic-specific state-to-state model

Let's consider here a three-temperature (of temperatures $T_{\mathrm{tr_h}}$ and T_{rot} and $T_{\mathrm{tr_e}}$) vibronic-specific state-to-state model. In this model, the particles of the s-th species (let's assume that it is molecular) follow a Boltzmann distribution in the translational and rotational energy modes but not necessarily in the vibrational and electronic ones. The number of s-th species particles in the j-th total energy level corresponds to

$$N_{s,k,l,m,n} = N_{s,m,n} \frac{g_{s,\mathrm{tr},k} \cdot g_{s,\mathrm{rot},n,m,l}\, e^{-\frac{\epsilon_{s,\mathrm{tr},k}}{k_B T_{\mathrm{tr_h}}} - \frac{\epsilon_{s,\mathrm{rot},n,m,l}}{k_B T_{\mathrm{rot}}}}}{Q_{s,\mathrm{tr}} \cdot Q_{s,\mathrm{rot},n,m}} \ . \qquad (2.11)$$

2.3 Thermodynamic variables

2.3.1 The case of the single-temperature model

The thermodynamic variables of interest are the mass-specific *internal energy* e_s, *enthalpy* $h_s = e_s + p_s/\rho_s$ and the *partial pressure* p_s associated to the s-th species (let's assume that it is molecular) as well as the respective quantities for the mixture, i.e. e, h and p. The quantity $\rho_s = M_s/V$ in the definition of h_s is the mass density of the s-th species, being $M_s = N_s m_s$ the mass of s-th species particles in the system. The internal energy associated to the s-th species in an element of fluid, E_s, is not the the sum of these particles' internal energies but the sum of the energies of their relative motions (as if their bulk velocity was taken as zero). Thus, E_s, is defined as the sum of the absolute energies of the

---

[2] The Schrödinger equation is one of the fundamental equations of Quantum Mechanics. From a conceptual perspective of view, one may state that the Schrödinger equation is for Quantum Mechanics what the Newtown's equation is for Classical Mechanics.

[3] A particle is considered to be free if it isn't being subjected to any force.

s-th species particles in the element of fluid, $E_s = \sum_j \epsilon'_{s,j} N_{s,j}$. The respective mass-specific quantity $e_s = E_s/M_s = \sum_j N_{s,j}\epsilon'_{s,j}/(N_s \cdot m_s)$ may be shown to be given by

$$e_s = R_s T^2 \left[\frac{\partial\left(\ln Q_s\right)}{\partial T}\right]_V + \frac{\epsilon_{s,0}}{m_s} = \underbrace{\frac{3}{2} R_s T}_{:=e_{s,\mathrm{tr}}} + \underbrace{R_s T}_{:=e_{s,\mathrm{rot}}} + \underbrace{\frac{\bar{\epsilon}_{s,\mathrm{vib}}(T)}{m_s}}_{:=e_{s,\mathrm{vib}}} + \underbrace{\frac{\bar{\epsilon}_{s,\mathrm{el}}(T)}{m_s}}_{:=e_{s,\mathrm{el}}} + \underbrace{\frac{\epsilon_{s,0}}{m_s}}_{:=e_{s,0}} \quad , \tag{2.12}$$

where $R_s = k_B/m_s$ is the *mass-specific gas constant* of the s-th species. The models (2.9) and (2.10) were used in the derivation of (2.12). The subscripted symbol V in (2.12) means that the derivative is taken at constant volume. Equation (2.12) shows that e_s is a sum of the contributions of the different energy modes, being $\bar{\epsilon}_{s,\mathrm{vib}} = \sum_{m,n} N_{s,m,n}\epsilon_{\mathrm{vib},n,m}/N_s$ and $\bar{\epsilon}_{s,\mathrm{el}} = \sum_n N_{s,n}\epsilon_{\mathrm{el},n}/N_s$ the average vibrational and electronic energies of the s-th species particles. By considering the definition of *entropy* according to *Statistical Mechanics* and the *first law of Thermodynamics* for a chemically reactive open system in thermal equilibrium [2], one may show that

$$p_s = N_s k_b T \left[\frac{\partial\left(\ln Q_s\right)}{\partial V}\right]_{T,N_s} = \rho_s R_s T \ . \tag{2.13}$$

This result is the well-known *ideal gas law*. From (2.12) and (2.13), the mass-specific enthalpy associated to the s-th species is simply given by $h_s = e_s + R_s T$.

The mixture mass-specific variables $q \in \{e, h\}$ are related to the species ones $q_s \in \{e_s, h_s\}$ through $q = \sum_s c_s q_s$, being $c_s = M_s/M$ the *mass fraction* of the s-th species and $M = \sum_s M_s$ the mixture mass. A mixture pressure can be defined according to the *Dalton's law of partial pressures*: $p = \sum_s p_s = \rho R T$, where $\rho = M/V$ and $R = \sum_s c_s R_s$ are the mass density and the mass-specific gas constant of the mixture.

2.3.2 The case of the multi-temperature model

For the case of the multi-temperature model, e_s is given by (2.12) with T substituted by the temperature of the energy mode which the contributions refer to:

$$e_s = \left\{\sum_i R_s T_i^2 \left[\frac{\partial\left(\ln Q_s\right)}{\partial T_i}\right]_V\right\} + \frac{\epsilon_{s,0}}{m_s} = \underbrace{\frac{3}{2} R_s T_{\mathrm{tr_h}}}_{:=e_{s,\mathrm{tr}}} + \underbrace{R_s T_{\mathrm{rot}}}_{:=e_{s,\mathrm{rot}}} + \underbrace{\frac{\bar{\epsilon}_{s,\mathrm{vib}}(T_{\mathrm{vib}})}{m_s}}_{:=e_{s,\mathrm{vib}}} + \underbrace{\frac{\bar{\epsilon}_{s,\mathrm{el}}(T_{\mathrm{el}})}{m_s}}_{:=e_{s,\mathrm{el}}} + \underbrace{\frac{\epsilon_{s,0}}{m_s}}_{:=e_{s,0}} \quad . \tag{2.14}$$

In (2.14) the s-th species was assumed to be molecular. If it was instead a free electron, only the translational and ground energy level contributions would be expressed, with $T_{\mathrm{tr_h}}$ substituted by $T_{\mathrm{tr_e}}$. It can be shown that only translation contributes to the partial pressure, and, therefore, $p_s = \rho_s R_s T_{\mathrm{tr}_s}$ being $T_{\mathrm{tr}_s} = T_{\mathrm{tr_h}}$ if the particles of the s-th species are heavy particles, or $T_{\mathrm{tr}_s} = T_{\mathrm{tr_e}}$ if they are free electrons. Consequently, the mass-specific enthalpy corresponds to $h_s = e_s + R_s T_{\mathrm{tr}_s}$.

2.3.3 The case of the vibronic-specific state-to-state model

For the case of the three-temperature (of temperatures $T_{\mathrm{tr_h}}$ and T_{rot} and $T_{\mathrm{tr_e}}$) vibronic-specific state-to-state model, the vibrational and electronic energy modes may not express themselves through appropriate temperatures. The quantity e_s is then defined as

$$e_s = \left\{ \sum_{i\in\{\mathrm{tr},\mathrm{rot}\}} R_s T_i^2 \left[\frac{\partial\left(\ln Q_s\right)}{\partial T_i}\right]_V \right\} + \frac{\bar{\epsilon}_{s,\mathrm{vib}}}{m_s} + \frac{\bar{\epsilon}_{s,\mathrm{el}}}{m_s} + \frac{\epsilon_{s,0}}{m_s} = \underbrace{\frac{3}{2}R_s T_{\mathrm{tr_h}}}_{:=e_{s,\mathrm{tr}}} + \underbrace{R_s T_{\mathrm{rot}}}_{:=e_{s,\mathrm{rot}}} + \underbrace{\frac{\bar{\epsilon}_{s,\mathrm{vib}}}{m_s}}_{:=e_{s,\mathrm{vib}}} + \underbrace{\frac{\bar{\epsilon}_{s,\mathrm{el}}}{m_s}}_{:=e_{s,\mathrm{el}}} + \underbrace{\frac{\epsilon_{s,0}}{m_s}}_{:=e_{s,0}} \quad , \tag{2.15}$$

in the case of the s-th species being molecular. Because in the model the translation temperatures $T_{\mathrm{tr_h}}$ and $T_{\mathrm{tr_e}}$ are regarded, the expressions for the partial pressure and mass-specific enthalpy are the same as in §2.3.2, i.e. $p_s = \rho_s R_s T_{\mathrm{tr}_s}$ and $h_s = e_s + R_s T_{\mathrm{tr}_s}$.

2.4 Collisional processes

2.4.1 The rate coefficient of a collisional process

Rate coefficients of collisional processes taking or not taking into account the involved energy levels may be defined in an identical way. By treating a particle in some energy level as a chemical species, the mathematical relation for the respective rate coefficient has the same form as the one for a homologous process in which the energy level isn't regarded. To properly define the rate coefficient for any collisional process, the term "species" will be employed here with some ambiguity: it may mean a chemical species - if the energy level is regarded - or a chemical species and its energy level - if it is indeed regarded.

2.4.1.1 Definition

Let's consider a collisional process and its reverse (if it has one) expressed in the general form

$$\nu_1 \mathrm{X}_1 + \nu_2 \mathrm{X}_2 + ... + \nu_{N_S} \mathrm{X}_{N_S} \rightleftharpoons \nu'_1 \mathrm{X}_1 + \nu'_2 \mathrm{X}_2 + ... + \nu'_{N_S} \mathrm{X}_{N_S} \Leftrightarrow \sum_{s=1}^{N_S} \nu_s \mathrm{X}_s \rightleftharpoons \sum_{s=1}^{N_S} \nu'_s \mathrm{X}_s \ , \tag{2.16}$$

where X_s is the s-th species in the plasma, ν_s and ν'_s are the associated *stoichiometric coefficients*[4] at the reactant and products sides, respectively. The index s goes from 1 to N_S, being N_S the number of species in the plasma. The variation in time of the amount concentration of s-th species particles $[\mathrm{X}_s]$ (number of particles per unit of volume) due to solely the forward process, and due to solely the backward process, assuming that they are simple single-step processes, are given by [2]

$$\left(\frac{d\left[\mathrm{X}_s\right]}{dt}\right)_f = \left(\nu'_s - \nu_s\right) k_f \prod_{q=1}^{N_S} \left[\mathrm{X}_q\right]^{\nu_q} \ , \tag{2.17}$$

$$\left(\frac{d\left[\mathrm{X}_s\right]}{dt}\right)_b = \left(\nu_s - \nu'_s\right) k_b \prod_{q=1}^{N_S} \left[\mathrm{X}_q\right]^{\nu'_q} \ , \tag{2.18}$$

respectively, where q refers to the q-th species, and k_f and k_b are the respective rate coefficients. By assuming that system is in a *quasi-steady-state condition* (QSS) [1] the rate coefficients k_f and k_b solely depend on a controlling temperature[5] T_c, and one rate coefficient can be obtained from the other as if thermodynamic equilibrium at a temperature T_c had occurred. When the plasma is in thermodynamic

---

[4] Note that if the s-th species isn't present in one side or the other of the equation (or it isn't at all present in the process) the correspondent value ν_s or (and) ν'_s are zero.

[5] The concept of a controlling temperature will turn to be more evident with the reading of section §2.4.1.2.

equilibrium, and therefore also in chemical equilibrium, the concentrations of the species don't change. The principle of *detailed balancing* should be invoked when speaking about chemical equilibrium: this occurs if each elementary process and his reverse are balanced. Therefore, the sum of (2.17) and (2.18) should be null at thermodynamic equilibrium, i.e.

$$0 = \left(\frac{d\,[\mathrm{X}_s]}{dt}\right)^*_f + \left(\frac{d\,[\mathrm{X}_s]}{dt}\right)^*_b \Leftrightarrow \frac{k_f(T_\mathrm{c})}{k_b(T_\mathrm{c})} = e^{-\frac{\Delta\epsilon_0}{k_B T_\mathrm{c}}} \prod_{s=1}^{N_S} \left[\frac{Q_s(T_\mathrm{c}, V)}{\mathscr{N}_A V}\right]^{\nu'_s - \nu_s} := K_c(T_\mathrm{c}) \ , \tag{2.19}$$

where $K_c(T_\mathrm{c})$ is the so-called *concentration-wise equilibrium constant*[6] of the combined processes (2.16), $[\ ]^*$ denotes thermodynamic equilibrium conditions, $Q_s(T_\mathrm{c}, V)$ is the s-th species partition function at equilibrium temperature T_c and volume V, $\mathscr{N}_A$ is the *Avogadro constant*, and $\Delta\epsilon_0 = \sum_{s=1}^{N_S} (\nu'_s - \nu_s)\,\epsilon_{s,0}$ corresponds to the difference between the sum of the products' ground level energies and the sum of the reactants' ones.

The variation in time of the s-th species amount concentration due the N_R processes and their reverse occurring in the system corresponds to the difference between the sum of (2.17) and the sum of (2.18) in all these processes, i.e.

$$\frac{d\,[\mathrm{X}_s]}{dt} = \sum_{r=1}^{N_R} \left(\left(\nu'_{s,r} - \nu_{s,r}\right) k_{f,r}(T_\mathrm{c}) \left\{ \prod_{q=1}^{N_S} [\mathrm{X}_q]^{\nu_{q,r}} - \frac{1}{K_{c,r}(T_\mathrm{c})} \prod_{q=1}^{N_S} [\mathrm{X}_q]^{\nu'_{q,r}} \right\} \right) \ , \tag{2.20}$$

where r refers to the r-th process. Note that the result (2.19) was used in (2.20). The variation in time of the s-th species mass density due to these processes is in its turn $\dot{\omega}_s := m_s \frac{d[\mathrm{X}_s]}{dt}$.

2.4.1.2 Computation

Let's consider a process which occurs through a collision between two particles, A and B, hence termed *binary collision*, producing particles C and possibly others:

$$\mathrm{A} + \mathrm{B} \rightleftharpoons \nu'_\mathrm{C}\mathrm{C} + \cdots \ . \tag{2.21}$$

Let at least one of the collision partners be a heavy particle. The rate coefficient k_f of the process may be obtained from the respective *process cross section* [41], σ_p. The process cross section is in its turn given by $\sigma_p = P \cdot \sigma$, being σ the *collisional cross section*, and P the *process probability*. The collisional cross section may be interpreted as the area of a plane surface transverse to the relative motion of the collision partners within which these must meet in order to scatter from each other. For instance, if the *Billiard Balls model* is regarded - in which the particles correspond to rigid spheres that can solely interact through contact - the collisional cross section is simply given by $\sigma = \pi d_\mathrm{AB}^2$, being $d_\mathrm{AB} = r_\mathrm{A} + r_\mathrm{B}$ the distance between the spheres centres when their surfaces touch each other (see Figure 2.5). Let's take the assumption that both collisional cross section and process probability solely depend on the relative speed of the collision partners, v.

---

[6] Although it isn't truly a constant, since it depends on the controlling temperature T_c.

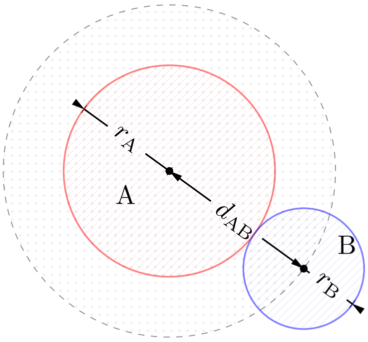

Figure 2.5: Collisional cross section (black circle) for a collision between the particles A (red circle) and B (blue circle) according to the Billiard Balls model. Note that here a tangential collision is depicted.

One may define a function $f(v)$, termed *distribution of relative speeds*, such that $\sigma_p(v) f(v) [\mathrm{A}][\mathrm{B}]\, dv$ is the number of forward processes, per unit of time, per unit of volume, induced by collisions between the particles A and B, with a relative speed $v \in [v,\, v + dv]$. It's easy to find that the change, per unit of time, of the amount concentration of the C species, is given by

$$\left(\frac{d\,[\mathrm{C}]}{dt}\right)_f = (\nu'_\mathrm{C} - \nu_\mathrm{C}) \left\{ \int_0^\infty \sigma_p(v) f(v)\, dv \right\} [\mathrm{A}][\mathrm{B}] \; . \tag{2.22}$$

By comparing (2.22) with (2.17), one can state that the forward rate coefficient corresponds to $k_f = \int_0^\infty \sigma_p(v) f(v)\, dv$. The distribution of relative speeds may be obtained from the distributions of absolute velocities of the collision partners. If the species A and B have their translational energy mode in self-equilibrium, translational temperatures $T_{\mathrm{tr,A}}$ and $T_{\mathrm{tr,B}}$ can be assigned to them, and their distributions of absolute velocities will correspond to *Maxwell-Boltzmann distributions* [2]. If the particles are both heavy particles with the same translational temperature, i.e. $T_{\mathrm{tr,A}} = T_{\mathrm{tr,B}} = T_{\mathrm{tr_h}}$, then the relative distribution of relative speeds can be shown to be $f(v, T_{\mathrm{tr_h}}) = \frac{4\pi}{1+\delta_{\mathrm{AB}}} \left(\frac{\mu}{2\pi k_B T_{\mathrm{tr_h}}}\right)^{\frac{3}{2}} v^3 e^{-\frac{\mu v^2}{2k_B T_{\mathrm{tr_h}}}}$, being $\mu = m_\mathrm{A} \cdot m_\mathrm{B} / (m_\mathrm{A} + m_\mathrm{B})$ the reduced mass of the particles, and δ_{AB} a *Kronecker delta* (giving 1 if $\mathrm{A} = \mathrm{B}$, and 0 if not). The rate coefficient would correspond to

$$k_f(T_{\mathrm{tr_h}}) = \frac{\sqrt{\frac{8k_B T_{\mathrm{tr_h}}}{\pi\mu}}}{1 + \delta_{\mathrm{AB}}} \cdot \underbrace{\frac{\int_0^\infty \sigma_p(v) v^3 e^{-\frac{\mu v^2}{2k_B T_{\mathrm{tr_h}}}}\, dv}{2\left(\frac{k_B T_{\mathrm{tr_h}}}{\mu}\right)^2}}_{:=\sigma_{p,\mathrm{av}}} \; , \tag{2.23}$$

being $\sigma_{p,\mathrm{av}} = \int_0^\infty \sigma_p(v) f(v, T_{\mathrm{tr_h}})\, dv / \int_0^\infty f(v, T_{\mathrm{tr_h}})\, dv$ the *average process cross section*. This quantity may be expressed using the relative kinetic energy of the collision partners, $E = \frac{1}{2}\mu v^2$, or the respective adimensional variable $u = \frac{E}{k_B T_{\mathrm{tr_h}}}$, instead of the relative speed, v, by performing a change of variables:

$$\sigma_{p,\mathrm{av}}(T_{\mathrm{tr_h}}) = \frac{\int_0^\infty \sigma_p(v) v^3 e^{-\frac{\mu v^2}{2k_B T_{\mathrm{tr_h}}}}\, dv}{2\left(\frac{k_B T_{\mathrm{tr_h}}}{\mu}\right)^2} = \frac{\int_0^\infty \sigma_p(E) E e^{-\frac{E}{k_B T_{\mathrm{tr_h}}}}\, dE}{(k_B T_{\mathrm{tr_h}})^2} = \int_0^\infty \sigma_p(u, T_{\mathrm{tr_h}})\, u\, e^{-u}\, du \; . \tag{2.24}$$

It's worthy to say that a *specific collisional frequency*, Z, such that $Z \cdot [\mathrm{A}] \cdot [\mathrm{B}]$ corresponds to the frequency of collisions between particles of the species A and B per unit of volume, may be easily obtained. This corresponds to (2.23) with σ_p substituted by σ, giving

$$Z(T_{\mathrm{tr_h}}) = \frac{\sqrt{\frac{8k_B T_{\mathrm{tr_h}}}{\pi\mu}}}{1+\delta_{AB}} \sigma_{\mathrm{av}}(T_{\mathrm{tr_h}}) \ , \tag{2.25}$$

where σ_{av} is the *average collisional cross section.* If one of the particles corresponds to a free electron with a translational temperature $T_{\mathrm{tr_e}}$, it's possible to show that the respective rate coefficient is given by (2.23) with $\delta_{\mathrm{AB}} = 0$, μ substituted by m_{e}, and $T_{\mathrm{tr_h}}$ substituted by $T_{\mathrm{tr_e}}$ [1]:

$$k_f(T_{\mathrm{tr_e}}) = \frac{\sqrt{\frac{8k_B T_{\mathrm{tr_e}}}{\pi m_{\mathrm{e}}}}}{2\left(\frac{k_B T_{\mathrm{tr_e}}}{m_{\mathrm{e}}}\right)^2} \int_0^\infty \sigma_p(v) v^3 e^{-\frac{m_{\mathrm{e}} v^2}{2k_B T_{\mathrm{tre}}}} \, dv. \tag{2.26}$$

The rate coefficient values obtained from the above-mentioned formulae may be conveniently modelled though curve fitting using the *modified Arrhenius equation*

$$k_f(T_{\mathrm{c}}) = A {T_{\mathrm{c}}}^n e^{-\frac{E_a}{k_B T_{\mathrm{c}}}} , \tag{2.27}$$

where A, n and E_a are the adjustable parameters. The constant E_a corresponds to the *activation energy* - the minimum relative kinetic energy which is required for the process to occur. If (2.27) can't properly reproduce the rate coefficient values, a function with a higher number of adjustable parameters may be tried. An example of such function is the one that Lopez et al. employed in their work [42].

2.5 Radiative processes

Radiative processes correspond to transitions between energy levels of the particles, or the assembly and disassembly of their components (nuclei and electrons), in which the involved energy change is transferred to or received from photons [2]. The photon is a massless particle corresponding to the *quantum* (the minimum amount) of electromagnetic radiation, having an energy $E = h\nu = hc/\lambda$ according to the Planck-Einstein relation, where ν and λ are its frequency and wavelength, respectively, and c the *speed of light.* The radiative processes can be divided into three groups: *bound-bound*, *bound-free* (and *free-bound*) and *free-free transitions.* The nomenclature is built with respect to the state of attachment or detachment of nuclei or/and electrons in the particles internal structure, before and after the transition occurs. Bound-bound transitions are radiative processes in which all the components that were previously attached (bound) still remain attached after the transitions. These transitions are therefore between internal energy levels, corresponding to spontaneous emission, induced (or stimulated) emission and absorption. For simplicity reasons, this work will only address vibronic-specific bound-bound transitions.

2.5.1 The radiation field

The radiation field of a system may be described by the so-called *specific radiant intensity* I_λ: the radiant energy at wavelengths $\lambda \in [\lambda,\, \lambda + d\lambda]$, transported by photons propagating at azimuthal angles $\varphi \in [\varphi,\, \varphi + d\varphi]$ and polar angles $\theta \in [\theta,\, \theta + d\theta]$, that cross an infinitesimal surface dS located in $\vec{r}$, normal to the direction of propagation, during the interval of time $[t,\, t+dt]$, per unit of area, time, solid angle and wavelength. A frequency-specific radiant intensity I_ν, which is given per unit of frequency instead of wavelength, can be shown to be related to the wavelength-specific counterpart I_λ simply by[7] $I_\nu = (c/\nu^2)I_\lambda$. It can also be proved that in thermodynamic equilibrium the distribution of the photon states' populations is such that the specific radiant intensity is given by [2]

$$I^*_\lambda(\vec{r}, t, \varphi, \theta, \lambda) = \frac{2hc^2}{\lambda^5\left(e^{\frac{hc}{\lambda k_B T}} - 1\right)} \ . \tag{2.28}$$

2.5.2 Bound-bound transitions

2.5.2.1 Line broadening and shift

Conversely to what one may at first think, the radiation field generated by bound-bound transitions is continuous. A plot of I_λ versus λ would show finite-height peaks - the so-called *broadened lines* - instead of infinite-height lines associated to *Dirac delta functions.* One contribution to this line broadening (and shift as well) corresponds to the *natural line broadening* which is closely related to the *Heisenberg uncertainty principle*: there's an uncertainty on the energy of the heavy particle, resulting in an uncertainty on the energy of the emitted or absorbed photon [2, 43–45]. This contribution is however usually negligible [44]. On the other hand, there's *collisional broadening*: collisions between the particles shorten the *lifetimes* of their states ultimately influencing the breadth of the lines [43, 45]. There's *Doppler broadening* which occurs with the thermal agitation motion of the particles making the frequency of the radiation observed from some reference point to be different from the one observed by the emitter or absorber [2, 43–45]. Additionally, the electric field produced by the particles in the system may induce a splitting of the particles energy levels and therefore also a splitting of the spectral lines. The phenomena may be associated to an interaction of a particle with a charged one - being termed *Stark broadening* - an interaction between two neutral particles through *van der Waals forces* - hence termed *van der Waals broadening* - or a *resonant* interaction between two particles of the same species - hence termed *resonance broadening* [44–46]. Van der Waals broadening was disregarded in this work since no reasonably practical model for the mechanism was found in the literature. Also, line shift was neglected.

2.5.2.2 The Einstein coefficients

Bound-bound transitions can be described quantitatively through the so-called *Einstein coefficients* [2]. The Einstein coefficient for spontaneous emission, $A^{e',v'}_{s,e,v}$, is defined such that the number of transitions of particles of the s-th species from the vibronic level (e, v) to (e', v')[8] per unit of volume, time and solid angle, in $\vec{r} \in [x,\, x+dx] \times [y,\, y+dy] \times [z,\, z+dz]$, during the interval of time $[t,\, t+dt]$, and spontaneously emitting photons at azimuthal angles $\varphi \in [\varphi,\, \varphi + d\varphi]$ and polar angles $\theta \in [\theta,\, \theta + d\theta]$, is given by

$$-\left(\frac{d^2 n_{s,e,v}}{dt\, d\Omega}\right)^{e',v',\mathrm{se}}_{s,e,v} (\vec{r}, t, \varphi, \theta) = \frac{A^{e',v'}_{s,e,v}}{4\pi}\, n_{s,e,v}(\vec{r}, t) \ , \tag{2.29}$$

---

[7] Note that one has $d\lambda = d(c/\nu) = -c/\nu^2 d\nu$.

[8] Let's assume in this section that the energy associated to the vibronic level $(e,\, v)$ is higher than the one associated to $(e',\, v')$.

where $n_{s,e,v} = dN_{s,e,v}/dV$ is the amount concentration of s-th species particles in the vibronic level (e,v). The superscript term "se" in (2.29) is a label for spontaneous emission. The Einstein coefficient associated to photon absorption, $B^{e,v}_{s,e',v'}$, is defined such that in a radiation field of specific radiant intensity I_λ, the number of transitions of particles of the s-th species from (e',v') to (e,v), per unit of volume, time and solid angle, by absorbing photons at angles $\varphi \in [\varphi,\, \varphi + d\varphi]$ and $\theta \in [\theta,\, \theta + d\theta]$, is

$$\left(\frac{d^2 n_{s,e,v}}{dt\, d\Omega}\right)^{e,v}_{s,e',v'} (\vec{r}, t, \varphi, \theta) = \frac{B^{e,v}_{s,e',v'}}{4\pi}\, n_{s,e',v'}(\vec{r},t) \left(\int_0^\infty I_\lambda(\vec{r},t,\varphi,\theta,\lambda) \cdot \phi^{e',v'}_{\lambda,s,e,v}(\vec{r},t,\lambda)\, d\lambda\right) , \tag{2.30}$$

The function $\phi^{e',v'}_{\lambda,s,e,v}$ corresponds the so-called *line-shape factor* [2] associated to the particular set of vibronic levels (e,v) and (e',v') of the s-th species. In absorption, it may be interpreted as the probability density function of an incident photon of wavelength λ to be absorbed, causing a transition of the s-th species particle from (e',v') to (e,v). Induced emission is the inverse of absorption, and therefore, one may easily see that the respective Einstein coefficient is $B^{e',v'}_{s,e,v}$ such that

$$-\left(\frac{d^2 n_{s,e,v}}{dt\, d\Omega}\right)^{e',v',\mathrm{ie}}_{s,e,v} (\vec{r}, t, \varphi, \theta) = \frac{B^{e',v'}_{s,e,v}}{4\pi}\, n_{s,e,v}(\vec{r},t) \left(\int_0^\infty I_\lambda(\vec{r},t,\varphi,\theta,\lambda) \cdot \phi^{e',v'}_{\lambda,s,e,v}(\vec{r},t,\lambda)\, d\lambda\right) , \tag{2.31}$$

where the superscript term "ie" is a label for induced emission. It can be shown that the three Einstein coefficients are related to each other by simply taking into account that these correspond to properties of the particles and not of the macroscopic system. In conditions of thermodynamic equilibrium, radiative emission and absorption are balanced. By further assuming that the conditions are such that the line broadening phenomena are negligible, and using relations (2.28), (2.29), (2.30) and (2.31) one gets

$$\frac{B^{e,v}_{s,e',v'}}{B^{e',v'}_{s,e,v}} = \frac{g_{s,e,v}}{g_{s,e',v'}} . \tag{2.32}$$

$$\frac{A^{e',v'}_{s,e,v}}{B^{e',v'}_{s,e,v}} = \frac{2hc^2}{\left(\lambda^{e',v'}_{s,e,v}\right)^5} . \tag{2.33}$$

2.5.2.3 Emission and absorption coefficients

The *emission coefficient* j_λ is defined as the radiative energy emitted at wavelengths $\lambda \in [\lambda,\, \lambda + d\lambda]$ and at angles $\varphi \in [\varphi,\, \varphi + d\varphi]$ and $\theta \in [\theta,\, \theta + d\theta]$, per unit of volume, time, solid angle and wavelength, by particles in the element of volume $[x,\, x+dx] \times [y,\, y+dy] \times [z,\, z+dz]$ during the interval of time $[t,\, t+dt]$. On the other hand, the *absorption coefficient* k_λ multiplied by the specific radiative intensity I_λ corresponds to the absorption counterpart. Thus, the variation in time of the volumetric radiative energy per unit of solid angle and wavelength, corresponds to

$$\frac{d^2\dot{\Omega}_{\mathrm{rad}}}{d\Omega d\lambda}(\vec{r},t,\varphi,\theta,\lambda) = j_\lambda(\vec{r},t,\varphi,\theta,\lambda) - k_\lambda(\vec{r},t,\varphi,\theta,\lambda) \cdot I_\lambda(\vec{r},t,\varphi,\theta,\lambda) \tag{2.34}$$

From the definitions of the Einstein coefficients for spontaneous emission (2.29) and induced emission (2.31) it can be shown that the emission coefficient is given by

$$j_\lambda(\vec{r},t,\varphi,\theta,\lambda) = \frac{hc}{\lambda}\left\{\left[\sum_{\mathrm{se}} \frac{A^{e',v'}_{s,e,v}}{4\pi}\, \phi^{e',v'}_{\lambda,s,e,v}(\vec{r},t,\lambda)\, n_{s,e,v}(\vec{r},t)\right] + I_\lambda(\vec{r},t,\varphi,\theta,\lambda)\left[\sum_{\mathrm{ie}} \frac{B^{e',v'}_{s,e,v}}{4\pi}\, \phi^{e',v'}_{\lambda,s,e,v}(\vec{r},t,\lambda)\, n_{s,e,v}(\vec{r},t)\right]\right\} , \tag{2.35}$$

where the sums are done in all the emission processes of all heavy particles. And similarly, from the definition of the Einstein coefficient for absorption (2.30), the absorption coefficient is given by

$$k_\lambda(\vec{r}, t, \varphi, \theta, \lambda) = \frac{hc}{\lambda} \left[\sum_{\text{a}} \frac{B^{e,v}_{s,e',v'}}{4\pi} \, \phi^{e',v'}_{\lambda,s,e,v}(\vec{r}, t, \lambda) \, n_{s,e',v'}(\vec{r}, t) \right] \ , \tag{2.36}$$

being the sum done in all the absorption processes of all heavy particles.

2.6 Fluid flow governing equations

Due to compactness reasons a full derivation of the governing equations of the fluid flow can't be made here, but their fundaments will be stated. The balance equations for the species and mixture masses, linear momenta, total energies, and modes energies, may be obtained by firstly defining a space $\mathscr{V}(t)$ whose boundary $\partial\mathscr{V}(t)$ moves with a velocity equal to the *mixture flow velocity*, $\vec{u}$. One then needs to define spaces $\mathscr{V}_s(t)$ that match $\mathscr{V}(t)$ at the instant t and whose boundaries $\partial\mathscr{V}_s(t)$ move with velocities equal to the ones of the species, $\vec{u}_s$. The variations in time of the species masses, linear momenta, total energies and modes energies in the spaces $\mathscr{V}_s(t)$ are given by the *Reynolds transport theorem*. The variations in time of the species masses can be solely due to kinetic processes, the variations of momenta are given by the *Euler's first law*, and the variations of the total energies and modes energies are given by the *first law of thermodynamics*. The variations of the mixture' quantities are the sum of the variations of the species' ones. The balance equation for the radiative energy may be obtained by considering a space $\mathscr{V}_\gamma(t)$ whose boundary moves with the photons. One then needs to take into account that the variation in time of the radiative energy in this space can only be due to emission and absorption, resulting in the so-called *equation of radiative transfer*:

$$\frac{1}{c}\frac{\partial I_\lambda}{\partial t} + \left(\vec{\nabla} I_\lambda \cdot \vec{e}_s \right) = j_\lambda - k_\lambda \cdot I_\lambda \ , \tag{2.37}$$

being $\vec{e}_s = \cos\varphi \sin\theta \vec{e}_x + \sin\varphi \sin\theta \vec{e}_y + \cos\theta \vec{e}_z$ the direction vector of propagation of the photons.

2.6.1 The case of the zero-dimensional vibronic-specific state-to-state model

In this work, the zero-dimensional vibronic-specific state-to-state model was employed assuming an equilibrium between the translational and rotational energy modes of the heavy particles. The equations to deal with in this model disregard all derivatives in space and the flow velocity vectors of the species. The equations are then

$$\left\{ \begin{aligned} &\frac{dc_{s,e,v}}{dt} = \frac{\dot{\omega}_{s,e,v}}{\rho}, \qquad \forall s,\ v \,\text{and}\ e \ , && \text{(2.38a)} \\ &\frac{dT_{\text{tr}_\text{h}}}{dt} = -\frac{\dot{\Omega}_{\text{rad}} + \left(\sum_s \dot{\Omega}^{\text{int}}_{s,\text{e}} \right) + \left(\sum_{s\in\{\text{h}\}} \dot{\omega}_s e_s \right) + \left[\sum_{s\in\{\text{h}\},e,v} \left(\dot{\omega}_{s,e,v} - \frac{c_{s,e,v}}{c_s} \dot{\omega}_s \right) \frac{\epsilon_{s,\text{el-vib},e,v}}{m_s} \right]}{\rho \left(\sum_{s\in\{\text{h}\}} c_s C_{V,s,\text{tr-rot}} \right)} , && \text{(2.38b)} \\ &\frac{dT_{\text{tr}_\text{e}}}{dt} = \frac{\left(\sum_s \dot{\Omega}^{\text{int}}_{s,\text{e}} \right) - \dot{\omega}_\text{e} e_\text{e}}{\rho c_\text{e} C_{V,\text{e}}} \ . && \text{(2.38c)} \end{aligned} \right.$$

Note that in the above equations, {h} denote the set of heavy species in the system. The quantity $C_{V,s,\text{tr-rot}} = de_{s,\text{tr}}/dT_{\text{tr}_\text{h}} + de_{s,\text{rot}}/dT_{\text{tr}_\text{h}}$ is the *translational-rotational specific heat at constant volume* of the s-th species particle, and $\epsilon_{s,\text{el-vib},e,v} = \epsilon_{s,\text{el},e} + \epsilon_{s,\text{vib},e,v}$ the sensible energy associated to the (e, v)-th vibronic level of the s-th species. It can be shown that $C_{V,s,\text{tr-rot}} = \frac{3}{2}R_s$ if the s-th species is atomic or $C_{V,s,\text{tr-rot}} = \frac{5}{2}R_s$ if the s-th species is molecular. The quantity $C_{V,\text{e}} = \frac{3}{2}R_\text{e}$ is the free electrons specific heat at constant volume. The term $\sum_s \dot{\Omega}^{\text{int}}_{s,\text{e}}$ corresponds to the energy transferred per unit of time per unit of volume from the inner particles of an element of fluid to the inner free electrons. And the term $\dot{\Omega}_\text{rad}$ is the variation in time of the volumetric radiative energy, as defined in (2.34). In order to simplify the modelling of radiative energy transfer in this work, it was decided to disregard induced emission and to introduce the concept of an *escape factor* [47]. Let $\Lambda^{e',v'}_{s,e,v} \in [0,\, 1]$ be the escape factor associated to bound-bound transitions of the s-th species between the vibronic levels (e, v) and (e', v'). This factor corresponds to the fraction of the emitted photons due to spontaneous emissions from $(e,\, v)$ to $(e',\, v')$ which escape the system, or in other words, that are not absorbed. One may then express $\dot{\Omega}_\text{rad}$ as

$$\dot{\Omega}_\text{rad} = hc\left(\sum_{\text{se}} \Lambda^{e',v'}_{s,e,v} A^{e',v'}_{s,e,v}\, n_{s,e,v} \int_0^\infty \frac{\phi^{e',v'}_{\lambda,s,e,v}}{\lambda}\, d\lambda\right) . \tag{2.39}$$

2.6.2 The case of the Euler one-dimensional vibronic-specific state-to-state model

The equations to deal with in the Euler one-dimensional vibronic-specific state-to-state model disregard all derivatives with respect to the y and z variables, the y and z-components of the flow velocity vector $\vec{u}$ - due to the one-dimensional hypothesis - as well as the transport phenomena - due to the Euler hypothesis. It was also assumed that the external body forces are negligible, that the flow is stationary, and that the translational and rotational energy modes of the heavy particles are in equilibrium with each other. The resultant fluid flow governing equations are then

$$\begin{cases} \dfrac{dc_{s,e,v}}{dx} = \dfrac{\dot{\omega}_{s,e,v}}{\rho u}, \quad \forall s,\, e \text{ and } v \;, & \text{(2.40a)} \\ \left(\dfrac{\rho u^2}{p} - 1\right)\dfrac{du}{dx} + \dfrac{u}{p}\left[\left(\displaystyle\sum_{s\in\{\text{h}\}} \dfrac{p_s}{T_{\text{tr}_\text{h}}}\dfrac{dT_{\text{tr}_\text{h}}}{dx}\right) + \dfrac{p_\text{e}}{T_{\text{tr}_\text{e}}}\dfrac{dT_{\text{tr}_\text{e}}}{dx}\right] = -\dfrac{1}{p\rho}\left[\left(\displaystyle\sum_{s\in\{\text{h}\}} \dfrac{\dot{\omega}_s p_s}{c_s}\right) + \dfrac{\dot{\omega}_\text{e} p_\text{e}}{c_\text{e}}\right] , & \text{(2.40b)} \\ \dfrac{dT_{\text{tr}_\text{h}}}{dx} + \dfrac{\left(\sum_{s\in\{\text{h}\}} c_s\right) u}{\sum_{s\in\{\text{h}\}} c_s C_{p,s,\text{tr-rot}}} \cdot \dfrac{du}{dx} = \\ = -\dfrac{\dot{\Omega}_\text{rad} + \left(\sum_s \dot{\Omega}^{\text{int}}_{s,\text{e}}\right) + \left[\sum_{s\in\{\text{h}\}} \dot{\omega}_s \left(h_s + \frac{1}{2}u^2\right)\right] + \left[\sum_{s\in\{\text{h}\},e,v} \left(\dot{\omega}_{s,e,v} - \frac{c_{s,e,v}}{c_s}\dot{\omega}_s\right) \frac{\epsilon_{s,\text{el-vib},e,v}}{m_s}\right]}{\rho u \left(\sum_{s\in\{\text{h}\}} c_s C_{p,s,\text{tr-rot}}\right)} , & \text{(2.40c)} \\ \dfrac{dT_{\text{tr}_\text{e}}}{dx} + \dfrac{u}{C_{p,\text{e}}}\dfrac{du}{dx} = \dfrac{\left(\sum_s \dot{\Omega}^{\text{int}}_{s,\text{e}}\right) - \dot{\omega}_\text{e}\left(h_\text{e} + \frac{1}{2}u^2\right)}{\rho u c_\text{e} C_{p,\text{e}}} \;. & \text{(2.40d)} \end{cases}$$

In these equations, u is x-component of the flow velocity vector, and $C_{p,s,\text{tr-rot}} = dh_{s,\text{tr}}/dT_{\text{tr}_\text{h}} + dh_{s,\text{rot}}/dT_{\text{tr}_\text{h}}$ is the *translational-rotational specific heat at constant pressure* of the s-th species particle. It can be shown that $C_{p,s,\text{tr-rot}} = \frac{5}{2}R_s$ if the s-th species is atomic or $C_{p,s,\text{tr-rot}} = \frac{7}{2}R_s$ if the s-th species is molecular.

The quantity $C_{p,\mathrm{e}} = \frac{5}{2} R_{\mathrm{e}}$ is the free electrons specific heat at constant pressure.

2.7 The Forced Harmonic Oscillator model

2.7.1 The case of V-T processes

The probability of a molecular particle AB to transit from some vibrational level to another by collision with an atomic particle C, according to the FHO theory [22, 23, 48], will be herein derived. The collision is assumed to be collinear (all the nuclei are positioned in the same line, and the relative velocity vector is aligned with this line) being depicted by Figure 2.6.

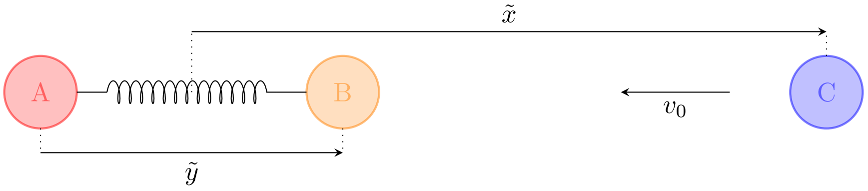

Figure 2.6: Collinear collision between a diatomic molecular particle AB and an atomic particle C.

Let $\tilde{x}_{\mathrm{A}}$, and m_{A} be the position of the nucleus A and its mass, respectively. The analogous notation follows for the other two nuclei, B and C. Let $\tilde{x}_R$ be the *centre of mass* of the whole system[9]. The coordinates presented by Figure 2.6 are: the separation between the nucleus C and the centre of mass of the molecular particle AB, $\tilde{x} = \tilde{x}_{\mathrm{C}} - \tilde{\tilde{x}}_{\mathrm{AB}}$, and the separation between the nuclei B and A, $\tilde{y} = \tilde{x}_{\mathrm{B}} - \tilde{x}_{\mathrm{A}}$. The quantity v_0 corresponds to the relative speed of the particles v when they are infinitely far away. There are four mass parameters whose employment will be useful throughout all this section to describe the dynamics of the system: factor $\gamma = m_{\mathrm{A}}/(m_{\mathrm{A}} + m_{\mathrm{B}})$, the *reduced mass* of the molecular particle $\mu = m_{\mathrm{A}} \cdot m_{\mathrm{B}}/(m_{\mathrm{A}} + m_{\mathrm{B}})$, the sum of all particles masses $\tilde{M} = m_{\mathrm{A}} + m_{\mathrm{B}} + m_{\mathrm{C}}$, and the reduced mass of the combination of the collision partners $\tilde{m} = (m_{\mathrm{A}} + m_{\mathrm{B}}) \cdot m_{\mathrm{C}}/\tilde{M}$. It's assumed that the interaction between the nuclei A and C is negligible when in comparison with the interaction between B and C, since B is much closer to C than A. The potential of the interaction between B and C is assumed to be exponentially repulsive, having the form $V'(\tilde{x}_{\mathrm{C}} - \tilde{x}_{\mathrm{B}}) = A\, e^{-\alpha(\tilde{x}_{\mathrm{C}} - \tilde{x}_{\mathrm{B}})}$, where A and α are two positive constants. By noting that $\tilde{x}_{\mathrm{C}} - \tilde{x}_{\mathrm{B}} = \tilde{x} - \gamma\tilde{y}$, one may express it through

$$V'(\tilde{x}, \tilde{y}) = A\, e^{-\alpha(\tilde{x} - \gamma\tilde{y})} \; . \tag{2.41}$$

The force that nucleus B imposes on C is given by the symmetric of the derivative of the interaction potential relatively to its dependence variable, i.e. $F_{\mathrm{BC}} = -\frac{dV'}{d(\tilde{x}_{\mathrm{C}} - \tilde{x}_{\mathrm{B}})}$. Because the molecular particle is assumed to be a harmonic oscillator, the force that A imposes on B follows Hooke's law, and therefore, it is given by $F_{\mathrm{AB}} = -f\,(\tilde{y} - \tilde{y}_0)$, being f the force constant and $\tilde{y}_0$ the separation between the nuclei of the molecular particle at equilibrium.

The FHO model is semiclassical since it considers the separation between the atomic particle and

---

[9] The centre of mass of a system of particles, with masses $\{m_i\}$ and positions $\{\tilde{x}_i\}$, is defined by: $\tilde{\tilde{x}} = \frac{\sum_{i=1} m_i \, \tilde{x}_i}{\sum_{i=1} m_i}$.

the molecular particle, $\tilde{x}$, and the molecular particle vibration, $\tilde{y} - \tilde{y}_0$, to be in agreement with Classical and Quantum Mechanics, respectively. Let's firstly try to obtain a solution for $\tilde{x}(t)$. Just for the sake of achieving this classical quantity, it's necessary to initially take the assumption of the whole system behaving classically, i.e. by considering the Newton's laws to be in fact applicable. According to the Newton's second law, one can write the equations of movement for each nucleus as

$$\begin{cases} m_{\mathrm{A}}\ddot{\tilde{x}}_{\mathrm{A}} = F_{\mathrm{BA}} + F_{\mathrm{CA}} \ , & (2.42\mathrm{a}) \\ m_{\mathrm{B}}\ddot{\tilde{x}}_{\mathrm{B}} = F_{\mathrm{AB}} + F_{\mathrm{CB}} \ , & (2.42\mathrm{b}) \\ m_{\mathrm{C}}\ddot{\tilde{x}}_{\mathrm{C}} = F_{\mathrm{AC}} + F_{\mathrm{BC}} \ , & (2.42\mathrm{c}) \end{cases}$$

where the double dot notation, $\ddot{[]}$, corresponds to a double derivative in time. By making a change of variables, and by substituting the already exposed approximations, one can transform the above equations into

$$\begin{cases} \mu\ddot{\tilde{y}} = -f\left(\tilde{y} - \tilde{y}_0\right) - \gamma\alpha A\, e^{-\alpha(\tilde{x} - \gamma\tilde{y})} \ , & (2.43\mathrm{a}) \\ \tilde{m}\ddot{\tilde{x}} = \alpha A\, e^{-\alpha(\tilde{x} - \gamma\tilde{y})} \ , & (2.43\mathrm{b}) \\ \tilde{M}\ddot{\tilde{x}}_R = 0 \ . & (2.43\mathrm{c}) \end{cases}$$

Equation (2.43c) can be disregarded: it only tells that no external forces are acting in the system. Conversely, equation (2.43b) tells something useful: since the exponential is a positive function, and α and A are positive constants, the relative acceleration is positive at all instants, i.e. $\ddot{\tilde{x}} > 0$, $\forall t$. On the other hand, it is known that initially (at $t = -\infty$) the relative velocity is negative. In fact, $\dot{\tilde{x}}(-\infty) = -v_0$, with $v_0 > 0$. Therefore, from these two propositions, one can infer that a turning point will for sure occur in the trajectory of the particles, at which the relative velocity becomes null and positive in the following instants. Let $\tilde{x}_t$ be the $\tilde{x}$ value at that point, and $t = 0$ the associated instant. One has therefore $\tilde{x}(0) = \tilde{x}_t$ and $\dot{\tilde{x}}(0) = 0$. Two changes of variables may be regarded to simplify the further work: $\tilde{X} = \tilde{x} - \tilde{x}_t$ and $\tilde{Y} = \tilde{y} - \tilde{y}_0$. Also, it will be assumed that the vibrational amplitude of the oscillator is not driven at large values during the collision, so that $|\tilde{Y}| \ll L$, being $L = 1/\alpha$ the characteristic length of the interaction of the collision partners. This allows one to write $e^{\alpha\gamma\tilde{Y}} \approx 1$. In these terms, to obtain the solution $\tilde{X}(t)$, only equation (2.43b) needs to be solved, being transformed into

$$\tilde{m}\ddot{\tilde{X}} = \alpha A''\, e^{-\alpha\tilde{X}} \ , \tag{2.44}$$

with $A'' = A\, e^{-\alpha(\tilde{x}_t - \gamma\tilde{y}_0)}$. The solution of this differential equation can be shown to be

$$\tilde{X}(t) = \frac{2}{\alpha}\ln\left[\cosh\left(\sqrt{\frac{A''}{2\tilde{m}}}\alpha t\right)\right] \ . \tag{2.45}$$

The relative velocity is then given by $\dot{\tilde{X}}(t) = \sqrt{\frac{2A''}{\tilde{m}}}\tanh\left(\sqrt{\frac{A''}{2\tilde{m}}}\alpha t\right)$. By applying the initial condition $\dot{\tilde{X}}(-\infty) = -v_0$, one can find that

$$A'' = \frac{1}{2}\tilde{m}v_0^2 := E_0 \ , \tag{2.46}$$

being E_0 the relative kinetic energy of the colliding particles at $t = -\infty$. By inserting the solution (2.45) and the relation (2.46) into the interaction potential defined by (2.41), the dependence on $\tilde{x}$ is substituted by a dependence on t, giving

$$V'(t, \tilde{Y}) = E_0 \operatorname{sech}^2 \left(\frac{\alpha v_0}{2} t \right) e^{\alpha \gamma \tilde{Y}} \ . \tag{2.47}$$

The interaction potential in this form is ready to be inserted into the Schrödinger equation of the whole system. Such Schrödinger equation is expressed by

$$\left[-\frac{\hbar^2}{2} \left(\frac{1}{m_{\mathrm{A}}} \frac{\partial^2}{\partial \tilde{x}_{\mathrm{A}}^2} + \frac{1}{m_{\mathrm{B}}} \frac{\partial^2}{\partial \tilde{x}_{\mathrm{B}}^2} + \frac{1}{m_{\mathrm{C}}} \frac{\partial^2}{\partial \tilde{x}_{\mathrm{C}}^2} \right) + V(t, \tilde{Y}) \right] \Psi = i\hbar \frac{\partial \Psi}{\partial t} \ , \tag{2.48}$$

being $V(t, \tilde{Y}) = V'(t, \tilde{Y}) + \frac{1}{2} f \tilde{Y}^2$ the sum of the potential energies of the interaction between the collision partners and the interaction between the nuclei of the molecular particle. By making a change of variables of $\tilde{x}_{\mathrm{A}}$, $\tilde{x}_{\mathrm{B}}$ and $\tilde{x}_{\mathrm{C}}$ to $\tilde{x}_R$, $\tilde{X}$ and $\tilde{Y}$, it's possible to transform equation (2.48) into

$$\left[-\frac{\hbar^2}{2} \left(\frac{1}{\tilde{M}} \frac{\partial^2}{\partial \tilde{x}_R^2} + \frac{1}{\tilde{m}} \frac{\partial^2}{\partial \tilde{X}^2} + \frac{1}{\mu} \frac{\partial^2}{\partial \tilde{Y}^2} \right) + V(t, \tilde{Y}) \right] \Psi = i\hbar \frac{\partial \Psi}{\partial t} \ . \tag{2.49}$$

Because the potential V doesn't depend on $\tilde{x}_R$ neither on $\tilde{X}$, the method of separation of variables can be applied, and the wave function Ψ can be transformed into a multiplication of other two: $\Psi(t, \tilde{x}_R, \tilde{X}, \tilde{Y}) = \theta(\tilde{x}_R, \tilde{X}) \psi(t, \tilde{Y})$. Two new equations result from (2.49): one associated to the motion of the collision partners and another associated to the vibration of the molecular particle. The latter is the equation that one needs to be concerned with. By invoking again the assumption $|\tilde{Y}| \ll L$ the interaction potential (2.47) can be approximated by $V'(t, \tilde{Y}) = -F(t) \left(\frac{1}{\alpha\gamma} + \tilde{Y} \right)$, with $F(t) = -\alpha \gamma E_0 \operatorname{sech}^2 \left(\frac{\alpha v_0}{2} t \right)$. The equation for the vibration of the molecular particle then becomes

$$\left[-\frac{\hbar^2}{2\mu} \frac{\partial^2}{\partial \tilde{Y}^2} + \lambda - F(t) \left(\frac{1}{\alpha\gamma} + \tilde{Y} \right) + \frac{1}{2} f \tilde{Y}^2 \right] \psi = i\hbar \frac{\partial \psi}{\partial t} \ , \tag{2.50}$$

being λ the separation constant. Let's now use the variable $\Phi(t, \xi) = \psi(t, \tilde{Y}) \cdot e^{-g(t)\tilde{Y} + \frac{i}{\hbar} \int_{-\infty}^{t} \left[\lambda - \frac{F(t')}{\alpha\gamma} \right] dt'}$, where $\xi(t, \tilde{Y}) = \tilde{Y} - u(t)$, and $u(t)$ and $g(t)$ are some functions of time. Equation (2.50) then becomes

$$\left(-\frac{\hbar^2}{2\mu} \frac{\partial^2}{\partial \xi^2} + \left[i\hbar \dot{u} - \frac{\hbar^2}{\mu} g \right] \frac{\partial}{\partial \xi} + \left\{ \left[\frac{1}{2} f u^2 - F u - i\hbar u \dot{g} - \frac{\hbar^2}{2\mu} g^2 \right] + \left[f u - F - i\hbar \dot{g} \right] \xi + \frac{1}{2} f \xi^2 \right\} \right) \Phi = i\hbar \frac{\partial \Phi}{\partial t} \ . \tag{2.51}$$

Note that no restrictions were imposed on the functions $u(t)$ and $g(t)$. They are arbitrary and can be defined in any useful manner. To simplify equation (2.51), one can choose $u(t)$ and $g(t)$ such that the multiplying coefficients of $\frac{\partial \Phi}{\partial \xi}$ and $\xi \Phi$ become null. These conditions result in two new equations:

$$\begin{cases} i\hbar g(t) = -\mu \dot{u}(t) \ , & \text{(2.52a)} \\ \mu \ddot{u}(t) + f u(t) = F(t) \ . & \text{(2.52b)} \end{cases}$$

Curiously, (2.52b) corresponds to the equation of motion of a classical harmonic oscillator of mass $m = \mu$ subjected to a force $F(t)$, being $u(t)$ the displacement relatively to equilibrium. For convenience the initial conditions were chosen to be $u(-\infty) = \dot{u}(-\infty) = 0$. By substituting (2.52a) and (2.52b) in (2.51) and performing the change of variables $\Theta(t,\xi) = \Phi(t,\xi)e^{\frac{i}{\hbar}\int_{-\infty}^{t}\delta(t')dt'}$, being $\delta(t) = \frac{1}{2}\mu\dot{u}^2(t) - \frac{1}{2}fu^2(t)$, one obtains

$$\left[-\frac{\hbar^2}{2\mu}\frac{\partial^2}{\partial\xi^2} + \frac{1}{2}f\xi^2\right]\Theta = i\hbar\frac{\partial\Theta}{\partial t} \ . \tag{2.53}$$

Equation (2.53) is the well-known Schrödinger equation for the *quantum free harmonic oscillator* with mass $m = \mu$, whose solution is

$$\Theta(t,\xi) = \sum_{n=0}^{\infty} c_n H_n(\xi) e^{-i\frac{E_n}{\hbar}t} \ , \tag{2.54}$$

In (2.54) c_n are some constants, $H_n(\xi)$ are the so-called *eigenfunctions* of the system and E_n are its *eigenenergies*. These are given by

$$H_n(\xi) = \left(\frac{\mu\omega}{\pi\hbar}\right)^{\frac{1}{4}} \left(2^n n!\right)^{-\frac{1}{2}} \mathscr{H}_n\left(\frac{\xi}{\sqrt{\frac{\hbar}{\mu\omega}}}\right) e^{-\frac{\mu\omega}{2\hbar}\xi^2} \ , \tag{2.55}$$

$$E_n = \left(n + \frac{1}{2}\right)\hbar\omega \ , \tag{2.56}$$

where $\mathscr{H}_n(x) = (-1)^n e^{x^2}\frac{d^n}{dx^n}\left(e^{-x^2}\right)$ are the *physicists' Hermite polynomials*, and $\omega = \sqrt{f/\mu}$ is the *natural angular frequency* of the oscillator. By reverting the previous changes of variables, it's possible to finally obtain a general solution for the vibrational wave function:

$$\psi(t,\tilde{Y}) = \sum_{n=0}^{\infty} c_n H_n(\xi) e^{\frac{i}{\hbar}\left(-E_n t + \mu\dot{u}(t)\tilde{Y} - \int_{-\infty}^{t}\left[\lambda + \delta(t') - \frac{F(t')}{\alpha\gamma}\right]dt'\right)} \ . \tag{2.57}$$

Being the particle initially in the n-th vibrational level, it can be shown that $c_m = \delta_{nm}$, $\forall m = 0,\ ...,\ \infty$. According to the *Born's rule*, the probability of the particle to transit to the m-th vibrational level is

$$P_n^m = \left|\int_{-\infty}^{\infty}\psi^*\left(\infty,\tilde{Y}\right)H_m(\tilde{Y})e^{-i\frac{E_m}{\hbar}t}\,d\tilde{Y}\right|^2 = n!m!\eta_0^{n+m}e^{-\eta_0}\left(\sum_{k=0}^{l}\frac{(-1)^k\eta_0^{-k}}{(n-k)!(m-k)!k!}\right)^2 \ , \tag{2.58}$$

where $l = \min{(n,\ m)}$, and η_0 is the energy of the classical harmonic oscillator at $t = +\infty$ divided by the quantum energy $\hbar\omega$. By solving equation (2.52b) one may show that

$$\eta_0 = \frac{2\pi^2\omega\tilde{m}^2\gamma^2}{\mu\hbar\alpha^2}\operatorname{csch}^2\left(\frac{\pi\omega}{\alpha v_0}\right) \ . \tag{2.59}$$

2.7.2 The case of V-V-T processes

Here, transitions between vibrational levels in a collision between two diatomic molecular particles, AB and CD, are accessed. Such collision is depicted by figure 2.7.

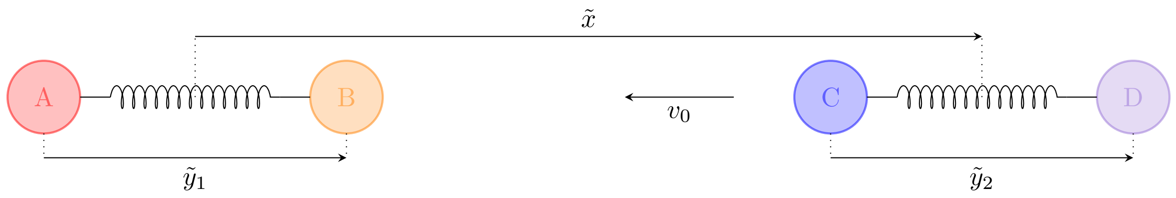

Figure 2.7: Collinear collision between two diatomic molecular particles AB and CD.

It's of interest to know the probability of the particle AB to transit from the vibrational level v_1 to v_1' and of the particle CD to transit from v_2 to v_2', $P_{v_1,v_2}^{v_1',v_2'}$. Although there's a well-based theoretical model for such quantity, being originally developed by Zelechow et al. [24] and adapted by Adamovich et al. [17], its implementation in this work would be impractical due to the amount of computational resources that it requires. Therefore, it was decided to consider the approximation suggested by Adamovich et al. [17]: if $T_{\mathrm{tr_h}} \gg T_{\mathrm{vib}}$, the transition probability of a V-V-T process corresponds to a multiplication of two uncoupled probabilities with V-T process resemblance:

$$P_{v_1,v_2}^{v_1',v_2'} = P_{v_1}^{v_1'} \cdot P_{v_2}^{v_2'} \ , \tag{2.60}$$

where $P_{v_1}^{v_1'}$ is given by (2.58) with the respective parameters substituted by the ones of the particle AB. The analogous follows for $P_{v_2}^{v_2'}$.

2.7.3 The case of V-D processes

In this work the FHO theory was also employed to model dissociation processes. For that purpose the assumption of Macheret and Adamovich [49] was taken: dissociation is said to occur if the energy of the final vibrational level is equal or higher than the potential well depth D_e. Vibrational levels above or at the dissociation limit (being termed *quasi-bound levels*) can be obtained by solving the Schrödinger equation. Let v_D be the vibrational quantum number associated to the lowest one. The probability of a particle, initially in the v-th vibrational level, to dissociate after a collision is then

$$P_v^D = \sum_{v' \geq v_D} P_v^{v'} \ , \tag{2.61}$$

being $P_v^{v'}$ given by (2.58). The number of quasi-bound levels involved in the sum is completely arbitrary, and may be conveniently chosen such that the resultant probability matches the experimental one.

2.7.4 Computation of vibrational transition and dissociation rate coefficients

Vibrational transition and dissociation rate coefficients can be defined in a similar way to the ones associated to chemical reactions that result from binary collisions. In fact, the processes can be expressed by a chemical equation with the form of (2.21). The rate of change of the amount concentration of molecular particles AB(v_1') due to collisions between AB(v_1) and CD(v_2), in which v_2' may represent a quasi-bound level (hence meaning a dissociation of CD), is according to (2.22)

$$\left(\frac{d\,[\mathrm{AB}(v_1')]}{dt}\right)_{v_1,v_2}^{v_1',v_2'} = \left(\nu'_{\mathrm{AB}(v_1')} - \nu_{\mathrm{AB}(v_1')}\right) k_{v_1,v_2}^{v_1',v_2'}\,[\mathrm{AB}(v_1)][\mathrm{CD}(v_2)] \ . \tag{2.62}$$

It can be shown that $\nu'_{\mathrm{AB}(v_1')} - \nu_{\mathrm{AB}(v_1')} = 1 - \delta_{v_1,v_1'} + \delta_{\mathrm{AB,CD}} \cdot \left(\delta_{v_2',v_1'} - \delta_{v_2,v_1'}\right)$, being δ the Kronecker delta. The respective rate coefficient is

$$k_{v_1,v_2}^{v_1',v_2'}(T_{\mathrm{tr_h}}) = \int_0^\infty \sigma_{v_1,v_2}^{v_1',v_2'}(v_0)\, f(v_0, T_{\mathrm{tr_h}})\, dv_0 \ , \tag{2.63}$$

being $\sigma_{v_1,v_2}^{v_1',v_2'}(v_0) = \sigma(v_0) \cdot P_{v_1,v_2}^{v_1',v_2'}(v_0)$ the process cross section and $\sigma(v_0)$ the collisional cross section. Due to the collinearity of the collisions assumed by the FHO model, it may not be appropriate to consider as the distribution function of relative speeds $f(v_0, T_{\mathrm{tr_h}})$ the one stated in §2.4.1.2 where v_0 is the norm g of a relative velocity $\vec{g}$ that may take any orientation with respect to the line of the centres. It was then decided to follow the rationale Adamovich et al. [17] who defined $f(v_0, T_{\mathrm{tr_h}})$ as the distribution of absolute values of the projection of the relative velocity on the line of the centres, $v_0 = g\cos\psi$, being ψ the angle that $\vec{g}$ makes with the line. Such distribution is given by

$$f(v_0, T_{\mathrm{tr_h}}) = \frac{4}{1+\delta_{\mathrm{AB}(v_1),\mathrm{CD}(v_2)}}\sqrt{\frac{\mu}{2\pi k_B T_{\mathrm{tr_h}}}} v_0 e^{-\frac{\mu v_0^2}{2k_B T_{\mathrm{tr_h}}}} \ . \tag{2.64}$$

One comment should be made about the uncoupling approximation of the transition probabilities for the case of V-V-T processes, given by equation (2.60). This approximation allows one to compute a rate coefficient for a vibrational transition of a particle, say from v_1 to v_1', that accounts all the possible transitions as well as dissociation of the other particle, from v_2 to v_2' (including the v_2' quasi-bound levels, meaning dissociation of CD). It can be shown that the rate of change of the amount concentration of molecular particles AB(v_1') due to collisions between AB(v_1) with CD(v_2) for all v_2 and v_2' is

$$\left(\frac{d\,[\mathrm{AB}(v_1')]}{dt}\right)_{v_1}^{v_1'} = \sum_{v_2,v_2'}\left(\frac{d\,[\mathrm{AB}(v_1')]}{dt}\right)_{v_1,v_2}^{v_1',v_2'} \approx \left(1-\delta_{v_1,v_1'}\right)\, k_{v_1}^{v_1'}(T_{\mathrm{tr_h}})\,[\mathrm{AB}(v_1)][\mathrm{CD}] \ , \tag{2.65}$$

being the referred rate coefficient

$$k_{v_1}^{v_1'}(T_{\mathrm{tr_h}}) = \int_0^\infty \sigma(v_0) P_{v_1}^{v_1'}(v_0) f(v_0, T_{\mathrm{tr_h}})\, dv_0 \ . \tag{2.66}$$

And for the case of dissociation of a particle independently of the fate of the collision partner, the rate coefficient is given by

$$k_{v_1}^{D}(T_{\mathrm{tr_h}}) = \int_0^\infty \sigma(v_0) P_{v_1}^{D}(v_0) f(v_0, T_{\mathrm{tr_h}})\, dv_0 \ . \tag{2.67}$$

2.7.5 Consideration of a better interaction potential

In the derivation of (2.58) it was assumed a very simple interaction potential for the collision partners: the repulsive exponential. A more reasonable potential would be one that yields the long-range attractive forces beyond the short-range repulsive ones, such as the *Morse potential.* The Morse interaction potential of two particles with separation $\tilde{z}$ and equilibrium separation $\tilde{z}_0$ is given by

$$V_{\mathrm{M}}'(\tilde{z}) = E_{\mathrm{M}}\left[e^{-\alpha(\tilde{z}-\tilde{z}_0)} - 2e^{-\frac{\alpha}{2}(\tilde{z}-\tilde{z}_0)}\right] , \tag{2.68}$$

being E_{M} the potential well depth, and α a reciprocal length parameter. Instead of deriving a whole new FHO theory departing from a Morse potential between the B and C nuclei, a different approach is considered [48], in which the interaction potential (2.41) is simply substituted by an adapted one:

$$V'(\tilde{x}, \tilde{Y}) = E_{\mathrm{M}}\left[e^{-\alpha(\tilde{x}-\tilde{x}_0)} - 2e^{-\frac{\alpha}{2}(\tilde{x}-\tilde{x}_0)}\right] e^{\alpha\gamma\tilde{Y}} \ , \tag{2.69}$$

being $\tilde{x}_0$ the $\tilde{x}$ equilibrium value. Note that this potential retains some of the repulsive exponential form due to the presence of the $\tilde{Y}$ coordinate in an identical way as before. It can be shown that the new transition probability is given by (2.58) with η_0 substituted by

$$\eta_0 = \frac{8\pi^2 \omega \tilde{m}^2 \gamma^2}{\hbar \mu \alpha^2} \operatorname{csch}^2\left(\frac{2\pi\omega}{\alpha v_0}\right) \cosh^2\left[\frac{2\pi\omega}{\alpha v_0}\left(\frac{1}{2} + \frac{\phi}{\pi}\right)\right] \ , \tag{2.70}$$

where $\phi = \arctan\left(\sqrt{E_{\mathrm{M}}/\frac{1}{2}\tilde{m}v_0^2}\right)$. If a full derivation from a pure Morse potential was performed, a different expression would have been attained for the interaction potential, and the derivation of the transition probability would have been unmanageable.

2.7.6 Corrections

There are three corrections that may be applied to the FHO model. These are with respect to the anharmonicity of the molecular particles, conservation of energy, and non-collinearity of the collisions, being detailed in the works of Billing [50], Billing and Fisher [51], and Adamovich et al. [15].

2.8 A study of the possibility of extension of the Landau-Zener and Rosen-Zener-Demkov models to the case of vibronic transition processes

The Landau-Zener model [26, 27] and the Rosen-Zener-Demkov model [28, 29] are two well-known semiclassical models for the probability of electronic transition of atomic particles by collision with other atomic particle. The physical intuition and the derivation of the respective formulae will not be shown here for compactness reasons, but the curious reader may access them through the cited references.

Let's consider a collision between a molecular particle and a heavy particle. The presence of the heavy particle would perturb the internuclear potential associated to the molecular particle. The nuclei of the molecular particle would then be subjected to an internuclear potential curve which changes parametrically with the position of the heavy particle. If another potential curve is sufficiently close to the current one for some particular internuclear distance values, a vibronic transition may occur [52]. Vibration of the molecular particle means that the nuclei may match the particular internuclear distance values several times during the collision, and therefore, successive vibronic transitions may happen. If the coupling is due to a *crossing* or an *avoided crossing* of the potential curves, then the Landau-Zener model may be applied to compute the probability of excitation of the molecular particle. The Rosen-Zener-Demkov model can't be applied in any circumstance since the coupling described by this model only occurs for internuclear distance values associated to the dissociation of the molecular particle.

One way of determining the probability of heavy particle-impact vibronic transition is by solving the classical equations of motion of the nuclei and applying the Landau-Zener model at the internuclear distances associated to the crossing or avoided crossing of the potential curves - the so-called *Trajectory Surface Hopping Approach* (TSHA) [53]. However, this approach requires the knowledge of the perturbation induced by the collision partner on the potential curves. No data for the parameters that define this perturbation were found in the literature for the case of the heavy particle-impact vibronic transition of N_2 and N_2^+. An overall lack of such data is indeed acknowledged by the scientific community, as underlined by Capitelli et al. [54].

There has been a recent attempt, done by Kirillov [55, 56], to account both Landau-Zener and Rosen-Zener-Demkov models through a general analytic expression using experimental results to calibrate the values of the involved parameters. However, not only the derivation of the analytic expression is somewhat puzzling, but the approach per se lacks physical coherency, since Kirillov applied both models assuming that the respective original formulae are directly valid for vibronic transitions of colliding molecular and heavy particles beyond electronic transitions of colliding atomic particles. The relative speed between the nuclei v which appears in Landau-Zener and Rosen-Zener-Demkov formulae should be the one associated to the nuclei of the same molecular particle, due to the fact that the considered vibronic transitions are the ones between electronic terms of this molecular particle. Kirillov erroneously regarded v as the relative speed of the collision partners, and used the above-mentioned expressions to obtain rate coefficients considering a distribution of relative speeds $f(v, T_{\mathrm{tr_h}})$. Curiously, the expression proposed by Kirillov for the average process cross section $\sigma_{p,\mathrm{av}}$ resembles some well-known semi-empiric relations for vibronic transitions. The Kirillov expression [55] corresponds to

$$\sigma_{p,\mathrm{av}}(T_{\mathrm{tr_h}}) = \begin{cases} \sigma_{\mathrm{el}}\left(T_{\mathrm{tr_h}}, |\Delta E|\right) \mathrm{FC}_1\, e^{-\frac{|\Delta E|}{2k_B T_{\mathrm{tr_h}}}}, & \text{if } \mathrm{M} = \mathrm{C}(e_2)\ , \\ \sigma_{\mathrm{el}}\left(T_{\mathrm{tr_h}}, |\Delta E|\right) \mathrm{FC}_1\, \mathrm{FC}_2\, e^{-\frac{|\Delta E|}{2k_B T_{\mathrm{tr_h}}}}, & \text{if } \mathrm{M} = \mathrm{CD}(e_2, v_2)\ , \end{cases} \tag{2.71}$$

where σ_{el} is the so-called *intrinsic electronic cross section* [32], being associated to the initial and final electronic levels of the collision partners e_1, e_2, e_1' and e_2'. In the case of the Kirillov approach, σ_{el} corresponds to the average cross section obtained from the application of the Landau-Zener or the Rosen-Zener-Demkov models. The quantities FC_1 and FC_2 are the so-called *Franck-Condon factors* [32] which are associated to the overlapping between the vibrational wave functions of the initial and final vibronic levels of the molecular particle AB, i.e. (e_1, v_1) and (e_1', v_1'), and of the initial and final vibronic levels of the collision partner CD, i.e. (e_2, v_2) and (e_2', v_2'), respectively. Finally, ΔE is the *energy defect*, i.e. the difference between the initial and final internal energies of the collision partners. Relation (2.71) for the case $\mathrm{M} = \mathrm{C}(e_2)$ (i.e. in which the collision partner M is atomic) differs just slightly from a more common model originally postulated by Katayama et al. [32]:

$$\sigma_{p,\mathrm{av}}\left(T_{\mathrm{tr_h}}\right) = \sigma_{\mathrm{el}}\, \mathrm{FC}_1\, e^{-\frac{|\Delta E|}{k_B T_{\mathrm{tr_h}}}}\ . \tag{2.72}$$

The difference is on the factor of 1/2 that appears in the argument of the exponential function in (2.71) but not in the argument of the exponential function in (2.72). These particular exponential functions express a type of “exponential gap law”: they tell that the average process cross section would decrease exponentially with the absolute value of the energy defect ΔE, and increase with the temperature $T_{\mathrm{tr_h}}$. Since relation (2.72) is a simplistic postulatory model it may lack some physical coherence. Conclusions reached by several researchers rose concern and doubt about its application. Bachmann et al. reported that the results of his works [30, 31] had no obvious correlation with the Franck-Condon factors, and that their use would be questionable since factors associated to the overlap of wave functions for the whole collision system should be regarded instead of Franck-Condon factors associated to isolated molecular particles. Bachmann et al. also added that in some works, such as the one of Bondybey et al. [57], the ones of and Katayama et al. [32–34] and the one of Dentamaro et al. [58], the dependence on the Franck-Condon factors is in qualitative agreement with the observations, but for others, such as the one of Jihua et al. [59], no correlation with the Franck-Condon factors was reported. In the latter, the authors referred that their results were "clearly inconsistent" with relation (2.72). Also, Piper [60] reported that, according to his results, the model fails to predict the energy level distributions of the species involved in the various studied energy transfer processes even qualitatively. Bachmann et al. [30, 31] considered the possibility, that for a constant temperature T_{ref}, the average cross section may be expressed by an exponential gap law of the form

$$\sigma_{p,\text{av}} = \sigma_0 \, e^{-\frac{|\Delta E|}{E_0}} \ , \tag{2.73}$$

being σ_0 a characteristic cross section and E_0 a characteristic energy. If the vibronic transition process is *resonant*, i.e. if $\Delta E = 0$ does hold, then one would have $\sigma_{p,\text{av}} = \sigma_0$, and therefore, σ_0 can be interpreted as the average cross section value for the case of energy resonance. The results of Bachmann et al. [30] agree considerably well with the relation (2.73). However, a more detailed work [31] showed some evidences of the behaviour of the average cross sections for endothermic vibronic transitions departing from the one associated to the exothermic ones, being the latter favoured over the former.

The exponential function which appears in (2.72) expressing the respective exponential gap law has been found to be incorrect. In the work of Katayama et al. [33] a decrease of the average process cross section with a decrease of the temperature was observed when the inverse was expected. Katayama et al. [35] said that the regarded exponential factor is characteristic of a repulsive interaction and that an attractive interaction would be more appropriate. They then suggested a substitution of the symmetric of the energy defect absolute value, $-|\Delta E|$, in the argument of the exponential function by the well depth of the interaction potential, ε. Such substitution is complacent with the results of the works of Parmenter et al. [61, 62]. By taking this analysis into account, it was decided to employ in this work an expression for the average process cross sections with the vibronic dependence suggested by Bachmann et al. [30, 31] and the thermal dependence suggested by Katayama et al. [35]:

$$\sigma_{p,\text{av}}\left(T_{\text{tr}_\text{h}}\right) = \sigma_0' \, e^{-\frac{|\Delta E|}{E_0} + \frac{\varepsilon}{k_B T_{\text{tr}_\text{h}}}} \ , \tag{2.74}$$

being $\sigma_0' = \sigma_0 e^{-\frac{\varepsilon}{k_B T_{\text{ref}}}}$ (implying that at $T_{\text{tr}_\text{h}} = T_{\text{ref}}$ one has $\sigma_{p,\text{av}}$ given by (2.73), i.e. $\sigma_{p,\text{av}} = \sigma_0 \, e^{-\frac{|\Delta E|}{E_0}}$) and ε the well depth of the potential energy curve associated to interaction between the collision partners. And from (**??**), the respective rate coefficient is given by

$$k_f(T_{\text{tr}_\text{h}}) = \frac{\sigma_0' \, e^{-\frac{|\Delta E|}{E_0}}}{1 + \delta_{\text{AB}(e_1,v_1),\text{M}}} \sqrt{\frac{8 k_B T_{\text{tr}_\text{h}}}{\pi \mu}} \, e^{\frac{\varepsilon}{k_B T_{\text{tr}_\text{h}}}} \ . \tag{2.75}$$

which may be conveniently expressed through a modified Arrhenius function (2.27).

Chapter 3

Implementation

3.1 Considered species and their energy levels

The species that were considered in this work correspond to molecular nitrogen N_2, molecular nitrogen ion N_2^+, atomic nitrogen N, atomic nitrogen ion N^+ and free electron e^-. The electronic energies ϵ_{el} of N_2 and N_2^+ were taken from the literature. The vibrational energies associated to each electronic level were obtained using the *Fourier Grid Hamiltonian method* [63] which is detailed in appendix A. Electronic energies of N and N^+ can be obtained from the NIST database [64]. Note, however, that it takes into account the *fine structure*[1] of the levels. Electronic levels which were obtained by ignoring them should now be "split" into a distinct (though very close) levels that differ in the value of the quantum number for the total angular momentum of the electrons in the particle, J. The most part of the studies on collisional and radiative processes found in the literature consider the non-split electronic levels instead of the split ones. The applicability of the compiled data for such processes in this work also requires the author to make the same assumption, and single representative levels for each set of split electronic levels need to be obtained. Herein, the sensible energy of the representative electronic level was defined as the mean sensible energy that a state belonging to that set may have. Let the representative electronic level and the set be denoted by e and $\{e^\dagger\}$, respectively. Mathematically, the definition of the sensible energy of the representative electronic level ϵ_e, is given by

$$\epsilon_e := \sum_{e^\dagger} P_{e^\dagger} \epsilon_{e^\dagger} = \sum_{e^\dagger} \frac{g_{e^\dagger}}{g_e} \epsilon_{e^\dagger} \ , \tag{3.1}$$

being $\epsilon_{e^\dagger}$ the sensible energy of the electronic level $e^\dagger$ that belongs to the set $\{e^\dagger\}$, and $P_{e^\dagger}$ the probability of a state of the set to belong to the electronic level $e^\dagger$. The sum in the expression is made in all the electronic levels of the set. By taking the assumption that all states of the set are equiprobable, this probability is simply given by the ratio between the number of states of the electronic level $e^\dagger$, $g_{e^\dagger}$, and the number of states of the set ($g_e := \sum_{e^\dagger} g_{e^\dagger}$).

All considered species and their energy levels are reported in Table 3.1.

---

[1] This fine structure comes into play when relativistic effects which depend on the spin of the electrons of the particle are regarded [65].

Table 3.1: Considered species and respective energy levels. The interval that appears between parenthesis immediately after the molecular term symbols of the electronic levels of N_2 and N_2^+ correspond to the set of values of vibrational quantum numbers for which bound vibrational levels were computed.

Type	Species	Energy levels	Reference
Molecule	N_2	$\mathrm{X}^1\Sigma_\mathrm{g}^+\,([0,61])$, $\mathrm{A}^3\Sigma_\mathrm{u}^+\,([0,31])$, $\mathrm{B}^3\Pi_\mathrm{g}\,([0,32])$, $\mathrm{W}^3\Delta_\mathrm{u}\,([0,44])$, $\mathrm{B}'^3\Sigma_\mathrm{u}^-\,([0,47])$, $\mathrm{a}'^1\Sigma_\mathrm{u}^-\,([0,57])$, $\mathrm{a}^1\Pi_\mathrm{g}\,([0,52])$, $\mathrm{w}^1\Delta_\mathrm{u}\,([0,49])$, $\mathrm{A}'^5\Sigma_\mathrm{g}^+\,([0,5])$, $\mathrm{C}^3\Pi_\mathrm{u}\,([0,4])$, $\mathrm{b}^1\Pi_\mathrm{u}\,([0,28])$, $\mathrm{c}_3{}^1\Pi_\mathrm{u}\,([0,4])$, $\mathrm{c}_4'{}^1\Sigma_\mathrm{u}^+\,([0,8])$, $\mathrm{b}'^1\Sigma_\mathrm{u}^+\,([0,54])$ and $\mathrm{o}_3{}^1\Pi_\mathrm{u}\,([0,4])$	This work
Molecular ion	N_2^+	$\mathrm{X}^2\Sigma_\mathrm{g}^+\,([0,65])$, $\mathrm{A}^2\Pi_\mathrm{u}\,([0,66])$, $\mathrm{B}^2\Sigma_\mathrm{u}^+\,([0,38])$, $\mathrm{D}^2\Pi_\mathrm{g}\,([0,38])$ and $\mathrm{C}^2\Sigma_\mathrm{u}^+\,([0,13])$	This work
Atom	N	$^4\mathrm{S_u}$, $^2\mathrm{D_u}$, $^2\mathrm{P_u}$, $^4\mathrm{P}$, $^2\mathrm{P}$, ... (131 levels) ([a])	NIST[64]
Atomic ion	N^+	$^3\mathrm{P}$, $^1\mathrm{D}$, $^1\mathrm{S}$, $^5\mathrm{S_u}$, $^3\mathrm{D_u}$, ... (81 levels) ([a])	NIST[64]
Free electron	e^-	—	—

[a] As a reminder to the reader: the electronic levels were obtained through the "lumping procedure" (3.1) applied on the ones issued by NIST.

3.2 Collisional processes

Forward rate coefficients k_f for processes that involve collisions between particles were computed through theoretical models, empirical correlations, or by relying on process cross sections σ_p and average process cross sections $\sigma_{p,\mathrm{av}}$ found in the literature. Also, whenever cross sections weren't found but forward rate constants k_f were, the latter were taken and a curve fitting procedure was performed. The determination of forward rate coefficients through the different methods will be described here for some particular processes. Section §3.2.1 illustrates the way that the Forced Harmonic Oscillator model was used in the determination of rates for vibrational transition and dissociation of N_2 and N_2^+ by collisions with heavy particles. In Section §3.2.2 rates for vibronic transition of N_2 by heavy particle impact are computed using the exponential gap law. Section §3.2.3 describes the way that rates for non-dissociative ionisation of N_2 by electron impact were obtained using process cross sections values taken from the literature. Section §3.2.4 describes the use of adapted *Drawin formulae* to model electronic excitation and ionisation of N and N^+ by electron impact. And Section §3.2.5 presents the way that the formula of Annaloro et al. [66] was employed in this work to compute rates for electronic excitation and ionisation of N and N^+ by heavy particle impact.

Table B.3 makes a synopsis on the regarded collisional processes due to heavy particle impact. And Table B.4 makes a synopsis on the regarded collisional processes due to electron impact. The two tables present the type of process, chemical equation, and reference from which data was taken to compute the forward rate k_f. Some processes reported in the literature which involve the vibrational levels of $N_2\left(\mathrm{X}^1\Sigma_\mathrm{g}^+\right)$ consider a database for these energy levels that is different from the one employed in this work. Therefore, to make such results applicable, it was determined to linearly interpolate the issued rates with respect to the vibrational energies if the issued energies are comprised to the in-work database, or to linearly extrapolate if they aren't - this procedure will be termed here by the name "Adaption in respect of the Database for the Vibrational energy levels" (ADV). In some processes, the vibrational redistribution procedure (VRP), considered by Julien Annaloro in his PhD thesis [14], was used to compute rates for a full set of vibrational quantum numbers from a rate coefficient for a particular vibrational quantum number or for the contribution of all of them. A codename for the type of process was defined to simplify the description of the process. It consists of three terms separated by hyphens. If the process corresponds solely to a transition in the internal energy modes of the collision partners, the first term of the codename will correspond to a set of capital letters each one representing the involved internal energy modes ("V" from "vibrational" or/and "E" from "electronic"). If the process corresponds to a bond breaking or/and forming of the internal structure, the first term will be defined by a set of capital letters, each one representing a type of bond breaking or forming ("I" from "ionisation", "R" from "recombination", "D" from "dissociation" or "A" from "association"). The second and third terms correspond to labels of minuscule letters representing the type of the collision partners ("h" from "heavy species", "m" from "molecular particle", "a" from "atomic particle", or "e" from "electron").

3.2.1 Vibrational transition and dissociation of N_2 and N_2^+ by heavy particle impact

By recalling the previously introduced theory of the FHO model (in Section §2.7), one can compute rates for vibrational transition and dissociation of molecular particles by collision with heavy species. Since in this work the considered heavy species were N_2, N_2^+, N and N^+, it's necessary to compute rates for the full set of vibronic-specific interactions associated to seven species-specific ones: N_2 - N, N_2 - N^+, N_2 - N_2, N_2 - N_2^+, N_2^+ - N, N_2^+ - N^+ and N_2^+ - N_2^+. These computations require the knowledge of some parameters that describe the interactions: the collisional cross section σ, reciprocal characteristic length α, and potential well depth E_{M} of the Morse interaction potential given by (2.68). Regarding the Morse parameters α and E_{M}, only values for the interaction $\mathrm{N_2(X^1\Sigma_g^+)}$ - $\mathrm{N_2(X^1\Sigma_g^+)}$ were found in the literature. These were defined by Adamovich et al. [17], who also employed the same values for the cases N_2 - O_2 and O_2 - O_2. It was then decided to extrapolate this assumption to all interactions regarded in this work. The respective values are $\alpha = 4.0\,\text{Å}^{-1}$ and $E_{\mathrm{M}} = 200\,k_B \cdot \mathrm{K}$. Regarding the collisional cross section σ, only a value for an intimate quantity for the interaction $\mathrm{N_2(X^1\Sigma_g^+)}$ - $\mathrm{N_2(X^1\Sigma_g^+)}$ was found in the literature (Svehla's technical report [67]). This quantity corresponds to the parameter d of the *Lennard-Jones (12-6) potential*, being termed *collision diameter*. It may be interpreted as the distance between the centres of the two hard spheres that represent the collision partners at the instant of contact. According to the definition of collisional cross section for hard spheres given in the Section §2.4.1.2, one has $\sigma = \pi d^2$. And by using particular notation for the $\mathrm{N_2(X^1\Sigma_g^+)}$ - $\mathrm{N_2(X^1\Sigma_g^+)}$ case, the formula translates itself to $\sigma_{\mathrm{N_2\text{ - }N_2}} = \pi d^2_{\mathrm{N_2\text{ - }N_2}} = 45.317\,\text{Å}^2$. Svehla's technical report also provides a collision diameter value for the case $\mathrm{N(^4S_u)}$ - $\mathrm{N(^4S_u)}$, which can be used in combination with the previous one to estimate the collisional cross section for $\mathrm{N_2(X^1\Sigma_g^+)}$ - $\mathrm{N(^4S_u)}$: $\sigma_{\mathrm{N_2\text{ - }N}} = \pi d^2_{\mathrm{N_2\text{ - }N}} = \frac{\pi}{4}\left(d_{\mathrm{N_2\text{ - }N_2}} + d_{\mathrm{N\text{ - }N}}\right)^2 = 39.547\,\text{Å}^2$. Since no data for the interactions that involve the excited electronic levels of N_2 and of N, and the ions N^+ and N_2^+ was found in the literature, it was assumed that the respective collisional cross sections values were the same as the ones that involve the ground electronic levels of the counterpart neutral species.

Rate coefficients for vibrational transition $k_v^{v'}(T_{\mathrm{tr_h}})$ and dissociation $k_v^D(T_{\mathrm{tr_h}})$ of N_2 and N_2^+, due to collisions with N_2, N_2^+, N and N^+, were computed. To illustrate one of those results, Figure 3.1 depict the rate coefficients for vibrational transition of $N_2(X^1\Sigma_g^+)$ by collision with N, at a heavy particle translational temperature $T_{tr_h} = 20,000$ K. It can be concluded that the vibrational transition process is more effective if the transition is between two adjacent levels, and even more effective if the two adjacent levels are of low energy. For the case of transitions between non-adjacent levels, it is found that rate coefficient values for de-excitation are in general greater than the ones for excitation. Excitation from the lowest energy levels to the highest ones, are the less effective.

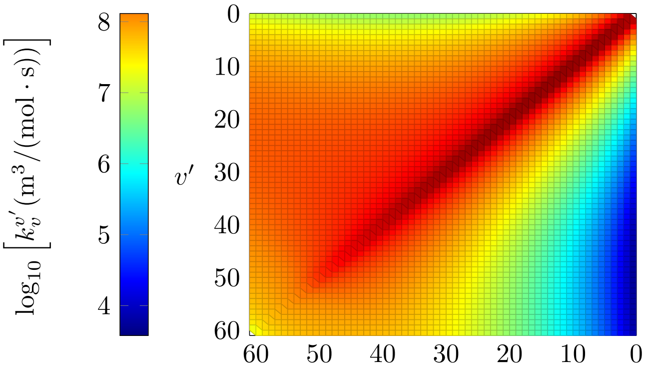

Figure 3.1: Contour plot of rate coefficient values for vibrational transition of $N_2(X^1\Sigma_g^+)$ by collision with N, at a heavy particle translational temperature $T_{tr_h} = 20,000$ K.

It's of paramount importance to validate the computed rates of vibrational transition $k_v^{v'}$ as well as the rates of dissociation k_v^D, for all the considered interactions. Unfortunately, experimental results expressed in the exact same form as these weren't found in the literature. What was found were experimental results for the dissociation of $N_2(X^1\Sigma_g^+)$ by impact with N and with N_2, in thermal equilibrium conditions. Note that the numerical computation of dissociation rates using the FHO model implies the assignment of a value for a free parameter that can't be a priori computed: the number of quasi-bound levels for the sum involved in the dissociation rate formula (2.61), as presented in Section §2.7.3. Instead of the number of quasi-bound levels, one can define a quantity corresponding to the difference between the upper bound value for the vibrational energy of the quasi-bound levels $G_{v'_u}$ and the potential well D_e, i.e. $G_{v'_u}^{D_e} := G_{v'_u} - D_e$. Therefore, the considered quasi-bound levels are the ones with a vibrational energy $G_{v'}$ higher than the potential well depth D_e and lower or equal to the upper bound vibrational energy $G_{v'_u}$, i.e. $D_e < G_{v'} \leq G_{v'_u}$. Such free parameter gives opportunity for calibration of the model by comparison with the aforementioned experimental results, increasing the reliability on the numerical dissociation rates, and at the same, on the numerical vibrational transition rates, since the former uses the latter for its computation. However, vibrational transition and dissociation rates of $N_2(X^1\Sigma_g^+)$ due to impact with N^+ and N_2^+ can't be calibrated since there is no experimental data for them. It was then decided to set the differences between the upper bound vibrational energy and the potential well for the interactions with N^+ and N_2^+ as the ones obtained from calibration of the interactions $N_2(X^1\Sigma_g^+)$ - N and $N_2(X^1\Sigma_g^+)$ - N_2, respectively. There's also no experimental data for the vibrational transition and dissociation rates of N_2^+ and the electronically excited N_2, due to impact with N, N_2, N^+ and N_2^+. In this case, it was decided to solely account the first quasi-bound level.

Numerical rate coefficients for thermal dissociation of $\mathrm{N_2(X^1\Sigma_g^+)}$ by collisions with $\mathrm{N_2}$ and N can be computed from the the respective vibronic-specific dissociation rates. The rate coefficient for the dissociation of particles of the X species in the e_1-th electronic level and v_1-th vibrational level, due to collisions with particles of the M species, corresponds to $k^D_{\mathrm{X}(e_1,v_1)\text{ - M}}$. If the rotational constants don't depend on the vibrational level, the rotational and vibrational energy modes are decoupled from each other, and it can be easily proved from relations (2.6) and (2.7) that the rate coefficient of thermal dissociation for the interaction X(e_1) - M, i.e. $k^D_{\mathrm{X}(e_1)\text{ - M}}(\mathrm{T})$ corresponds to

$$k^D_{\mathrm{X}(e_1)\text{ - M}}(T) = \sum_{v_1} \frac{e^{-\frac{\epsilon_{X,\mathrm{vib},e_1,v_1}}{k_B T}}}{Q_{X,\mathrm{vib},e_1}(T)} k^D_{\mathrm{X}(e_1,v_1)\text{ - M}}(T) \ . \tag{3.2}$$

The addressed experimentally obtained thermal dissociation rates are listed in Table 3.2.

Table 3.2: Coefficients A, n and E_a/k_B of the modified Arrhenius function (2.27) for experimentally obtained rates for the thermal dissociation of $\mathrm{N_2(X^1\Sigma_g^+)}$ by collision with N and $\mathrm{N_2}$, as well as the respective interval of temperatures $T \in [T_{\mathrm{min}},\, T_{\mathrm{max}}]$ in which they are valid.

Experiment	Interaction	A [$\mathrm{cm^3 \cdot K^{-\eta}/(mol \cdot s)}$]	n	E_a/k_B [K]	[T_{min}, T_{max}] [K]
Cary (1965) [68]	$\mathrm{N_2(X^1\Sigma_g^+)}$ - N	7.1×10^{19}	-1.0	$113,310$	$[6,000;\ 10,000]$
	$\mathrm{N_2(X^1\Sigma_g^+)}$ - $\mathrm{N_2}$	5.6×10^{22}	-1.7		
Byron (1966) [69]	$\mathrm{N_2(X^1\Sigma_g^+)}$ - N	4.3×10^{22}	-1.5	$113,200$	$[6,000;\ 9,000]$
	$\mathrm{N_2(X^1\Sigma_g^+)}$ - $\mathrm{N_2}$	4.8×10^{17}	-0.5		
Appleton et al. (1968) [70]	$\mathrm{N_2(X^1\Sigma_g^+)}$ - N	1.6×10^{22}	-1.6	$113,200$	$[8,000;\ 15,000]$
	$\mathrm{N_2(X^1\Sigma_g^+)}$ - $\mathrm{N_2}$	3.7×10^{21}	-1.6		
Hanson and Baganoff (1972) [71]	$\mathrm{N_2(X^1\Sigma_g^+)}$ - N	2.2×10^{26}	-2.5	$113,000$	$[5,700;\ 12,000]$
	$\mathrm{N_2(X^1\Sigma_g^+)}$ - $\mathrm{N_2}$	3.9×10^{33}	-4.5		
Kewley and Hornung (1974) [72]	$\mathrm{N_2(X^1\Sigma_g^+)}$ - N	8.5×10^{25}	-2.5	$113,200$	$[6,000;\ 14,000]$
	$\mathrm{N_2(X^1\Sigma_g^+)}$ - $\mathrm{N_2}$	2.3×10^{29}	-3.5		
Park (1988) [73] ([a])	$\mathrm{N_2(X^1\Sigma_g^+)}$ - N	3×10^{22}	-1.6	$113,200$	$[6,000;\ 13,000]$
	$\mathrm{N_2(X^1\Sigma_g^+)}$ - $\mathrm{N_2}$	7×10^{21}	-1.6		

[a] Although the work done by Park is labelled here as an experiment, it is actually a theoretical study involving the other experimental works.

In all experiments previous to the ones done by Hanson and Baganoff [71], a test gas composed by molecular nitrogen and a diluted inert gas was considered. Such mixture was chosen with the objective of inducing dissociation of nitrogen from lower shock speeds. Therefore, one may expect the experiments of Hanson and Baganoff [71] and of Kewley and Hornung [72] to be more reliable than the ones of Cary [68], Byron [69] and Appleton et al. [70]. The study performed by Park [73] wasn't an experiment but a reinterpretation of the previously obtained experimental results which accounted the possibility of the translational and vibrational modes of the particles not being in equilibrium with each other, i.e. $T_{\mathrm{tr_h}} \neq T_{\mathrm{vib}}$. The other authors assumed that thermal equilibrium occurred, which may not be reasonable. Park issues thermal dissociation rates considering as control temperature $T_{\mathrm{a}} = \sqrt{T_{\mathrm{tr_h}} T_{\mathrm{vib}}}$. Note, however, that in thermal equilibrium one has $T = T_{\mathrm{tr_h}} = T_{\mathrm{vib}}$, and the average temperature T_{a} match the single-temperature. The results of Park are considered to be the most reliable ones [74, 75], and, therefore, it was decided to use them in the calibration of the numerical thermal dissociation rates $k^D_{\mathrm{N_2(X^1\Sigma_g^+)\text{ - }N_2}}(T)$ and $k^D_{\mathrm{N_2(X^1\Sigma_g^+)\text{ - }N}}(T)$ obtained in this work. This calibration consisted in the minimisation of the *root* *mean square deviation* (a cost function) between the numerical rates and the Park's ones by sweeping the difference between the upper bound value for the vibrational energy of the quasi-bound levels and the potential well, $G^{D_e}_{v'_{\mathrm{u}}} = G_{v'_{\mathrm{u}}} - D_e$. Let $G^{D_e,\mathrm{opt}}_{v'_{\mathrm{u}},\mathrm{N_2(X^1\Sigma_g^+)\text{ - }N_2}}$ and $G^{D_e,\mathrm{opt}}_{v'_{\mathrm{u}},\mathrm{N_2(X^1\Sigma_g^+)\text{ - }N}}$ be the respective optimum values. The root mean square deviations of $k^D_{\mathrm{N_2(X^1\Sigma_g^+)\text{ - }M}}(T)$, with $\mathrm{M} \in \{\mathrm{N_2}, \mathrm{N}\}$, from the Park's values, are defined as

$$\Delta_{\mathrm{N_2(X^1\Sigma_g^+)\text{ - }M}}(G^{D_e}_{v'_{\mathrm{u}}}) = \sqrt{\frac{\sum_n \left[k^D_{\mathrm{N_2(X^1\Sigma_g^+)\text{ - }M}}(T_n) - k^{D,(\mathrm{Park})}_{\mathrm{N_2(X^1\Sigma_g^+)\text{ - }M}}(T_n)\right]^2}{N}} \, . \tag{3.3}$$

being $k^{D,(\mathrm{Park})}_{\mathrm{N_2(X^1\Sigma_g^+)\text{ - }M}}(T_n)$ the Park's rate coefficients, T_n the n-th temperature value at which the rate coefficients were evaluated, and N the number of temperature values. Only the experimentally valid range of temperatures was considered for the optimisation process. For the case of the interaction $\mathrm{N_2(X^1\Sigma_g^+)}$ - $\mathrm{N_2}$, a minimum for the root mean squared deviation was found, being the minimiser $G^{D_e,\mathrm{opt}}_{v'_{\mathrm{u}},\mathrm{N_2(X^1\Sigma_g^+)\text{ - }N_2}} = 1{,}100$ "cm^{-1}". For the case of the interaction $\mathrm{N_2(X^1\Sigma_g^+)}$ - N, no minimum was found in the range $G^{D_e}_{v'_{\mathrm{u}}} \in [0; 10{,}000]$ "cm^{-1}" as only some of the decreasing part of the full curve is supported by this domain. It was then decided to choose $G^{D_e,\mathrm{opt}}_{v'_{\mathrm{u}},\mathrm{N_2(X^1\Sigma_g^+)\text{ - }N}}$ as the the $G^{D_e}_{v'_{\mathrm{u}}}$ value that minimises the root mean squared deviation in this range, i.e. $G^{D_e,\mathrm{opt}}_{v'_{\mathrm{u}},\mathrm{N_2(X^1\Sigma_g^+)\text{ - }N}} = 9{,}900$ "cm^{-1}". Figures 3.2 and 3.3 show the calibrated rate coefficient curves and the experimental ones listed in Table 3.2, for the cases $\mathrm{N_2(X^1\Sigma_g^+)}$ - $\mathrm{N_2}$ and $\mathrm{N_2(X^1\Sigma_g^+)}$ - N, respectively. These figures also show recent numerical rate coefficient values individually obtained by Bender et al. [76], Macdonald et al. [77], Esposito and Capitelli [78], and Jaffe et al. [79], using the Quasi-Classical Trajectory model (QCT), which has a greater degree of fidelity than the FHO model. In the second subfigure of each figure, the ratio between the FHO rate coefficient values and the ones obtained by Park [73], as well as the ones obtained through the QCT model are depicted.

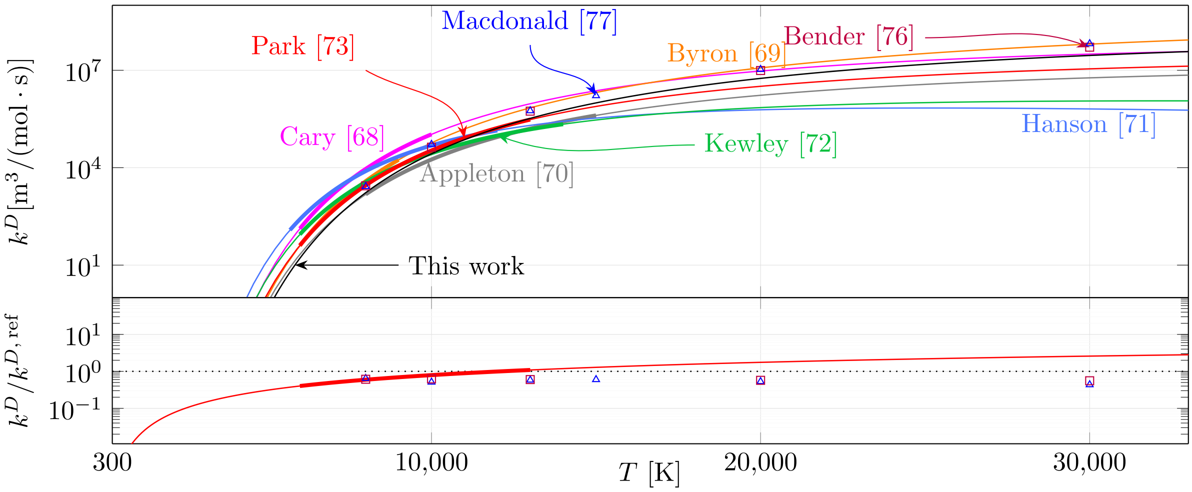

Figure 3.2: Thermal dissociation rates of $\mathrm{N_2(X)}$ by collision with $\mathrm{N_2}$, and ratio between the FHO result and the one obtained by Park [73], as well as the ones obtained by the QCT model (Bender et al. [76], and Macdonald et al. [77]). The thick part of the lines is associated to the experimentally valid domains.

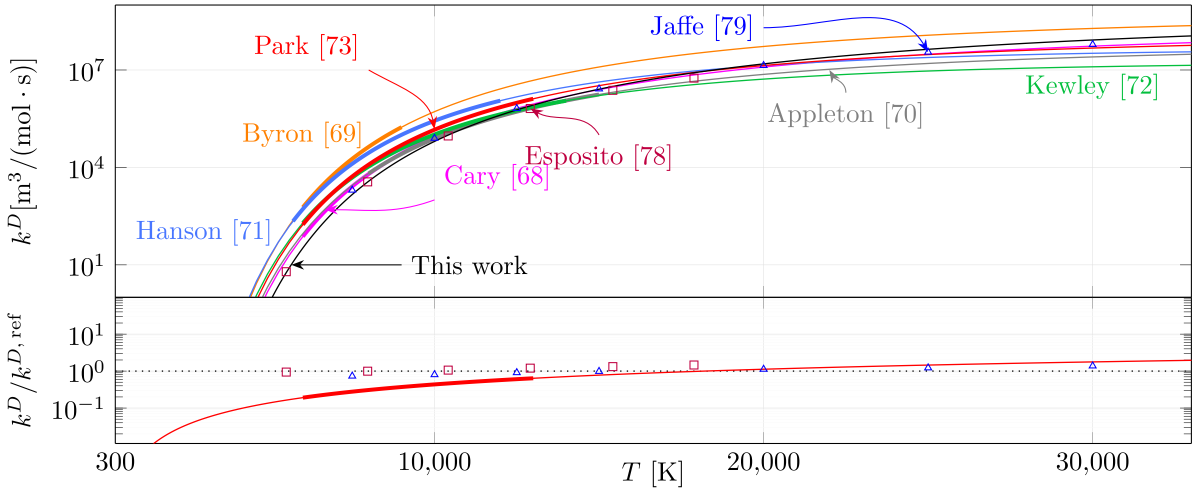

Figure 3.3: Thermal dissociation rates of $N_2(X)$ by collision with N, and ratio between the FHO result and the one obtained by Park [73], as well as the ones obtained by the QCT model (Esposito and Capitelli [78], and Jaffe et al. [79]). The thick part of the lines is associated to the experimentally valid domains.

The two figures evidence some overall discrepancies between the experimental results, either in offset and in trend. For both the interactions $N_2(X^1\Sigma_g^+)$ - N_2 and $N_2(X^1\Sigma_g^+)$ - N, it's found an underestimation of the Park [73] results by the FHO model in the low to medium temperatures region, and an overestimation in the high temperatures region. There's a better agreeability between the two results in the experimentally valid region for the former case (a maximum underestimation of 59.9% and overestimation of 8.9% in contrast with a maximum underestimation of 80.9% and minimum underestimation of 36.1% for the latter case). This was expected since it was only in the former case that the optimisation procedure was successful in the minimisation of the cost function. The FHO results underestimate all the QCT results for the case of the interaction $N_2(X^1\Sigma_g^+)$ - N_2, with maximum absolute relative deviations of 44.3% and 56.5% from the values of Bender et al. [76] and Macdonald et al. [77], respectively. For the case of $N_2(X^1\Sigma_g^+)$ - N, the FHO results underestimate the QCT results at the lower temperatures and overestimate them at the higher ones, with maximum absolute relative deviations of 46.2% and 37.9% from the values of Esposito and Capitelli [78] and Jaffe et al. [79].

3.2.2 Vibronic transition of $\mathbf{N_2}(\mathbf{A}^3\Sigma_\mathbf{u}^+, v_1)$ to $\mathbf{N_2}(\mathbf{B}^3\Pi_\mathbf{g}, v_1')$ by collision with $\mathbf{N_2}(\mathbf{X}^1\Sigma_\mathbf{g}^+, v_2)$ and $\mathbf{N}(^4\mathbf{S_u})$

Herein the proposed model (2.75) will be implemented for the cases of vibronic transitions of $N_2(A^3\Sigma_u^+, v_1)$ to $N_2(B^3\Pi_g, v_1')$ by collisions of $N_2(A^3\Sigma_u^+, v_1)$ with $N_2(X^1\Sigma_g^+, v_2)$ and $N(^4S_u)$. For that purpose, the average process cross sections experimentally obtained by Bachmann et al. [31], at room temperature $T_{\mathrm{tr_h}} = 300\,\mathrm{K} := T_{\mathrm{ref}}$, were used. Bachmann et al. studied intramolecular vibronic transition processes of the form

$$N_2(A^3\Sigma_u^+, v_1) + M \longrightarrow N_2(B^3\Pi_g, v_1') + M\ , \tag{3.4}$$

being M the collision partner which may correspond to an atomic particle, $M \in \{\mathrm{He}, \mathrm{Ne}, \mathrm{Ar}, \mathrm{Kr}, \mathrm{Xe}\} := \{M_a\}$, or to a molecular particle, $M \in \{H_2, N_2, \mathrm{NO}\} := \{M_m\}$ in its ground energy level. The authors, however, strongly believed that two intermolecular vibronic transition processes for the case $M = N_2$ were found due to their quasi-resonance [31]:

$$N_2(A^3\Sigma_u^+, 15) + N_2(X^1\Sigma_g^+, 0) \longrightarrow N_2(B^3\Pi_g, 4) + N_2(X^1\Sigma_g^+, 1) \ , \tag{3.5}$$

$$N_2(A^3\Sigma_u^+, 17) + N_2(X^1\Sigma_g^+, 0) \longrightarrow N_2(B^3\Pi_g, 5) + N_2(X^1\Sigma_g^+, 1) \ . \tag{3.6}$$

This consideration was also regarded in this work. Although the work of Bachmann et al. doesn't provide data for the case M = N, a model applied on the available results would allow one to infer values for such case. The final objective would be to obtain rates through the law (2.75) for the vibronic transitions

$$N_2(A^3\Sigma_u^+, v_1) + N_2(X^1\Sigma_g^+, v_2) \longrightarrow N_2(B^3\Pi_g, v_1') + N_2(X^1\Sigma_g^+, v_2'), \qquad \forall\, v_1,\ v_1',\ v_2, \text{ and } v_2' \ , \tag{3.7}$$

$$N_2(A^3\Sigma_u^+, v_1) + N(^4S_u) \longrightarrow N_2(B^3\Pi_g, v_1') + N(^4S_u), \qquad \forall\, v_1 \text{ and } v_1' \ . \tag{3.8}$$

By fitting (2.73) to the set of points with absolute energy defects $|\Delta E|$ as abscissas, and average process cross sections $\sigma_{p,\text{av}}$ as ordinates, it's possible to obtain characteristic cross sections σ_0 and energies E_0 for each collision partner. The resultant curves are depicted by Figures 3.4 and 3.5.

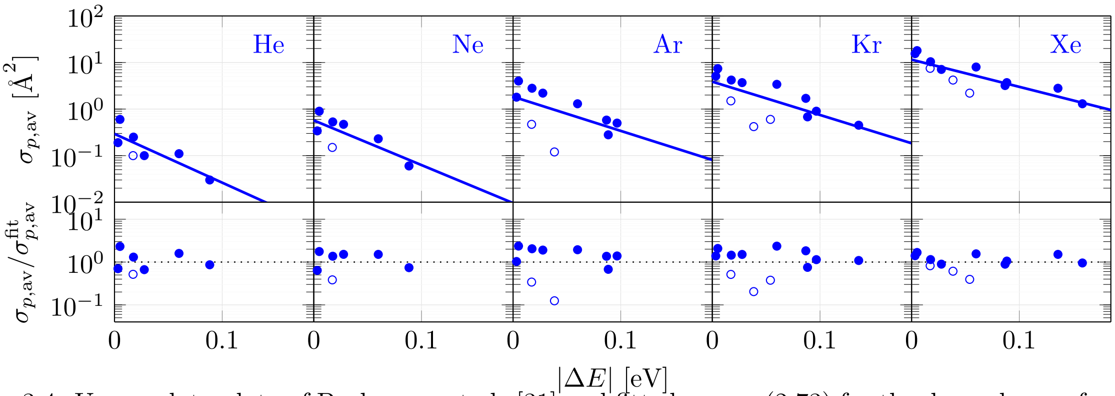

Figure 3.4: Upper plots: data of Bachmann et al. [31] and fitted curves (2.73) for the dependence of $\sigma_{p,\text{av}}$ on $|\Delta E|$, regarding the atomic collision partners. Lower plots: values for the ratios between the data and the fitted curves. Intramolecular exothermic processes: ●; intramolecular endothermic processes: ○.

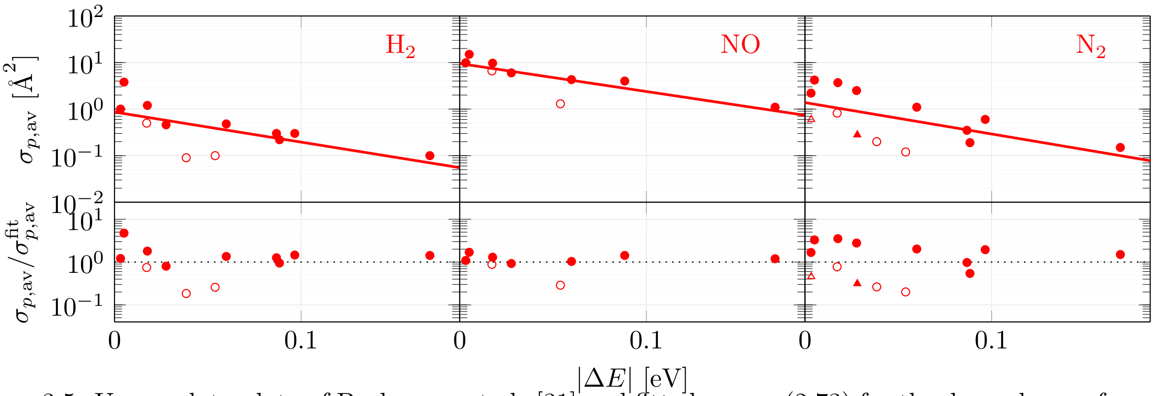

Figure 3.5: Upper plots: data of Bachmann et al. [31] and fitted curves (2.73) for the dependence of $\sigma_{p,\text{av}}$ on $|\Delta E|$, regarding the molecular collision partners. Lower plots: values for the ratios between the data and the fitted curves. Intramolecular exothermic processes: ●; Intramolecular endothermic processes: ○; intermolecular exothermic processes: ▲; intermolecular endothermic processes: △.

Bachmann et al. refer that the data associated to the endothermic processes appears to follow a law which is distinct from the one associated to the exothermic processes. However, the number of points associated to the former is not reasonable enough to properly build a different model for them. It was then decided to fit the data altogether. In general, the fitted curves underestimated the rate coefficients for the exothermic processes and overestimated the ones for the endothermic processes. The ratio between the data average process cross sections and the fit ones was between 0.1 and 4.7.

By analysing the obtained values for the characteristic cross sections σ_0 and energies E_0 associated to processes involving the atomic collision partners, it was found that these quantities increased exponentially with the hard-sphere diameter d_{M} of the latter. It was then decided to obtain the values of σ_0 and E_0 for the processes involving the collision partner $\mathrm{M} = \mathrm{N}$ by fitting exponential curves to the data $(d_{\mathrm{M}}, \sigma_0)$ and (d_{M}, E_0), respectively. The results are depicted by Figure 3.6, which additionally reveal that the data points for the processes involving molecular particles seems to not follow any evident law (though the number of only three data points for each plot is too small to make a proper judgement). The data σ_0 and E_0 values deviate from the fit ones between -34.6% and 9.7%, and between -2.6% and 2.7%, respectively, thus, showing a much greater agreeability on the latter quantity than on the former.

The computation of the respective rate coefficients through expression (2.75) requires the knowledge of the potential well depths for the interactions between N_2 and the collision partners M, i.e. $\varepsilon := \varepsilon_{\mathrm{N}_2\text{ - }\mathrm{M}}$. For that purpose, values of Lennard-Jones (12-6) potential well depths $\varepsilon_{\mathrm{M\text{ - }M}} := E_{\mathrm{LJ,M\text{ - }M}}$ were extracted from the work of Svehla [67]. The quantities ε were then assumed to be $\varepsilon = \sqrt{\varepsilon_{\mathrm{N}_2\text{ - }\mathrm{N}_2} \cdot \varepsilon_{\mathrm{M\text{ - }M}}}$, as suggested by Parmenter et al. [61, 62].

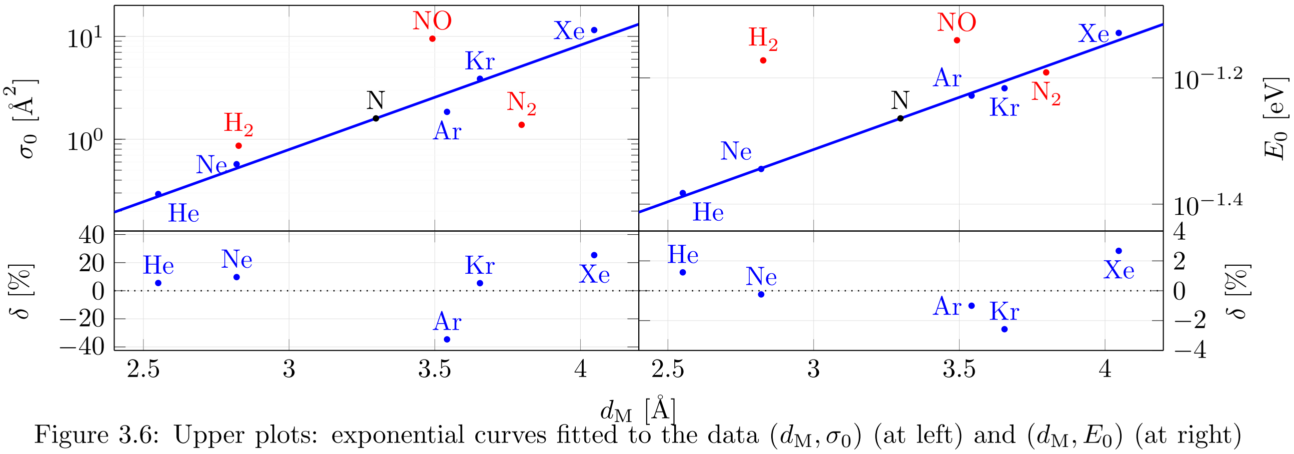

Figure 3.6: Upper plots: exponential curves fitted to the data $(d_{\mathrm{M}}, \sigma_0)$ (at left) and (d_{M}, E_0) (at right) for the processes involving the atomic collision partners. Lower plots: relative deviations of the data, $\delta = (\sigma_0 - \sigma_{0,\mathrm{fit}}) / \sigma_{0,\mathrm{fit}}$ (at left) and $\delta = (E_0 - E_{0,\mathrm{fit}}) / E_{0,\mathrm{fit}}$ (at right). Atomic collision partners: ●; molecular collision partners: ●; nitrogen atom N: ●.

The chemical equation (3.7) represents a large number of different kinetic processes, each one associated to particular set of values of vibrational quantum numbers v_1, v_1', v_2 and v_2'. Since accounting all of these kinetic processes would require too much computational resources for the incoming CFD simulations, it was decided to regard only the most significant ones. The accounted kinetic processes of (3.7) were the ones for which the ratio between the rate coefficient $k_{v_1,v_2}^{v_1',v_2'}$ given by (2.75) and the specific collisional frequency Z given by (2.25) in the limit of the high temperatures (since this will correspond to the simulated regime) was higher or equal to an arbitrated factor of 2×10^{-2}, i.e

$$\lim_{T_{\mathrm{tr_h}} \to +\infty} \frac{k_{v_1,v_2}^{v_1',v_2'}}{Z} = \frac{\sigma_0}{\sigma} e^{-\left(\frac{\varepsilon}{k_B T_{\mathrm{ref}}} + \frac{|\Delta E|}{E_0}\right)} \geq 2 \times 10^{-2} \ .$$

This reduced the number of regarded processes from the unbearable $4,059,264$ to the reasonably manageable $7,436$.

A synopsis on the relevant obtained data is issued by Table 3.3.

Table 3.3: Hard-sphere diameters d_{M}, collisional cross sections σ, interaction potential well depths $\varepsilon_{\mathrm{M\ -\ M}}$ and ε, particle masses m_{M}, reduced masses μ, characteristic cross sections σ_0 and characteristic energies E_0 for the interactions with collision partners N and N_2.

M [-]	d_{M} [Å]	σ [Å^2]	$\varepsilon_{\mathrm{M\ -\ M}}$ [$k_B \cdot$ K]	ε [$k_B \cdot$ K]	m_{M} [u]	μ [u]	σ_0 [Å^2]	E_0 [eV]
N	3.298	39.547	71.400	71.400	14.007	9.338	1.594	0.054
N_2	3.798	45.317	71.400	71.400	28.014	14.007	1.380	0.064

3.2.3 Non-dissociative ionisation of N_2 by electron impact

Let's now consider the process of non-dissociative ionisation of $N_2\left(X^1\Sigma_g^+,\, v\right)$ by electron impact

$$N_2\left(X^1\Sigma_g^+,\, v\right) + e^- \longrightarrow N_2^+\left(e', v'\right) + 2\,e^- \ . \tag{3.9}$$

The work of Laricchiuta el al. [80] issues process cross sections values for (3.9). These are however summed in the electronic levels of N_2^+, $e' \in \{X^2\Sigma_g^+,\, A^2\Pi_u,\, B^2\Sigma_u^+\}$ as well as in the final vibrational levels v' - let these cross sections be denoted by $\sigma_v(E)$, being E the relative translational energy of the collision partners. Also, the data is restricted to $E \in [0, 50]$ eV, and $v \in [0, 40]$ from a database[2] that regards a total of 47 vibrational levels for $N_2\left(X^1\Sigma_g^+\right)$. It's worthy to say that Laricchiuta el al. [80] additionally issue values for the process cross sections for each electronic level e' of N_2^+ for the case $v = 0$, i.e. $\sigma_v^{e'}(E)$ with $v = 0$. These data allows one to compute electronically specific *branching ratios* $\mathfrak{R}_v^{e'}(E) := \sigma_v^{e'}(E)/\sigma_v(E)$ for the case $v = 0$, which are by definition the ratios between the process cross sections for each electronic level e', $\sigma_v^{e'}(E)$, and the sum of all of these, $\sigma_v(E)$. In order to implement in this work the results of Laricchiuta el al., it was decided to assume that the branching ratios $\mathfrak{R}_v^{e'}(E)$ were the same regardless of the vibrational level v of N_2, implying $\mathfrak{R}_v^{e'}(E) = \mathfrak{R}_0^{e'}(E)\, \forall\, v,\, e'$.

The computation of process rate coefficients $k_v^{e'}(T_{\mathrm{tr_e}})$ involves an improper integral (the upper limit corresponds to infinity). Because only finite discrete data points for the process cross section are available, the integration in (2.26) can't be performed in all its domain, and on the other hand, numerical methods are required for its evaluation[3]. Regarding the upper limit of integration, one should first look to the integrand function to know if it's reasonable or not to approximate the improper integral by a proper one. Let's rewrite (2.26) such that the integrand function corresponds to a multiplication between the

---

[2] The database for the vibrational levels of $N_2\left(X^1\Sigma_g^+\right)$ was directly sent from Dr. Laricchiuta to the author.

[3] The employed numerical method was the *composite trapezoidal rule*.

process cross section, $\sigma_v^{e'}$, and a normalised distribution function, say $\tilde{f}$. One may obtain

$$k_v^{e'}(T_{\mathrm{tr_e}}) = \sqrt{\frac{8 k_B T_{\mathrm{tr_e}}}{\pi m_{\mathrm{e}}}} \int_0^{\infty} \sigma_v^{e'}(u) \tilde{f}(u)\, du \ , \tag{3.10}$$

where $u = \frac{E}{k_B T_{\mathrm{tr_e}}}$ is an adimensional variable. The normalised distribution function can be shown to be $\tilde{f}(u) = \tilde{f}\left(\frac{E}{k_B T_{\mathrm{tr_e}}}\right) = \frac{E}{k_B T_{\mathrm{tr_e}}} e^{-\frac{E}{k_B T_{\mathrm{tr_e}}}} = k_B T_{\mathrm{tr_e}} f(E)$. This function goes to zero when $\frac{E}{k_B T_{\mathrm{tr_e}}}$ goes to infinity. And because the variable of dependence is the ratio between E and $k_B T_{\mathrm{tr_e}}$, one can say that the higher the temperature $T_{\mathrm{tr_e}}$, the higher the energy E needed to attain the same small $\tilde{f}$ value. Let's now introduce a new convenient variable: E_{max}, corresponding to the relative kinetic energy value above which there's no process cross section data available. One can say that if $\sigma_v^{e'}(u)$ is a well behaved function (not increasing too much) and E_{max} is sufficiently large, the contribution of the interval $E \in \,]E_{\mathrm{max}}, +\infty[$ to the integral will be negligible when in comparison with the one associated to the adjunct interval $E \in [0,\, E_{\mathrm{max}}]$. In such circumstances it would be right to set E_{max} as the upper limit of the integral.

Figure 3.7 depicts the way that the normalised distribution function $\tilde{f}$ varies with the relative kinetic energy E, for different temperature values, $T_{\mathrm{tr_e}} = 20,000;\ 40,000;\ ...;\ 100,000$ K. Other significant details are present in the figure: the dotted vertical lines correspond to the relative kinetic energy values $E = E_c(T_{\mathrm{tr_e}})$, that if considered as the one in the upper limit of the integration of the normalised distribution function with respect to the variable u, the respective integral would give the value 0.99, i.e. $E_c(T_{\mathrm{tr_e}}) = u_{\mathrm{sup}}\, k_B T_{\mathrm{tr_e}} \, : \, \int_0^{u_{\mathrm{sup}}} \tilde{f}(u)\, du = 0.99$. These may be interpreted as the cutoff energy values that allows a fulfilment of 99% of the normalised distribution function, for each of the given temperatures. The black solid vertical line in the figure corresponds to the maximum data energy value, $E_{\mathrm{max}} = 50$ eV. And the associated label, $F = 97.945\,\%$, corresponds to the percentage of fulfilment of the distribution function for the temperature $T_{\mathrm{tr_e}} = 100,000$ K by the data energy values. This F value is high, and it is for sure higher for the other temperatures (the lower the temperature, the higher the percentage of fulfilment of the distribution function, when fixing the energy value in the upper limit of integration).

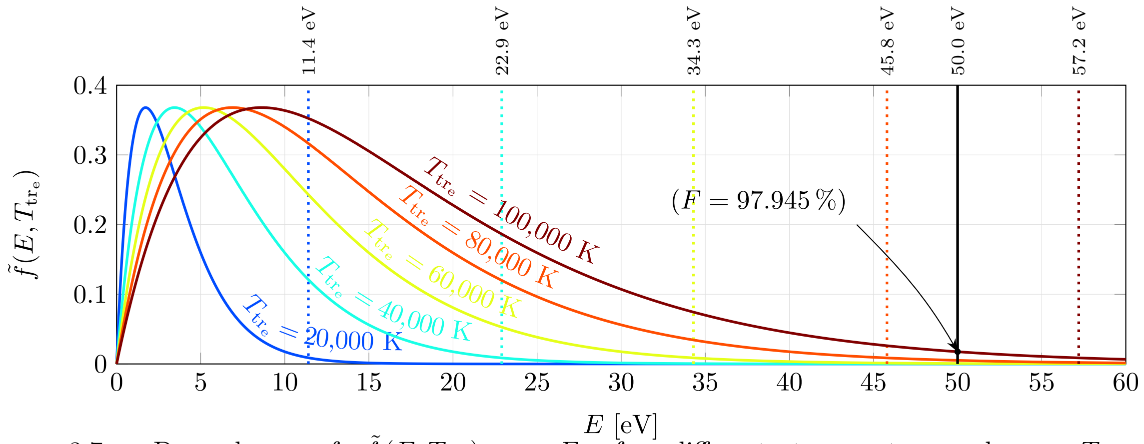

Figure 3.7: Dependence of $\tilde{f}\,(E, T_{\mathrm{tr_e}})$ on E, for different temperature values: $T_{\mathrm{tr_e}} = 20,000;\ 40,000;\ ...;\ 100,000$ K. The vertical dotted lines correspond to the cutoff energies associated to a 99 % fulfilment of the distribution function, at the temperature values. The black solid vertical line corresponds to the maximum data energy value E_{max}.

Figure 3.8 shows the fitted rates $k_v^{e',\mathrm{fit}}(T_{\mathrm{tr_e}})$, as well as the relative fitting error $\delta_v^{e'}(T_{\mathrm{tr_e}}) =$

$\left[k_v^{e',\mathrm{fit}}(T_{\mathrm{tr_e}}) - k_v^{e'}(T_{\mathrm{tr_e}})\right] / k_v^{e'}(T_{\mathrm{tr_e}})$, for $v = 0, 10, 20, 30, 40$ and $e' =$X. The figure shows that the rate coefficients increase with the vibrational quantum number v. Also, the absolute value of the relative error is less than 2%, indicating a good agreement between the fitted curves and the data points.

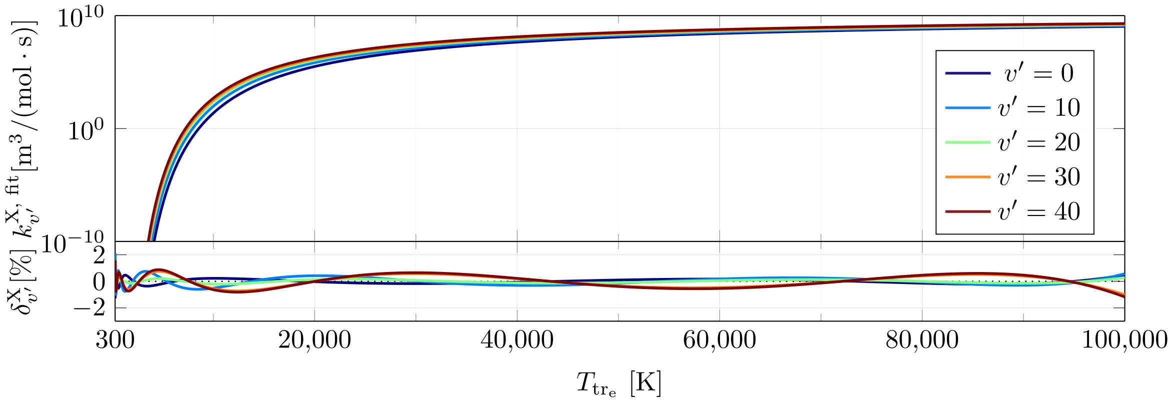

Figure 3.8: Fitted reaction rate curves $k_v^{e',\mathrm{fit}}(T_{\mathrm{tr_e}})$, and relative fitting error $\delta_v^{e'}(T_{\mathrm{tr_e}})$, for $v = 0, 10, 20, 30, 40$ and $e' = \mathrm{X}^2\Sigma_\mathrm{g}^+$.

Note that since the rate coefficients $k_v^{e',\mathrm{fit}}(T_{\mathrm{tr_e}})$ are summed on the vibrational level v' of N_2^+, and vibrational-specific rate coefficients were wanted, a vibrational redistribution was performed on them.

3.2.4 Electronic excitation and ionisation of N and N^+ by electron impact

The author considered the theoretical values obtained by Berrington et al. [81] for the process cross sections associated to the excitation of $\mathrm{N}\left({}^4\mathrm{S_u}\right)$ to $\mathrm{N}\left({}^2\mathrm{D_u}\right)$ and $\mathrm{N}\left({}^2\mathrm{P_u}\right)$, as well as the excitation of $\mathrm{N}\left({}^2\mathrm{D_u}\right)$ to $\mathrm{N}\left({}^2\mathrm{P_u}\right)$. The experimental values for the process cross sections obtained by Brook et al. [82] were considered for the ionisation of $\mathrm{N}\left({}^4\mathrm{S_u}\right)$, and the numerical values for the process cross sections computed by Wang et al. [83] were regarded for the ionisation of $\mathrm{N}\left({}^2\mathrm{D_u}\right)$ and $\mathrm{N}\left({}^2\mathrm{P_u}\right)$. Since no experimental or accurate theoretical data were found for the other electronic levels of N, it was necessary to rely on empirical correlations to complete the database. And the same applied for the case electronic excitation of N^+ for all of its electronic levels. Rate coefficients for the excitation and ionisation of an atomic particle by electron impact can be computed through the well-known empirical correlations originally obtained by Drawin [84, 85]. In this work, the Drawin expressions adapted by Panesi et al. [86] were preferred due to their simplicity. The rate coefficient for the electronic excitation of an atomic particle from the e-th electronic level to the e'-th electronic level may then be computed through

$$k_e^{e'}(T_{\mathrm{tr_e}}) = \begin{cases} 4\pi a_0^2 \alpha \sqrt{\dfrac{8k_B T_{\mathrm{tr_e}}}{\pi m_\mathrm{e}}} \left(\dfrac{\mathrm{Ry}}{k_B T_{\mathrm{tr_e}}}\right)^2 I_1(a_e^{e'}), & \text{if } l_{e'} \neq l_e \ , \\ 4\pi a_0^2 \alpha \sqrt{\dfrac{8k_B T_{\mathrm{tr_e}}}{\pi m_\mathrm{e}}} \left(a_e^{e'}\right)^2 I_2(a_e^{e'}), & \text{if } l_{e'} = l_e \ , \end{cases} \tag{3.11}$$

where a_0 is the *Bohr radius*, $\alpha = 0.05$ is a parameter, Ry is the Rydberg unit of energy, l_e and $l_{e'}$ are the *orbital quantum numbers* of the most energetic electrons in the e and e' electronic levels of the atomic particle, and $a_e^{e'} = (\epsilon_{e'} - \epsilon_e) / (k_B T_{\mathrm{tr_e}})$ is a reduced difference between the final sensible electronic energy $\epsilon_{e'}$ and the initial one ϵ_e. The quantities $I_1(a_e^{e'})$ and $I_2(a_e^{e'})$ are two functions of $a_e^{e'}$ given by

$$I_1(a_e^{e'}) = 0.63255 \left(a_e^{e'}\right)^{-1.6454} e^{-a_e^{e'}} \ , \qquad (3.12) \qquad I_2(a_e^{e'}) = 0.23933 \left(a_e^{e'}\right)^{-1.4933} e^{-a_e^{e'}} \ . \qquad (3.13)$$

Also, the rate coefficient for the ionisation of an atomic particle from the e-th electronic may be computed through the expression

$$k_e^+(T_{\mathrm{tr_e}}) = 4\pi a_0^2 \alpha^+ \sqrt{\frac{8k_B T_{\mathrm{tr_e}}}{\pi m_\mathrm{e}}} \left(\frac{\mathrm{Ry}}{k_B T_{\mathrm{tr_e}}}\right)^2 I_1(a_e^+) \ , \tag{3.14}$$

being $\alpha^+ = 1$ a parameter, and $a_e^+ = (\epsilon^+ - \epsilon_e) / (k_B T_{\mathrm{tr_e}})$ a reduced difference between the *ionisation energy* of the atomic particle from its electronic ground level ϵ^+ and the initial electronic energy ϵ_e.

3.2.5 Electronic excitation and ionisation of N and N$^+$ by heavy particle impact

Due to an overall lack of experimental data for the electronic excitation and ionisation of N and N$^+$ by heavy particle impact, it was decided to rely on semi-empirical formulae to compute the respective rate coefficients. The relation obtained by Annaloro et al. [66] was regarded:

$$k_f(T_{\mathrm{tr_h}}) = \alpha\sigma_0 \left(\frac{\Delta E}{k_B T_{\mathrm{tr_h}}}\right)^\beta \sqrt{\frac{8k_B T_{\mathrm{tr_h}}}{\pi\mu}} e^{-\frac{\Delta E}{k_B T_{\mathrm{tr_h}}}} \ , \tag{3.15}$$

being ΔE the energy defect, i.e. $\Delta E = \epsilon_{e'} - \epsilon_e$ for the case of electronic excitation and $\Delta E = \epsilon^+ - \epsilon_e$ for the case of ionisation. The variables e, e', ϵ_e, $\epsilon_{e'}$ and ϵ^+ have the same meaning has the ones declared in Section §3.2.4. The quantities $\alpha = 0.39534$ and $\beta = 0.3546$ correspond to two convenient parameters, $\sigma_0 = 10^{-20}\,\mathrm{m}^2$ a characteristic cross section, and μ the reduced mass of the collision partners.

3.3 Radiative processes

3.3.1 Spontaneous emission of the molecular species, N$_2$ and N$_2^+$

Einstein coefficients for spontaneous emission $A_{e,v}^{e',v'}$ of N$_2$ and N$_2^+$ were directly extracted from the literature or were computed through a theoretical expression involving the so-called *sums of the electronic-vibrational transition moments* $\left(\sum R_e^2\right)_{e,v}^{e',v'}$ [87], being these also taken from the literature. Such expression corresponds to [88]

$$A_{e,v}^{e',v'} = \frac{16\pi^3}{3\varepsilon_0 c^3 h} \left(\nu_{e,v}^{e',v'}\right)^3 \frac{\left(\sum R_e^2\right)_{e,v}^{e',v'}}{(2-\delta_{0,\Lambda})(2S+1)} \ , \tag{3.16}$$

where $\nu_{e,v}^{e',v'}$ is the frequency of the emitted photon, Λ is the initial quantum number for the projection of the total electronic orbital angular momentum vector on the internuclear axis, and S is the initial total spin quantum number. Table B.1 assembles all the accounted molecular spontaneous emission processes, listing the name of the *electronic system*[4], the initial and final electronic levels, the maximum initial and final vibrational quantum numbers, as well as the reference from which the data were taken from.

3.3.2 Spontaneous emission of the atomic species, N and N^+

For the case of N and N^+, Einstein coefficients for spontaneous emission $A^{e^{\dagger\dagger}}_{s,e^\dagger}$ were extracted from the NIST database [64]. These coefficients are in respect of electronic levels that take into account the fine structure. Since this work considers representative electronic levels computed from the ones with fine structure, it's necessary to compute Einstein coefficients in respect of these representative electronic levels as well. Let's assign the symbol $A^{e'}_{s,e}$ and the name "representative Einstein coefficient for spontaneous emission" to the resultant Einstein coefficient. It can be shown that it is given by

$$A^{e'}_{s,e} = \sum_{e^\dagger,\, e^{\dagger\dagger}} \frac{g_{s,e^\dagger}}{g_{s,e}} A^{e^{\dagger\dagger}}_{s,e^\dagger} \ . \tag{3.17}$$

A synopsis on all of the considered atomic spontaneous emission processes is presented in Table B.2.

3.3.3 The line-shape factor

In this work, the line-shape factor $\phi^{e',v'}_{\lambda,s,e,v}$ is considered to be the result of four contributions: Doppler, collisional, Stark, and resonance broadening. One may determine a line-shape factor for each isolated contribution, and then compute the global line-shape factor $\phi^{e',v'}_{\lambda,s,e,v}$ through a triple convolution [44]:

$$\begin{split}\phi^{e',v'}_{\lambda,s,e,v}(\vec{r},t,\lambda) = \int_{-\infty}^{\infty} \left(\phi^{e',v'}_{\lambda,s,e,v}\right)_{\mathrm{D}} (\vec{r},t,\lambda^{e',v'}_{s,e,v}+\lambda') \left\{ \int_{-\infty}^{\infty} \left(\phi^{e',v'}_{\lambda,s,e,v}\right)_{\mathrm{col}} (\vec{r},t,\lambda^{e',v'}_{s,e,v}+\lambda'') \Bigg[\right.\\ \left. \int_{-\infty}^{\infty} \left(\phi^{e',v'}_{\lambda,s,e,v}\right)_{\mathrm{S}} (\vec{r},t,\lambda^{e',v'}_{s,e,v}+\lambda''') \cdot \left(\phi^{e',v'}_{\lambda,s,e,v}\right)_{\mathrm{res}} (\vec{r},t,\lambda-\lambda'-\lambda''-\lambda''')\, d\lambda''' \Bigg]\, d\lambda'' \right\} d\lambda' \ .\end{split} \tag{3.18}$$

The line-shape factor for isolated Doppler broadening can be shown to be given by [43]

$$\left(\phi^{e',v'}_{\lambda,s,e,v}\right)_{\mathrm{D}}(\vec{r},t,\lambda) = \frac{\lambda^{e',v'}_{s,e,v}}{\lambda^2}\sqrt{\frac{m_s c^2}{2\pi k_B T_{\mathrm{tr_h}}(\vec{r},t)}} \cdot e^{-\frac{m_s c^2}{2k_B T_{\mathrm{tr_h}}(\vec{r},t)}\left(\frac{\lambda-\lambda^{e',v'}_{s,e,v}}{\lambda}\right)^2} \tag{3.19}$$

It's important to mention that the relation for the frequency-specific line-shape factor for Doppler broadening $\left(\phi^{e',v'}_{\nu,s,e,v}\right)_{\mathrm{D}} = (\lambda^2/c)\cdot\left(\phi^{e',v'}_{\lambda,s,e,v}\right)_{\mathrm{D}}$ has a well-known form as against the wavelength-specific one:

$$\left(\phi^{e',v'}_{\nu,s,e,v}\right)_{\mathrm{D}}(\vec{r},t,\nu) = \frac{1}{\nu^{e',v'}_{s,e,v}}\sqrt{\frac{m_s c^2}{2\pi k_B T_{\mathrm{tr_h}}(\vec{r},t)}} \cdot e^{-\frac{m_s c^2}{2k_B T_{\mathrm{tr_h}}}\left(\frac{\nu-\nu^{e',v'}_{s,e,v}}{\nu^{e',v'}_{s,e,v}}\right)^2} \tag{3.20}$$

Expression (3.20) corresponds to a *Gaussian function* $G(\nu, w_G, \nu_{0G})$ of *half-width at half-maximum* $\left(w^{e',v'}_{\nu,s,e,v}\right)_{\mathrm{D}} = \nu^{e',v'}_{s,e,v}\sqrt{[2\ln 2\, k_B T_{\mathrm{tr_h}}(\vec{r},t)]/(m_s c^2)} := w_G$, centred at $\nu = \nu^{e',v'}_{s,e,v} := \nu_{0G}$ [44]:

$$G(\nu, w_G, \nu_{0G}) = \frac{\sqrt{\ln 2}}{\sqrt{\pi}\cdot w_G} \cdot e^{-\ln 2\left(\frac{\nu-\nu_{0G}}{w_G}\right)^2} \ . \tag{3.21}$$

---

[4] The term "electronic system" is attributed to the set constituted by the initial and the final electronic levels of the particle in the radiative process.

One may anyway always approximate the wavelength-specific line-shape factor by a Gaussian function [44] since the condition $[\left(w^{e',v'}_{\nu,s,e,v}\right)_\mathrm{D} \cdot \left(\lambda^{e',v'}_{s,e,v}\right)^2/c]/\lambda^{e',v'}_{s,e,v} = \left(w^{e',v'}_{\nu,s,e,v}\right)_\mathrm{D}/\nu^{e',v'}_{s,e,v} \ll 1$ holds, i.e. the half-width at half-maximum of the frequency-specific line-shape factor is much lesser than its centre. For the case of collisional broadening, the formula for the frequency-specific line-shape factor based on the *electron theory of Lorentz* and referred by Penner [43] was considered:

$$\left(\phi^{e',v'}_{\nu,s,e,v}\right)_\mathrm{col}(\vec{r},t,\nu) = \frac{1}{\pi\,\frac{Z_{\mathrm{opt},s,e,v}+Z_{\mathrm{opt},s,e',v'}}{2\pi}} \cdot \frac{1}{1+\left(\frac{\nu-\nu^{e',v'}_{s,e,v}}{\frac{Z_{\mathrm{opt},s,e,v}+Z_{\mathrm{opt},s,e',v'}}{2\pi}}\right)^2} \ , \tag{3.22}$$

being $Z_{\mathrm{opt},s,e,v}$ the *optical collisional frequency per s-th species particle* in (e,v) with the other particles:

$$Z_{\mathrm{opt},s,e,v} = \left(\sum_{q\in\{\mathrm{h}\},e'',v''} \frac{n_{q,e'',v''}\cdot\sigma^{q,e'',v''}_{\mathrm{opt},s,e,v}}{1+\delta^{q,e'',v''}_{s,e,v}}\sqrt{\frac{8k_BT_{\mathrm{tr_h}}}{\pi\,\mu_{s,q}}}\right) + n_\mathrm{e}\cdot\sigma^\mathrm{e}_{\mathrm{opt},s,e,v}\sqrt{\frac{8k_BT_{\mathrm{tr_e}}}{\pi\,m_\mathrm{e}}} \ . \tag{3.23}$$

The sum in (3.23) is done in all the heavy species, their electronic levels and vibrational levels. The quantity $\delta^{q,e'',v''}_{s,e,v}$ is a Kronecker delta giving 1 if $(s,e,v)=(q,e'',v'')$, and 0 if not. The quantity $\sigma^{q,e'',v''}_{\mathrm{opt},s,e,v}$ corresponds to the *optical collisional cross section* for a collision between a particle of the s-th species in (e,v) with a particle of the q-th species in (e'',v''). And the quantity $\sigma^\mathrm{e}_{\mathrm{opt},s,e,v}$ corresponds to $\sigma^{q,e'',v''}_{\mathrm{opt},s,e,v}$ for the case of the q-th species being a free electron. Penner [43] refers that, according to the available data, such quantities have the same order of magnitude as the respective collisional cross sections $\sigma^{q,e'',v''}_{s,e,v}$, and therefore, it was decided to consider $\sigma^{q,e'',v''}_{\mathrm{opt},s,e,v} \approx \sigma^{q,e'',v''}_{s,e,v}$. No data were found for the case of collisions with free electrons, and therefore, its contributio was disregarded. Note that $Z_{\mathrm{opt},s,e',v'}$ in (3.22) corresponds to the optical collisional frequency per particle of s-th species particles in (e',v') with the other particles. It is given by (3.23) with e and v substituted by e' and v', respectively. It is worthy to mention that expression (3.22) corresponds to a *Lorentzian function* $L(\nu,w_L,\nu_{0L})$ of half-width at half-maximum $\left(w^{e',v'}_{\nu,s,e,v}\right)_\mathrm{col} = (Z_{\mathrm{opt},s,e,v}+Z_{\mathrm{opt},s,e',v'})/(2\pi) := w_L$, centred at $\nu = \nu^{e',v'}_{s,e,v} := \nu_{0L}$ [44]. The function is given by

$$L(\nu,w_L,\nu_{0L}) = \frac{1}{\pi w_L}\cdot\frac{1}{1+\left(\frac{\nu-\nu_{0L}}{w_L}\right)^2} \ . \tag{3.24}$$

Note that by assuming the half-width at half-maximum of the frequency-specific line-shape factor to be much lesser than its centre, it's possible to express the wavelength-specific line-shape factor $\left(\phi^{e',v'}_{\lambda,s,e,v}\right)_\mathrm{col}$ through also a Lorentzian function $L(\lambda,w_L,\lambda_{0L})$ being this of half-width at half-maximum $\left(w^{e',v'}_{\lambda,s,e,v}\right)_\mathrm{col} = [(\lambda^{e',v'}_{s,e,v})^2/c]\cdot\left(w^{e',v'}_{\nu,s,e,v}\right)_\mathrm{col} := w_L$, centred at $\lambda = \lambda^{e',v'}_{s,e,v} := \lambda_{0L}$ [44]. For the case of Stark broadening, it was decided to consider in this work the approach of Johnston [89], which solely accounts the contribution of free electrons. The associated wavelength-specific line-shape factor $\left(\phi^{e'v'}_{\lambda,s,e,v}\right)_\mathrm{S}$ is given by a Lorentzian function $L(\lambda,w_L,\nu_{0L})$ of half-width at half-maximum $\left(w^{e',v'}_{\lambda,s,e,v}\right)_\mathrm{S}$, centred at $\lambda = \lambda^{e',v'}_{s,e,v}$:

$$\left(\phi^{e'v'}_{\lambda,s,e,v}\right)_\mathrm{S}(\vec{r},t,\lambda) = \frac{1}{\pi\left(w^{e',v'}_{\lambda,s,e,v}\right)_\mathrm{S}}\cdot\frac{1}{1+\left[\frac{\lambda-\lambda^{e',v'}_{s,e,v}}{\left(w^{e',v'}_{\lambda,s,e,v}\right)_\mathrm{S}}\right]^2} \ . \tag{3.25}$$

The half-width at half-maximum regarded by Johnston has a form identical to the one of Park [90]:

$$\left(w_{\lambda,s,e,v}^{e',v'}\right)_{\mathrm{S}} = \left(w_{\lambda,s,e,v,\mathrm{ref}}^{e',v'}\right)_{\mathrm{S}} \left(\frac{T_{\mathrm{tr_e}}}{T_{\mathrm{tr_e},\mathrm{ref}}}\right)^{n} \cdot \left(\frac{n_{\mathrm{e}}}{n_{\mathrm{e},\mathrm{ref}}}\right) \ , \tag{3.26}$$

where $\left(w_{\lambda,s,e,v,\mathrm{ref}}^{e',v'}\right)_{\mathrm{S}}$ is the half-width at half-maximum at a free electron translational temperature $T_{\mathrm{tr_e}} = 10,000\,\mathrm{K} := T_{\mathrm{tr_e},\mathrm{ref}}$ and at a free electron number density $n_{\mathrm{e}} = 10^{16}\,\mathrm{cm}^{-3} := n_{\mathrm{e},\mathrm{ref}}$. Park [90] solely treated the case of argon, obtaining the exponent $n = 0.33$ by fitting the curve (3.26) to the values of half-width at half-maximum $\left(w_{\lambda,s,e,v}^{e',v'}\right)_{\mathrm{S}}$ at $n_{\mathrm{e}} = n_{\mathrm{e},\mathrm{ref}}$ for different $T_{\mathrm{tr_e}}$, issued by Griem [91–93]. Johnston considers this exponent value to be also acceptable for the case of the nitrogen and oxygen atoms. In this work, it was decided to take such assumption one step further by regarding this same value for all the considered species. Johnston then considers a model for the reference half-width at half-maximum of the form

$$\left(w_{\lambda,s,e,v,\mathrm{ref}}^{e',v'}\right)_{\mathrm{S}} = \frac{C \cdot \left(\lambda_{s,e,v}^{e',v'}\right)^{2}}{\left(\epsilon_s^{+} - \epsilon_{s,e,v}\right)^{n}} \ , \tag{3.27}$$

being ϵ_s^{+} the ionisation energy of the a s-th species particle from its ground level, and C and n correspond to some constants. The values for the ionisation energies of all the species considered in this work were taken from the literature, being listed in Table 3.4.

Table 3.4: Ionisation energies from the ground level of N, N^+, N_2 and N_2^+.

s	ϵ_s^{+} [eV]	Reference
N	14.534	Biémont et al. [94]
N^+	29.601	Biémont et al. [94]
N_2	15.581	Trickl et al. [95]
N_2^+	27.9	Bahati et al. [96]

Model (3.27) is a variant of the one considered by Cowley in its theoretical work [97]. Johnston obtained $C = 1.69 \times 10^{10}\,[(\text{“cm}^{-1}\text{”})^{2.623}/\mathrm{cm}^2] \cdot \mathrm{cm}$ and $n = 2.623$ by fitting the curve (3.27) to the values of $\left(w_{\lambda,s,e,v,\mathrm{ref}}^{e',v'}\right)_{\mathrm{S}}$ for the nitrogen and oxygen atoms, issued by Griem [93] and by Wilson and Nicolet [98]. For the case of resonance broadening, the theory developed by Griem [92] was considered. The wavelength-specific line-shape factor corresponds to a Lorentzian function centred at $\lambda = \lambda_{s,e,v}^{e',v'}$ and of half-width at half-maximum

$$\left(w_{\lambda,s,e,v}^{e',v'}\right)_{\mathrm{res}} = \frac{3}{32}\sqrt{\frac{g_{s,e,v}}{g_{s,e',v'}}}\,\frac{\left(\lambda_{s,e,v}^{e',v'}\right)^{5} A_{s,e,v}^{e',v'}}{\pi^{3} c}\, n_{s,e',v'} \ . \tag{3.28}$$

Being all the broadening mechanisms here described, it is now the time to obtain the global line-shape factor defined by (3.18). By noting that the convolution of two Lorentzian functions is also a Lorentzian function whose half-width at half-maximum and centre is the sum of them, one gets

$$\phi_{\lambda,s,e,v}^{e',v'}(\vec{r},t,\lambda) = \int_{-\infty}^{\infty} G(\lambda_{s,e,v}^{e',v'} + \lambda', \left(w_{\lambda,s,e,v}^{e',v'}\right)_{\mathrm{D}}, \lambda_{s,e,v}^{e',v'}) \cdot L(\lambda - \lambda', \left(w_{\lambda,s,e,v}^{e',v'}\right)_{\mathrm{col}} + \left(w_{\lambda,s,e,v}^{e',v'}\right)_{\mathrm{S}} + \left(w_{\lambda,s,e,v}^{e',v'}\right)_{\mathrm{res}}, \lambda_{s,e,v}^{e',v'})\, d\lambda' \ . \tag{3.29}$$

The improper integral that appears in (3.29) corresponds to a *Voigt function* of Gaussian and Lorentzian half-widths at half-maxima $w_G = \left(w^{e',v'}_{\lambda,s,e,v}\right)_{\mathrm{D}}$ and $w_L = \left(w^{e',v'}_{\lambda,s,e,v}\right)_{\mathrm{col}} + \left(w^{e',v'}_{\lambda,s,e,v}\right)_{\mathrm{S}} + \left(w^{e',v'}_{\lambda,s,e,v}\right)_{\mathrm{res}}$, centred at $\lambda = \lambda^{e',v'}_{s,e,v} := \lambda_{0V}$ [44]:

$$V(\lambda, w_G, w_L, \lambda_{0V}) = \int_{-\infty}^{+\infty} G(\lambda_{0V} + \lambda', w_G, \lambda_{0V}) \cdot L(\lambda - \lambda', w_L, \lambda_{0V}) \, d\lambda' \; . \tag{3.30}$$

The integral in (3.30) is not analytically solvable, and therefore, one should consider a numerical method such as the trapezoidal integral rule, or an empirical approximation such as the formula proposed by Whiting [99], to account it. Although the former may give better results, it requires much more computational resources than the latter. The empirical formula of Whiting was then chosen, which according to his words, matches the exact function within 5 per cent at worst, corresponding to

$$\begin{aligned} V(\lambda, w_G, w_L, \lambda_{0V}) \approx {} & \frac{1}{2\, w_V \left[1.065 + 0.447 \frac{w_L}{w_V} + 0.058 \left(\frac{w_L}{w_V}\right)^2\right]} \left\{ \left(1 - \frac{w_L}{w_V}\right) e^{-\ln 2 \left(\frac{\lambda - \lambda_{0V}}{w_V}\right)^2} + \frac{w_L}{w_V} \cdot \frac{1}{1 + \left(\frac{\lambda - \lambda_{0V}}{w_V}\right)^2} \right. \\ & \left. + 0.016 \left(1 - \frac{w_L}{w_V}\right) \frac{w_L}{w_V} \left[e^{-0.084 \left|\frac{\lambda - \lambda_{0V}}{w_V}\right|^{2.25}} - \frac{10}{10 + 0.210 \left|\frac{\lambda - \lambda_{0V}}{w_V}\right|^{2.25}} \right] \right\} \; . \end{aligned} \tag{3.31}$$

The formula of Olivero and Longbothum [100] for the half-width at half-maximum of the Voigt function w_V was considered. It has an accuracy of about 0.01 per cent, being expressed by

$$w_V \approx (w_L + w_G) \left\{ 1 - 0.18121 \left[1 - \left(\frac{w_L - w_G}{w_L + w_G}\right)^2 \right] - \left(0.023665\, e^{0.6 \frac{w_L - w_G}{w_L + w_G}} + 0.00418\, e^{-1.9 \frac{w_L - w_G}{w_L + w_G}} \right) \sin\left(\pi \frac{w_L - w_G}{w_L + w_G} \right) \right\} \; . \tag{3.32}$$

3.4 Simulations of post-shock flows generated by a shock tube

Herein a detailed description will be made with respect to the implementation of the zero and Euler one-dimensional vibronic-specific state-to-state models in simulations of post-shock flows generated by a shock tube. The studied experiment corresponded to the test 62 of the EAST shock tube done in 2018, whose results are issued by Brandis and Cruden [39]. For the case of the zero-dimensional model, the fluid flow governing equations to deal with correspond to (2.38a), (2.38b) and (2.38c). And for the case of the one-dimensional model, they correspond to (2.40a), (2.40b), (2.40c), and (2.40d).

The unknowns of the equations for the zero-dimensional model are $c_{s,v,e}$ ($\forall s$, v and e), $T_{\mathrm{tr_h}}$ and $T_{\mathrm{tr_e}}$. And the unknowns of the equations for the one-dimensional model are all of these plus the x-component of the flow velocity vector u. Note that in the case of the zero-dimensional model, the mixture mass density ρ is an invariable and its value may be taken as the initial one. Initial values then need to be assigned to $c_{s,v,e}$, $T_{\mathrm{tr_h}}$, $T_{\mathrm{tr_e}}$, u and ρ. These are associated to the conditions of the post-shock flow immediately downstream of the shock wave - which will be labelled here by "2". There are no chemical processes neither electronic or vibrational excitation occurring throughout the thickness of the shock wave - the mixture is said to be *frozen* while passing through the shock wave. Hence, $c_{s,v,e,2} = c_{s,v,e,\infty}$, where the symbol "$\infty$" denotes the upstream conditions. Due to the very fast excitation of the rotational energy mode, an equilibration with the translational one is reached immediately downstream of the shock wave, and a heavy particle translational-rotational temperature $T_{\mathrm{tr_h-rot},2}$ may be considered. Particular attention should be given to the free electron translational temperature $T_{\mathrm{tr_e}}$: since the free electrons are much lighter than the heavy particles, the excitation of their translation energy modes occurs in a different way, and it's not certain that an equilibration between them may occur immediately downstream of the shock wave. It was decided to consider the equality $T_{\mathrm{tr_e},2} = T_{\mathrm{tr_h},2}$, as also regarded by Kadochnikov and Arsentiev [101]. The low T_∞ value (of 300 K) allows one to disregard the contribution of the vibrational and electronic energy modes to the particles energy [102] throughout the shock wave. This means that both mixture specific heat at constant volume C_V and mixture specific heat at constant pressure C_p, from the upstream to the immediately downstream conditions, only depend on the translational and rotational energy modes of the particles. It's then possible to obtain the well-known *Rankine-Hugoniot jump conditions*, which allows one to compute the conditions immediately downstream of the shock wave from the ones upstream of it [2]. For the cases of the mass density ρ_2, the x-component of the flow velocity vector u_2, the heavy particle translational-rotational temperature $T_{\mathrm{tr_h},2}$ and the free electron translational temperature $T_{\mathrm{tr_e},2}$, the respective Rankine-Hugoniot jump conditions give

$$\rho_2 = \frac{(\gamma+1)\,\mathrm{Ma}_\infty^2}{(\gamma-1)\,\mathrm{Ma}_\infty^2+2}\rho_\infty \ , \qquad (3.33) \qquad\qquad u_2 = \frac{(\gamma-1)\,\mathrm{Ma}_\infty^2+2}{(\gamma+1)\,\mathrm{Ma}_\infty^2}u_\infty \ , \qquad (3.34)$$

$$T_{\mathrm{tr_h},2} = T_{\mathrm{tr_e},2} = \frac{\left[(\gamma-1)\,\mathrm{Ma}_\infty^2+2\right]\left[2\gamma\mathrm{Ma}_\infty^2-(\gamma-1)\right]}{(\gamma+1)^2\,\mathrm{Ma}_\infty^2}T_\infty \ , \qquad (3.35)$$

being $\gamma = C_p/C_V$ the ratio of specific heats.

Brandis and Cruden considered in their experiment a test gas of pure N_2 at room temperature $T_\infty =$ 300 K and pressure $p_\infty = 0.2$ Torr. Different shock wave speeds u_s were tested. Note that u_s is equal to the upstream flow speed u_∞ being this defined in a reference of frame that moves with the wave.

The numerical results obtained from the zero-dimensional simulations may be regarded as the ones of an element of fluid which passes through the shock wave, being immediately constrained to a transparent fixed-volume box, and removed from the flow. Conversely to the actual element of fluid, this hypothetical one would not be subjected to transport phenomena - mass diffusion, heat conduction and viscosity - mass density change, neither would receive radiative energy from the complementary system. The results of the zero-dimensional simulations depend on the amount of time elapsed after the passage of the element of fluid through the shock wave, t, while the experimental results depend on the distance travelled with respect to the shock wave, x. Assuming the speed of the post-shock flow to be nearly constant, i.e. $u \approx u_2$, one has $x(t) = u_2 \cdot t$, or equivalently, $t(x) = x/u_2$, allowing one to express the numerical and experimental results through the same variable dependence, x.

The one-dimensional simulations take into account the effects of momentum transfer in the flow by regarding a momentum balance equation, and therefore, the respective numerical results are expected to agree better with the experimental results than the ones of the zero-dimensional simulations.

Brandis and Cruden measured the post-shock specific radiative intensity I_λ associated to photons propagating in a radial direction of the tube, say $\vec{e}_y$, at the furthest radial point of the plasma, $y = D/2$, being $D = 10.16$ cm the shock tube inner diameter [39]. Figure 3.9 depicts the geometry of the apparatus, as well as the regarded inertial frame of reference whose origin moves with the shock wave. The x-axis is aligned with the shock tube axis, pointing downstream, the z-axis points upwards, and the y-axis makes a direct dihedral with the other two. The $\vec{e}_y$ direction is defined by $\varphi = \pi/2$ and $\theta = \pi/2$.

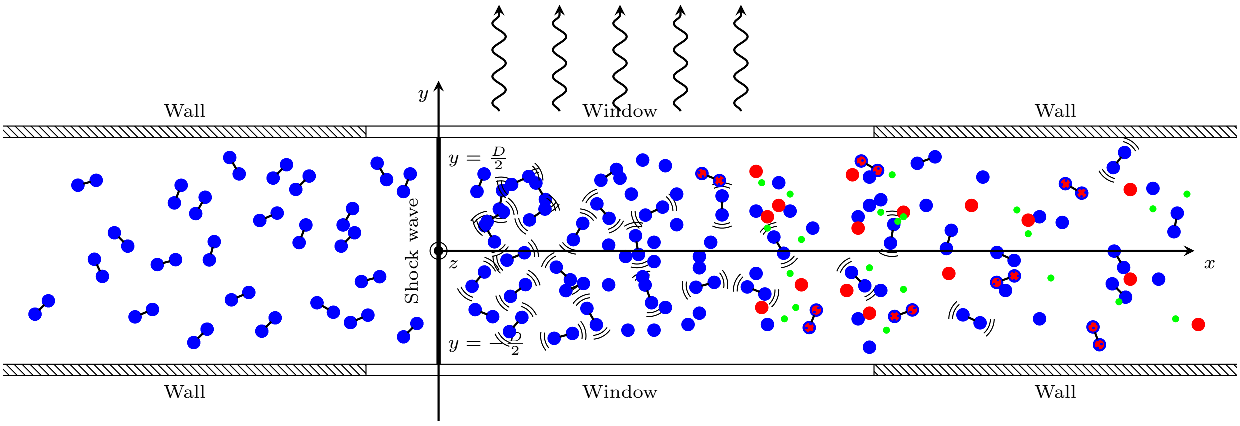

Figure 3.9: Longitudinal cross-section of the shock tube, showing the measured radiative field.

One may further quantify the radiative intensity through the equation of radiative transfer (2.37) for the direction $\vec{e}_s = \vec{e}_y$ disregarding the time-variation term (the flow is approximately stationary when observed from a reference of frame which moves with the shock wave):

$$\frac{\partial I_\lambda}{\partial y}(x, y, 0, \frac{\pi}{2}, \frac{\pi}{2}, \lambda) = j_\lambda(x, y, 0, \frac{\pi}{2}, \frac{\pi}{2}, \lambda) - k_\lambda(x, y, 0, \frac{\pi}{2}, \frac{\pi}{2}, \lambda) \cdot I_\lambda(x, y, 0, \frac{\pi}{2}, \frac{\pi}{2}, \lambda) \ . \tag{3.36}$$

By assuming the emission and absorption coefficients to not depend on y, initially assuming the medium to be *optically thin* and then introducing the concept of an escape factor, as well as suppressing the labels $z = 0$, $\varphi = \pi/2$, and $\theta = \pi/2$, one may show that the specific radiative intensity at $y = \frac{D}{2}$ is given by

$$I_\lambda(x, \frac{D}{2}, \lambda) = \frac{hcD}{\lambda} \left[\sum_{\text{se}} \Lambda_{s,e,v}^{e',v'} \frac{A_{s,e,v}^{e',v'}}{4\pi} \phi_{s,e,v}^{e',v'}(\lambda) \, n_{s,e,v}(x) \right] \ . \tag{3.37}$$

To simplify even more the notation, the label $y = D/2$ in the argument of I_λ will also be suppressed.

Brandis and Cruden used in their experiment four spectrometers, each one measuring the specific radiative intensity for a particular interval of wavelengths. These intervals of wavelengths are labelled as VUV - from **v**acuum **u**ltra-**v**iolet radiation[5] - “Blue”, “Red” and IR - from **i**nfra-**r**ed radiation. Among the issued data there are the *instrumentally resolved radiative intensities* $\hat{I}(x)$ and the *instrumentally resolved non-equilibrium metrics* $\hat{I}_\lambda^{\text{ne}}(\lambda)$ for each of the four wavelength intervals of 42 shots. The hat denotes instrumentally resolved quantities, in contrast to the real quantities. The former are the ones that are actually obtained in the experiment, being related to the latter through a transformation “applied” by the instruments. The instrumentally resolved radiative intensity associated to the l-th wavelength

---

[5] Such designation has its historical reasons: ultra-violet radiation of higher energy was found when Victor Schumann placed his spectroscopy apparatus under vacuum instead of air (which absorbs it) [103].

interval, with $l \in \{\text{VUV}, \text{“Blue”}, \text{“Red”}, \text{IR}\}$, is given by an integration of the *instrumentally resolved specific radiative intensity* $\hat{I}_\lambda(x,\lambda)$ with respect to the wavelength λ from $\lambda = \lambda^l_{\text{min}}$ to $\lambda = \lambda^l_{\text{max}}$:

$$\hat{I}^l(x) = \int_{\lambda^l_{\text{min}}}^{\lambda^l_{\text{max}}} \hat{I}_\lambda(x,\lambda)\, d\lambda \ . \tag{3.38}$$

And the instrumentally resolved non-equilibrium metric associated to the l-th wavelength interval is given by an integration of the instrumentally resolved specific radiative intensity $\hat{I}_\lambda(x,\lambda)$ with respect to the position x from $x = x^l_{\text{min}}$ to $x = x^l_{\text{max}}$ - a region characterised by a strong thermodynamic non-equilibrium - divided by the shock tube inner diameter D:

$$\hat{I}^{\text{ne},l}_\lambda(\lambda) = \frac{1}{D}\int_{x^l_{\text{min}}}^{x^l_{\text{max}}} \hat{I}_\lambda(x,\lambda)\, dx \ . \tag{3.39}$$

One should note here that it is not possible to know the exact position of the shock wave through the spectra obtained in the shock tube experiments done by Brandis and Cruden for multiple reasons: the onset of the radiative field is associated to an increase of the number of excited species (which occurs at some distance downstream of the shock wave), and each spectrometer captures the spectra with a different reaction time [104]. The x axis that Brandis and Cruden work with doesn’t correspond to the one depicted in Figure 3.9. The issued position values are actually with respect to a particular origin for each shot and wavelength region which doesn’t coincide with the shock wave, and therefore they will be denoted here as $\hat{x}$ and termed “relative positions” to distinguish them from the previously introduced ones, x, which are with respect to an origin that coincides with the shock wave. The relative position of the shock wave for some shot and the l-th wavelength region, say $\hat{x}^l_{\text{sw}}$, was defined in this work as the point where the instrumentally resolved radiative intensity starts to rise abruptly, as also considered by Cruden in his work [104]. The position x is then given by $x = \hat{x} - \hat{x}^l_{\text{sw}}$.

The wavelength integration limits $[\lambda^l_{\text{min}}, \lambda^l_{\text{max}}]$, and relative position integration limits $[\hat{x}^l_{\text{min}}, \hat{x}^l_{\text{max}}]$ are issued by Brandis and Cruden in their work.

The instrumentally resolved specific radiative intensity $\hat{I}^l_\lambda(x,\lambda)$ departs from the real one, $I^l_\lambda(x,\lambda)$, either spectrally and spatially. The non-ideality of the instrumental apparatus is such that the measured specific radiative intensity $\hat{I}^l_\lambda(x,\lambda)$ associated to some particular wavelength λ and position x is in fact the result of a distribution of the real radiative intensity on intervals of wavelengths and positions around the reference values. Or, mathematically

$$\hat{I}_\lambda(x,\lambda) = \int_{-\infty}^{\infty} \hat{\phi}^{\text{spa}}(x') \left[\int_{-\infty}^{\infty} \hat{\phi}^{\text{spe}}(\lambda') I_\lambda(x-x',\lambda-\lambda')\, d\lambda'\right] dx' \ , \tag{3.40}$$

being $\hat{\phi}^{\text{spe}}(\lambda')$ and $\hat{\phi}^{\text{spa}}(x')$ the so-called *instrument line-shape factor* and *spatial resolution function*, respectively, which are issued by Brandis and Cruden in their work.

The validation of the models employed in this work requires a comparison of the numerical radiative intensities and non-equilibrium metrics with the experimental ones. For that purpose, it’s necessary to impose on the former the same transformations “applied” by the instruments on the latter.

Chapter 4

Results

4.1 The test matrix

Brandis and Cruden [39] issue benchmark data for a total of 17 shock tube shots which may be used for validation of the numerically obtained results. Due to compactness reasons, it was decided to regard solely 3 of these 17 shots, more precisely, shots that spawned conditions of low, medium, and high speed hypersonic flows. In this way, the dependence of the physical quantities on the free stream speed u_∞ may be accessed. Also, greater importance was given to shots whose results were considered to be of benchmark quality in the four wavelength intervals (VUV, "Blue", "Red", and IR), allowing the validation to be performed with respect to the whole spectrum. Under such criteria, the shots 40 (with $u_\infty = 6.88$ m/s), 19 (with $u_\infty = 10.32$ m/s), and 20 (with $u_\infty = 11.16$ m/s) and were taken.

4.2 The analysis methodology

In the following sections, the numerical and experimental results are compared, and possible causes for their discrepancies are enunciated. The tested standard database of kinetic processes corresponds to the set constituted by the collisional processes reported in Table B.3 and Table B.4, and the radiative processes reported in Table B.1 and Table B.2. The dependence of the results on different adjustable parameters of the simulations was reported. To properly guide the reader over the extensive set of obtained results, it was decided to treat simultaneously the three shots for each of the four wavelength intervals and to show side-by-side the respective graphs for the two quantities that were measured in the experiments: the instrumentally resolved radiative intensities $\hat{I}^l$ and non-equilibrium metrics $\hat{I}_\lambda^{\mathrm{ne},l}$, with $l \in \{\mathrm{VUV}, \text{“Blue”}, \text{“Red”}, \mathrm{IR}\}$. Further comments on the behaviour of important physical quantities such as temperatures and mole fractions, as well as on the evolution of the system to equilibrium are provided.

4.3 Zero-dimensional simulations of post-shock flows generated by a shock tube

4.3.1 The case of the VUV radiation

The instrumentally resolved radiative intensities $\hat{I}^{\mathrm{VUV}}(x)$ and non-equilibrium metrics $\hat{I}_{\lambda}^{\mathrm{ne,VUV}}(x)$ obtained from the zero-dimensional simulations are depicted in Figure 4.2 and Figure 4.3, respectively. The three graphs appearing in each figure are ordered by increasing free stream speed u_{∞} from top to bottom - the top one is with respect to shot 40, the middle one to 19, and the bottom one to 20. The solid coloured lines represent the numerically obtained contributions of the different systems of spontaneous emission processes to $\hat{I}^{\mathrm{VUV}}$ and $\hat{I}_{\lambda}^{\mathrm{ne,VUV}}$. The solid black lines represent the numerically obtained overall quantities (i.e. the sums of the contributions). And the dotted black lines represent the experimentally obtained overall quantities. The numerical values are quantified in the left y-axis and the experimental ones in the right y-axis. These y-axes are scaled differently in order to make the two sets of values visually comparable. In the case of $\hat{I}^{\mathrm{VUV}}$, the scales are such that the heights of the peaks match each other. And in the case of $\hat{I}_{\lambda}^{\mathrm{ne,VUV}}$, the scales are such that there's a coincidence between the peaks associated to spontaneous emission of N at $\lambda = 149\,\mathrm{nm}$. The necessity of using different scales unveils immediately a significant discrepancy: the numerically obtained values are much lower than the experimental ones. In fact, the heights of the experimental $\hat{I}^{\mathrm{VUV}}$ peaks are 342, 63 and 71 times higher than the numerical ones for the low, medium and high speed shots, respectively (see Figure 4.1). And the heights of the experimental $\hat{I}_{\lambda}^{\mathrm{ne,VUV}}$ peaks at $\lambda = 149\,\mathrm{nm}$ are 455, 641 and 1695 times higher than the numerical ones.

Let's now focus on the relative discrepancies, i.e. the discrepancies between the numerical and experimental results as if they were scaled to the same order of magnitude. Figure 4.2 reveals that the increase of $\hat{I}^{\mathrm{VUV}}$ from nil to peak maximum value and the decrease of $\hat{I}^{\mathrm{VUV}}$ from the peak maximum value to nil are slower (the latter with a much greater significance) than the ones in the experiment, for the case of the low speed shot. This seems to be due to a relative overestimation of the number of spontaneous emissions of the type $\mathrm{N}_2^+(\mathrm{C}-\mathrm{X})$, whose contribution to the overall radiative intensity corresponds to a more flattened and delayed peak than the others. In fact, Figure 4.3 shows many $\hat{I}_{\lambda}^{\mathrm{ne,VUV}}$ peaks of considerable heigh assigned to $\mathrm{N}_2^+(\mathrm{C}-\mathrm{X})$ which were not actually observed in the experiment. Although the two peaks that appear at $\lambda = 156\,\mathrm{nm}$ and $\lambda = 166\,\mathrm{nm}$ seem to overlap others of $\mathrm{N}_2^+(\mathrm{C}-\mathrm{X})$, this should be mere coincidence. The two peaks may be predicted if one considers atomic carbon C - a contaminant species - in the database, as Cruden and Brandis [105] did. Furthermore, according to Cruden and Brandis [105], the experimental peak at $\lambda = 193\,\mathrm{nm}$ - which was not predicted by the database used in this work - should also be due to C. The two most prominent peaks of the experimental $\hat{I}_{\lambda}^{\mathrm{ne,VUV}}$, appearing at $\lambda = 149\,\mathrm{nm}$ and $\lambda = 174\,\mathrm{nm}$, are a result of spontaneous emission of N. However, the respective features appearing in the obtained numerical spectra stand out as much as the ones for $\mathrm{N}_2^+(\mathrm{C}-\mathrm{X})$, showing another evidence of a relative overestimation of the number of spontaneous emissions associated to the latter. Also, one finds the peak at $\lambda = 149\,\mathrm{nm}$ to be higher than the peak at $\lambda = 174\,\mathrm{nm}$ in the numerical spectra, but lower in the experimental one. Such discrepancy may be due to the absorption of radiation associated to the first peak being greater than the one associated to the second peak in the experiment. Meanwhile, in the simulation, absorption was completely disregarded. The discrepancy may also be due to an improper modelling of the rate coefficients which dictate the population of the nitrogen atoms that spontaneously emit radiation at wavelengths $\lambda = 149\,\mathrm{nm}$ and $\lambda = 174\,\mathrm{nm}$. One way of making the ratio between the heights of the two peaks more agreeable with the experimental result is by decreasing the rate of excitation of atomic nitrogen to the upper level of the system associated to the first peak and increasing the one associated to the second. However, for the present case, the upper levels of the system associated to the two peaks are the same, corresponding to the fifth level, say[1] N(4). The first peak is a result of the transitions N(4 − 1), and the second is a result of the transitions N(4 − 2). Therefore, changing the values of the rate coefficients for excitation would not make any difference to the ratio between the heights of the peaks. One should, however, mention here that this inability is in some part due to the lumping procedure performed on the energy levels of N. If split levels were instead regarded, the first peak would actually correspond to a sum of three peaks with their centres very close to each other, and the second peak would correspond to a sum of four. The number of upper energy levels associated to the respective spontaneous emission systems would be two instead of one. By changing the values of the rate coefficients for excitation of the two split levels one could actually obtain the right ratio of heights. Furthermore, it's important to say that the reduction of the number of peaks due to lumping procedure may also affect the numerical spectra obtained for the other wavelength intervals, which, in its turn, may lead to unfair judgments on the structure of the database. Note that this lumping procedure is however virtually unavoidable, since the most part of the processes reported in the literature disregard the fine structure of the particles, and therefore, the application of the respective rate coefficients requires the author to make the same consideration.

The experimental instrumentally resolved radiative intensity $\hat{I}^{\mathrm{VUV}}$ obtained for the case of the medium speed shot has a peak proceeded by a plateau. The shape of the peak is well predicted by the numerical model, but the plateau isn't at all. A transition to nil occurs instead. And for the case of the high speed shot, the experiment didn't produce a sole peak, but a coalescence between a peak and a plateau surpassing it. This feature wasn't also predicted by the numerical model.

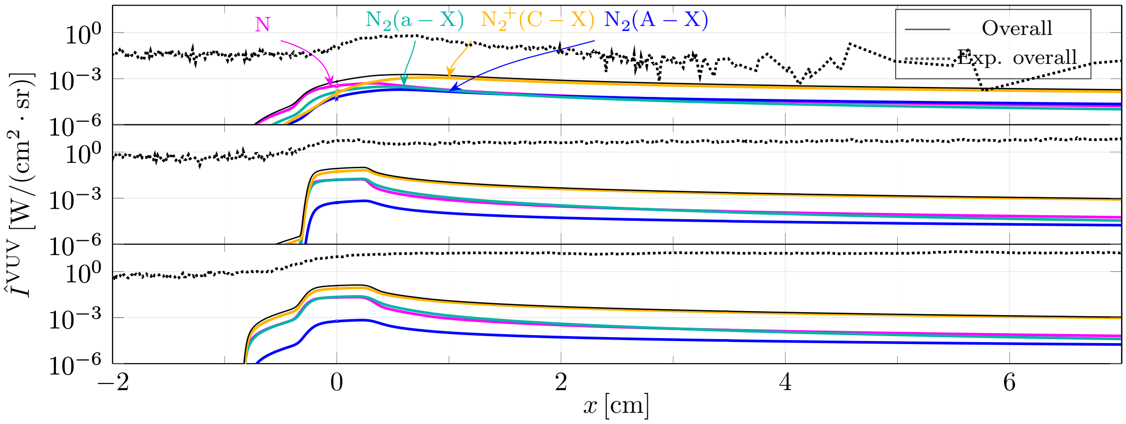

Figure 4.1: Numerical (solid lines) and experimental (dotted lines) instrumentally resolved radiative intensities $\hat{I}^{\mathrm{VUV}}(x)$ obtained for the low, medium and high speed shots.

---

[1] The electronic levels of the atomic particles will be labelled here by integer numbers $e = 0, 1, \ldots$

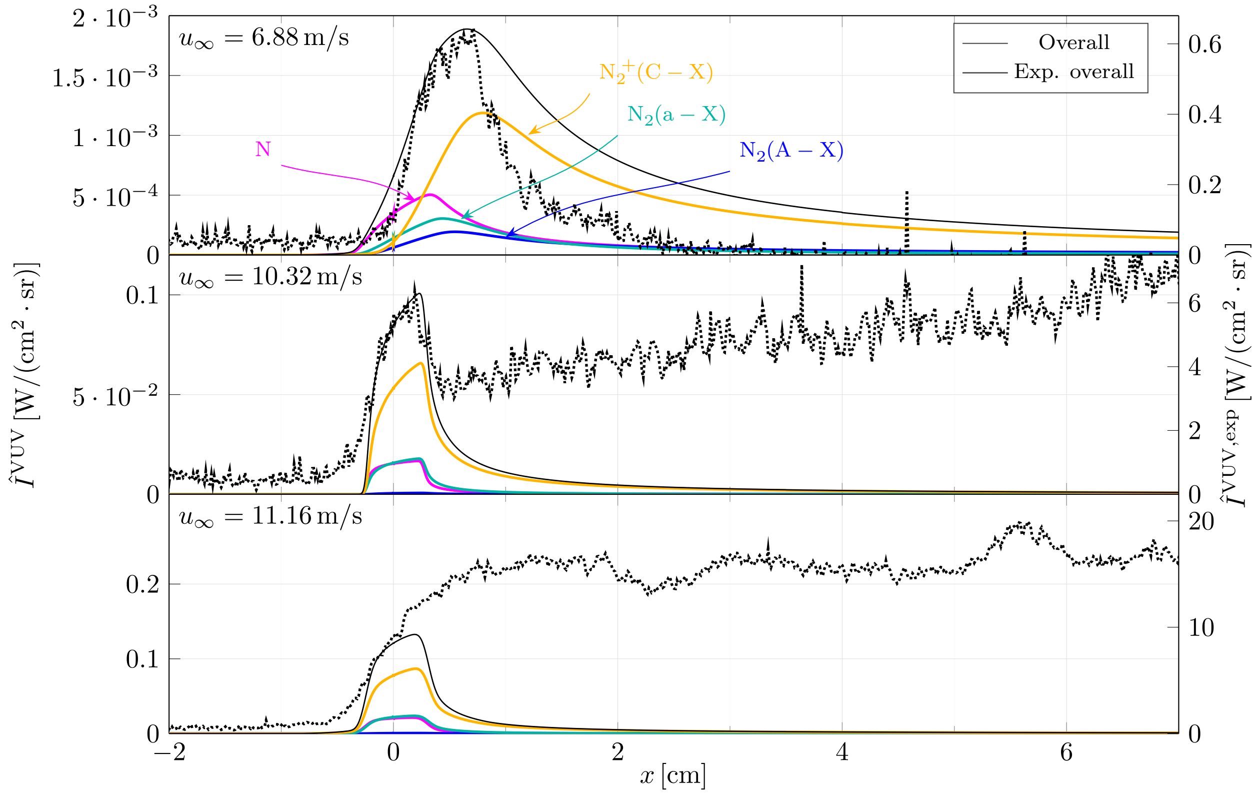

Figure 4.2: The same as Figure 4.1

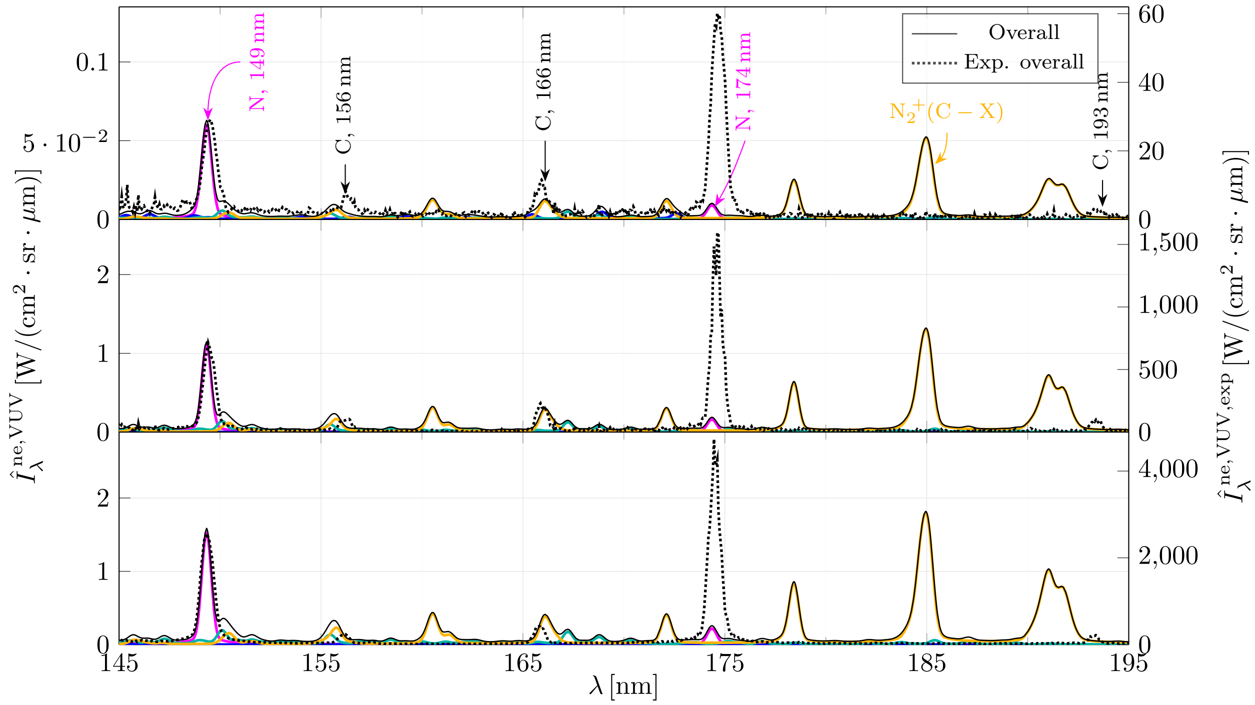

Figure 4.3: Numerical (solid lines) and experimental (dotted lines) instrumentally resolved non-equilibrium metrics $\hat{I}_\lambda^{\mathrm{ne,VUV}}(x)$ obtained for the low, medium and high speed shots.

4.3.2 The case of the "Blue" radiation

The obtained instrumentally resolved radiative intensities $\hat{I}^{\text{Blue}}(x)$ and non-equilibrium metrics $\hat{I}_{\lambda}^{\text{ne,Blue}}(x)$ are depicted in Figure 4.4 and Figure 4.5, respectively. The main contributors to the overall quantities are $\text{N}_2(\text{C}-\text{B})$ and $\text{N}_2^+(\text{B}-\text{X})$. And the residual contributors correspond to $\text{N}_2(\text{A}-\text{X})$ and N for the three shots, and also $\text{N}_2^+(\text{A}-\text{X})$ for the low speed shot. Meanwhile, Cruden and Brandis [105] showed that $\text{N}_2(\text{C}-\text{B})$, $\text{N}_2^+(\text{B}-\text{X})$, N, and the contaminant species CN (cyanogen radical) are enough to describe the experimentally obtained spectrum for the case of the medium speed shot.

As happened for the case of the VUV radiation, the instrumentally resolved radiative intensities and non-equilibrium metrics are underestimated by 2 to 3 orders of magnitude. The scales of the y-axes of the non-equilibrium metrics graphs are such that there's a coincidence between the numerical and experimental peaks associated to spontaneous emission of $\text{N}_2^+(\text{B}-\text{X})$ at $\lambda = 391\,\text{nm}$. The heights of the experimental $\hat{I}^{\text{Blue}}$ peaks are 730, 68, and 45 times higher than the numerical ones for the low, medium and high speed shots, respectively. And the heights of the experimental $\hat{I}_{\lambda}^{\text{ne,Blue}}$ peaks at $\lambda = 391\,\text{nm}$ are 636, 49 and 66 times higher than the numerical ones. The profile of the numerical radiative intensity $\hat{I}^{\text{Blue}}$ obtained in the low speed shot corresponds to a peak, similar to the experimental one. However, the transitions from nil to the maximum and from the maximum to nil are slower in the former. In the case of the medium and high speed shots, the shape of the peaks are remarkably well predicted, contrary to the plateaus that proceed them: the numerical radiative intensities transit to nil instead of converging to these plateaus. Such behaviour was also obtained in the case of the VUV radiation.

Sets of peaks appearing in the experimental non-equilibrium metrics $\hat{I}_{\lambda}^{\text{ne,Blue}}$ may be discerned, being these in some way predicted by the numerical model. However, the heights of the individual peaks of each set don't agree particularly well with the experimental ones, namely, the ones associated to spontaneous emissions of the types $\text{N}_2(\text{C},0-\text{B},0)$ and $\text{N}_2^+(\text{B},0-\text{X},0)$, at $\lambda = 337\,\text{nm}$ and $\lambda = 391\,\text{nm}$, respectively. These were undoubtedly overestimated, prevailing over the others. The discrepancies between the numerical and experimental non-equilibrium metrics may in some part be due to the fact that the regarded spontaneous emissions are vibronic-specific and not rovibronic. If rovibronic-specific spontaneous emissions were instead considered, the peaks associated to the vibronic levels would be divided into several others (each one associated to a rotational level) whose centres may be more or less far from each other, depending on the energy of the rotational levels. The importance of the rotational levels to the spectra should be accessed in the future.

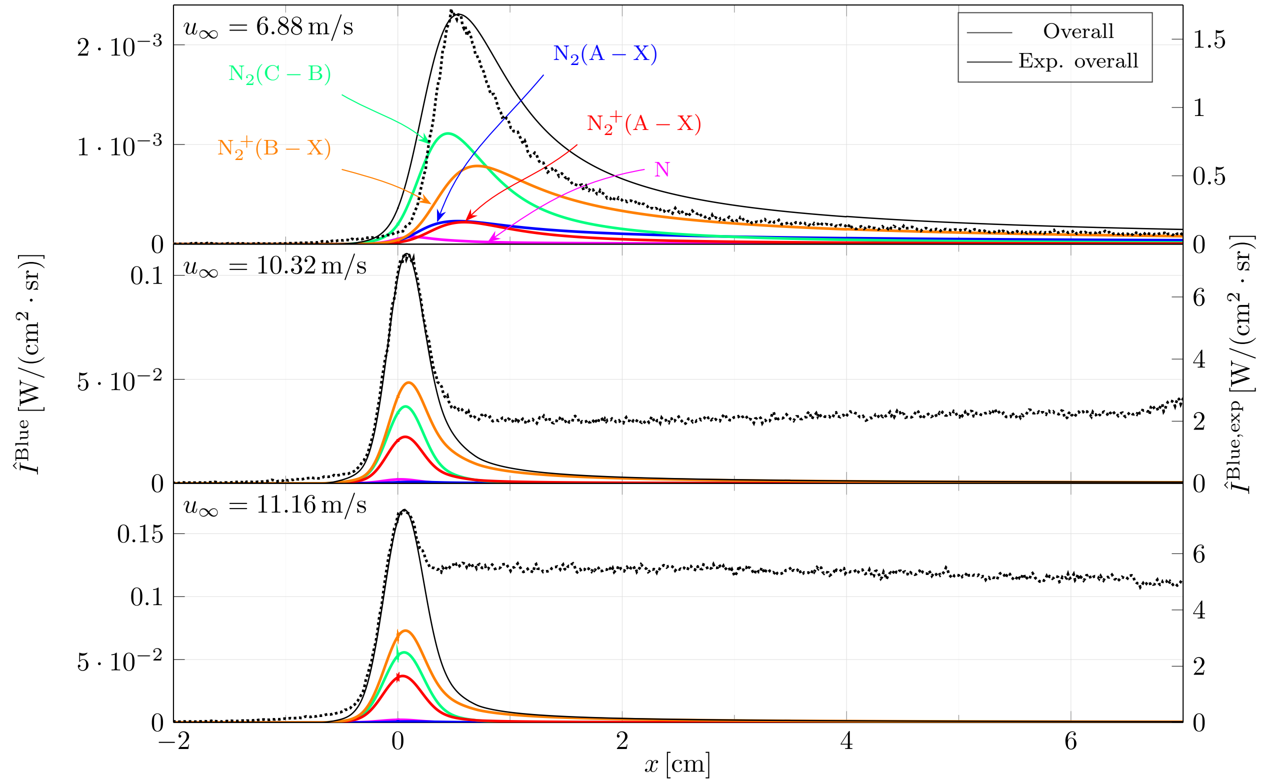

Figure 4.4: Numerical (solid lines) and experimental (dotted lines) instrumentally resolved radiative intensities $\hat{I}^{\mathrm{Blue}}(x)$ obtained for the low, medium and high speed shots.

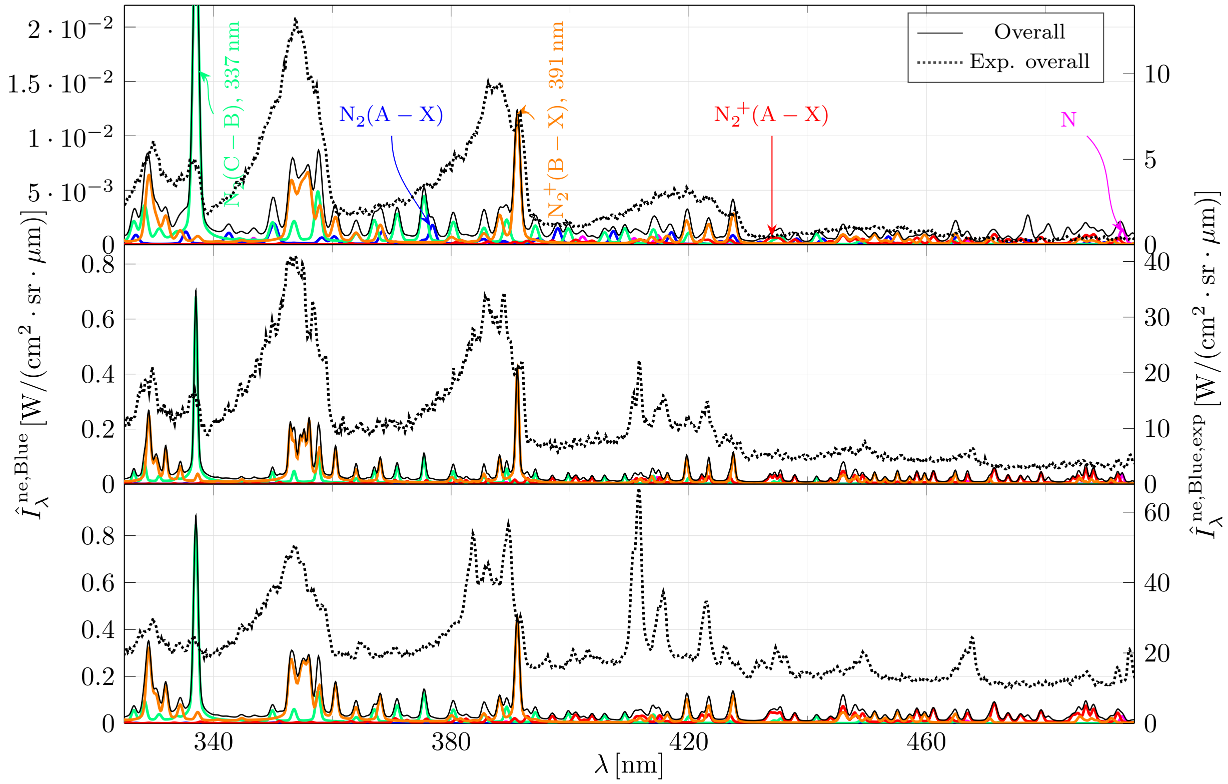

Figure 4.5: Numerical (solid lines) and experimental (dotted lines) instrumentally resolved non-equilibrium metrics $\hat{I}_\lambda^{\mathrm{ne,Blue}}(x)$ obtained for the low, medium and high speed shots.

4.3.3 The case of the "Red" radiation

Figures 4.6 and 4.7 depict the obtained instrumentally resolved radiative intensities $\hat{I}^{\mathrm{Red}}(x)$ and non-equilibrium metrics $\hat{I}_{\lambda}^{\mathrm{ne,Red}}(x)$, respectively. The scales of the $\hat{I}_{\lambda}^{\mathrm{ne,Red}}$ graphs are such that the experimental and numerical peaks at $\lambda = 869\,\mathrm{nm}$ match each other. The experimental $\hat{I}^{\mathrm{Red}}$ peaks are 144, 19, and 30 times higher than the numerical peaks for the low, medium and high speed shots, respectively. And the experimental $\hat{I}_{\lambda}^{\mathrm{ne,Red}}$ peaks at $\lambda = 869\,\mathrm{nm}$ are 167, 430 and 1305 higher than the numerical ones. As happened for the case of the VUV radiation, in the low speed shot, the transition of the numerical radiative intensity $\hat{I}_{\lambda}^{\mathrm{ne,Red}}$ from the peak maximum value to nil was significantly slower than the experimental one. In the medium and high speed shots, plateaus proceeding peaks were obtained from the experiment. These were not predicted by the numerical model.

There is strong evidence of a relative underestimation of spontaneous emissions of N, since the most prominent peaks (such as the ones at $\lambda = 649$, 745, 821, 862 and 869 nm) of the experimental spectra, which are due to N, are surpassed in the numerical spectra by the ones associated to $\mathrm{N_2(B-A)}$. Also, spontaneous emissions of the type $\mathrm{N_2^+(A-X)}$ should not be as relevant as they were found to be in the numerical spectra. Cruden and Brandis [105] considered in this wavelength interval, for the case of the medium speed shot, solely spontaneous emissions of the type N (the dominant ones), $\mathrm{N_2(B-A)}$ and H (atomic hydrogen was found to be a contaminant species).

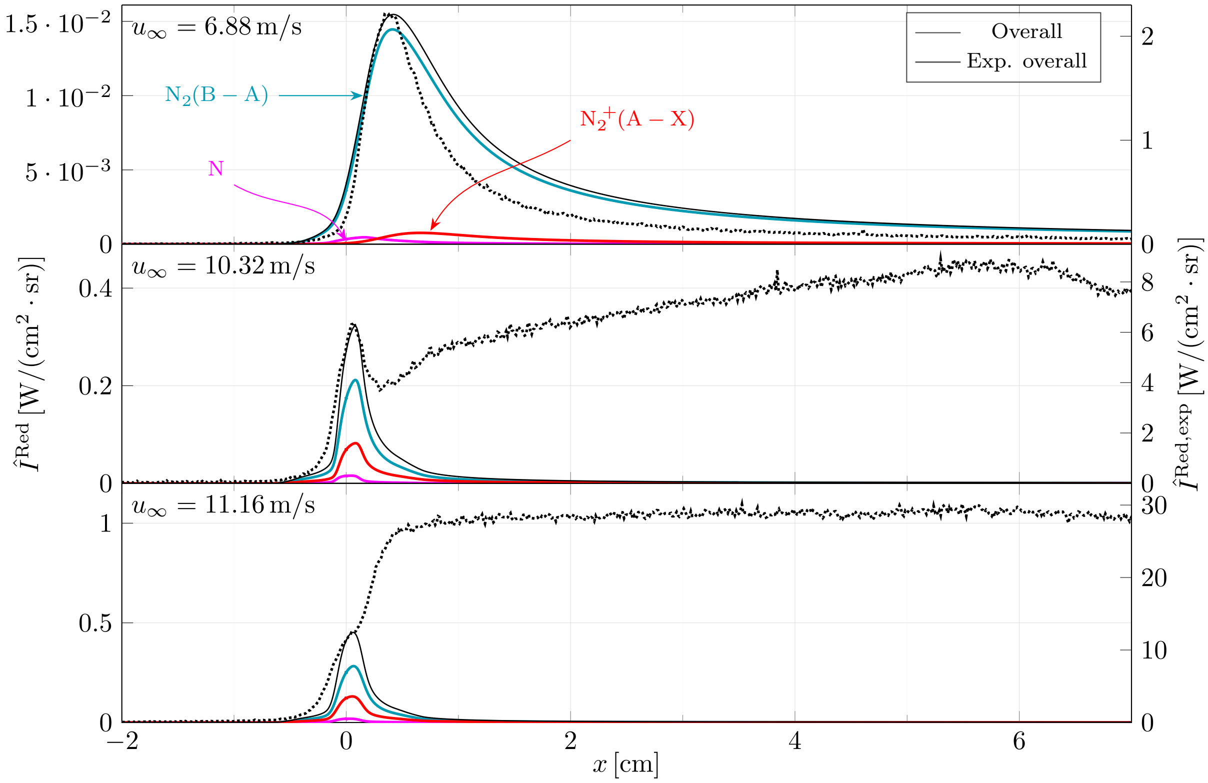

Figure 4.6: Numerical (solid lines) and experimental (dotted lines) instrumentally resolved radiative intensities $\hat{I}^{\mathrm{Red}}(x)$ obtained for the low, medium and high speed shots.

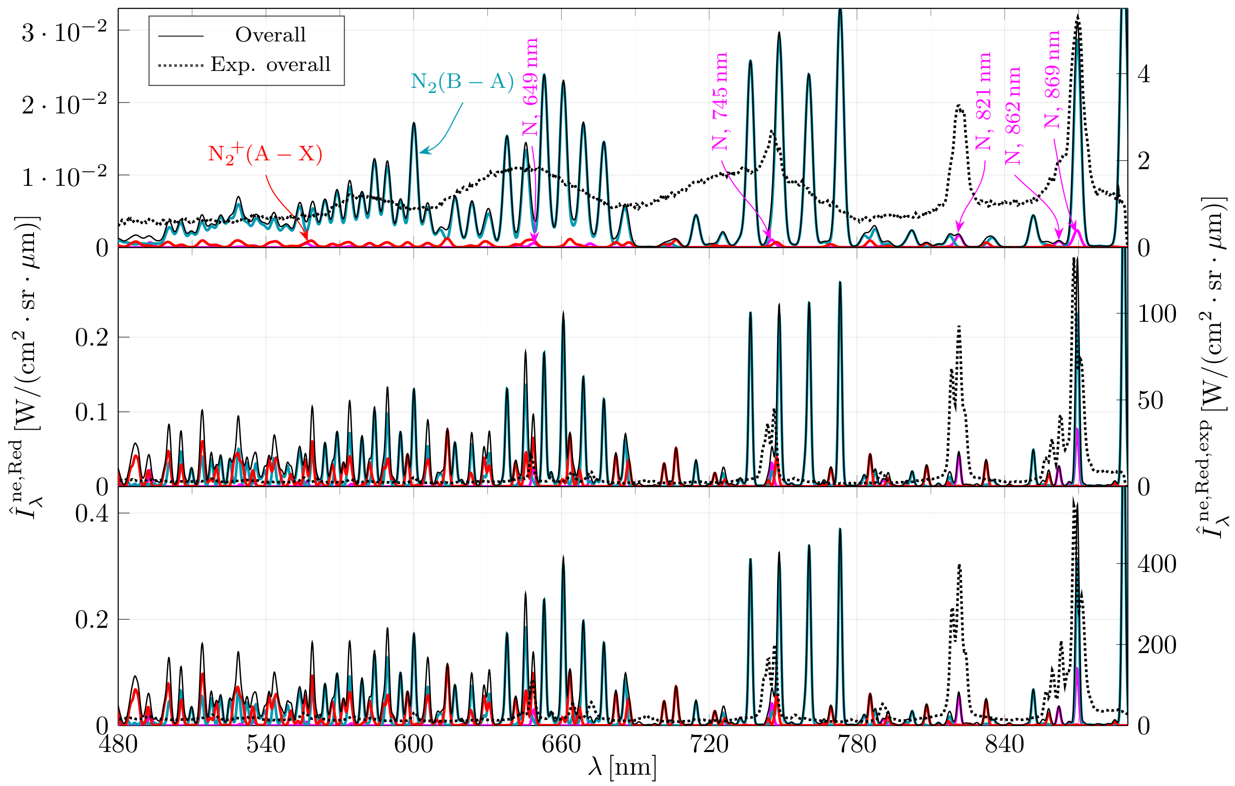

Figure 4.7: Numerical (solid lines) and experimental (dotted lines) instrumentally resolved non-equilibrium metrics $\hat{I}_\lambda^{\mathrm{ne,Red}}(x)$ obtained for the low, medium and high speed shots.

4.3.4 The case of the IR radiation

Figures 4.8 and 4.9 depict the obtained instrumentally resolved radiative intensities $\hat{I}^{\mathrm{IR}}(x)$ and non-equilibrium metrics $\hat{I}_\lambda^{\mathrm{ne,IR}}(x)$, respectively. The scales of the $\hat{I}_\lambda^{\mathrm{ne,IR}}$ graphs are such that the experimental and numerical peaks at $\lambda = 940\,\mathrm{nm}$ match each other. Unsurprisingly, it was found that the numerical model underestimated the radiative intensities and non-equilibrium metrics by 2 to 3 orders of magnitude, as in the other cases. The experimental $\hat{I}^{\mathrm{IR}}$ peaks are 116, 105, and 352 times higher than the numerical peaks for the low, medium and high speed shots, respectively. And the experimental $\hat{I}_\lambda^{\mathrm{ne,IR}}$ peaks at $\lambda = 940\,\mathrm{nm}$ are 274, 887 and 1784 higher than the numerical ones. In the case of the low speed shot, the numerical $\hat{I}^{\mathrm{IR}}$ values rise and fall slightly less abruptly than the experimental values. And in the cases of the medium and high speed shots, sole peaks can't be discerned from the experiment but coalescences between peaks and plateaus occurring above them. Again, such phenomena wasn't predicted by the numerical model.

The obtained non-equilibrium metrics show that spontaneous emissions of the type $N_2(B-A)$ seem to be relatively overestimated, specially the ones at $\lambda = 1047\,\mathrm{nm}$ - due to transitions from $v = 0$ to $v' = 0$ - and $\lambda = 1232\,\mathrm{nm}$ - due to transitions from $v = 0$ to $v' = 1$ - which prevail over the others. Conversely, the peaks associated to spontaneous emission of N (such as the ones at $\lambda = 905\,\mathrm{nm}$, $\lambda = 940\,\mathrm{nm}$, $\lambda = 1012\,\mathrm{nm}$ and $\lambda = 1053\,\mathrm{nm}$) seem to be relatively underestimated, since these predominate in the experimental spectra but not in the numerical spectra.

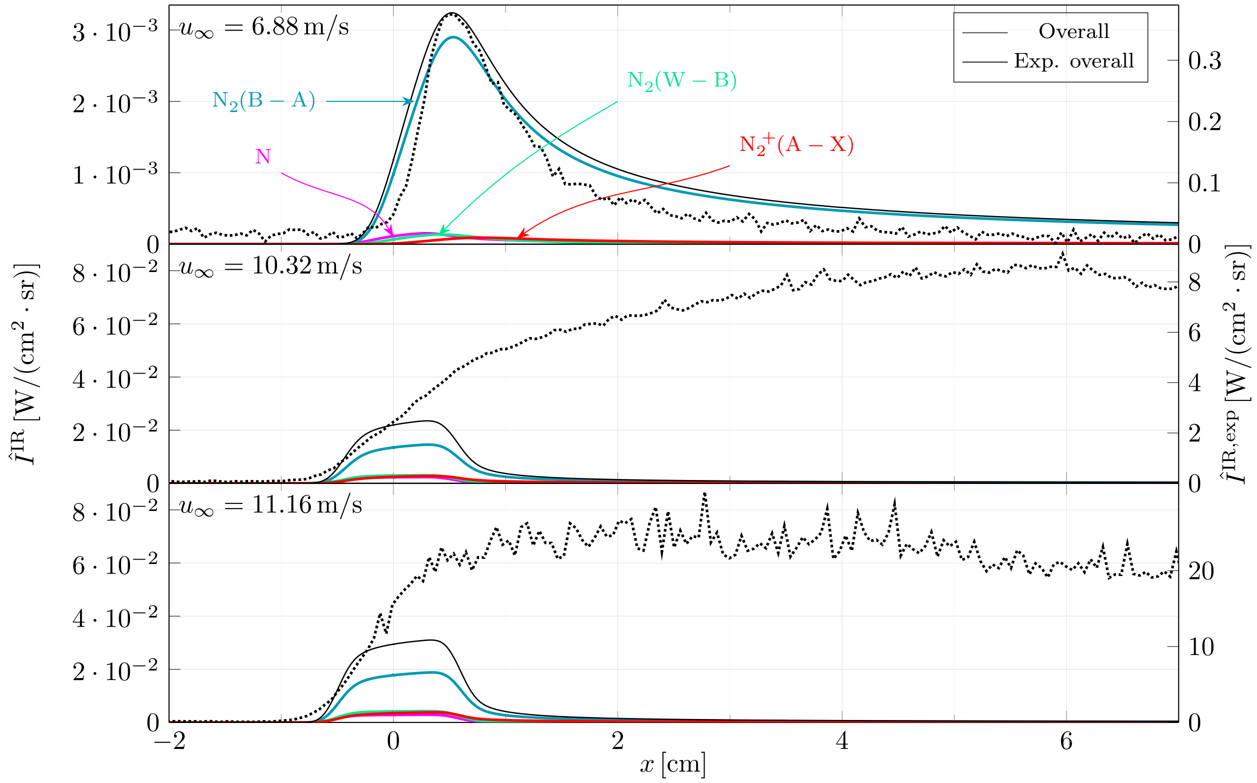

Figure 4.8: Numerical (solid lines) and experimental (dotted lines) instrumentally resolved radiative intensities $\hat{I}^{\mathrm{IR}}(x)$ obtained for the low, medium and high speed shots.

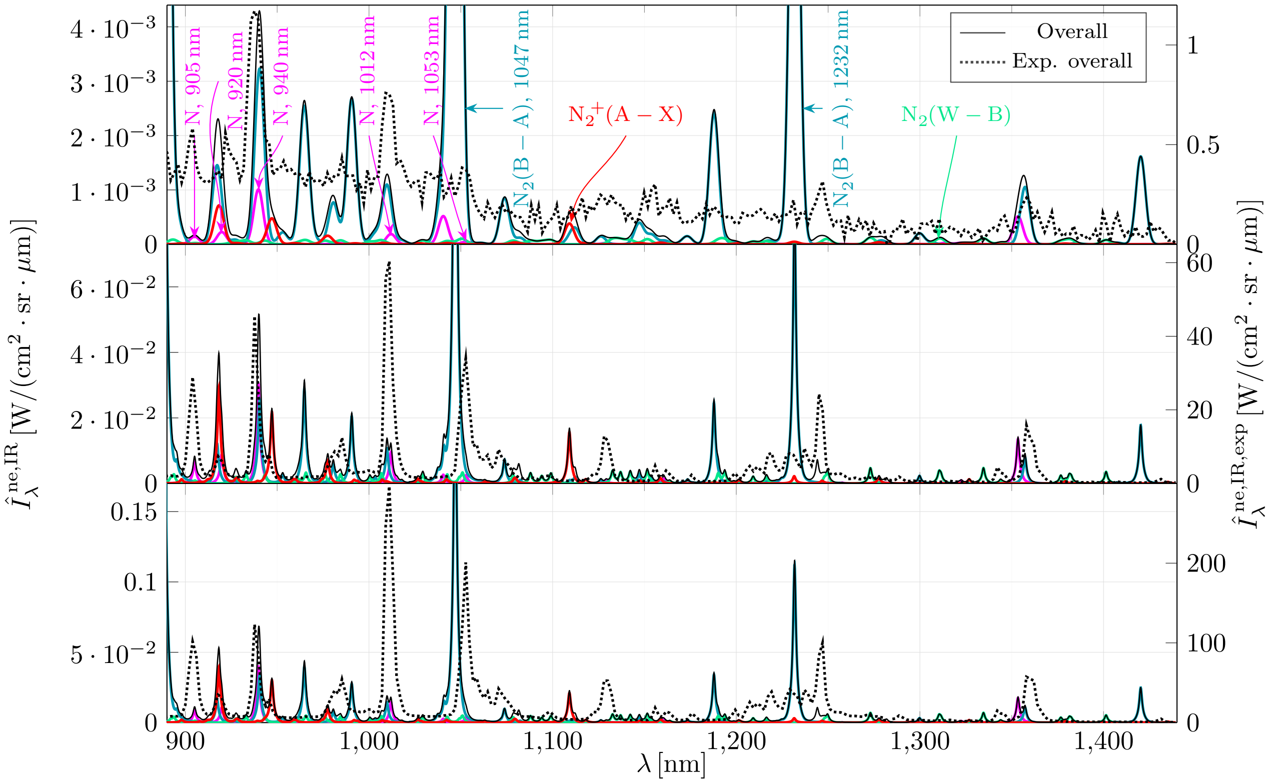

Figure 4.9: Numerical (solid lines) and experimental (dotted lines) instrumentally resolved non-equilibrium metrics $\hat{I}_\lambda^{\mathrm{ne,IR}}(x)$ obtained for the low, medium and high speed shots.

4.4 Euler one-dimensional simulations of post-shock flows generated by a shock tube

The values of the radiation variables obtained from the the Euler one-dimensional simulations are presented by Figures 4.10 to 4.17. The peak values of the instrumentally resolved radiative intensities are still significantly underestimated - by one to two order magnitudes. These peak values are greater than the ones obtained from the zero-dimensional simulations: for the case of the low speed shot, the quintuple was obtained in the VUV and “Blue” wavelength regions, and the triple in the “Red” and IR, and for the case of the medium and high speed shots, the double was obtained. Therefore, the transfer of momentum between elements of fluid should not be neglected. As happened in the zero-dimensional simulations, the plateaus weren’t predicted at all. In relative terms, the rises from nil to the peak values and the falls from the peak values to nil of the radiative intensities for the case of the low speed shots were found to be steeper than the ones obtained from the zero-dimensional simulations. The rising parts of the profiles of the numerical peaks now agree relatively well with the experimental ones, but not the falling parts in the “Blue”, “Red”, and IR wavelength regions which are steeper (being once slighter) than the experimental counterparts.

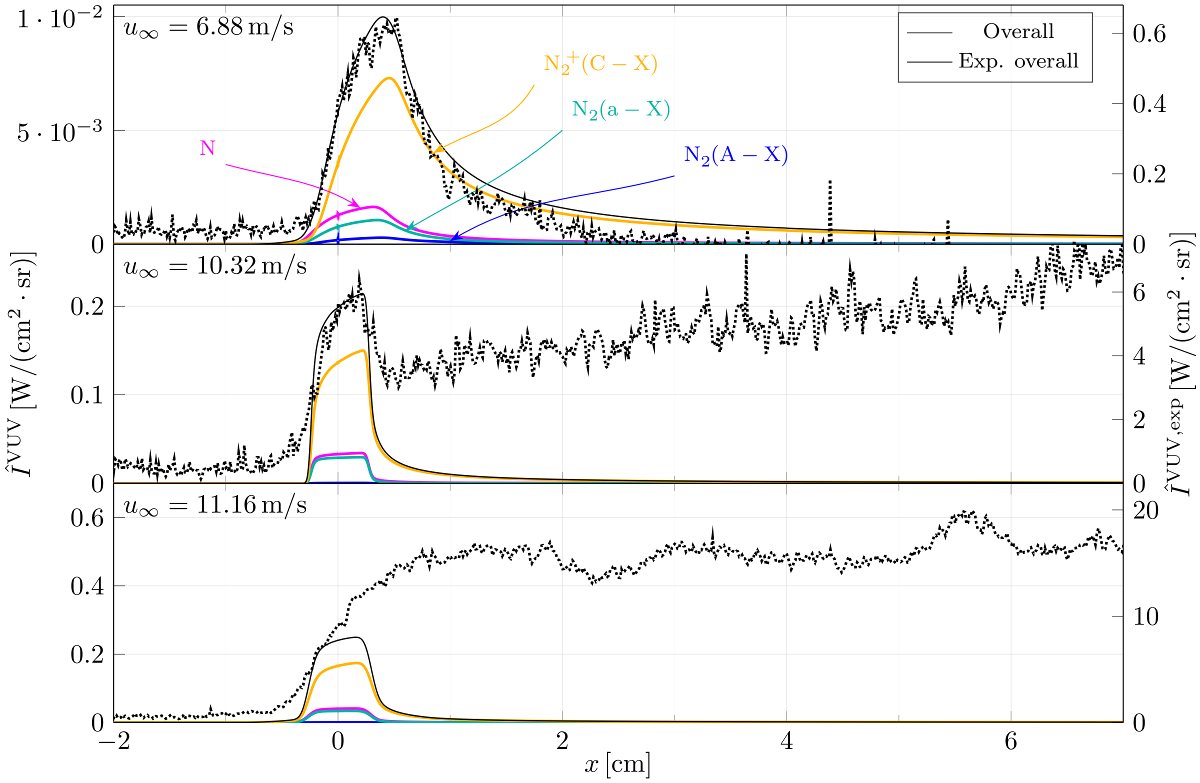

Figure 4.10: Numerical (solid lines) and experimental (dotted lines) instrumentally resolved radiative intensities $\hat{I}^{\mathrm{VUV}}(x)$ obtained for the low, medium and high speed shots.

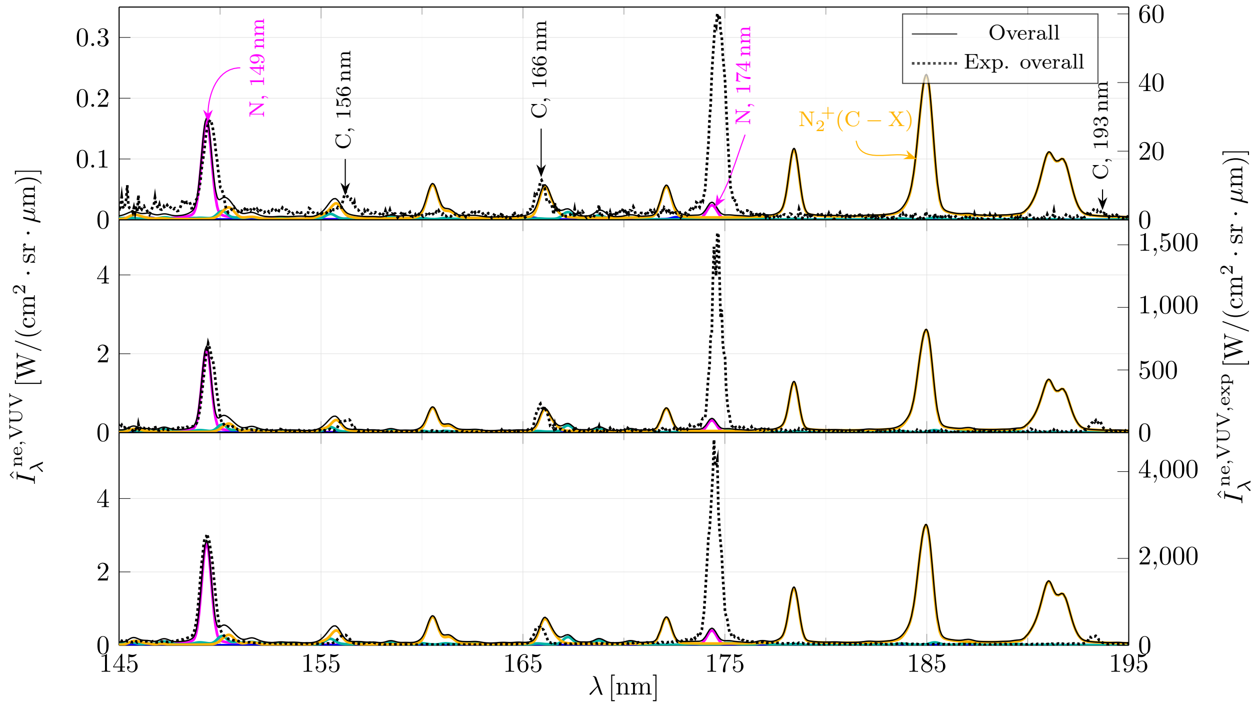

Figure 4.11: Numerical (solid lines) and experimental (dotted lines) instrumentally resolved non-equilibrium metrics $\hat{I}_\lambda^{\mathrm{ne,VUV}}(x)$ obtained for the low, medium and high speed shots.

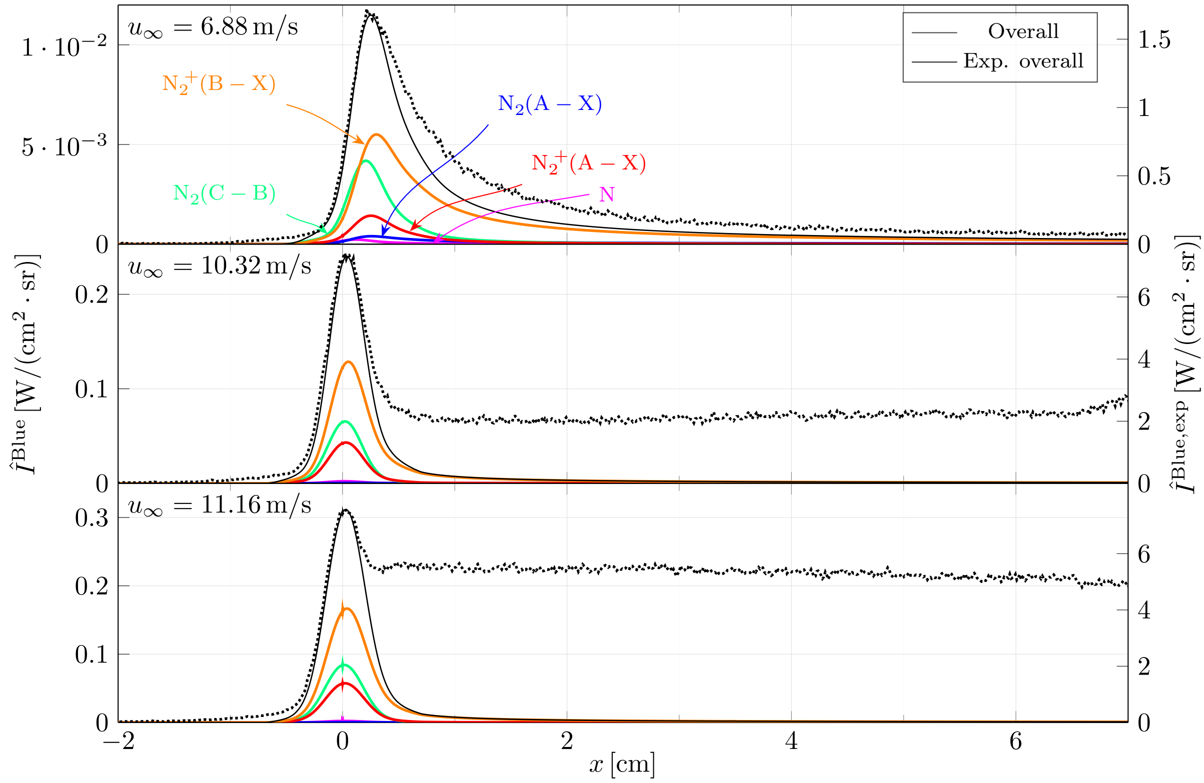

Figure 4.12: Numerical (solid lines) and experimental (dotted lines) instrumentally resolved radiative intensities $\hat{I}^{\mathrm{Blue}}(x)$ obtained for the low, medium and high speed shots.

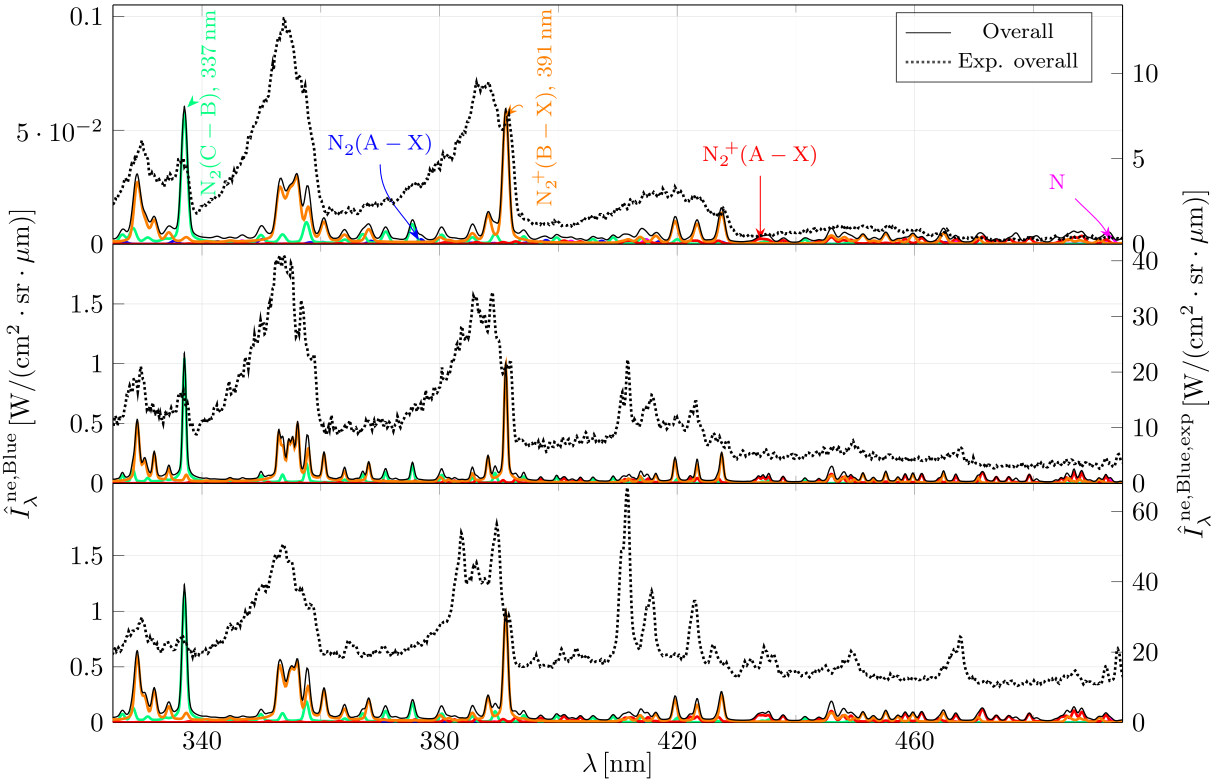

Figure 4.13: Numerical (solid lines) and experimental (dotted lines) instrumentally resolved non-equilibrium metrics $\hat{I}_{\lambda}^{\text{ne,Blue}}(x)$ obtained for the low, medium and high speed shots.

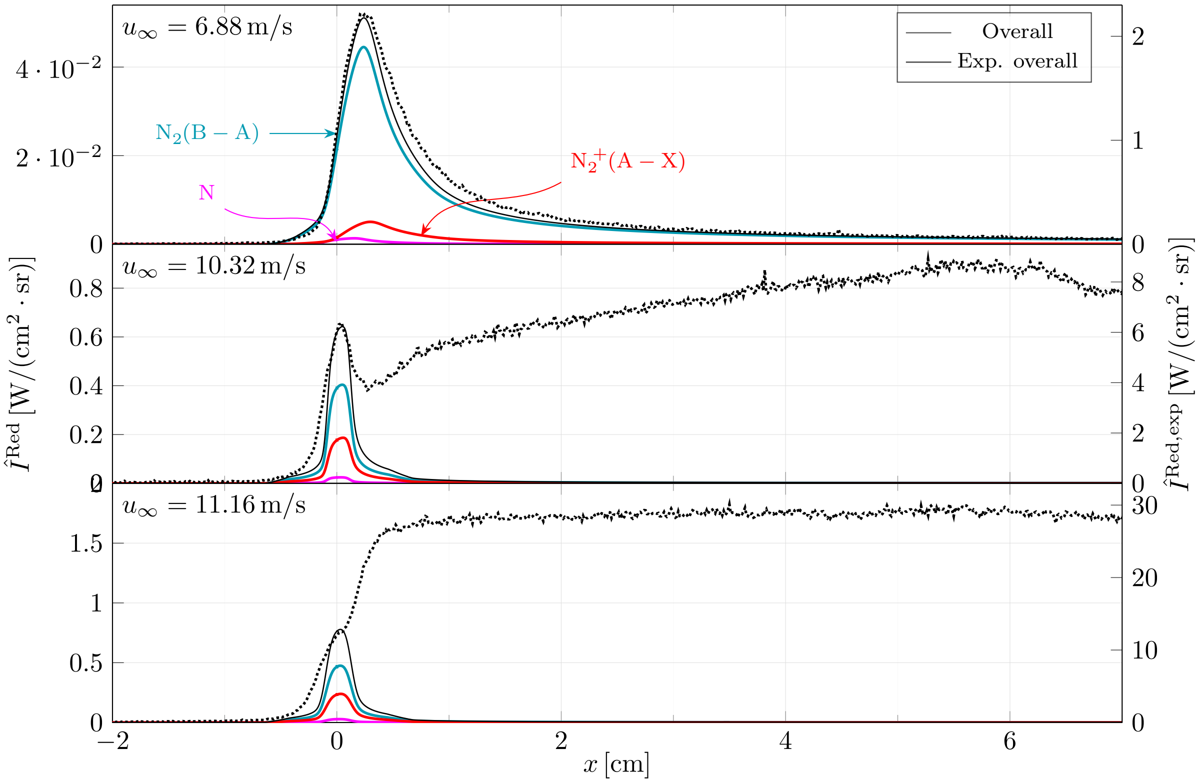

Figure 4.14: Numerical (solid lines) and experimental (dotted lines) instrumentally resolved radiative intensities $\hat{I}^{\text{Red}}(x)$ obtained for the low, medium and high speed shots.

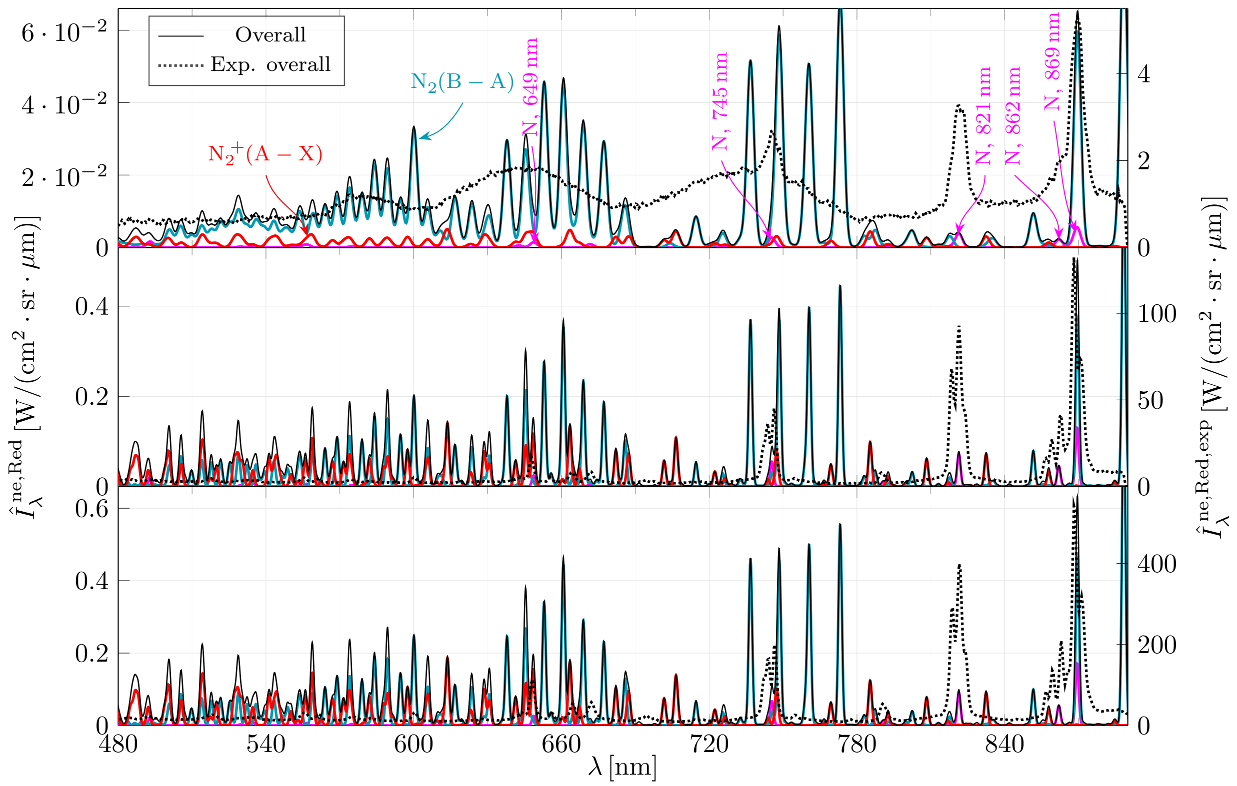

Figure 4.15: Numerical (solid lines) and experimental (dotted lines) instrumentally resolved non-equilibrium metrics $\hat{I}_\lambda^{\text{ne,Red}}(x)$ obtained for the low, medium and high speed shots.

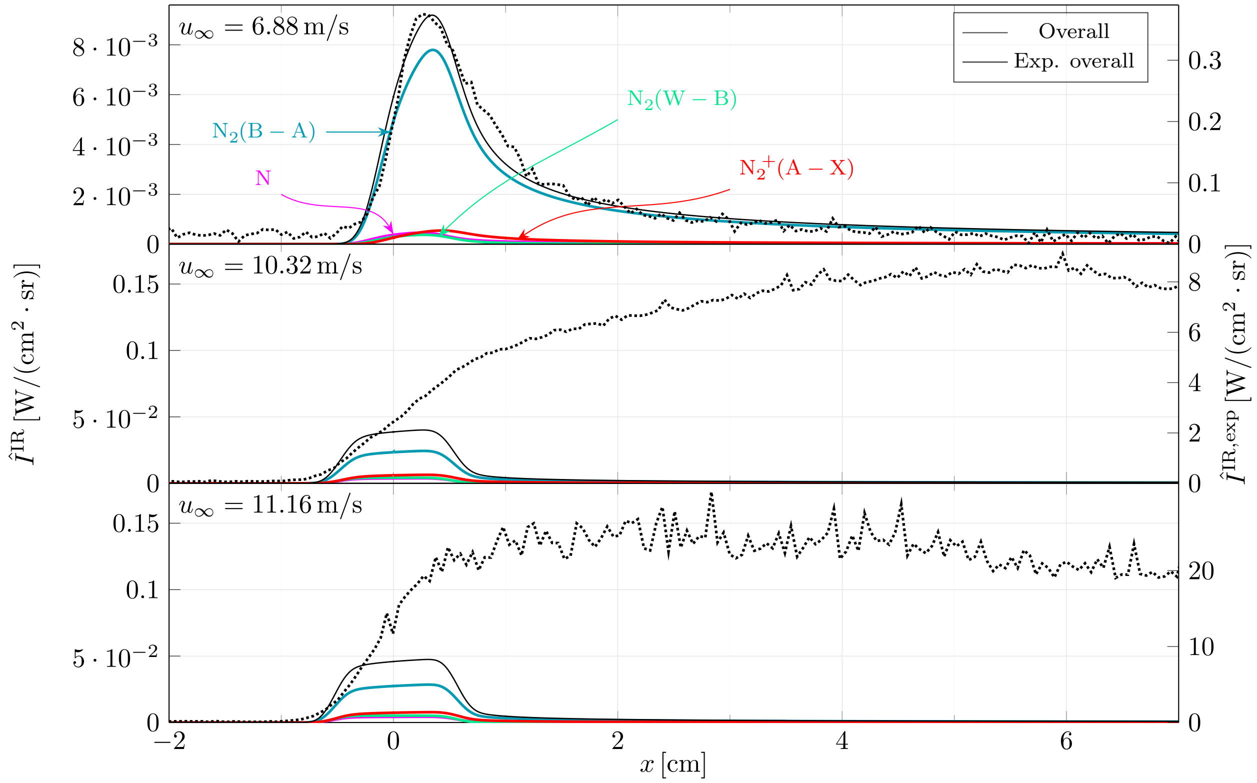

Figure 4.16: Numerical (solid lines) and experimental (dotted lines) instrumentally resolved radiative intensities $\hat{I}^{\text{IR}}(x)$ obtained for the low, medium and high speed shots.

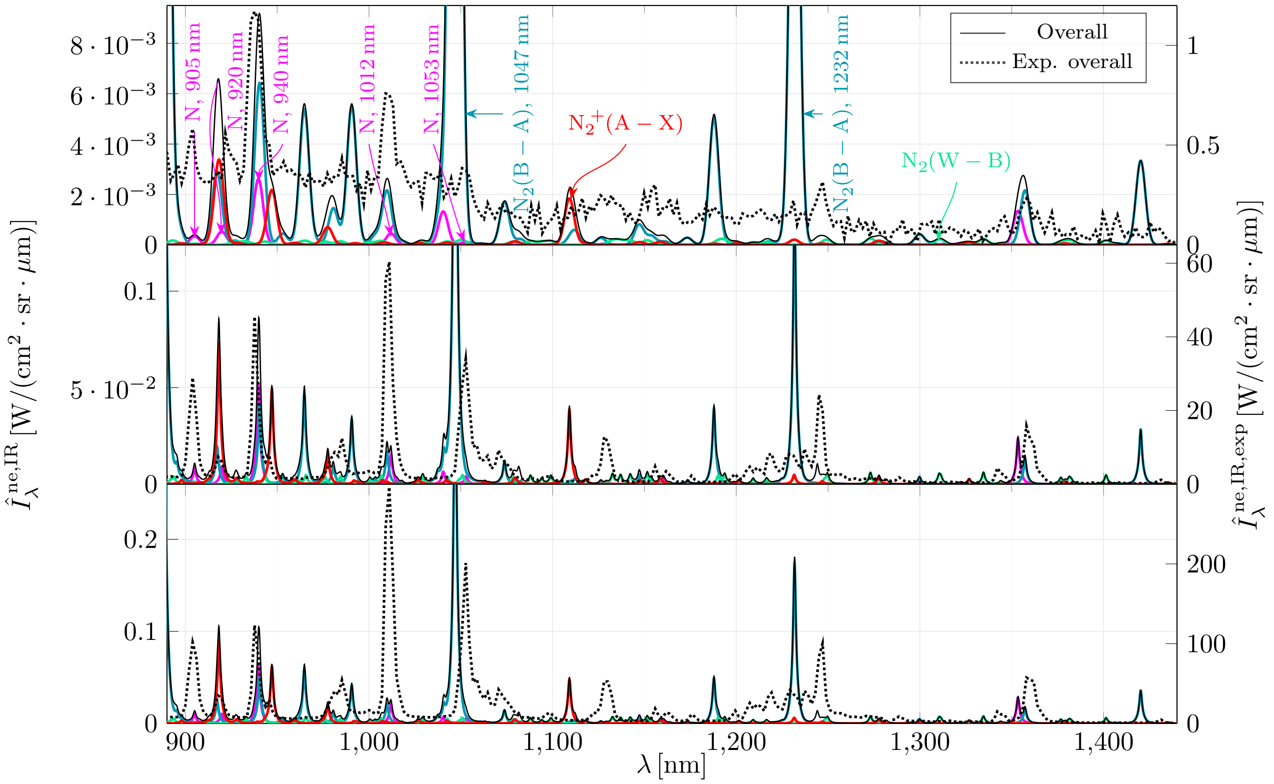

Figure 4.17: Numerical (solid lines) and experimental (dotted lines) instrumentally resolved non-equilibrium metrics $\hat{I}_\lambda^{\mathrm{ne,IR}}(x)$ obtained for the low, medium and high speed shots.

4.4.1 Mole fractions, temperatures, and evolution to equilibrium

Figure 4.18 depicts the obtained heavy particle and free electron translational temperatures, $T_{\mathrm{tr_h}}(x)$ and $T_{\mathrm{tr_e}}(x)$. As according to (3.35), the values of these temperatures, immediately downstream of the shock wave ($x = 0$), correspond to $T_{\mathrm{tr_h},2} = T_{\mathrm{tr_e},2} = 22,434\,\mathrm{K}$, $50,122\,\mathrm{K}$ and $58,565\,\mathrm{K}$ for the low, medium and high speed shots, respectively. As expected, these decrease along x, due to the endothermic processes, to some identical values, and with a rate which is as high as the immediately downstream temperature.

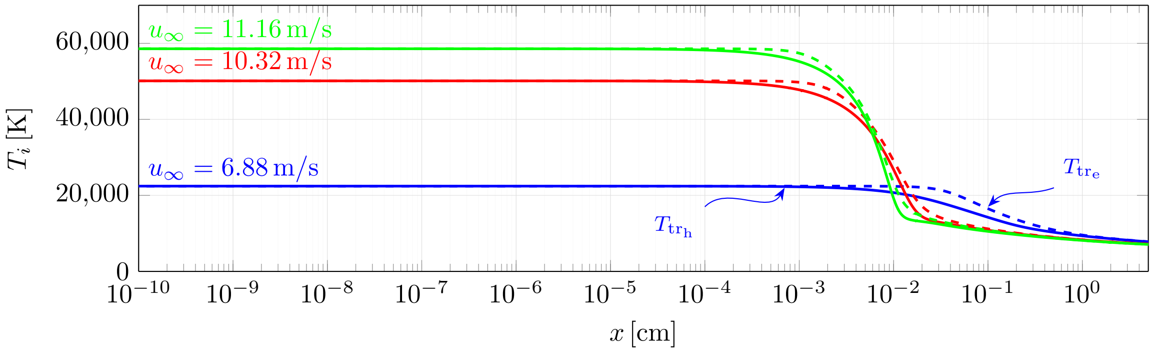

Figure 4.18: Heavy particle (solid lines) and free electron (dashed lines) translational temperatures, $T_{\mathrm{tr_h}}(x)$ and $T_{\mathrm{tr_e}}(x)$, obtained for the low (blue), medium (red) and high (green) speed shots.

Figure 4.19 presents the evolutions of the mole fractions $x_s(x)$ of the five species considered in the simulations - N_2, N, N_2^+, N^+ and e^- - for the low, medium and high speed shots. One finds that an higher upstream speed implies an earlier dissociation and ionisation of the particles. In the medium and high speed shots, the dissociation is such that the mole fraction of atomic nitrogen N surpasses the mole fraction of molecular nitrogen N_2. There's an increase and posterior decrease of the mole fractions of atomic nitrogen ions N^+, molecular nitrogen ions N_2^+ and free electrons e^-. The former is associated to ionisation and the latter to recombination. The higher the upstream speed, the more abrupt the increases and decreases of the mole fractions of the charged particles are.

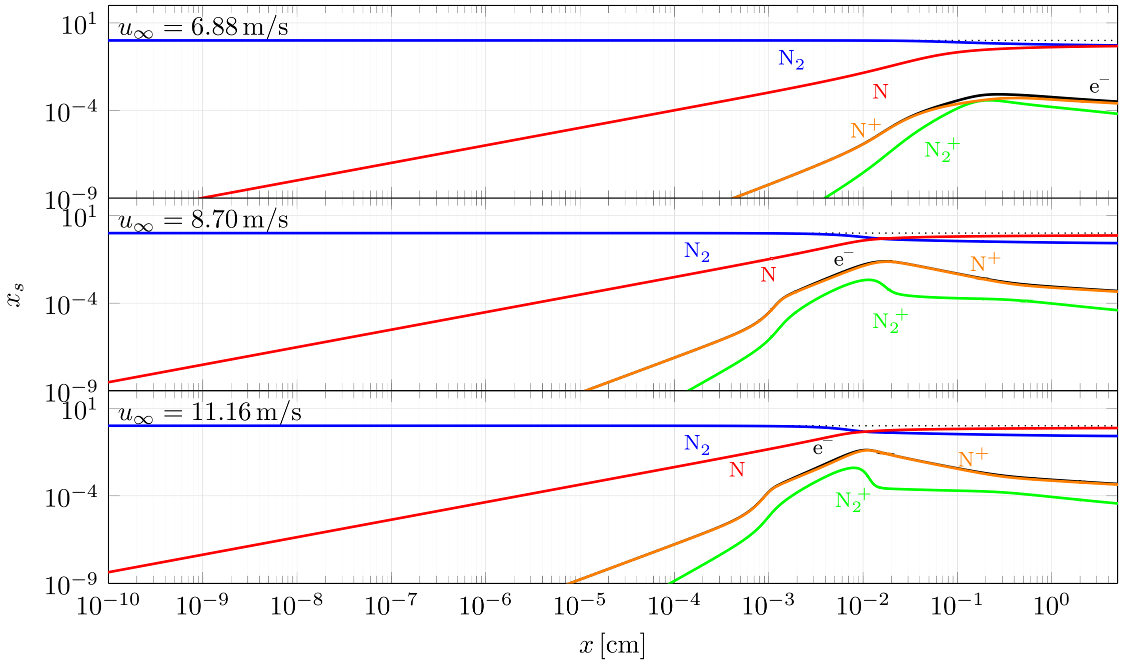

Figure 4.19: Species-specific mole fractions $x_s(x)$ obtained for the low, medium and high speed shots.

Table 4.1 makes a synopsis on the temperatures $T_{\mathrm{tr_h}}$ and $T_{\mathrm{tr_e}}$, and mole fractions x_s, obtained from the simulations of the three shots, at a far downstream point from the shock wave, $x = 5\,\mathrm{cm}$ - where the radiation intensities were found stagnated. The table also shows the values issued by Cruden and Brandis [105] for the medium speed shot. These were obtained by fitting the conditions of a hypothetical system such that the computed "Blue" and "Red" spectra matched the experimental ones, using the NEQAIR tool [47, 106], at a x position for which the plateaus of radiative intensities occurred. With that objective, a two-temperature model - of temperatures $T_{\mathrm{tr_h-rot}}$ and $T_{\mathrm{vib-el-tr_e}}$ - was assumed and the populations of some particular energy levels were adjusted. Regarding the values of the temperatures at $x = 5\,\mathrm{cm}$ obtained in the present work, one can say that the heavy particle translational temperature departed from the free electron translational temperature by $-18\,\mathrm{K}$ (or $-0.23\,\%$), $-3\,\mathrm{K}$ (or $-0.04\,\%$) and $-1\,\mathrm{K}$ (or $-0.03\,\%$) for the cases of the low, medium and high speed shots. These values are sufficiently small for one to assume that an equilibrium between the respective energy modes was attained. The values of the temperatures obtained by Cruden and Brandis are significantly higher than the ones of this work. The analysis of the "Blue" spectra resulted in a $T_{\mathrm{tr_h}}$ value which is greater by $(1,986 \pm 170)$ K (or (28 ± 2) %) and a $T_{\mathrm{tr_e}}$ value which is greater by $(3,213 \pm 300)$ K (or (45 ± 4) %). The analysis of the "Red" spectra resulted in a $T_{\mathrm{tr_h}}$ value which is greater by $(2,606 \pm 2,490)$ K (or (36 ± 35) %) and a $T_{\mathrm{tr_e}}$ value which is greater by $(2,013 \pm 130)$ K (or (28 ± 2) %). The mole fraction of N obtained from the simulation of the medium speed shot in the present work, at $x = 5\,\mathrm{cm}$, is almost the double of the one obtained from the simulation of the low speed shot, evidencing a very meaningful augmentation on the dissociation of N_2. The mole fraction of N_2^+ is lower (by 38 %) - due to a much faster recombination - and the one of N^+ is almost the double. The differences between the values of the mole fractions obtained from the simulation of the high speed shot and the ones obtained from the simulation of the medium speed shot aren't significant enough, as also aren't the differences between the upstream speeds. Regarding the results of the work of Cruden and Brandis [105] for the medium speed shot, one can say that not only the differences between the obtained chemical compositions and the one of the present work are staggering but also the difference between the chemical composition resulting from the analysis of the "Blue" spectra and the one resulting from the analysis of the "Red" spectra. The results of the analysis of the "Blue" spectra showed a greater importance of the molecular particles N_2 and N_2^+ and free electrons e^- in the composition, while the results of the analysis of the "Red" spectra showed a greater importance of atomic nitrogen N. In fact, the mole fractions of N_2, N_2^+ and e^- obtained in the the former case are 22, 133 and 30 times greater than the ones obtained in the latter case, and the mole fraction of N is 57 % lower. This incoherence evidences that the models regarded in NEQAIR may not represent sufficiently well the reality. The results of Cruden and Brandis also evidence a much stronger dissociation of N_2 and ionisation of N than the ones of the present work: the predicted mole fraction of N_2 is at least 9 times lower, and the mole fraction of N^+ is at least 20 times greater. Moreover, this greater dissociation and ionisation are accomplished with a much lower cost of heavy particle and free electron translational temperatures. Such result means that the post-shock elements of fluid simulated in the present work may have lost more energy than they should, or didn't gain as much. Since it was found that the radiation variables were underpredicted by several orders of magnitude, the former hypothesis should be disregarded. Two possible ways of the elements of fluid gaining more energy are by absorption of radiation and conduction of heat, being both not taken into account in the simulations. The former contribution should be more important since it makes the overall system to loose less than before (part of the radiative energy which was once lost is retained) while the latter contribution simply redistributes the energy within it without reducing the losses.

Table 4.1: Temperatures $T_{\mathrm{tr_h}}$ and $T_{\mathrm{tr_e}}$, and mole fractions x_s, at $x = 5\,\mathrm{cm}$, obtained from the simulations of the low, medium and high speed shots, as well as the ones obtained by Cruden and Brandis [105].

u_∞ [m/s]	Ref.	$T_{\mathrm{tr_h}}$ [K]	$T_{\mathrm{tr_e}}$ [K]	$x_{\mathrm{N_2}}$	x_{N}	$x_{\mathrm{N_2^+}}$	$x_{\mathrm{N^+}}$	$x_{\mathrm{e^-}}$	x_{CN}	x_{H}
6.88	This work	$7,793$	$7,811$	0.52	0.48	6.5×10^{-5}	2.6×10^{-4}	3.2×10^{-4}	—	—
10.32	This work	$7,184$	$7,187$	0.27	0.73	4.0×10^{-5}	4.5×10^{-4}	4.9×10^{-4}	—	—
	NEQAIR, "Blue" [105]	$9,170 \pm 170$	$10,400 \pm 300$	0.029	0.42	0.016	0.27	0.27	7.3×10^{-4}	—
	NEQAIR, "Red" [105]	$9,790 \pm 2,490$	$9,200 \pm 130$	0.0013	0.98	1.2×10^{-4}	0.0089	0.0089	—	0.0010
11.16	This work	$7,098$	$7,100$	0.26	0.74	3.7×10^{-5}	4.4×10^{-4}	4.7×10^{-4}	—	—

To ascertain the impact of energy loss by radiation on the developed conditions of the post-shock flow, it was decided to perform simulations disregarding spontaneous emission processes and to compare the respective results with the ones obtained when regarding them. Table 4.2 makes a synopsis on the resultant temperatures $T_{\mathrm{tr_h}}$ and $T_{\mathrm{tr_e}}$, and mole fractions x_s, at $x = 5\,\mathrm{cm}$. All of the temperatures are higher than the respective ones obtained when regarding spontaneous emission processes, and increasing with the upstream speed. While the differences are negligible for the case of the low speed shot - $T_{\mathrm{tr_h}}$ differs by just 266 K (or 3.4 %) - they are meaningful for the case of the medium and high speed shots - $T_{\mathrm{tr_h}}$ differs by 2080 K (or 29 %) and $3,016$ K (or 42 %). Meanwhile, a greater dissociation and ionisation had occurred, as evidenced by the lower value for the mole fraction of $\mathrm{N_2}$ and the higher values for the mole fractions of N and $\mathrm{N^+}$. These results show that the energy dumped by spontaneous emission in the highly excited systems has a much higher proportion than in the less excited ones. The more excited the particles are, the higher the number of spontaneous emissions and the higher the energy that is lost through radiation. Surprisingly, the conditions for the medium speed shot disregarding spontaneous emission processes are now coherent with the ones obtained by Cruden and Brandis [105], with the exception of the mole fraction of $\mathrm{N_2^+}$ which is substantiality lower. This result sheds light to the previously enunciated hypothesis of the simulated elements of fluid not receiving the energy that their counterparts seem to receive in the experiment.

Table 4.2: Temperatures $T_{\mathrm{tr_h}}$ and $T_{\mathrm{tr_e}}$, and mole fractions x_s, obtained from the simulations of the low, medium and high speed shots, at $x = 5\,\mathrm{cm}$, disregarding spontaneous emission processes.

u_∞ [m/s]	$T_{\mathrm{tr_h}}$ [K]	$T_{\mathrm{tr_e}}$ [K]	$x_{\mathrm{N_2}}$	x_{N}	$x_{\mathrm{N_2^+}}$	$x_{\mathrm{N^+}}$	$x_{\mathrm{e^-}}$
6.88	$8,059$	$8,076$	0.46	0.54	1.0×10^{-4}	4.6×10^{-4}	5.7×10^{-4}
10.32	$9,264$	$9,265$	0.022	0.93	3.1×10^{-5}	0.022	0.022
11.16	$10,114$	$10,114$	0.0041	0.89	2.4×10^{-5}	0.052	0.052

Another important result that may be ascertained from the numerical simulations is the disparity from thermal equilibrium of the systems conditions. This can be done through computation of *representative temperatures*. A representative temperature with respect to a particular energy mode is quantified by the populations of its energy levels, and solely corresponds to a true temperature if self-equilibrium of the energy mode was attained. In this work, a *representative electronic temperature* was considered for each heavy species, as well as a *representative vibrational temperature* for each electronic level of each molecular species. The way that these variables were defined will be now described.

By invoking the reasoning presented in section §2.2, assuming uncoupling between the rotational and the vibrational energy modes[2], one may infer that if the s-th species particles in the n-th electronic level are at a vibrational temperature $T_{s,\mathrm{vib},n}$, the population of its m-th vibrational level is simply given by

$$N_{s,m,n} = N_{s,n} \frac{g_{s,\mathrm{vib},n,m}\, e^{-\frac{\epsilon_{s,\mathrm{vib},n,m}}{k_B T_{s,\mathrm{vib},n}}}}{Q_{s,\mathrm{vib},n}(T_{s,\mathrm{vib},n})} \ . \tag{4.1}$$

And, by further manipulating (4.1), it's possible to obtain

$$\ln\left(\frac{x_{s,m,n}}{g_{s,\mathrm{el},n} \cdot g_{s,\mathrm{vib},n,m}}\right) = -\frac{1}{k_B T_{s,\mathrm{vib},n}} \epsilon_{s,\mathrm{vib},n,m} + \ln\left(\frac{x_{s,n}}{g_{s,\mathrm{el},n} \cdot Q_{s,\mathrm{vib},n}(T_{s,\mathrm{vib},n})}\right) \ , \tag{4.2}$$

where $x_{s,m,n} = N_{s,m,n}/N$ is the mole fraction of s-th species particles in their n-th electronic level and m-th vibrational level, and $x_{s,n} = N_{s,n}/N$ is the mole fraction of s-th species particles in their n-th electronic level. Equation (4.2) tells that under vibrational self-equilibrium, the natural logarithm of

---

[2] In the SPARK code, the spectroscopic constant α_e was disregarded.

the mole fraction of s-th species particles in a state of the n-th electronic level and m-th vibrational level, i.e. $\ln(x_{s,m,n}/(g_{s,\text{el},n} \cdot g_{s,\text{vib},n,m}))$, decreases linearly with their vibrational energy $\epsilon_{s,\text{vib},n,m}$. A plot of $\ln(x_{s,m,n}/(g_{s,\text{el},n} \cdot g_{s,\text{vib},n,m}))$ against $\epsilon_{s,\text{vib},n,m}$ with s and n fixed, would show points positioned in a line of slope $-1/(k_B T_{s,\text{vib},n})$ and of ordinate of the y-intercept $\ln(x_{s,n}/[g_{s,\text{el},n} \cdot Q_{s,\text{vib},n}(T_{s,\text{vib},n})])$. The representative vibrational temperature associated to the n-th electronic level of the s-th species $T_{s,\text{vib},n}$ which may or may not be in vibrational self-equilibrium is defined in this work as the respective value obtained from a fit of the curve (4.2) to the numerically obtained points of abscissae $\epsilon_{s,\text{vib},n,m}$ and ordinates $\ln(x_{s,m,n}/(g_{s,\text{el},n} \cdot g_{s,\text{vib},n,m}))$. If the s-th species particles are at an electronic temperature $T_{s,\text{el}}$, and uncoupling between the rotational and vibrational energy modes is further assumed as well as between the rotational and the electronic energy modes[3], the population of its n-th electronic level is simply given by

$$N_{s,n} = N_s \frac{g_{s,\text{el},n}\, e^{-\frac{\epsilon_{s,\text{el},n}}{k_B T_{s,\text{el}}}} Q_{s,\text{vib},n}(T_{s,\text{vib},n})}{Q_{s,\text{el-vib}}(\{T_{s,\text{vib},n}\}, T_{s,\text{el}})} \ , \tag{4.3}$$

being $Q_{s,\text{el-vib}} = \sum_n g_{s,\text{el},n}\, e^{-\frac{\epsilon_{s,\text{el},n}}{k_B T_{s,\text{el}}}} Q_{s,\text{vib},n}(T_{s,\text{vib},n})$. Expression (4.3) may be conveniently transformed into

$$\ln\left(\frac{x_{s,n}}{g_{s,\text{el},n}}\right) = -\frac{1}{k_B T_{s,\text{el}}}\epsilon_{s,\text{el},n} + \ln\left(\frac{x_s \cdot Q_{s,\text{vib},n}(T_{s,\text{vib},n})}{Q_{s,\text{el-vib}}(\{T_{s,\text{vib},n}\}, T_{s,\text{el}})}\right) \ . \tag{4.4}$$

The representative electronic temperature associated to the s-th species $T_{s,\text{el}}$ which may or may not be in electronic self-equilibrium is defined in this work as the respective value obtained from a fit of the curve (4.4) to the numerically obtained points of abscissae $\epsilon_{s,\text{el},n}$ and ordinates $\ln(x_{s,n}/g_{s,\text{el},n})$. In thermal equilibrium conditions, one has $T_{\text{tr}_\text{h}} = T_{\text{tr}_\text{e}} = T_{s,\text{vib},n} = T_{s,\text{el}} := T$, $\forall$ s and n. By inserting (4.4) into (4.2) one gets in such conditions

$$\ln\left(\frac{x_{s,m,n}}{g_{s,\text{el},n} \cdot g_{s,\text{vib},n,m}}\right) = -\frac{1}{k_B T}\left(\epsilon_{s,\text{el},n} + \epsilon_{s,\text{vib},n,m}\right) + \ln\left(\frac{x_s}{Q_{s,\text{el-vib}}(T)}\right) \ . \tag{4.5}$$

Therefore, at thermal equilibrium, the points of abscissae $\epsilon_{s,\text{el},n}+\epsilon_{s,\text{vib},n,m}$ and ordinates $\ln(x_{s,m,n}/(g_{s,\text{el},n} \cdot g_{s,\text{vib},n,m}))$, with s fixed, lay in the same curve, being this of slope $-1/(k_B T)$ and of y-intercept $\ln(x_s/Q_{s,\text{el-vib}}(T))$. And if the the vibrational partition function $Q_{s,\text{vib},n}$ doesn't vary too much with the electronic level n such that $Q_{s,\text{vib},n} \approx Q_{s,\text{vib}}$, one may also show from relation (4.4) that in thermal equilibrium the points of abscissae $\epsilon_{s,\text{el},n}$ and ordinates $\ln(x_{s,n}/g_{s,\text{el},n})$, with s fixed, lay in the same curve, being this of slope $-1/(k_B T)$ and of y-intercept $\ln(x_s/Q_{s,\text{el}}(T))$. The representative vibrational and electronic temperatures may in their turn be used to compute *Boltzmann representative vibronic mole fractions* $x^B_{s,n,m} := x_{s,n,m}(T_{s,\text{vib},n})$ - given by (4.2) - and *Boltzmann representative electronic mole fractions* $x^B_{s,n} := x_{s,n}(T_{s,\text{vib},n}, T_{s,\text{el}})$ - given by (4.4).

Figure 4.20 shows the electronic state-specific mole fractions $x_{s,e}/g_{s,\text{el},e}$ (markers) and respective Boltzmann representatives $x^\text{B}_{s,e}/g_{s,\text{el},e}$ (lines) obtained from the simulations of the low, medium and high speed shots, at $x = 5\,\text{cm}$. The markers in the figure sparsely agree with the respective lines. This result shows that self-equilibrium of the electronic energy modes of the different species wasn't attained at

---

[3] In the SPARK code, the spectroscopic constant B_e was approximated by the respective one for the ground electronic level.

$x = 5\,\mathrm{cm}$.

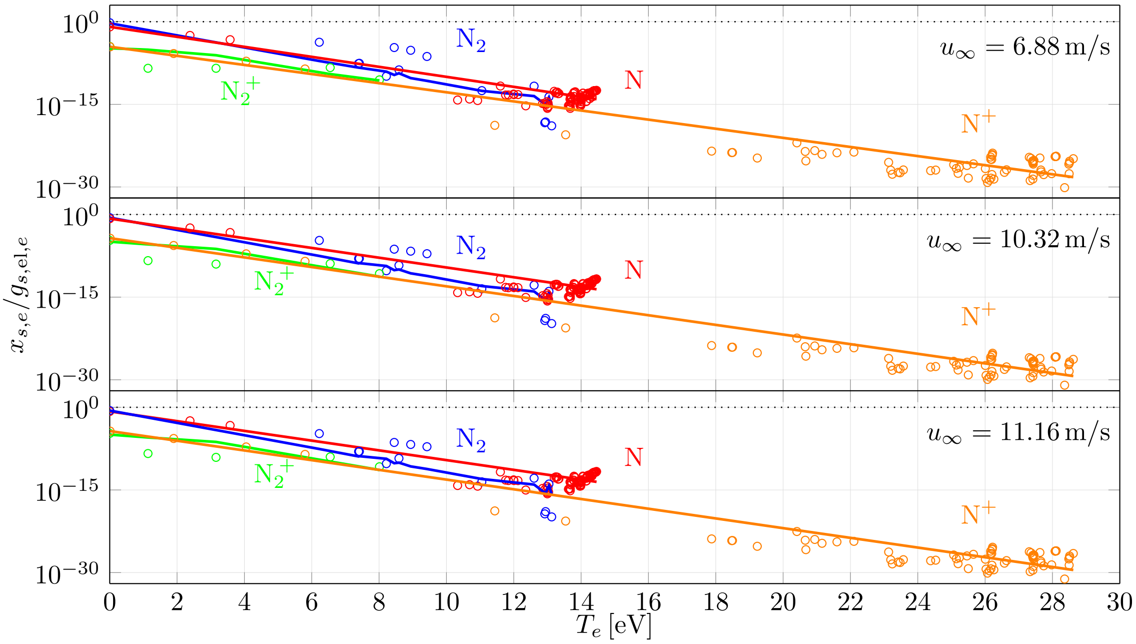

Figure 4.20: Electronic state-specific mole fractions $x_{s,e}/g_{s,\mathrm{el},e}$ (markers) and respective Boltzmann representatives $x^{\mathrm{B}}_{s,e}/g_{s,\mathrm{el},e}$ (lines) as functions of the electronic energies T_e, obtained from the simulations of the low, medium and high speed shots, at $x = 5\,\mathrm{cm}$.

The obtained representative electronic temperatures are presented by Table 4.3. It shows that these temperatures depart from each other and from the obtained heavy particle and free electron translational ones in the order of the thousands of kelvins. In fact, the variables $T_{s,\mathrm{el}}$ are all lower than $T_{\mathrm{tr_h}}$, by amounts from $3,359\,\mathrm{K}$ (or $43.10\,\%$) to $1,407\,\mathrm{K}$ (or $18.05\,\%$), $2,811\,\mathrm{K}$ (or $39.13\,\%$) to $968\,\mathrm{K}$ (or $13.47\,\%$), and $2740\,\mathrm{K}$ (or $38.60\,\%$) to $932\,\mathrm{K}$ (or $13.13\,\%$), for the cases of the low, medium and high speed shots, respectively. Therefore, one cannot state that the electronic and the translational energy modes attained an equilibrium between themselves at $x = 5\,\mathrm{cm}$.

Table 4.3: Heavy particle and free electron translational temperatures $T_{\mathrm{tr_h}}$ and $T_{\mathrm{tr_e}}$, and representative electronic temperatures $T_{s,\mathrm{el}}$ obtained from the simulations of the low, medium and high speed shots, at $x = 5\,\mathrm{cm}$.

$u_\infty\,[\mathrm{m/s}]$	$T_{\mathrm{tr_h}}\,[\mathrm{K}]$	$T_{\mathrm{tr_e}}\,[\mathrm{K}]$	$T_{\mathrm{N_2,el}}\,[\mathrm{K}]$	$T_{\mathrm{N,el}}\,[\mathrm{K}]$	$T_{\mathrm{N_2^+,el}}\,[\mathrm{K}]$	$T_{\mathrm{N^+,el}}\,[\mathrm{K}]$
6.88	7,793	7,811	4,434	5,551	6,386	6,093
10.32	7,184	7,187	4,373	5,682	6,216	5.762
11.16	7,098	7,100	4,358	5,699	6,166	5,719

Figure 4.21 shows the obtained vibronic state-specific mole fractions $x_{s,e,v}/(g_{s,\mathrm{el},e} \cdot g_{s,\mathrm{vib},e,v})$ and respective Boltzmann representatives $x^{\mathrm{B}}_{s,e,v}/(g_{s,\mathrm{el},e} \cdot g_{s,\mathrm{vib},e,v})$ at $x = 5\,\mathrm{cm}$. In this figure, there are markers that agree remarkably well with the respective lines (vibrational self-equilibrium was in those cases achieved), and others (the ones associated to the seemingly horizontal lines) which don't agree at all. It can be shown that the deviations of the latter are due to the non-modelling of the spontaneous emission processes of the higher vibronic levels, implying these to not be depopulated through spontaneous emission in contrast to the lower ones. When fitting the respective vibronic state-specific mole fractions, a nearly

horizontal line is obtained, which is associated to a very high representative vibrational temperature. This result is clearly unphysical. To avoid it in the future, one should consider a redistribution procedure on the Einstein coefficients for spontaneous emission to model the vibronic levels whose data aren't available.

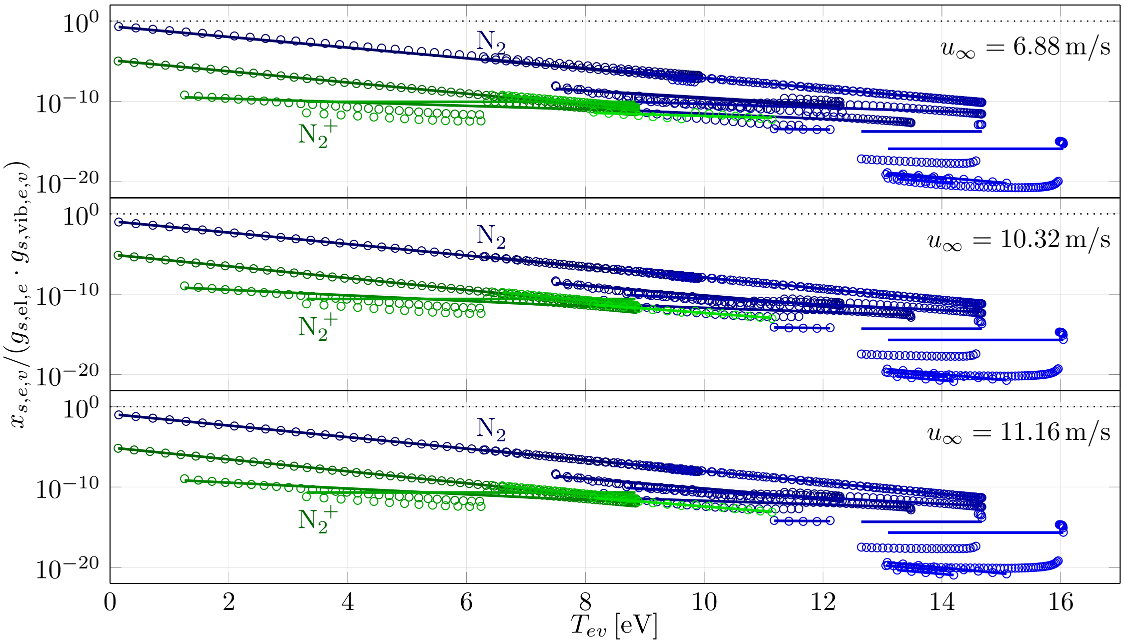

Figure 4.21: Vibronic state-specific mole fractions $x_{s,e,v}/(g_{s,\mathrm{el},e} \cdot g_{s,\mathrm{vib},e,v})$ (markers) and respective Boltzmann representatives $x^{\mathrm{B}}_{s,e,v}/(g_{s,\mathrm{el},e} \cdot g_{s,\mathrm{vib},e,v})$ (lines) as functions of the vibronic energies T_{ev}, obtained from the simulations of the low, medium and high speed shots, at $x = 5\,\mathrm{cm}$.

The non-absurd values of $T_{s,\mathrm{vib},n}$ deviate from $T_{\mathrm{tr_h}}$ by amounts from $-843\,\mathrm{K}$ (or $-10.82\,\%$) to $3,730\,\mathrm{K}$ (or $47.86\,\%$), $-383\,\mathrm{K}$ (or $-5.33\,\%$) to $1,112\,\mathrm{K}$ (or $15.48\,\%$), and $-311\,\mathrm{K}$ (or $-4.38\,\%$) to $1,188\,\mathrm{K}$ (or $16.74\,\%$), for the cases of the low, medium and high speed shots, respectively. These values are too large for one to assume that equilibrium between the vibrational and translational energy modes was attained for all the considered electronic levels. It's important to note that markers associated to the same species don't lay on the same line, showing that the respective electronic energy mode isn't at self-equilibirum (as also evidenced by the fact that the markers in Figure 4.20 don't coincide with their Boltzmann representatives).

Since no absorption and induced emission processes weren't considered in this work, spontaneous emission occurred without any counterbalance. This may have led to the observed self-non-equilibrium of the electronic energy modes. Figure 4.22 shows the electronic state-specific mole fractions $x_{s,e}/g_{s,\mathrm{el},e}$ and respective Boltzmann representatives $x^{\mathrm{B}}_{s,e}/g_{s,\mathrm{el},e}$ obtained from the simulations of the low, medium and high speed shots, at $x = 5\,\mathrm{cm}$, disregarding spontaneous emission. The markers in this figure agree much more with the respective lines than in Figure 4.20, whose results were obtained assuming spontaneous emission. Self-equilibrium of the electronic energy modes seems to be attained by all species with the exception of N_2 and N in the case of the low speed shot, as the respective markers slightly depart from the lines. Table 4.4 presents the obtained representative electronic temperatures. The variables $T_{s,\mathrm{el}}$ depart from $T_{\mathrm{tr_h}}$, by amounts from $-948\,\mathrm{K}$ (or $-11,76\,\%$) to $432\,\mathrm{K}$ (or $5.36\,\%$), $-83\,\mathrm{K}$ (or $-0.90\,\%$) to $39\,\mathrm{K}$ (or $0.42\,\%$), and $-81\,\mathrm{K}$ (or $-0.80\,\%$) to $11\,\mathrm{K}$ (or $0.11\,\%$), for the cases of the low, medium and high speed shots, respectively. All these values are negligibly small with the exception of the ones of the former case, being the lower limit due to N and the higher limit due to N_2, which, as mentioned above, were also found to not be at electronic self-equilibrium. One can state that the electronic and the translational energy modes of the particles attained an equilibrium between themselves at $x = 5\,\mathrm{cm}$, with the exception of N and N_2 in the case of low speed shot.

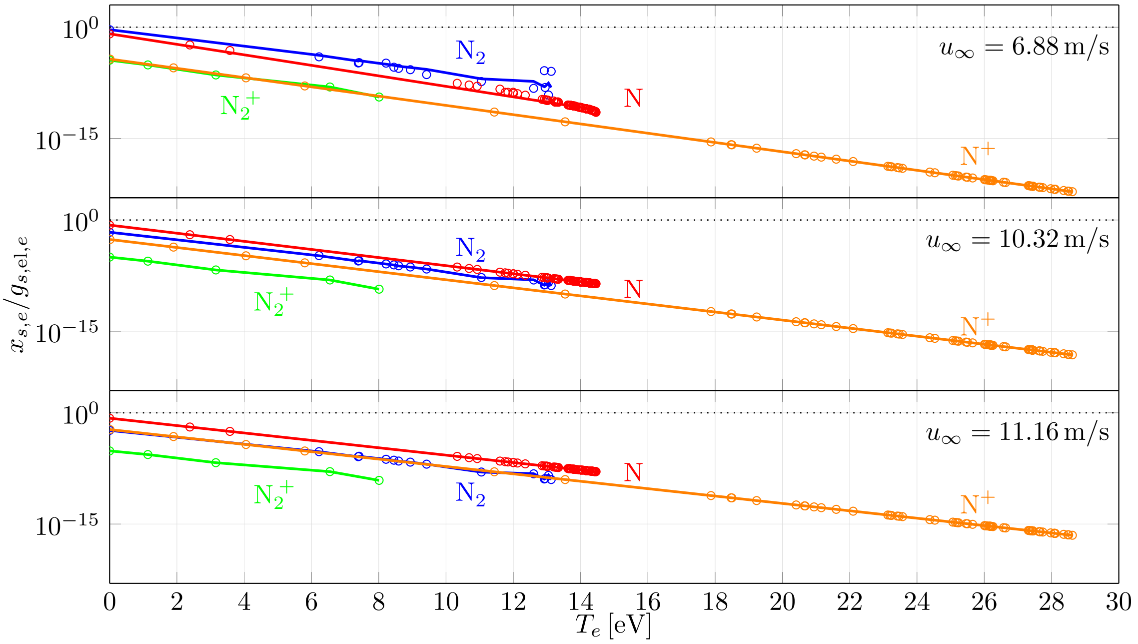

Figure 4.22: Electronic state-specific mole fractions $x_{s,e}/g_{s,\mathrm{el},e}$ (markers) and respective Boltzmann representatives $x^{\mathrm{B}}_{s,e}/g_{s,\mathrm{el},e}$ (lines) as functions of the electronic energies T_e, obtained from the simulations of the low, medium and high speed shots, at $x = 5\,\mathrm{cm}$, disregarding spontaneous emission processes.

Table 4.4: Heavy particle and free electron translational temperatures $T_{\mathrm{tr_h}}$ and $T_{\mathrm{tr_e}}$, and representative electronic temperatures $T_{s,\mathrm{el}}$ obtained from the simulations of the low, medium and high speed shots, at $x = 5\,\mathrm{cm}$, disregarding spontaneous emission.

$u_\infty\,[\mathrm{m/s}]$	$T_{\mathrm{tr_h}}\,[\mathrm{K}]$	$T_{\mathrm{tr_e}}\,[\mathrm{K}]$	$T_{\mathrm{N_2,el}}\,[\mathrm{K}]$	$T_{\mathrm{N,el}}\,[\mathrm{K}]$	$T_{\mathrm{N_2^+,el}}\,[\mathrm{K}]$	$T_{\mathrm{N^+,el}}\,[\mathrm{K}]$
6.88	8,059	8,078	8,491	7,111	8,100	8.063
10.32	9,264	9,271	9,181	9.216	9.303	9.271
11.16	10,114	10,116	10,033	10,113	10,125	10,116

Figure 4.23 shows the vibronic state-specific mole fractions $x_{s,e,v}/(g_{s,\mathrm{el},e} \cdot g_{s,\mathrm{vib},e,v})$ and respective Boltzmann representatives $x^{\mathrm{B}}_{s,e,v}/(g_{s,\mathrm{el},e} \cdot g_{s,\mathrm{vib},e,v})$, obtained from the simulations of the low, medium and high speed shots, at $x = 5\,\mathrm{cm}$, disregarding spontaneous emission. All markers in Figure 4.23 lay in the respective lines, evidencing that vibrational self-equilibrium occurs. However, the lines associated to N_2 for the case of the low speed shot depart slightly from each other. This is a result of an electronic self-non-equilibrium of N_2, which was already mentioned before. The values of $T_{s,\mathrm{vib},n}$ deviate from $T_{\mathrm{tr_h}}$ by amounts from $-1,557\,\mathrm{K}$ (or $-19.32\,\%$) to $46\,\mathrm{K}$ (or $0.57\,\%$), $-1,052\,\mathrm{K}$ (or $-11.36\,\%$) to $42\,\mathrm{K}$ (or $0.45\,\%$), and $-729\,\mathrm{K}$ (or $-7.21\,\%$) to $13\,\mathrm{K}$ (or $0.13\,\%$), for the cases of the low, medium and high speed shots, respectively. The lower limits of the deviations are significant and in the same order of magnitude as the ones obtained when considering spontaneous emission. The upper limits are, however, much smaller.

The vibrational and translational energy modes should therefore be closer to an equilibrium between each other when disregarding spontaneous emission than when regarding.

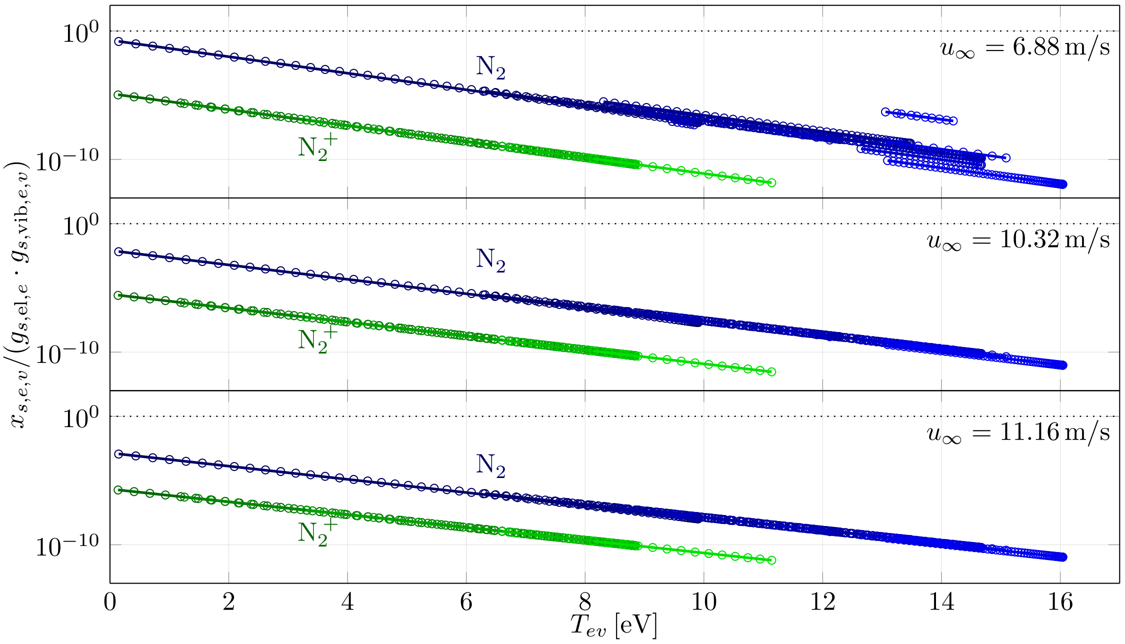

Figure 4.23: Vibronic state-specific mole fractions $x_{s,e,v}/(g_{s,\mathrm{el},e} \cdot g_{s,\mathrm{vib},e,v})$ (markers) and respective Boltzmann representatives $x^{\mathrm{B}}_{s,e,v}/(g_{s,\mathrm{el},e} \cdot g_{s,\mathrm{vib},e,v})$ (lines) as functions of the vibronic energies T_{ev}, obtained from the simulations of the low, medium and high speed shots, at $x = 5\,\mathrm{cm}$, disregarding spontaneous emission processes.

All of the above-mentioned results allow the author to conclude that the spontaneous emission processes strongly contribute to the observed thermal non-equilibrium conditions of the systems at $x = 5\,\mathrm{cm}$. It should be ascertained in the future if the consideration of absorption and induced emission processes may reduce this thermal non-equilibrium. The results also showed that collisional processes, alone, don't ensure equilibrium between the electronic and translational energy modes of N_2 and N in the case of the low speed shot.

4.4.2 Dependence on the escape factor

It is well known that the emitted VUV radiation is strongly absorbed by the particles in the medium [105] and, therefore, the assumption of it being optically thin may not be valid. By considering an escape factor $\Lambda^{\mathrm{VUV}} < 1$ in the simulations, it's possible to take into account, in a crude way, the effect of auto-absorption (i.e. absorption by the same emitting source) of the VUV radiation on the resultant radiation variables. Part of the energy which was once lost due to emitted VUV radiation escaping from the system may now be used in other processes. More energy becomes available for excitation of the particles, and as a consequence, more energy is radiated in the other wavelength intervals. There's even the possibility of more radiative energy in the VUV wavelength interval escaping from the system, since though a significant fraction of the photons don't escape, the number of emitted photons becomes as high as the number excited particles. Values of $\Lambda^{\mathrm{VUV}} = 0.1$ and 0.01 were tried, and the respective overall radiation variables are shown in Figures C.1 to C.8. Figure C.1 shows that by decreasing the escape factor, the peak values of the instrumentally resolved radiative intensities in the VUV wavelength region decreased as much as a half in the three shots. On the other hand, the contributions of N increased significantly becoming now much more dominant than the others (i.e. the ones of $N_2^+(C-X)$, $N_2(a-X)$ and $N_2(A-X)$), as shown in Figure C.2). The obtained spectra show better agreeability with the experimental result. The radiative intensity profiles show steeper rises and falls, and, in the case of the low speed shot, it got closer to the experimental one. Still, no plateaus were predicted in the cases of the medium and high speed shots. For the case of the "Blue" wavelength region, the decrease in the escape factor made the peak values of the instrumentally resolved radiative intensities to increase with some significance: as much as 10% in the low speed shot, and 40% in the medium and high speed shots. The change on the shape of the peaks isn't noticeable to the eye (see Figure C.3). Regarding the shape of the instrumentally resolved non-equilibrium metric, Figure C.4 shows that solely the peak associated to $N_2(C-B)$ at $\lambda = 337\,\mathrm{nm}$ suffered a meaningful change, increasing its height with the decrease in the escape factor value. For the case of the "Red" and IR wavelength regions, the peak values of the instrumentally resolved radiative intensities also increased: as much as 10% in the low speed shot, and 60% (for the case of the former) and 80% (for the case of the latter) in the medium and high speed shots. The shapes of the peaks didn't change significantly. And the contributions of N to the non-equilibrium metrics were preferentially augmented (in particular in the medium and high speed shots), agreeing better with the experimental results.

These results show strong evidence for the medium being optically thick in the VUV wavelength region.

4.4.3 Dependence on the dissociation rates of N_2

The evolution of the post-shock conditions is highly dependent on the dissociation rates of N_2. Greater dissociation rates would imply a production of a greater number of N particles. And, being dissociation an endothermic process, lesser energy would be available for excitation. However, it's hard to say how an increase of the dissociation rates could affect the excitation of the particles to some energy level. Note that being lesser the population of N_2, a lower number of N_2 particles would be left to be excited. Conversely, being greater the population of N, a greater number of N particles would be left to be excited. Therefore, one cannot say, in straight forward manner, if the number of particles in some excited energy level should get lower or higher. To test the dependence of the numerical results on the dissociation rates of N_2, it was decided to consider dissociation rates of $N_2(X^1\Sigma_g^+)$ (the ground electronic level of molecular nitrogen[4]) scaled by 0.1 and 10, and to keep $\Lambda^{\mathrm{VUV}} = 0.01$. The obtained results are shown by Figures C.9 to C.16. These figures show that the peak values of the instrumentally resolved radiative intensities increased with a decrease of the rates of dissociation, being this more relevant for the case of all wavelength intervals of the low speed shot and the wavelength intervals "Blue", "Red" and IR of the medium and high speed shots. The increase went from as low as insignificant to as high as the double. And for the case of an increase of the rates of dissociation, the decrease of the peak values went from as

---

[4] The ground electronic level of N_2 is usually more populated than the other ones, being, therefore, more important in what concerns dissociation.

low as 20 % to as high as 70 %. The figures for the non-equilibrium metrics show that both contributions of N and N_2 to the radiation variables increased with the decrease of the rates of dissociation, being the effect on the latter contribution much more significant. The energy that was once spent in dissociation was then spent in excitation of N and N_2, and because more N_2 and less N particles were obtained, the effect on N_2 had a greater importance. Note, however, that in order to get a better agreeability with the experimental spectra, the contributions of N should be the ones to get enhanced and not N_2. Also, one should point out that in the case of the low speed shot, the peaks of radiative intensity widened with the decrease of the rates of dissociation, agreeing better with the experimental profiles for all wavelength intervals except for VUV. And in the case of the other shots, the change on the peaks shape wasn't significant. The increase of the rates of dissociation made the peaks to narrow in the case of the low speed shot, agreeing worse with experimental counterparts. Conversely, the increase made the peaks to widen in the case of the "Blue" wavelength interval of the medium and high speed shots, getting closer to the experimental results.

Concluding, a sole decrease or increase of the rates of dissociation of $N_2(X)$ don't unequivocally lead to better results.

4.4.4 Dependence on the excitation rates of N

In §4.4.2 it was found that the contributions of N to the radiation variables were still underestimated when compared with the molecular contributions in the "Red" and IR wavelength intervals. It was then decided to try scaling the excitation rate coefficients of N, keeping $\Lambda^{\mathrm{VUV}} = 0.01$, in order to enhance them. The crude formulae of Annaloro et al. [66] and Panesi et al. [86] employed in this work[5] as models for excitation of N by heavy particle and electron impact, respectively, may indeed accommodate some degree of uncertainty. Their multiplication by 10 and 100 was tried, and solely for the case of low speed shot the numerical simulations converged. This is an indication of the rate coefficients being actually high enough in the conditions of the medium and high speed shots, and by increasing their values, a physical incoherence may have been obtained. The results are shown in Figures C.17 and C.18. With the increase in the rate coefficients for excitation of N, the peaks values of the instrumentally resolved radiative intensities rose as much as to the quintuple in the case of the VUV radiation, the double in the case of the "Blue" and "Red" radiation, and the quadruple in the case of the IR radiation. However, the values are still one to two orders of magnitude lower than the experimental ones. Regarding the shape of the profiles, it was found that the rising and falling parts got steeper deviating significantly from the experimental profiles. This result may be justified by the fact that a greater rate of excitation of N produces a greater rate of emission of radiation, and therefore, the radiative intensity rises faster and higher. As a higher excitation requires more energy, which is then lost in the form of radiation, the system suddenly gets incapable of continually exciting the particles, and the radiative intensity falls faster. The Figure C.18. show that the contribution of N to the instrumentally resolved non-equilibrium metrics increased in all wavelength regions, agreeing better with the experimental spectra except in the "Blue" wavelength region, for which the contributions of the molecular particles should prevail over the

---

[5] See Section §3.2.4 and §3.2.5 for more details.

ones of the atomic particles.

Concluding, it can't be said that a sole increase of the rate coefficients for excitation of N unequivocally leads to better results.

4.4.5 A synopsis about the dependence of the results on the different parameters

Figure 4.24 shows the peak values of the instrumentally resolved radiative intensities $\hat{I}^{l}_{\mathrm{peak}}$ (with $l \in \{\mathrm{VUV}, \text{“Blue”}, \text{“Red”}, \mathrm{IR}\}$) obtained with the different models and in the experiment for the low, medium and high speed shots. And Figure 4.25 and Figure 4.26 show the temperatures $T_{\mathrm{tr_h}}$ and $T_{\mathrm{tr_e}}$ and mole fractions x_s attained at $x = 5\,\mathrm{cm}$, respectively, which were obtained with the different models of this work and of the work of Cruden and Brandis [105].

As referred before, the peak values of the instrumentally resolved radiative intensities obtained in the zero-dimensional simulation (labelled by “0D” in the figures) are several times lower than the ones obtained in the one-dimensional simulation (labelled by “1D”) and even more lower than the ones of the experiment. On the other hand, the attained temperatures are much greater than the ones of the one-dimensional simulation ($T_{\mathrm{tr_h}}$ differs by 1105 K, 1761 K and 1881 K for the cases of the low, medium and high speed shots), agreeing better with the values of Cruden and Brandis (labelled by “NEQAIR, “Blue”” and “NEQAIR, “Red””). Figure 4.26 shows that dissociation of N_2 is weaker than in the case of the one-dimensional simulation. The attained mole fractions of N_2^+ and N^+ at $x = 5\,\mathrm{cm}$ are higher (with the exception of N^+ in the low speed shot). However, this can be shown to be simply due to a slower recombination. It can be said that in the one-dimension simulation more energy was spent in excitation, dissociation and ionisation of the particles. The results of Cruden and Brandis evidence that these endothermic processes were even more stronger in the experiment.

By considering escape factors $\Lambda^{\mathrm{VUV}} = 0.1$ and $\Lambda^{\mathrm{VUV}} = 0.01$ for the VUV wavelength interval, the peak values of the instrumentally resolved radiative intensities increase for all wavelength intervals except VUV, for which it decreases. The attained temperatures rise just slightly, but the mole fractions of the species don't change appreciably. Part of the energy which was once lost through VUV radiation is now lost through “Blue”, “Red” and IR radiations.

Decreasing the rates of dissociation of $N_2(X^1\Sigma_g^+)$, keeping $\Lambda^{\mathrm{VUV}} = 0.01$, makes the peak values of the instrumentally resolved radiative intensities to increase, and increasing the rates of dissociations makes them to decrease. The impact is, however, not so relevant for the case of the VUV wavelength interval of the medium and high speed shots. Figure 4.25 shows that by decreasing the rates of dissociation, less energy is spent on endothermic processes (since higher translational temperatures are attained). Curiously, increasing the rates of dissociation doesn't decrease the attained translational temperatures in the cases of the medium and high speed shots (the translational energy is then redistributed in a different way). It's important to mention here that the values of all of the referred temperatures are still much lower (by several thousands of kelvins) than the ones inferred by Cruden and Brandis. Figure 4.26 shows a tendency for an increase of the attained mole fractions of N and N^+ and decrease of the ones of N_2 and N_2^+ with an increase of the rates of dissociation. The increase on the mole fraction of N^+ and the decrease on the one of N_2^+ can be justified by the fact that a stronger dissociation implies that, in contrast with N_2, more N particles become available to be ionised. The values of the mole fractions obtained by increasing the rate coefficients are actually the ones of all the tried models (regarding spontaneous emission) who better agree with the ones of Cruden and Brandis. Still, their results indicate that the system should have suffered stronger dissociation and ionisation.

By keeping $\Lambda^{\mathrm{VUV}} = 0.01$, and increasing the excitation rates of N (which was only successful for the case of the low speed shot), a meaningful rise of the peak radiation values occurs, in particular the ones of the IR and VUV wavelength intervals. Still, these are one to two orders of magnitude lower than the ones obtained in the experiment (labelled by "Exp."). The increase in the radiation variables comes with a cost of the translational temperatures ($T_{\mathrm{tr_h}}$ decreases as much as 698 K) and a weaker dissociation and ionisation of N_2. The mole fraction of N^+ at $x = 5\,\mathrm{cm}$ gets lower due to a faster recombination. The peak value of the mole fraction of N^+ actually increases as the highly excited N particles are more easily ionised. It can be concluded that more energy is used in endothermic processes, being excitation of N the mainly one.

As shown by Figures 4.25 and 4.26, the translational temperatures and the mole fractions of all species except N_2^+ attained in the one-dimension simulations disregarding spontaneous emission (labelled by "1D, no s. emission") agree well with the ones derived by Cruden and Brandis. This endorses the hypothesis of the simulated elements of fluid, when regarding spontaneous emission, not receiving the amount of energy that they should, as only by disregarding spontaneous emission (therefore, retaining a lot more energy) the thermodynamic conditions get reasonably closer to the inferred ones.

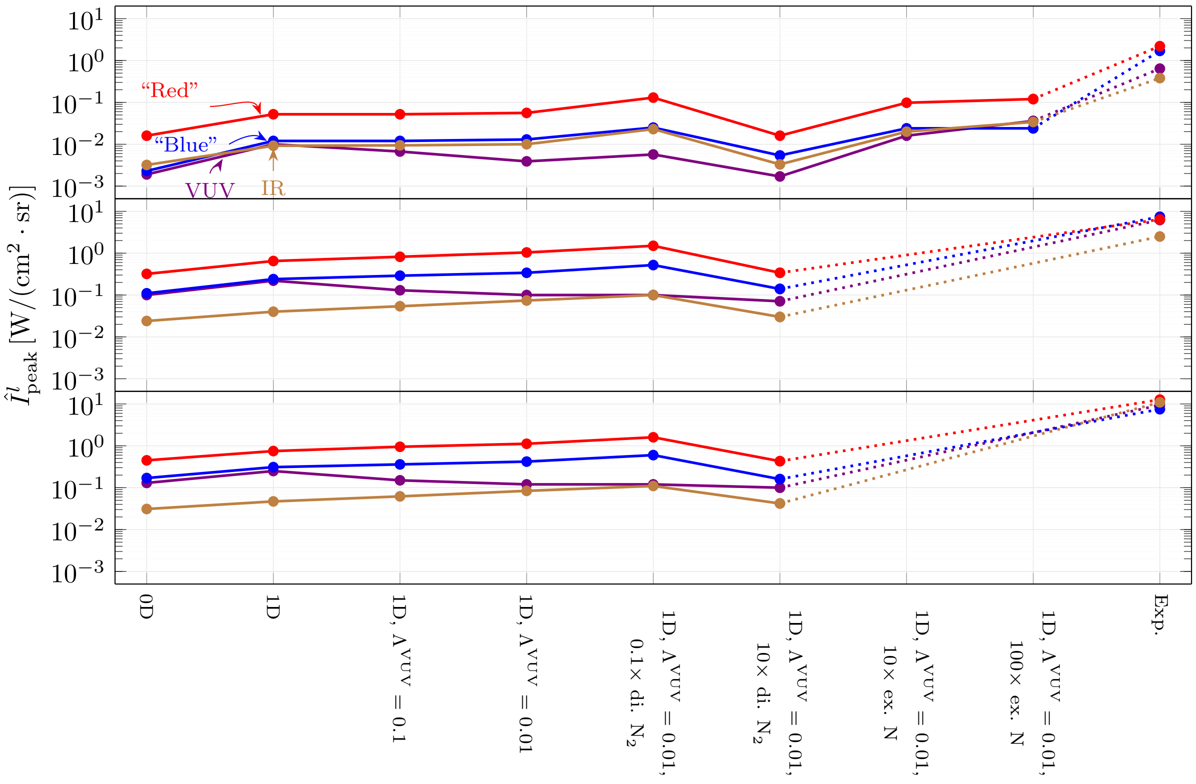

Figure 4.24: Peak values of the instrumentally resolved radiative intensities $\hat{I}^l_{\mathrm{peak}}$ obtained with the different models and in the experiment for the low, medium and high speed shots.

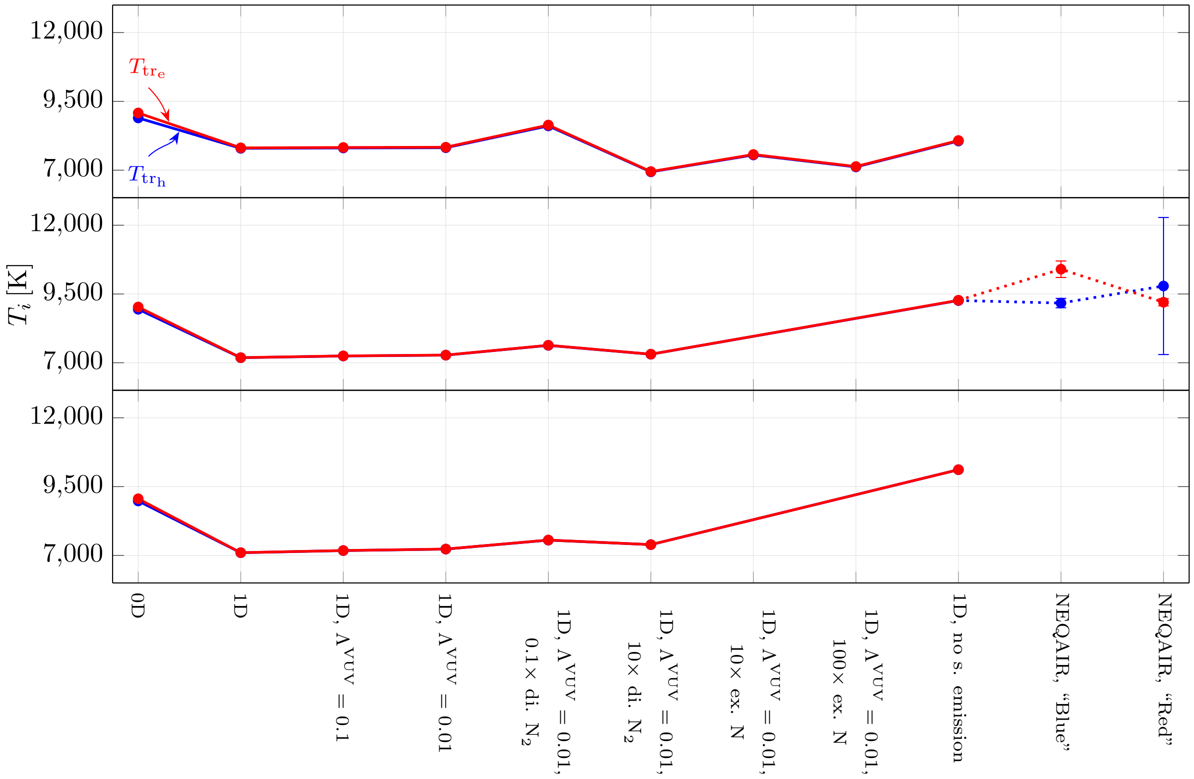

Figure 4.25: Temperatures $T_{\mathrm{tr_h}}$ and $T_{\mathrm{tr_e}}$ at $x = 5\,\mathrm{cm}$ obtained with the different models for the low, medium and high speed shots.

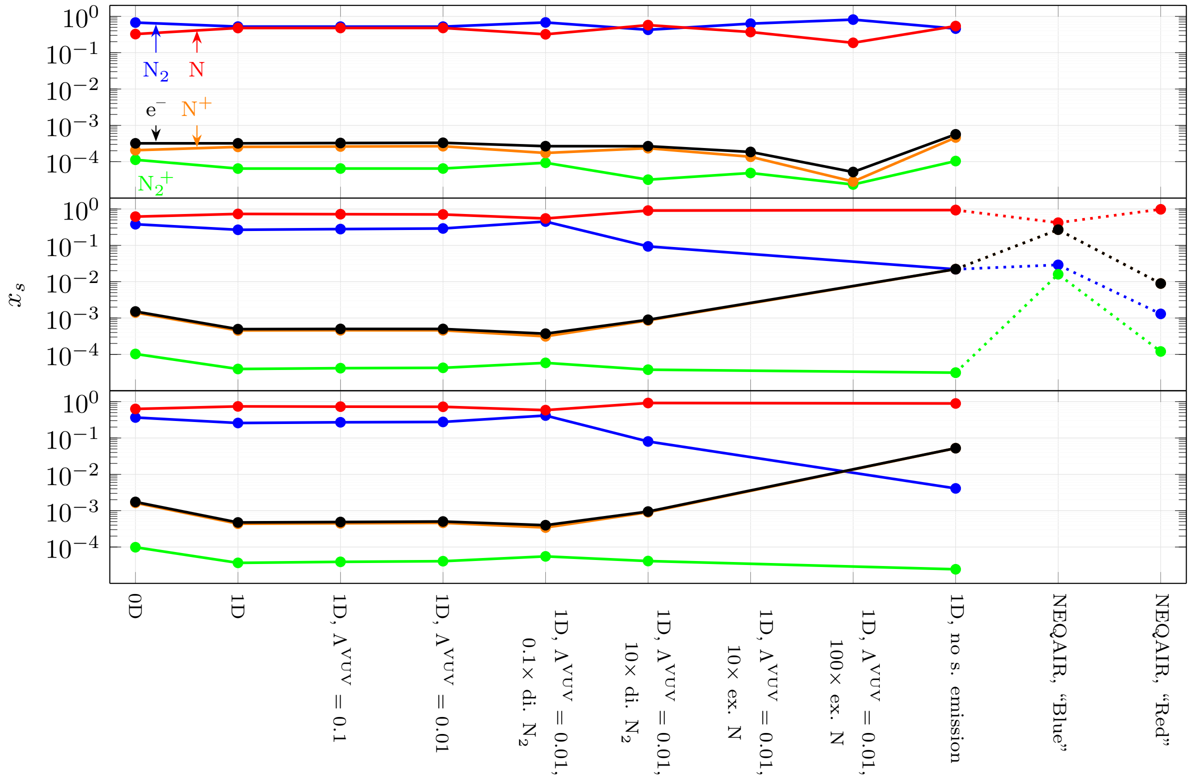

Figure 4.26: Mole fractions x_s at $x = 5\,\mathrm{cm}$ obtained with the different models for the low, medium and high speed shots.

4.4.6 Other possible causes of the significant underestimation of the experimental results by the numerical ones

Several studies in the literature reported the occurrence of analytical and numerical models which significantly underestimated the radiation variables obtained trough shock tube experiments. In fact, these discrepancies had been so recurrently observed that Cruden et al. [107] even used the term "long-standing" to describe the problem regarding results obtained from the Japan Aerospace Exploration Agency's High-Enthalpy Shock Tunnel (JAXA-HIEST). Cruden et al. [107] studied the impact that contamination species have on the numerical results, fitting their concentrations in order to match some particular JAXA-HIEST experimental results. They concluded that it may well be possible for contaminants such as Fe (atomic iron) and CN (cyanogen radical) to cause the observed discrepancies. In the case of the experiments that the produced benchmark data regarded in the present work - the EAST test 62 - Cruden and Brandis [105] found evidence for the presence of the contaminants C (atomic carbon), H (atomic hydrogen) and CN. However, it seems improbable that this could explain the deviations in several orders of magnitude on the obtained radiation variables, since the observed spectrum is almost completely dominated by the non-contaminant species (namely N, N_2 and N_2^+). Furthermore, Brandis et al. [108] refer that in the latest EAST campaigns many upgrades to the system have been made in order to reduce the level of contamination.

A more feasible contribution to the discrepancies between the numerical and experimental results is the non-modelling of the so-called *precursor phenomena*: some of the VUV radiation emitted by highly excited particles in the shock layer is absorbed by others upstream of the shock wave, inducing their excitation, photoionisation and photodissociation. This changes the conditions upstream of the shock wave and, inevitably, also the conditions downstream of it: Nomura et al. [109] refer that the shock layer thickness and the non-equilibrium temperatures are increased, yielding an excess of radiation. Yamada et al. [110] compared experimental results with numerical ones obtained through a model that doesn't account the precursor phenomena, and found that the measured radiation intensities for N_2, N_2^+ and N started to increase upstream of the shock wave. The radiation profiles in the shock layer differed significantly, showing that the precursor phenomena had a great influence on the thermochemical processes that occurred downstream of the shock wave.

Another feasible contribution to the discrepancies corresponds to heating of the driven gas due to downstream plasma subjected to a stronger shock wave, and radiative energy transfer from the driver gas and the EAST electric arc. Bogdanoff and Park [111] performed several shock tube experiments, finding the temperature downstream of the shock wave in the observation point to be three to four times the one obtained through the Rankine-Hugoniot relations. The electric arc of the shock tube increases the temperature of the driver gas to very high values (several tens of thousands of kelvins) which causes it to radiate a lot of energy, some of it to the driven gas upstream and downstream of the shock wave. Also, it is known that the shock wave decelerates through the shock tube, heating more the part of the driven gas near the diaphragm than the part of the driven gas near the observation point. A transfer of energy from the former to the later may then also occur.

Chapter 5

Conclusions

5.1 Achievements

In this work a extensive set of vibronic energy levels for N_2, N_2^+, N and N^+ was built using the most up-to-date data available in the literature. A near complete database of vibronic-specific kinetic processes involving these species was congregated. Special caution was taken to ensure physical consistency up to the highest temperatures. The database comprises chemical processes such as dissociation, ionisation and charge exchange, as well as non-chemical processes, i.e. excitation and de-excitation of the energy levels of the particles. The term "near complete" was herein used to describe it, since it misses transitions between the highest electronic energy levels, as well as bound-free and free-free radiative processes.

Rates for vibrational transition and dissociation of the molecular particles were computed using the FHO model. Thermal dissociation rate coefficients of $N_2(X^1\Sigma_g^+)$ by collisions with N_2 and N were obtained and calibrated using state-of-the-art experimental results, showing an agreeability between -59.9 and $8.9\,\%$, and between -80.9 and $-36.1\,\%$ for the former and latter interactions, respectively. Also, the values were compared with the most recent QCT calculations deviating by a maximum of $56.5\,\%$. Note that although these values seem to be too large, they should be regarded as reasonable, since the deviations are evaluated within an extensive set of temperatures (varying in many thousands of kelvins) for which the rate coefficients suffer changes of several orders of magnitude.

It was ascertained in this work if the well-known Landau-Zener and Rosen-Zener-Demkov models could be extended to vibronic transitions of molecular particles by heavy particle impact beyond electronic transitions of atomic particles by atomic particle impact. As a verdict, it was found impractical, mainly due to a current lack of knowledge about the characteristic constants that describe the models and to the necessity of solving the classical equations of motion of the nuclei. An exponential gap law was then preferred. However, the curve that represents the law was shown to deviate from experimental points by as much as one order magnitude, reducing the confidence on the model.

The developed kinetic database was tested in zero and Euler one-dimensional simulations of the shots 19, 20 and 40 of the test 62 of EAST. The peak values of the radiative intensities obtained from the Euler one-dimensional simulation were found to be between the double and the quintuple of the ones obtained from the zero-dimensional simulation, showing the hypothesis of the momentum transfer being negligible (which is taken by the latter) to be invalid. Such result discourages the use in future works of the zero-dimensional model as an approximation of the flow generated by shock tubes. Still, the one-dimensional model underpredicted the experimental radiation variables by one to two orders of magnitude. And the sensibility tests performed on the rate coefficients were unsuccessful in getting a reasonable agreeability. The shape of the radiative intensities profiles of the low speed shot was correctly predicted, but not the ones of the medium and high speed shots which revealed non-null plateaus proceeding or coalescing with peaks. These plateaus weren't predicted at all. The analysis of Cruden and Brandis on the spectra obtained in the test 62 of EAST showed that higher values of the radiation variables were attained with a lower cost of translation temperature. There's a strong evidence for the underestimation of the radiation variables observed in this work to result from the non-modelling of heat transfer by radiation within the test gas, and possibly, between the driver gas (as well as the driver arc) and the test gas. The latter hypothesis has been suggested by Bogdanoff and Park as a possible cause for such underestimations also observed in other works.

5.2 Future Work

One of the next steps that should be taken in the future would be to test other kinetic databases reported in the literature and to compare their results with the ones of this work, such that particular qualities which were actually improved or, on the contrary, worsen may be identified. And to quantify the possible divergences between the herein implemented vibronic-specific state-to-state model and the simpler models such as the multi and single-temperature ones, these latter should also be tried.

In order to ascertain the effect of heat transfer within the test gas subjected to strong shock waves generated by shock tubes, higher fidelity one-dimensional simulations should be performed. The crude concept of an escape factor should be disregarded, and an equation of radiative transfer should be solved instead. Also, the transport phenomena should be introduced in the balance equations. It's of capital importance to know if a lack of such complexities in the numerical model was the reason for the significant underestimation of the radiation variables.

The database of radiative processes developed in this work should be extended, accommodating absorption, induced emission, photodissociation, photoassociation, photoionisation, photorecombination and bremsstrahlung, beyond spontaneous emission processes. And these processes should be treated as rovibronic instead of simply vibronic, as the numerical spectra associated to the molecular contributions obtained in this work showed pointier profiles when compared to the ones obtained in the experiments.

An extrapolation of the Einstein coefficients for spontaneous emission to the energy levels whose data aren't available should be performed to avoid getting unphysical populations distributions.

And finally, as more ambitious goals, the impact on the radiation variables of the precursor phenomena, the absorption of radiation emitted by the driver gas and the EAST electric arc, and the conduction of heat from the driver to the test gas should be studied.

Bibliography

[1] Chul Park. *Nonequilibrium Hypersonic Aerothermodynamics.* John Wiley and Sons Ltd, New York, United States, April 1990.

[2] W. G. Vincenti and C. H. Kruger. *Introduction to physical gas dynamics.* John Wiley & Sons, 1965.

[3] John J. Bertin. *Hypersonic Aerothermodynamics.* American Institute of Aeronautics and Astronautics, Inc., Washington, DC, 1994.

[4] Jong-Hun Lee. Basic governing equations for the flight regimes of aeroassisted orbital transfer vehicles. In *19th Thermophysics Conference*, June 1984. doi:10.2514/6.1984-1729.

[5] Chul Park. Assessment of two-temperature kinetic model for ionizing air. *Journal of Thermophysics and Heat Transfer*, 3(3):233–244, 1989. doi:10.2514/3.28771.

[6] Chul Park. Modeling of hypersonic reacting flows. In Ballmann J. Bertin J.J., Periaux J., editor, *Advances in Hypersonics*, number 8/9 in Progress in Scientific Computing, pages 104–127. Birkhäuser, Boston, MA, 1992. doi:10.1007/978-1-4612-0371-1_4.

[7] Graham Candler. On the computation of shock shapes in nonequilibrium hypersonic flows. In *27th Aerospace Sciences Meeting.* January 1989. doi:10.2514/6.1989-312.

[8] H. G. Hornung. Non-equilibrium dissociating nitrogen flow over spheres and circular cylinders. *Journal of Fluid Mechanics*, 53(1):149–176, 1972. doi:10.1017/S0022112072000084.

[9] R. Kenneth Lobb. Chapter 26 - Experimental Measurement of Shock Detachment Distance on Spheres Fired in Air at Hypervelocities. In Wilbur C. Nelson, editor, *The High Temperature Aspects of Hypersonic Flow*, volume 68 of *AGARDograph*, pages 519–527. Elsevier, 1964. doi:10.1016/B978-1-4831-9828-6.50031-X.

[10] Graham V. Candler, Joseph Olejniczak, and Brent Harrold. Detailed simulation of nitrogen dissociation in stagnation regions. *Physics of Fluids*, 9(7):2108–2117, 1997. doi:10.1063/1.869330.

[11] Alessandro Munafó, Marco Panesi, Richard Jaffe, Thierry Magin, and Andrea Lani. Vibrational State to State Kinetics in Expanding and Compressing Nitrogen Flows. In *10th AIAA/ASME Joint Thermophysics and Heat Transfer Conference*, June 2010. doi:10.2514/6.2010-4335.

[12] Christophe O. Laux, Laurent Pierrot, and Richard J. Gessman. State-to-state modeling of a recombining nitrogen plasma experiment. *Chemical Physics*, 398:46–55, 2012. doi:10.1016/j.chemphys.2011.10.028.

[13] J. Vargas. Improvement of state-resolved kinetic models applied to N2–CH4 hypersonic entry flows. Master's thesis, Instituto Superior Técnico, 2015. url:`https://bibliotecas.utl.pt/cgi-bin/koha/opac-detail.pl?biblionumber=526938`. Accessed: 2020-09-14.

[14] J. Annaloro. *Modèles collisionnels-radiatifs appliqués aux situations d'entrée atmosphérique martienne et terrestre*. PhD thesis, Université de Rouen, 2013. url:`http://www.coria.fr/spip.php?article908&titre_mot=these&lang=en`. Accessed: 2020-09-14.

[15] Igor V Adamovich, Sergey O Macheret, J William Rich, and Charles E Treanor. Vibrational relaxation and dissociation behind shock waves. Part 1 - Kinetic rate models. *AIAA journal*, 33(6):1064–1069, June 1995. doi:10.2514/3.12528.

[16] Igor V Adamovich, Sergey O Macherett, J William Rich, and Charles E Treanor. Vibrational relaxation and dissociation behind shock waves part 2: Master equation modeling. *AIAA journal*, 33(6):1070–1075, June 1995. doi:10.2514/3.48339.

[17] Igor V Adamovich, Sergey O Macheret, J William Rich, and Charles E Treanor. Vibrational energy transfer rates using a forced harmonic oscillator model. *Journal of Thermophysics and Heat Transfer*, 12(1):57–65, January 1998. doi:10.2514/2.6302.

[18] RN Schwartz, ZI Slawsky, and KF Herzfeld. Calculation of vibrational relaxation times in gases. *The Journal of Chemical Physics*, 20(10):1591–1599, May 1952. doi:10.1063/1.1700221.

[19] Don Secrest and B Robert Johnson. Exact Quantum-Mechanical Calculation of a Collinear Collision of a Particle with a Harmonic Oscillator. *The Journal of Chemical Physics*, 45(12):4556–4570, December 1966. doi:10.1063/1.1727537.

[20] GD Billing. Vibration-vibration and vibration-translation energy transfer, including multiquantum transitions in atom-diatom and diatom-diatom collisions. In *Nonequilibrium vibrational kinetics*, pages 85–112. Springer, Berlin, Heidelberg, 1986. doi:10.1007/978-3-642-48615-9_4.

[21] Donald G. Truhlar and James T. Muckerman. Reactive scattering cross sections III: Quasiclassical and semiclassical methods. In *Atom-Molecule Collision Theory*, pages 505–566. Springer, Boston, MA, 1979. doi:10.1007/978-1-4613-2913-8_16.

[22] Edward H Kerner. Note on the forced and damped oscillator in quantum mechanics. *Canadian Journal of Physics*, 36(3):371–377, 1958. doi:10.1139/p58-038.

[23] Charles E Treanor. Vibrational Energy Transfer in High-Energy Collisions. *The Journal of Chemical Physics*, 43(2):532–538, July 1965. doi:10.1063/1.1696777.

[24] Ann Zelechow, Donald Rapp, and Terry E Sharp. Vibrational–vibrational–translational energy transfer between two diatomic molecules. *The Journal of Chemical Physics*, 49(1):286–299, July 1968. doi:10.1063/1.1669823.

[25] M. Lino da Silva, V. Guerra, and J. Loureiro. State-resolved dissociation rates for extremely nonequilibrium atmospheric entries. *Journal of Thermophysics and Heat Transfer*, 21(1):40–49, 2007. doi:10.2514/1.24114.

[26] L. D. Landau. *Phys. Zts. Sov.*, 2(46), 1932.

[27] Clarence Zener and Ralph Howard Fowler. Non-adiabatic crossing of energy levels. *Proceedings of the Royal Society of London. Series A, Containing Papers of a Mathematical and Physical Character*, 137(833):696–702, 1932. doi:10.1098/rspa.1932.0165.

[28] N. Rosen and C. Zener. Double Stern-Gerlach Experiment and Related Collision Phenomena. *Phys. Rev.*, 40:502–507, May 1932. doi:10.1103/PhysRev.40.502.

[29] Yu N Demkov. Charge transfer at small resonance defects. *Sov. Phys. JETP*, 18(1):138–142, 1964.

[30] R. Bachmann, X. Li, Ch. Ottinger, and A. F. Vilesov. Molecular-beam study of the collisional intramolecular coupling of $\mathrm{N_2(B^3\Pi_g)}$ with the $\mathrm{N_2(A^3\Sigma_u^+)}$ and $\mathrm{N_2(W^3\Delta_u)}$ states. *The Journal of Chemical Physics*, 96(7):5151–5164, 1992. doi:10.1063/1.462756.

[31] R. Bachmann, X. Li, Ch. Ottinger, A. F. Vilesov, and V. Wulfmeyer. Vibrational-state-to-state collision-induced intramolecular energy transfer $\mathrm{N_2(A^3\Sigma_u^+}, v'' \rightarrow \mathrm{B^3\Pi_g}, v')$. *The Journal of Chemical Physics*, 98(11):8606–8625, 1993. doi:10.1063/1.464469.

[32] D. H. Katayama, Terry A. Miller, and V. E. Bondybey. Radiative decay and radiationless deactivation in selectively excited CN. *The Journal of Chemical Physics*, 71(4):1662–1669, 1979. doi:10.1063/1.438504.

[33] D. H. Katayama and J. A. Welsh. The effect of isotopic substitution on the collisional quenching of vibronically excited $\mathrm{CO^+}$. *The Journal of Chemical Physics*, 79(8):3627–3632, 1983. doi:10.1063/1.446299.

[34] D.H. Katayama and J.A. Welsh. The effect of temperature on the collisional deactivation of electronically excited $\mathrm{CO^+}$. *Chemical Physics Letters*, 106(1):74–78, 1984. doi:10.1016/0009-2614(84)87014-1.

[35] D. H. Katayama, A. V. Dentamaro, and J. A. Welsh. State specific electronic quenching rates for $\mathrm{^{14}N_2^+}$ and $\mathrm{^{15}N_2^+}$. *The Journal of Chemical Physics*, 87(12):6983–6987, 1987. doi:10.1063/1.453394.

[36] Clabon Walter Allen and Arthur N Cox. *Allen's Astrophysical Quantities*. Springer-Verlag New York, 4th edition, 2002. doi:10.1007/978-1-4612-1186-0, ISBN:978-0-387-95189-8.

[37] Julien Annaloro and Arnaud Bultel. Vibrational and electronic collisional-radiative model in air for Earth entry problems. *Physics of Plasmas*, 21(12):123512, 2014. doi:10.1063/1.4904817.

[38] Bruno Lopez and Mário Lino da Silva. SPARK: A Software Package for Aerodynamics, Radiation and Kinetics. In *46th AIAA Thermophysics Conference*, page 4025, June 2016. doi:10.2514/6.2016-4025.

[39] Aaron M Brandis and Brett A Cruden. Shock Tube Radiation Measurements in Nitrogen. In *2018 Joint Thermophysics and Heat Transfer Conference*, 2018. doi:10.2514/6.2018-3437.

[40] Jorge Loureiro and Jayr Amorim. *Kinetics and spectroscopy of low temperature plasmas*. Springer, 2016. doi:10.1007/978-3-319-09253-9, ISBN:978-3-319-09252-2.

[41] A Kuppermann and EF Greene. Chemical reaction cross sections and rate constants. *Journal of Chemical Education*, 45(6):361–369, 1968. doi:10.1021/ed045p361.

[42] Bruno Lopez, Mario Lino Da Silva, Vasco Guerra, and Jorge Loureiro. *Coupled Hydrodynamic/State-Specific High-Temperature Modeling of Nitrogen Vibrational Excitation and Dissociation*. June 2013. doi:10.2514/6.2013-3149.

[43] S. S. Penner. *Quantitative molecular spectroscopy and gas emissivities*. Addison-Wesley Pub. Co., 1959.

[44] Hans R. Griem. *Principles of Plasma Spectroscopy*. Cambridge Monographs on Plasma Physics. Cambridge University Press, 1997. doi:10.1017/CBO9780511524578.

[45] W. Heitler. *The Quantum Theory of Radiation*. Dover Books on Physics Series. Dover Publications, 1984.

[46] Gerhard Herzberg. *Molecular spectra and molecular structure. Vol. III: Electronic spectra and electronic structure of polyatomic molecules*. Krieger Publishing Company, 1966.

[47] Ellis E. Whiting, Chul Park, Yen Liu, James O. Arnold, and John A. Paterson. NEQAIR96, Nonequilibrium and Equilibrium Radiative Transport and Spectra Program: User's Manual. Technical Report NASA-RP-1389, A-962456, NAS 1.61:1389, NASA Ames Research Center, Moffett Field, CA United States, Dec 1996. url:`https://ntrs.nasa.gov/search.jsp?R=19970004690`. Accessed: 2020-09-14.

[48] Donald Rapp and Thomas Kassal. Theory of vibrational energy transfer between simple molecules in nonreactive collisions. *Chemical Reviews*, 69(1):61–102, February 1969. doi:10.1021/cr60257a003.

[49] Sergey O. Macheret and Igor V. Adamovich. Semiclassical modeling of state-specific dissociation rates in diatomic gases. *The Journal of Chemical Physics*, 113(17):7351–7361, 2000. doi:10.1063/1.1313386.

[50] Gert Due Billing. WKB approximations in inelastic collision theory. *The Journal of Chemical Physics*, 59(11):6147–6152, 1973. doi:10.1063/1.1679983.

[51] Gert Due Billing and Edward R. Fisher. VV and VT rate coefficients in H_2 by a quantum-classical model. *Chemical Physics*, 18(1):225–232, 1976. doi:10.1016/0301-0104(76)87049-8.

[52] Evgeny E. Nikitin. *Theory of elementary atomic and molecular processes in gases*. Clarendon Press, Oxford, 1974.

[53] John C. Tully and Richard K. Preston. Trajectory Surface Hopping Approach to Nonadiabatic Molecular Collisions: The Reaction of H+ with D2. *The Journal of Chemical Physics*, 55(2):562–572, 1971. doi:10.1063/1.1675788.

[54] M. Capitelli, C.M. Ferreira, B.F. Gordiets, and A.I. Osipov. *Plasma Kinetics in Atmospheric Gases*. Springer-Verlag Berlin Heidelberg, 1st edition, 2000. doi:10.1007/978-3-662-04158-1.

[55] A.S. Kirillov. Application of Landau–Zener and Rosen–Zener approximations to calculate rates of electron energy transfer processes. *Advances in Space Research*, 33(6):993–997, 2004. doi:10.1016/j.asr.2003.06.009.

[56] A.S. Kirillov. Calculation of rate coefficients of electron energy transfer processes for molecular nitrogen and molecular oxygen. *Advances in Space Research*, 33(6):998–1004, 2004. doi:10.1016/j.asr.2003.06.014.

[57] V. E. Bondybey and Terry A. Miller. Radiative and radiationless vibronic deactivation rates in selectively excited CO^+. *The Journal of Chemical Physics*, 69(8):3597–3602, 1978. doi:10.1063/1.437066.

[58] Anthony V. Dentamaro and Daniel H. Katayama. Collision induced transitions between the $A^2\Pi_i(v = 0)$ and $X^2\Sigma^+(v = 10)$ states of CO^+. *The Journal of Chemical Physics*, 90(1):91–95, 1989. doi:10.1063/1.456473.

[59] Guo Jihua, Ashraf Ali, and Paul J. Dagdigian. State-to-state collisional interelectronic and intraelectronic energy transfer involving CN $A^2\Pi$ $v = 3$ and $X^2\Sigma^+$ $v = 7$ rotational levels. *The Journal of Chemical Physics*, 85(12):7098–7105, 1986. doi:10.1063/1.451396.

[60] Lawrence G. Piper. State-to-state $N_2(A^3\Sigma^+u)$ energy pooling reactions. II. The formation and quenching of $N_2(B^3\Pi_g, v' = 1 - 12)$. *The Journal of Chemical Physics*, 88(11):6911–6921, 1988. doi:10.1063/1.454388.

[61] Charles S. Parmenter and Mark Seaver. A method to estimate intermolecular potential well depths for species in both ground and excited electronic states. *The Journal of Chemical Physics*, 70(12):5458–5462, 1979. doi:10.1063/1.437457.

[62] H.-M. Lin, Mark Seaver, K. Y. Tang, Alan E. W. Knight, and Charles S. Parmenter. The role of intermolecular potential well depths in collision-induced state changes. *The Journal of Chemical Physics*, 70(12):5442–5457, 1979. doi:10.1063/1.437456.

[63] C. Clay Marston and Gabriel G. Balint-Kurti. The Fourier grid Hamiltonian method for bound state eigenvalues and eigenfunctions. *The Journal of Chemical Physics*, 91(6):3571–3576, 1989. doi:10.1063/1.456888.

[64] Alexander Kramida, Yuri Ralchenko, Joseph Reader, et al. NIST Atomic Spectra Database (version 5.7), October 2019. url:`https://www.nist.gov/pml/atomic-spectra-database`. Accessed: 2019-12-15.

[65] L. D. Landau and E. M. Lifshitz. *Quantum Mechanics.* Pergamon, 3^{rd} edition, 1977. doi:10.1016/C2013-0-02793-4.

[66] Julien Annaloro, Arnaud Bultel, and Pierre Omaly. Collisional-Radiative Modeling Behind Shock Waves in Nitrogen. *Journal of Thermophysics and Heat Transfer*, 28(4):608–622, 2014. doi:10.2514/1.T4263.

[67] Roger A. Svehla. *Estimated viscosities and thermal conductivities of gases at high temperatures.* NASA Lewis Research Center, January 1962. url:`https://ntrs.nasa.gov/archive/nasa/casi.ntrs.nasa.gov/19630012982.pdf`. Accessed: 2020-09-14.

[68] Boyd Cary. Shock-Tube Study of the Termal Dissociation of Nitrogen. *The Physics of Fluids*, 8(1):26–35, 1965. doi:10.1063/1.1761099.

[69] Stanley Byron. Shock-Tube Measurement of the Rate of Dissociation of Nitrogen. *The Journal of Chemical Physics*, 44(4):1378–1388, 1966. doi:10.1063/1.1726870.

[70] J. P. Appleton, M. Steinberg, and D. J. Liquornik. Shock-Tube Study of Nitrogen Dissociation using Vacuum-Ultraviolet Light Absorption. *The Journal of Chemical Physics*, 48(2):599–608, 1968. doi:10.1063/1.1668690.

[71] Ronald K. Hanson and Donald Baganoff. Shock-Tube Study of Nitrogen Dissociation Rates Using Pressure Measurements. *AIAA Journal*, 10(2):211–215, 1972. doi:10.2514/3.50082.

[72] D.J. Kewley and H.G. Hornung. Free-piston shock-tube study of nitrogen dissociation. *Chemical Physics Letters*, 25(4):531–536, 1974. doi:10.1016/0009-2614(74)85360-1.

[73] Chul Park. Two-temperature interpretation of dissociation rate data for N_2 and O_2. In *26th Aerospace Sciences Meeting*, January 1988. doi:10.2514/6.1988-458.

[74] Richard L. Jaffe, Maninder Grover, Simone Venturi, David. W. Schwenke, Paolo Valentini, Thomas E. Schwartzentruber, and Marco Panesi. Comparison of potential energy surface and computed rate coefficients for n2 dissociation. *Journal of Thermophysics and Heat Transfer*, 32(4):869–881, 2018. doi:10.2514/1.T5417.

[75] Graham Candler and Joseph Olejniczak. Nitrogen dissociation rates in complex hypersonic flows. In *32^{nd} Thermophysics Conference*, 1997. doi:10.2514/6.1997-2500.

[76] Jason D. Bender, Paolo Valentini, Ioannis Nompelis, Yuliya Paukku, Zoltan Varga, Donald G. Truhlar, Thomas Schwartzentruber, and Graham V. Candler. An improved potential energy surface and multi-temperature quasiclassical trajectory calculations of $N_2 + N_2$ dissociation reactions. *The Journal of Chemical Physics*, 143(5):054304, 2015. doi:10.1063/1.4927571.

[77] R. L. Macdonald, R. L. Jaffe, D. W. Schwenke, and M. Panesi. Construction of a coarse-grain quasi-classical trajectory method. I. Theory and application to N_2 - N_2 system. *The Journal of Chemical Physics*, 148(5):054309, 2018. doi:10.1063/1.5011331.

[78] F. Esposito and M. Capitelli. Quasiclassical molecular dynamic calculations of vibrationally and rotationally state selected dissociation cross-sections: $N + N_2(v, J) \longrightarrow 3\,N$. *Chemical Physics Letters*, 302(1):49–54, 1999. doi:10.1016/S0009-2614(99)00099-8.

[79] Richard Jaffe, David Schwenke, and Galina Chaban. Vibration-Rotation Excitation and Dissociation in N_2 - N_2 Collisions from Accurate Theoretical Calculations. In *10th AIAA/ASME Joint Thermophysics and Heat Transfer Conference*, 2010. doi:10.2514/6.2010-4517.

[80] Annarita Laricchiuta, Mario Capitelli, Roberto Celiberto, and Gianpiero Colonna. *Dissociation and Ionization Cross Sections and Rate Coefficients of Air Molecules by Electron Impact: the Role of Vibrational Energy.* doi:10.2514/6.2006-2898.

[81] K. A. Berrington, P. G. Burke, and W. D. Robb. The scattering of electrons by atomic nitrogen. *Journal of Physics B: Atomic and Molecular Physics*, 8(15):2500–2511, Oct 1975. doi:10.1088/0022-3700/8/15/012.

[82] E. Brook, M. F. A. Harrison, and A. C. H. Smith. Measurements of the electron impact ionisation cross sections of He, C, O and N atoms. *Journal of Physics B: Atomic and Molecular Physics*, 11(17):3115–3132, Sep 1978. doi:10.1088/0022-3700/11/17/021.

[83] Yang Wang, Oleg Zatsarinny, and Klaus Bartschat. B-spline R-matrix-with-pseudostates calculations for electron-impact excitation and ionization of nitrogen. *Phys. Rev. A*, 89:062714, Jun 2014. doi:10.1103/PhysRevA.89.062714.

[84] HW Drawin. Atomic cross-sections for inelastic electronic collisions. *Report EURCEA-FC*, 1963.

[85] Hans-Werner Drawin. Zur formelmäßigen Darstellung des Ionisierungsquerschnitts für den Atom-Atomstoß und über die Ionen-Elektronen-Rekombination im dichten Neutralgas. *Zeitschrift für Physik A Hadrons and nuclei*, 211(2):404–4017, 1963. doi:10.1007/BF01379963.

[86] Marco Panesi, Thierry Magin, Anne Bourdon, Arnaud Bultel, and O. Chazot. Fire II Flight Experiment Analysis by Means of a Collisional-Radiative Model. *Journal of Thermophysics and Heat Transfer*, 23(2):236–248, 2009. doi:10.2514/1.39034.

[87] Christophe O. Laux and Charles H. Kruger. Arrays of radiative transition probabilities for the N_2 first and second positive, no beta and gamma, N_2^+ first negative, and O_2 Schumann-Runge band systems. *Journal of Quantitative Spectroscopy and Radiative Transfer*, 48(1):9–24, 1992. doi:10.1016/0022-4073(92)90003-M.

[88] Ellis E. Whiting and Ralph W. Nicholls. Reinvestigation of Rotational-Line Intensity Factors in Diatomic Spectra. *The Astrophysical Journal Supplement Series*, 27:1, Jan 1974. doi:10.1086/190286.

[89] Christopher Owen Johnston. *Nonequilibrium shock-layer radiative heating for Earth and Titan entry*. PhD thesis, Virginia Tech, 2006. url:`https://vtechworks.lib.vt.edu/handle/10919/29769`. Accessed: 2020-11-01.

[90] Chul Park. Calculation of radiation from argon shock layers. *Journal of Quantitative Spectroscopy and Radiative Transfer*, 28(1):29–40, 1982. doi:10.1016/0022-4073(82)90094-2.

[91] Hans R. Griem. Stark Broadening of Isolated Spectral Lines from Heavy Elements in a Plasma. *Phys. Rev.*, 128:515–523, Oct 1962. doi:10.1103/PhysRev.128.515.

[92] Hans R. Griem. *Spectral Line Broadening by Plasmas*. McGraw-Hill, 1964.

[93] Hans R. Griem. *Spectral Line Broadening by Plasmas*. Academic Press, 1st edition, January 1974.

[94] E. Biémont, Y. Frémat, and P. Quinet. Ionization Potentials of Atoms and Ions from Lithium to Tin ($Z = 50$). *Atomic Data and Nuclear Data Tables*, 71(1):117–146, 1999. doi:10.1006/adnd.1998.0803.

[95] T. Trickl, E. F. Cromwell, Y. T. Lee, and A. H. Kung. State-selective ionization of nitrogen in the $\mathrm{X}^2\Sigma_\mathrm{g}^+$ $v_+ = 0$ and $v_+ = 1$ states by two-color $(1+1)$ photon excitation near threshold. *The Journal of Chemical Physics*, 91(10):6006–6012, 1989. doi:10.1063/1.457417.

[96] E. M. Bahati, J. J. Jureta, D. S. Belic, H. Cherkani-Hassani, M. O. Abdellahi, and P. Defrance. Electron impact dissociation and ionization of N_2^+. *Journal of Physics B: Atomic, Molecular and Optical Physics*, 34(15):2963–2973, jul 2001. doi:10.1088/0953-4075/34/15/303.

[97] C. R. Cowley. An approximate Stark broadening formula for use in spectrum synthesis. *The Observatory*, 91:139–140, Aug 1971. `https://ui.adsabs.harvard.edu/abs/1971Obs....91..139C/abstract`.

[98] K.H. Wilson and W.E. Nicolet. Spectral absorption coefficients of carbon, nitrogen and oxygen atoms. *Journal of Quantitative Spectroscopy and Radiative Transfer*, 7(6):891–941, 1967. doi:10.1016/0022-4073(67)90005-2.

[99] E.E. Whiting. An empirical approximation to the Voigt profile. *Journal of Quantitative Spectroscopy and Radiative Transfer*, 8(6):1379–1384, 1968. doi:10.1016/0022-4073(68)90081-2.

[100] J.J. Olivero and R.L. Longbothum. Empirical fits to the Voigt line width: A brief review. *Journal of Quantitative Spectroscopy and Radiative Transfer*, 17(2):233–236, 1977. doi:10.1016/0022-4073(77)90161-3.

[101] I. N. Kadochnikov and I. V. Arsentiev. Modelling of vibrational nonequilibrium effects on the H_2-air mixture ignition under shock wave conditions in the state-to-state and mode approximations. *Shock Waves*, 30:491–504, 7 2020. doi:10.1007/s00193-020-00961-0.

[102] John D Anderson Jr. *Hypersonic and high-temperature gas dynamics*. American Institute of Aeronautics and Astronautics, 2nd edition, 2006. doi:10.2514/4.861956.

[103] Theodore Lyman. Victor Schumann. *The Astrophysical Journal*, 38:1, January 1914. doi:10.1086/142050.

[104] Brett A. Cruden. Recent Progress in Entry Radiation Measurements in the NASA Ames Electric ARC Shock Tube Facility. In 5^{th} *International Workshop on Radiation of High Temperature Gases in Atmospheric Entry Workshop*, Barcelona, October 2012. url:`https://ntrs.nasa.gov/search.jsp?R=20130001599`.

[105] Brett A. Cruden and Aaron M. Brandis. *Analysis of Shockwave Radiation Data in Nitrogen.* Jun 2019. doi:10.2514/6.2019-3359.

[106] Brett A Cruden and Aaron M Brandis. Updates to the neqair radiation solver. *Radiation in High Temperature Gases*, 2014. `https://ntrs.nasa.gov/api/citations/20150022164/downloads/20150022164.pdf`.

[107] Brett A. Cruden, Aaron M. Brandis, Jay H. Grinstead, Joseph Olejniczak, Lindsay Kirk, Randolph P. Lillard, Hideyuki Tanno, and Tomoyuki Komuro. *Measurement of Ultraviolet Radiative Heating Augmentation in HIEST Reflected Shock Tunnel.* Jun 2015. doi:10.2514/6.2015-2512.

[108] Aaron Brandis, Brett Cruden, Dinesh Prabhu, Deepak Bose, Matthew McGilvray, Richard Morgan, and Richard Morgan. *Analysis of Air Radiation Measurements Obtained in the EAST and X2 Shocktube Facilities.* Jun 2010. doi:10.2514/6.2010-4510.

[109] Satoshi Nomura, Taito Kawakami, and Kazuhisa Fujita. Nonequilibrium Effects in Precursor Electrons Ahead of Shock Waves. *Journal of Thermophysics and Heat Transfer*, 0(0):1–6, 2020. doi:10.2514/1.T6057.

[110] Gouji Yamada, Mizuki Kajino, and Kiyonobu Ohtani. Experimental and numerical study on radiating shock tube flows for spacecraft reentry flights. *Journal of Fluid Science and Technology*, 14(3):JFST0022–JFST0022, 2019. doi:10.1299/jfst.2019jfst0022.

[111] D.W. Bogdanoff and C. Park. Radiative interaction between driver and driven gases in an arc-driven shock tube. *Shock Waves*, 12:205–214, Nov 2002. doi:10.1007/s00193-002-0157-y.

[112] Christophe O Laux. Radiation and nonequilibrium collisional-radiative models. *von Karman Institute Lecture Series*, 7, 2002.

[113] J. L. Dunham. The Energy Levels of a Rotating Vibrator. *Phys. Rev.*, 41:721–731, Sep 1932. doi:10.1103/PhysRev.41.721.

[114] Ragnar Rydberg. Graphische Darstellung einiger bandenspektroskopischer Ergebnisse. *Zeitschrift für Physik*, 73(5):376–385, May 1932. doi:10.1007/BF01341146.

[115] Ragnar Rydberg. Über einige Potentialkurven des Quecksilberhydrids. *Zeitschrift für Physik*, 80(7):514–524, Feb 1933. doi:10.1007/BF02057312.

[116] O. Klein. Zur Berechnung von Potentialkurven für zweiatomige Moleküle mit Hilfe von Spektraltermen. *Zeitschrift für Physik*, 76(3):226–235, Mar 1932. doi:10.1007/BF01341814.

[117] A. L. G. Rees. The calculation of potential-energy curves from band-spectroscopic data. *Proceedings of the Physical Society*, 59(6):998–1008, nov 1947. doi:10.1088/0959-5309/59/6/310.

[118] Mark S Child. *Semiclassical mechanics with molecular applications.* Oxford University Press, USA, 2014. doi:10.1093/acprof:oso/9780199672981.001.0001.

[119] Hugh M. Hulburt and Joseph O. Hirschfelder. Potential Energy Functions for Diatomic Molecules. *The Journal of Chemical Physics*, 9(1):61–69, 1941. doi:10.1063/1.1750827.

[120] Philip Huxley and John N. Murrell. Ground-state diatomic potentials. *J. Chem. Soc., Faraday Trans. 2*, 79:323–328, 1983. doi:10.1039/F29837900323.

[121] Alf Lofthus and Paul H. Krupenie. The Spectrum of Molecular Nitrogen. *Journal of Physical and Chemical Reference Data*, 6(1):113–307, 1977. doi:10.1063/1.555546.

[122] Harry Partridge, Stephen R. Langhoff, Charles W. Bauschlicher, and David W. Schwenke. Theoretical study of the $\mathrm{A}'^5\Sigma_\mathrm{g}^+$ and $\mathrm{C}''^5\Pi_\mathrm{u}$ states of N_2: Implications for the N_2 afterglow. *The Journal of Chemical Physics*, 88(5):3174–3186, 1988. doi:10.1063/1.453962.

[123] Sophie Chauveau. *Constitution de bases de données spectroscopiques relatives à un plasma d'air : application au calcul de transferts radiatifs.* PhD thesis, École centrale de Paris, 2001. Thèse de doctorat dirigée par Perrin, Marie-Yvonne Energétique Châtenay-Malabry, url:`http://www.theses.fr/2001ECAP0697`. Accessed: 2020-09-14.

[124] Russ R. Laher and Forrest R. Gilmore. Improved Fits for the Vibrational and Rotational Constants of Many States of Nitrogen and Oxygen. *Journal of Physical and Chemical Reference Data*, 20(4):685–712, 1991. doi:10.1063/1.555892.

[125] Ch. Ottinger and A. F. Vilesov. Laser spectroscopy of perturbed levels in $\mathrm{N_2(B^3\Pi_g},v = 10)$ and the first experimental determination of the $\mathrm{N_2(A'^5\Sigma_g^+)}$ term energy. *The Journal of Chemical Physics*, 100(7):4862–4869, 1994. doi:10.1063/1.467206.

[126] K. P. Huber and G. Herzbeg. *Molecular Spectra and Molecular Structure: IV. Constants of Diatomic Molecules.* Van Nostrand Reinhold Company, New York, 1979. doi:10.1007/978-1-4757-0961-2.

[127] J.W. McGowan. *The Excited State in Chemical Physics, Part 2*, volume 45 of *Advances in Chemical Physics.* Wiley, 2009. url:`https://www.wiley.com/en-us/Excited+State+in+Chemical+Physics%2C+Part+2%2C+Volume+45-p-9780470143100`.

[128] M. Hochlaf, H. Ndome, and D. Hammoutène. Quintet electronic states of N_2. *The Journal of Chemical Physics*, 132(10):104310, 2010. doi:10.1063/1.3359000.

[129] K. P. Huber and M. Vervloet. High-Resolution Fourier Transform Spectroscopy of Supersonic Jets. The $C''^5\Pi_u \rightarrow A'^5\Sigma_g^+$ Herman Infrared Bands of $^{14}N_2$. *Journal of Molecular Spectroscopy*, 153(1):17–25, 1992. doi:10.1016/0022-2852(92)90453-U.

[130] Z. Qin, J.M. Zhao, and L.H. Liu. Radiative transition probabilities for the main diatomic electronic systems of N_2, N_2^+, NO, O_2, CO, CO^+, CN, C_2 and H_2 produced in plasma of atmospheric entry. *Journal of Quantitative Spectroscopy and Radiative Transfer*, 202:286–301, 2017. doi:10.1016/j.jqsrt.2017.08.010.

[131] Z. Qin, J.M. Zhao, and L.H. Liu. Supplemental data of our research paper "Radiative transition probabilities for the main diatomic electronic systems of N_2, N_2^+, NO, O_2, CO, CO^+, CN, C_2 and H_2 produced in plasma of atmospheric entry". url:`https://www.researchgate.net/publication/337928363_Supplemental_datarar`. Accessed: 2020-04-01.

[132] Heiko Liebhart, Markus Fertig, Georg Herdrich, and Hans-Peter Röser. *Contribution of Vacuum-Ultraviolet Transitions of Molecular Nitrogen to Radiation During Atmospheric Reentry.* 2010. doi:10.2514/6.2010-4774.

[133] Lawrence G. Piper. The excitation of $N(^2P)$ by $N_2(A^3\Sigma_u^+, v' = 0, 1)$. *The Journal of Chemical Physics*, 90(12):7087–7095, 1989. doi:10.1063/1.456237.

[134] Ch. Ottinger, L. G. Smirnova, and A. F. Vilesov. Collision-induced transitions from $N_2(A'^5\Sigma_g^+)$ to $N_2(B^3\Pi_g)$ via the gateway mechanism. *The Journal of Chemical Physics*, 100(7):4848–4861, 1994. doi:10.1063/1.467205.

[135] D. Levron and A. V. Phelps. Quenching of $N_2(A^3\Sigma_u^+, v = 0,\ 1)$ by N_2, Ar, and H_2. *The Journal of Chemical Physics*, 69(5):2260–2262, 1978. doi:10.1063/1.436788.

[136] Lawrence G. Piper. State-to-state $N_2(A^3\Sigma_u^+)$ energy pooling reactions. II. The formation and quenching of $N_2(B^3\Pi_g, v' = 1\text{–}12)$. *The Journal of Chemical Physics*, 88(11):6911–6921, 1988. doi:10.1063/1.454388.

[137] Lawrence G. Piper. State-to-state $N_2(A^3\Sigma_u^+)$ energy-pooling reactions. I. The formation of $N_2(C^3\Pi_u)$ and the Herman infrared system. *The Journal of Chemical Physics*, 88(1):231–239, 1988. doi:10.1063/1.454649.

[138] W. Freysinger, F. A. Khan, P. B. Armentrout, P. Tosi, O. Dmitriev, and D. Bassi. Charge-transfer reaction of $^{14.15}N^+(^3P_J) + N_2(^1\Sigma_g^+)$ from thermal to 100 eV. Crossed-beam and scattering-cell guided-ion beam experiments. *The Journal of Chemical Physics*, 101(5):3688–3695, 1994. doi:10.1063/1.467553.

[139] V. Laporta, D. A. Little, R. Celiberto, and J. Tennyson. Electron-impact resonant vibrational excitation and dissociation processes involving vibrationally excited N_2 molecules. *Plasma Sources Science and Technology*, 23(6):065002, aug 2014. doi:10.1088/0963-0252/23/6/065002.

[140] Phys4Entry - Planetary Entry Integrated Models - Seventh Framework Programme. url:`http://phys4entrydb.ba.imip.cnr.it/Phys4EntryDB/`. Accessed: 2019-12-15.

[141] M. Brunger, S. J. Buckman, and M. T. Elford. *6.4 Excitation cross sections*, volume 17C, chapter 6 Cross sections for scattering- and excitation-processes in electron-molecule collisions. Springer-Verlag Berlin Heidelberg, 2003. doi:10.1007/10874891_7.

[142] Charles P. Malone, Paul V. Johnson, Xianming Liu, Bahar Ajdari, Isik Kanik, and Murtadha A. Khakoo. Integral cross sections for the electron-impact excitation of the $b^1\Pi_u$, $c_3{}^1\Pi_u$, $o_3{}^1\Pi_u$, $b'^1\Sigma_u^+$, $c_4'{}^1\Sigma_u^+$, $G^3\Pi_u$ and $F^3\Pi_u$ states of N_2. *Phys. Rev. A*, 85:062704, Jun 2012. doi:10.1103/PhysRevA.85.062704.

[143] Yukikazu Itikawa. Cross Sections for Electron Collisions with Nitrogen Molecules. *Journal of Physical and Chemical Reference Data*, 35(1):31–53, 2006. doi:10.1063/1.1937426.

[144] D. H. Crandall, W. E. Kauppila, R. A. Phaneuf, Paul O. Taylor, and Gordon H. Dunn. Absolute cross sections for electron-impact excitation of N_2^+. *Phys. Rev. A*, 9:2545–2551, Jun 1974. doi:10.1103/PhysRevA.9.2545.

[145] M. Capitelli, R. Celiberto, A. Eletskii, and A. Laricchiuta. Electron-molecule dissociation cross-sections of H_2, N_2 and O_2 in different vibrational levels. In *Atomic and Plasma-material Interaction Data for Fusion (IAEA)*, number 9, pages 47–64. International Atomic Energy Agency, Vienna, 2001. url:`https://www.iaea.org/publications/6321/atomic-and-plasma-material-interaction-data-for-fusion`. Accessed: 2020-09-14.

[146] Steven L. Guberman. The vibrational dependence of dissociative recombination: Rate constants for N_2^+. *The Journal of Chemical Physics*, 141(20):204307, 2014. doi:10.1063/1.4901892.

Appendix A

Spectroscopy: the internal energy of a diatomic molecular particle

There are three contributions to the internal energy: vibrational energy G_v, rotational energy F_{vJ}, and electronic sensible energy T_e [112]. The letters v and J subscripted in the symbols G_v and F_{vJ}, denote the vibrational and rotational quantum numbers of the molecule, respectively ($v = 0$, 1, 2, ... and $J = 0$, 1, 2, ...). The letter e subscripted in the symbol T_e denotes the electronic level per se, and not an electronic quantum number. Note that although e doesn't appear in the G_v and F_{vJ} notations, these quantities also depend on it. The *rovibrational energy*, the *vibronic energy* and the *rovibronic energy* are given by $T_{vJ} = G_v + F_{vJ}$, $T_{ev} = T_e + G_v$, and $T_{evJ} = T_e + G_v + F_{vJ}$, respectively. The first one can be expressed through an infinite series known as *Dunham expansion* [113]:

$$T_{vJ} = \sum_{i,j=0}^{\infty} Y_{ij} \left(v + \frac{1}{2}\right)^i \left[J\left(J+1\right)\right]^j \ , \tag{A.1}$$

where Y_{ij} are the *Dunham parameters*. The vibrational and rotational energies are according to (A.1)

$$G_v = T_{v0} = \sum_{i=0}^{\infty} Y_{i0} \left(v + \frac{1}{2}\right)^i = Y_{00} + \omega_e \left(v + \frac{1}{2}\right) - \omega_e x_e \left(v + \frac{1}{2}\right)^2 + \omega_e y_e \left(v + \frac{1}{2}\right)^3 + \omega_e z_e \left(v + \frac{1}{2}\right)^4 + \ldots \ , \tag{A.2}$$

$$F_{vJ} = T_{vJ} - G_v = \sum_{\substack{i=0 \\ j=1}}^{\infty} Y_{ij} \left(v + \frac{1}{2}\right)^i \left[J\left(J+1\right)\right]^j = B_v J\left(J+1\right) - D_v \left[J\left(J+1\right)\right]^2 + H_v \left[J\left(J+1\right)\right]^3 + \ldots \ , \tag{A.3}$$

respectively, being the function B_v introduced in (A.3) given by

$$B_v = \sum_{i=0}^{\infty} Y_{i1} \left(v + \frac{1}{2}\right)^i = B_e - \alpha_e \left(v + \frac{1}{2}\right) + \gamma_e \left(v + \frac{1}{2}\right)^2 + \delta_e \left(v + \frac{1}{2}\right)^3 + \eta_e \left(v + \frac{1}{2}\right)^4 + \ldots \ . \tag{A.4}$$

The constants multiplying the monomials in (A.2) and (A.4) are the so-called *spectroscopic constants* corresponding apart from sign to Dunham parameters Y_{ij}.

A.1 General procedure for obtaining vibrational energy levels

If all the Dunham parameters Y_{i0} (which correspond to an infinite set) in equation (A.2) were known, the vibrational energy G_v would be well defined for all vibrational quantum numbers. But the truth is that only a finite set of parameters can be obtained from experiment, making the series only valid for the first quantum numbers. To obtain the vibrational energies for all of the allowable vibrational quantum numbers, a more reliable method should be considered, as is example the Fourier Grid Hamiltonian method (FGH) [63]. This method consists in a numerical algorithm that determines the eigenenergies and eigenfunctions of the system described by the so-called *radial Schrödinger equation*. Note, however, that this requires the knowledge of the internuclear potential energy function $V(r)$. The Rydberg [114, 115]–Klein [116]–Rees [117] method (RKR), which is based on Semiclassical Mechanics, allows the determination of $V(r)$ from the spectroscopic constants of the diatomic molecule. The book of Child [118] explains the foundations of the method within a great detail. Note that the obtained potential is only valid within the interval of internuclear separations r for which it doesn't surpass the maximum vibrational energy value described by the spectroscopic constants. The non-supported parts of the potential $V(r)$ can be obtained through extrapolation. The supported part of the potential, $V_{\mathrm{RKR}}(r)$, corresponds to the middle of the desired full curve and, therefore, the short-range (left) part needs to be extrapolated as well as the long-range (right) one. Let $V_{\mathrm{sr}}(r)$ be the former and $V_{\mathrm{lr}}(r)$ the latter. The short-range part of the potential was assumed to have the form of a "repulsive monomial" $V_{\mathrm{sr}}(r) = \alpha r^{-\beta}$, being α and β two positive constants determined by fitting the curve $V_{\mathrm{sr}}(r)$ to the three leftest points repulsive part of $V_{\mathrm{RKR}}(r)$. The long-range part of the potential was assumed to have the form of a *Hulburt-Hirschfelder potential* [119] $V_{\mathrm{HH}}(r)$ or an *Extended Rydberg potential* [120] $V_{\mathrm{ER}}(r)$, being their parameters fitted to the three rightest points repulsive part of $V_{\mathrm{RKR}}(r)$. In contrast with the Extended Rydberg potential, the fit resultant Hulburt-Hirschfelder potential may express an upward "bump" at the right of the potential well[1], which may or may not exist in reality. If it is known that such "bump" doesn't exist in reality[2], then the Extended Rydberg potential should be considered instead.

A.2 Potential curves for N_2 in its different electronic levels

Potential curves $V(r)$ for the electronic levels $\mathrm{X}^1\Sigma_\mathrm{g}^+$, $\mathrm{A}^3\Sigma_\mathrm{u}^+$, $\mathrm{B}^3\Pi_\mathrm{g}$, $\mathrm{W}^3\Delta_\mathrm{u}$, $\mathrm{B}'^3\Sigma_\mathrm{u}^-$, $\mathrm{a}'^1\Sigma_\mathrm{u}^-$, $\mathrm{a}^1\Pi_\mathrm{g}$, $\mathrm{w}^1\Delta_\mathrm{u}$, $\mathrm{A}'^5\Sigma_\mathrm{g}^+$, $\mathrm{C}^3\Pi_\mathrm{u}$, $\mathrm{b}^1\Pi_\mathrm{u}$, $\mathrm{c}_3{}^1\Pi_\mathrm{u}$, $\mathrm{c}_4'{}^1\Sigma_\mathrm{u}^+$, $\mathrm{b}'^1\Sigma_\mathrm{u}^+$ and $\mathrm{o}_3{}^1\Pi_\mathrm{u}$ of the nitrogen molecule N_2 were obtained. All curves were constructed by application of the RKR method and posterior extrapolation. Values for the Dunham parameters which are the input variables of the RKR method, were required. Table A.1 shows such values, being taken from the literature. The potential curves $V_e(r) = V(r) + T_e$ obtained for each of the electronic levels of molecular nitrogen N_2, are depicted in Figure A.1. All of the dissociation products shown in Figure A.1 were taken from reference [121] with the exception of the one associated to the electronic level $\mathrm{A}'^5\Sigma_\mathrm{g}^+$, which was taken from reference [122].

---

[1] The states of the molecule associated to this "bump" are called *quasi-bound states*.

[2] To verify if the molecule assumes, or not, quasi-bound states, accurate potentials in the literature, which correspond the curves that the author intend to reconstruct, were reviewed.

Table A.1: Sensible electronic energy T_e, potential well depth D_e, equilibrium internuclear separation r_e, maximum vibrational quantum number $v_{\max}$ for which the respective Dunham expansion is valid, Dunham parameters Y_{i0} with $i = 0, 1, ..., 6$ and Y_{i1} with $i = 0, 1, ..., 4$ and the shape of the extrapolated long-range part of the potential $V_{\rm lr}$ of the different electronic levels of molecular nitrogen N_2.

e	$X^1\Sigma_g^+$	$A^3\Sigma_u^+$	$B^3\Pi_g$	$W^3\Delta_u$	$B'^3\Sigma_u^-$	$a'^1\Sigma_u^-$	$a^1\Pi_g$	$w^1\Delta_u$	$A'^5\Sigma_g^+$	$C^3\Pi_u$	$b^1\Pi_u$	$c_3{}^1\Pi_u$	$c_4'{}^1\Sigma_u^+$	$b'^1\Sigma_u^+$	$o_3{}^1\Pi_u$
Ref. for T_e	[123] (a)	[123] (a)	[123] (a)	[124] (a)	[124] (a)	[124] (a)	[124] (a)	[124] (a)	[125]	[123] (a)	[123] (a)	[123] (a)	[123] (a)	[123] (a)	[123] (a)
T_e [“cm^{-1}”]	0.00	50203.66	59618.77	59805.85	66271.53	68152.79	69283.34	72097.31	75990.03	89137.92	101660.02	104217.77	104418.37	105215.38	105873.81
Ref. for D_e	[123] (b)	[123] (b)	[123] (b)	[121] (b)	[121] (b)	[121] (b)	[121] (b)	[121] (b)	[122]	[123] (b)	[123] (b)	[123] (b)	[123] (b)	[123] (b)	[123] (b)
D_e [“cm^{-1}”]	79886.67	29686.89	39499.33	39308.13	42456.54	50186.28	49055.63	46241.86	3450.00	9980.02	16677.65	47196.90	87946.60	24185.10	88858.57
Ref. for r_e	[126]	[126]	[126]	[127]	[121]	[121]	[121]	[121]	[128]	[126]	[126]	[126]	[126]	[126]	[126]
r_e [Å]	1.09768	1.28660	1.21260	1.28	1.27838	1.27542	1.22025	1.26883	1.60840	1.14860	1.28400	1.11630	1.10800	1.44390	1.17840
Ref. for $v_{\max}$	[123]	[123]	[123]	[124]	[124]	[124]	[124]	[124]	This work (c)	[123]	[123]	[123]	[123]	[123]	[123]
$v_{\max}$	15	16	21	11	17	18	14	5	5	4	19	4	8	28	4
Ref. for Y_{i0}	[123]	[123]	[123]	[124]	[124]	[124]	[124]	[124]	(c)	[123]	[123]	[123]	[123]	[123]	[123]
Y_{00} [“cm^{-1}”]	7.30(−2)	−1.89(−1)	−8.30(−2)	—	1.38(−1)	1.67(−1)	1.20(−2)	1.05(−1)	−2.50(−2)	−1.79(0)	6.53(0)	3.90(0)	7.27(−1)	2.89(−1)	4.24(0)
Y_{10} [“cm^{-1}”]	2.36(3)	1.46(3)	1.73(3)	1.51(3)	1.52(3)	1.53(3)	1.69(3)	1.56(3)	7.31(2)	2.05(3)	6.42(2)	2.20(3)	2.17(3)	7.59(2)	1.97(3)
Y_{20} [“cm^{-1}”]	−1.43(1)	−1.40(1)	−1.44(1)	−1.26(1)	−1.22(1)	−1.21(1)	−1.39(1)	−1.20(1)	−1.09(1)	−2.89(1)	2.17(1)	−2.56(1)	−1.33(1)	−3.40(0)	−1.09(1)
Y_{30} [“cm^{-1}”]	−3.31(−3)	2.40(−2)	−3.30(−3)	3.09(−2)	4.19(−2)	4.13(−2)	7.94(−3)	4.54(−2)	−2.25(0)	2.25(0)	−1.41(0)	—	−2.94(−1)	1.78(−2)	—
Y_{40} [“cm^{-1}”]	−1.95(−4)	2.56(−3)	−7.90(−4)	−7.10(−4)	−7.30(−4)	−2.9(−4)	2.9(−4)	—	—	−5.51(−1)	2.29(−2)	—	—	−1.78(−3)	—
Y_{50} [“cm^{-1}”]	—	—	4.20(−5)	—	—	—	—	—	—	—	—	—	—	—	—
Y_{60} [“cm^{-1}”]	—	—	1.68(−6)	—	—	—	—	—	—	—	—	—	—	—	—
Ref. for Y_{i1}	[123]	[123]	[123]	[124]	[124]	[124]	[124]	[124]	[128]	[123]	[123]	[123]	[123]	[123]	[123]
Y_{01} [“cm^{-1}”]	2.00(0)	1.45(0)	1.64(0)	1.47(0)	1.47(0)	1.48(0)	1.62(0)	1.50(0)	9.31(−1)	1.83(0)	1.39(0)	1.98(0)	1.93(0)	1.16(0)	1.73(0)
Y_{11} [“cm^{-1}”]	−1.73(−2)	−1.75(−2)	−1.79(−2)	−1.70(−2)	−1.67(−2)	−1.66(−2)	−1.79(−2)	−1.63(−2)	−1.71(−2)	−2.40(−2)	−1.42(−2)	−3.80(−2)	−1.96(−2)	−1.04(−2)	−2.75(−2)
Y_{21} [“cm^{-1}”]	−3.01(−5)	−1.40(−4)	−1.00(−4)	−1.01(−5)	1.84(−5)	2.41(−5)	−2.93(−5)	—	—	1.90(−3)	−5.21(−4)	—	—	3.90(−4)	—
Y_{31} [“cm^{-1}”]	−6.93(−8)	—	5.00(−6)	3.30(−7)	−4.50(−7)	—	—	—	—	−6.00(−4)	—	—	—	−1.73(−5)	—
Y_{41} [“cm^{-1}”]	—	—	2.10(−7)	—	—	—	—	—	—	—	—	—	—	—	—
$V_{\rm lr}$	$V_{\rm HH}$	$V_{\rm ER}$	$V_{\rm ER}$	$V_{\rm ER}$	$V_{\rm ER}$	$V_{\rm ER}$	$V_{\rm ER}$	$V_{\rm ER}$	$V_{\rm HH}$	$V_{\rm HH}$	$V_{\rm ER}$	(d)	(d)	$V_{\rm ER}$	(d)

The number between parenthesis in the Y_{i0} and Y_{i1} cells correspond to the orders of magnitude of these quantities.

[a] This reference only reports the value for $\Delta T_{e0} := T_{e0} - T_{X0}$, in which T_{e0} is the quantity $T_{ev} = T_e + G_v$ with $v = 0$ for the electronic level e, and T_{X0} is the homologous quantity for the ground electronic level X. Therefore, and sticking with the introduced notation, one can obtain T_e by using the relation $T_e = \Delta T_{e0} + G_0^X - G_0^e$.

[b] This reference only reports the value for the dissociation energy $D_0 := D_e - G_0$, and therefore the potential well depth needs to be computed using the relation $D_e = D_0 + G_0$.

[c] The values for Y_{i0}, with $i = 0, 1, ..., 3$ for the case $e = A'^5\Sigma_g^+$ were obtained by fitting the vibrational energies values G_v, with $v = 0, 1, ..., 5$, taken from the literature, considering as fitting function a Dunham expansion of third order, i.e. $G_v = \sum_{i=0}^{3} Y_{i0} \left(v + \frac{1}{2}\right)^i$, with Y_{00} approximated by [118] $\frac{B_e}{4} + \frac{\alpha_e \omega_e}{12 B_e} + \frac{(\alpha_e \omega_e)^2}{144 B_e^3} - \frac{\omega_e x_e}{4}$. The G_0 value was taken from [129], and the others G_v values were taken from [128] (note that in the article these appear subtracted by G_0).

[d] Since it is known that the potential curve for this electronic level doesn't have a conventional shape like the $V_{\rm HH}(r)$ or $V_{\rm ER}(r)$ curves, and its dissociation products weren't already determined, no attempt to extrapolate the RKR potential was performed. Therefore, it was assumed that the dissociation of the molecule in this electronic level doesn't occur, and only the vibrational levels restrained to RKR determined part may be accessed.

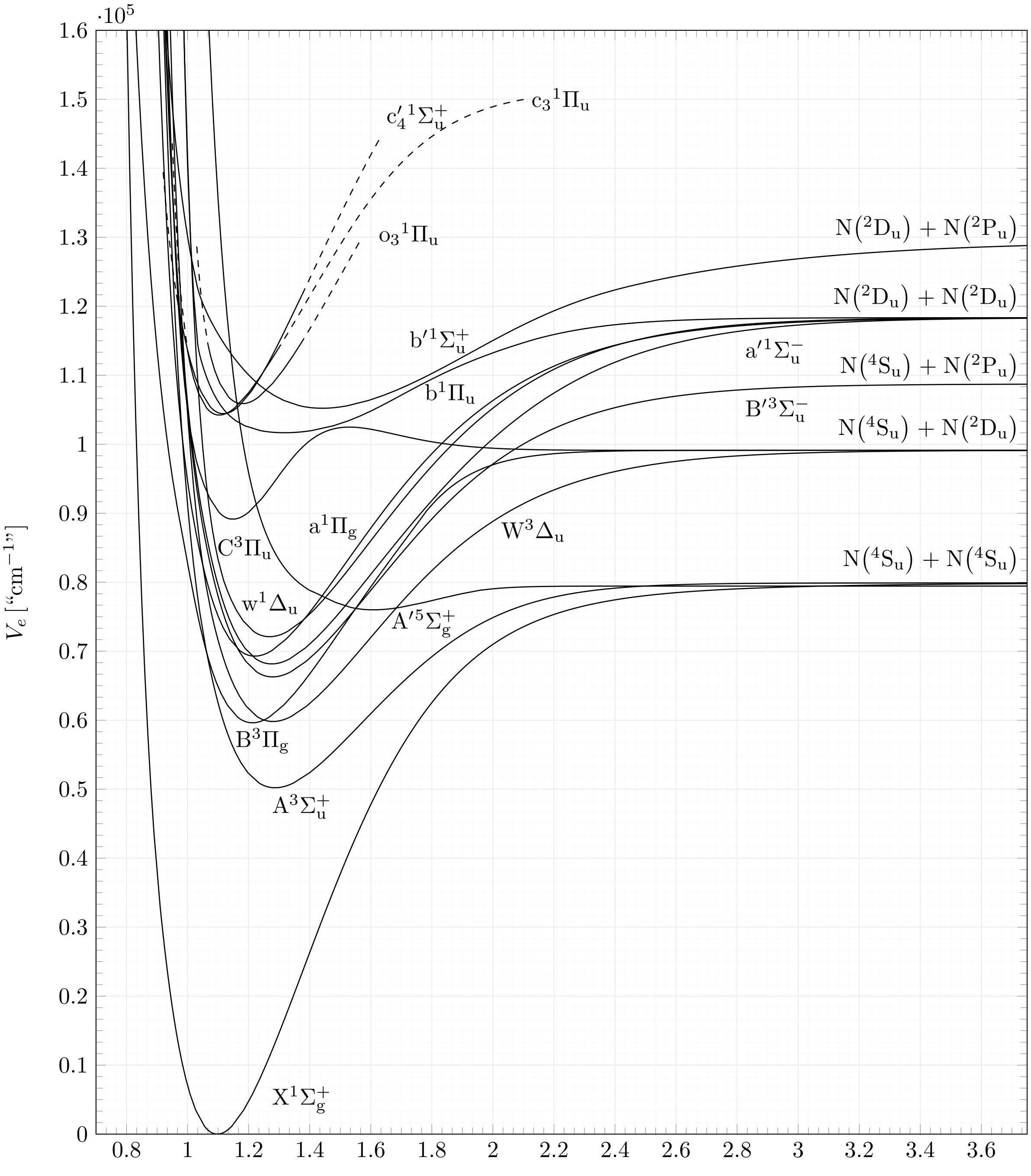

Figure A.1: Full reconstructed potential curves $V_e(r) = T_e + V(r)$ for the different electronic levels of the nitrogen molecule N_2. The terms $N(^4S_u) + N(^4S_u)$, $N(^4S_u) + N(^2D_u)$, $N(^4S_u) + N(^2P_u)$, $N(^2D_u) + N(^2D_u)$ and $N(^2D_u) + N(^2P_u)$ represent the dissociation products of the nitrogen molecule in the electronic levels associated to the immediately below potential curves.

A.3 Potential curves for N_2^+ in its different electronic levels

All the data required to obtain the potential curves $V(r)$ for the different electronic levels of the nitrogen molecular ion N_2^+, is found in Table A.2. The considered electronic levels for this species were $X^2\Sigma_g^+$, $A^2\Pi_u$, $B^2\Sigma_u^+$, $D^2\Pi_g$ and $C^2\Sigma_u^+$. The resultant potential curves $V_e(r) = V(r) + T_e$, are depicted in Figure A.2. All of the dissociation products shown in Figure A.2 were taken from reference [121].

Table A.2: Sensible electronic energy T_e, potential well depth D_e, equilibrium internuclear separation r_e, maximum vibrational quantum number $v_{\max}$ for which the respective Dunham expansion is valid, Dunham parameters Y_{i0} with $i = 0, 1, ..., 7$ and Y_{i1} with $i = 0, 1, ..., 3$ and the shape of the extrapolated long-range part of the potential V_{lr} of the different electronic levels of nitrogen molecular ion N_2^+.

e	$\mathrm{X}^2\Sigma_\mathrm{g}^+$	$\mathrm{A}^2\Pi_\mathrm{u}$	$\mathrm{B}^2\Sigma_\mathrm{u}^+$	$\mathrm{D}^2\Pi_\mathrm{g}$	$\mathrm{C}^2\Sigma_\mathrm{u}^+$
Ref. for T_e	[123] (a)	[123] (a)	[123] (a)	[121] (a)	[123] (a)
T_e [“cm^{-1}”]	0.00	9167.34	25462.43	52814.06	64610.79
Ref. for D_e	[123] (b)	[123] (b)	[123] (b)	[121] (b)	[123] (b)
D_e [“cm^{-1}”]	71368.43	62201.49	45903.08	18557.87	25988.34
Ref. for r_e	[126]	[126]	[126]	[121]	[126]
r_e [Å]	1.11642	1.17490	1.07400	1.47082	1.26200
Ref. for $v_{\max}$	[123]	[123]	[123]	—	[123]
$v_{\max}$	21	27	8	5	6
Ref. for Y_{i0}	[123]	[123]	[123]	[121]	[123]
Y_{00} [“cm^{-1}”]	−1.20(−1)	1.70(−2)	−1.43(0)	1.67(−1)	−1.80(0)
Y_{10} [“cm^{-1}”]	2.21(3)	1.90(3)	2.42(3)	9.12(2)	2.07(3)
Y_{20} [“cm^{-1}”]	−1.62(1)	−1.51(1)	−2.41(1)	−1.26(1)	−8.30(0)
Y_{30} [“cm^{-1}”]	4.00(−3)	1.12(−2)	−3.00(−1)	5.55(−2)	−6.30(−1)
Y_{40} [“cm^{-1}”]	−6.10(−3)	−2.70(−4)	−6.67(−2)	—	1.30(−2)
Y_{50} [“cm^{-1}”]	3.90(−4)	—	—	—	—
Y_{60} [“cm^{-1}”]	−1.40(−5)	—	—	—	—
Y_{70} [“cm^{-1}”]	2.00(−7)	—	—	—	—
Ref. for Y_{i1}	[123]	[123]	[123]	[121]	[123]
Y_{01} [“cm^{-1}”]	1.93(0)	1.74(0)	2.09(0)	1.11(0)	1.51(0)
Y_{11} [“cm^{-1}”]	−1.88(−2)	−1.87(−2)	−2.12(−2)	−2.00(−2)	1.00(−3)
Y_{21} [“cm^{-1}”]	−6.77(−5)	−6.00(−5)	−5.00(−4)	—	−1.50(−3)
Y_{31} [“cm^{-1}”]	−2.32(−6)	−1.10(−6)	−8.80(−5)	—	6.00(−5)
V_{lr}	V_{ER}	V_{ER}	V_{ER}	V_{ER}	V_{HH}

The number between parenthesis in the Y_{i0} and Y_{i1} cells correspond to the orders of magnitude of these quantities.

[a] This reference only reports the value for $\Delta T_{e0} := T_{e0} - T_{\mathrm{X}0}$, in which T_{e0} is the quantity $T_{ev} = T_e + G_v$ with $v = 0$ for the electronic level e, and $T_{\mathrm{X}0}$ is the homologous quantity for the ground electronic level X. Therefore, and sticking with the introduced notation, one can obtain T_e by using the relation $T_e = \Delta T_{e0} + G_0^X - G_0^e$.

[b] This reference only reports the value for the dissociation energy $D_0 := D_e - G_0$, and therefore the potential well depth needs to be computed using the relation $D_e = D_0 + G_0$.

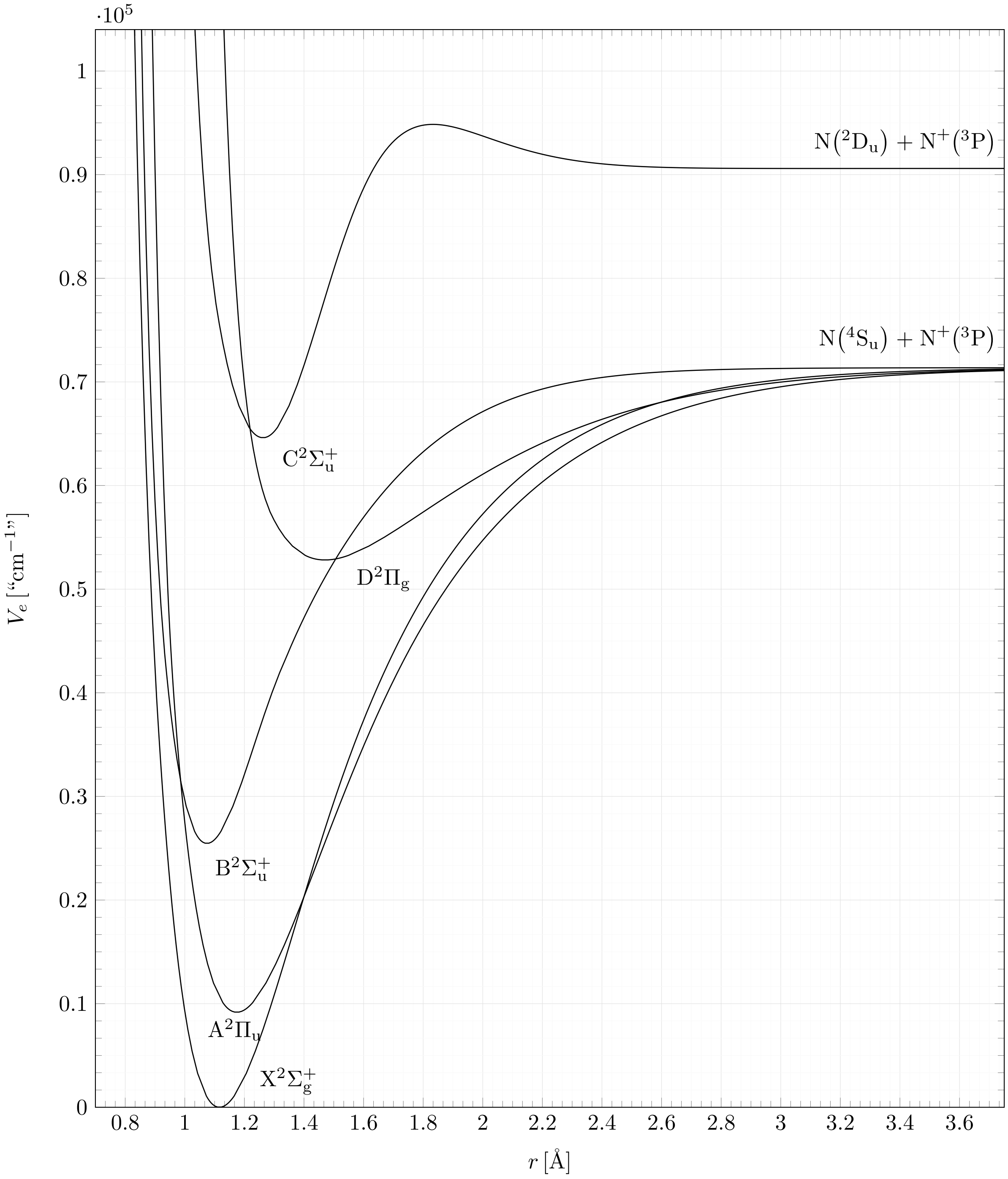

Figure A.2: Full reconstructed potential curves $V_e(r) = T_e + V(r)$ for the different electronic levels of the nitrogen molecular ion N_2^+. The terms $N(^4S_u) + N^+(^3P)$ and $N(^2D_u) + N^+(^3P)$ represent the dissociation products of the nitrogen molecular ion in the electronic levels associated to the immediatly below potential curves.

Appendix B

The database of kinetic processes

Tables B.1 to B.4 present the database of kinetic processes developed in this work.

Table B.1: Molecular spontaneous emission processes for which Einstein coefficients were obtained. The symbol after the reference in the column “Reference” represents the quantity which was extracted from it: Einstein coefficient (if A) or sum of the electronic-vibrational transition moments (if $\sum R_e^2$).

Species	Electronic system	e - e'	$(v_{\max}, v'_{\max})$	Reference
N_2	Vegard-Kaplan	$A^3\Sigma_u^+$ - $X^1\Sigma_g^+$	$(21, 21)$	[130] - A (from [131])
	First positive	$B^3\Pi_g$ - $A^3\Sigma_u^+$	$(21, 21)$	[87] - A
	Wu-Benesch	$W^3\Delta_u$ - $B^3\Pi_g$	$(21, 17)$	[130] - A (from [131])
	IR afterglow	$B'^3\Sigma_u^-$ - $B^3\Pi_g$	$(21, 21)$	[130] - A (from [131])
	Lyman-Birge-Hopfield	$a^1\Pi_g$ - $X^1\Sigma_g^+$	$(21, 21)$	[130] - A (from [131])
	Second positive	$C^3\Pi_u$ - $B^3\Pi_g$	$(4, 21)$	[87] - A
	Birge-Hopfield I	$b^1\Pi_u$ - $X^1\Sigma_g^+$	$(24, 60)$	[132] - $\sum R_e^2$
	Worley-Jenkins	$c_3{}^1\Pi_u$ - $X^1\Sigma_g^+$	$(11, 60)$	[132] - $\sum R_e^2$
	Carroll-Yoshino	$c_4'{}^1\Sigma_g^+$ - $X^1\Sigma_g^+$	$(11, 60)$	[132] - $\sum R_e^2$
	Birge-Hopfield II	$b'^1\Sigma_u^+$ - $X^1\Sigma_g^+$	$(46, 60)$	[132] - $\sum R_e^2$
	Worley	$o_3{}^1\Pi_u$ - $X^1\Sigma_g^+$	$(21, 60)$	[132] - $\sum R_e^2$
N_2^+	Meinel	$A^2\Pi_u$ - $X^2\Sigma_g^+$	$(27, 27)$	[130] - A (from [131])
	First negative	$B^2\Sigma_u^+$ - $X^2\Sigma_g^+$	$(12, 21)$	[87] - A
	Second negative	$C^2\Sigma_u^+$ - $X^2\Sigma_g^+$	$(6, 27)$	[130] - A (from [131])

Table B.2: Atomic spontaneous emission processes for which Einstein coefficients were computed.

Species	Number of processes	Reference
N	279 ([a])	NIST[64]
N^+	276 ([a])	NIST[64]

[a] As a reminder to the reader: representative Einstein coefficients were computed considering the lumping procedure performed on the split electronic levels.

Table B.3: Collisional processes due to heavy particle impact for which forward rate constants were obtained. The symbol after the reference in the column "Reference" represents the physical quantity which was extracted from it: process cross section (if σ_p), average process cross section (if $\sigma_{p,\mathrm{av}}$) or forward rate constant (if k_f).

Type	Chemical equation	Remarks	Reference
V-m-h	$\mathrm{N_2}(e,v) + \mathrm{M} \rightleftharpoons \mathrm{N_2}(e,v') + \mathrm{M}$	$e \in \{\mathrm{X, A, B, W, B', a', a, w, A', C, b, c_3, c_4', b', o_3}\}$, $\forall\, v$, $\forall\, v' > v$ and $\mathrm{M} \in \{\mathrm{N_2, N_2^+, N, N^+}\}$	This work (a)
V-m-h	$\mathrm{N_2^+}(e,v) + \mathrm{M} \rightleftharpoons \mathrm{N_2^+}(e,v') + \mathrm{M}$	$e \in \{\mathrm{X, A, B, D, C}\}$, $\forall\, v$, $\forall\, v' > v$ and $\mathrm{M} \in \{\mathrm{N_2, N_2^+, N, N^+}\}$	This work (a)
VE-m-a	$\mathrm{N_2}(\mathrm{A},v) + \mathrm{N}(^4\mathrm{S_u}) \rightleftharpoons \mathrm{N_2}(\mathrm{X},v') + \mathrm{N}(^2\mathrm{P_u})$	$\forall\, v$, and $\forall\, v'$	[133]-k_f
VE-m-a	$\mathrm{N_2}(\mathrm{A},v) + \mathrm{N}(^4\mathrm{S_u}) \rightleftharpoons \mathrm{N_2}(\mathrm{B},v') + \mathrm{N}(^4\mathrm{S_u})$	$\forall\, v$, and $\forall\, v'$	[31]-$\sigma_{p,\mathrm{av}}$
VE-m-a	$\mathrm{N_2}(\mathrm{W},v) + \mathrm{N}(^4\mathrm{S_u}) \rightleftharpoons \mathrm{N_2}(\mathrm{B},v') + \mathrm{N}(^4\mathrm{S_u})$	$\forall\, v$, and $\forall\, v'$	[31]-$\sigma_{p,\mathrm{av}}$
VE-m-a	$\mathrm{N_2}(\mathrm{A'},0) + \mathrm{N}(^4\mathrm{S_u}) \rightleftharpoons \mathrm{N_2}(\mathrm{B},10) + \mathrm{N}(^4\mathrm{S_u})$	—	[134]-$\sigma_{p,\mathrm{av}}$
VE-m-m	$\mathrm{N_2}(\mathrm{A},v_1) + \mathrm{N_2}(\mathrm{X},v_2) \rightleftharpoons \mathrm{N_2}(\mathrm{X},v_1') + \mathrm{N_2}(\mathrm{X},v_2')$	$\forall\, v_1$, $\forall\, v_2$, $\forall\, v_1'$ and $\forall\, v_2'$	[135]-k_f
VE-m-m	$\mathrm{N_2}(\mathrm{A},v_1) + \mathrm{N_2}(\mathrm{X},v_2) \rightleftharpoons \mathrm{N_2}(\mathrm{B},v_1') + \mathrm{N_2}(\mathrm{X},v_2')$	$\forall\, v_1$, $\forall\, v_2$, $\forall\, v_1'$ and $\forall\, v_2'$	[31]-$\sigma_{p,\mathrm{av}}$
VE-m-m	$\mathrm{N_2}(\mathrm{A},v_1) + \mathrm{N_2}(\mathrm{A},v_2) \rightleftharpoons \mathrm{N_2}(\mathrm{B},v_1') + \mathrm{N_2}(\mathrm{X},v_2')$	$\forall\, v_1$, $\forall\, v_2$, $\forall\, v_1'$ and $\forall\, v_2'$	[136]-k_f
VE-m-m	$\mathrm{N_2}(\mathrm{A},v_1) + \mathrm{N_2}(\mathrm{A},v_2) \rightleftharpoons \mathrm{N_2}(\mathrm{C},v_1') + \mathrm{N_2}(\mathrm{X},v_2')$	$\forall\, v_1$, $\forall\, v_2$, $\forall\, v_1'$ and $\forall\, v_2'$	[137]-k_f
VE-m-m	$\mathrm{N_2}(\mathrm{W},v_1) + \mathrm{N_2}(\mathrm{X},v_2) \rightleftharpoons \mathrm{N_2}(\mathrm{B},v_1') + \mathrm{N_2}(\mathrm{X},v_2')$	$\forall\, v_1$, $\forall\, v_2$, $\forall\, v_1'$ and $\forall\, v_2'$	[31]-$\sigma_{p,\mathrm{av}}$
VE-m-m	$\mathrm{N_2}(\mathrm{A'},0) + \mathrm{N_2}(\mathrm{X},0) \rightleftharpoons \mathrm{N_2}(\mathrm{B},10) + \mathrm{N_2}(\mathrm{X},0)$	—	[134]-$\sigma_{p,\mathrm{av}}$
E-a-h	$\mathrm{N}(e) + \mathrm{M} \rightleftharpoons \mathrm{N}(e') + \mathrm{M}$	$\forall e$, $\forall e' > e$ and $\mathrm{M} \in \{\mathrm{N, N_2}\}$	[37]-k_f
E-a-h	$\mathrm{N^+}(e) + \mathrm{M} \rightleftharpoons \mathrm{N^+}(e') + \mathrm{M}$	$\forall e$, $\forall e' > e$ and $\mathrm{M} \in \{\mathrm{N, N_2}\}$	[37]-k_f
D-m-h	$\mathrm{N_2}(e,v) + \mathrm{M} \rightleftharpoons \mathrm{N}(e_1') + \mathrm{N}(e_2') + \mathrm{M}$	$e \in \{\mathrm{X, A, B, W, B', a', a, w, A', C, b, b'}\}$, $\forall\, v$ and $\mathrm{M} \in \{\mathrm{N_2, N_2^+, N, N^+}\}$	This work (a)
D-m-h	$\mathrm{N_2^+}(e,v) + \mathrm{M} \rightleftharpoons \mathrm{N}(e_1') + \mathrm{N^+}(e_2') + \mathrm{M}$	$e \in \{\mathrm{X, A, B, D, C}\}$, $\forall\, v$ and $\mathrm{M} \in \{\mathrm{N_2, N_2^+, N, N^+}\}$	This work (a)
I-a-h	$\mathrm{N}(e) + \mathrm{M} \rightleftharpoons \mathrm{N^+}(^3\mathrm{P}) + \mathrm{M} + \mathrm{e^-}$	$\forall e$ and $\mathrm{M} \in \{\mathrm{N, N_2}\}$	[37]-k_f
IR-m-a	$\mathrm{N_2}(\mathrm{X},v) + \mathrm{N^+}(^3\mathrm{P}) \rightleftharpoons \mathrm{N_2^+}(\mathrm{X},v') + \mathrm{N}(^4\mathrm{S_u})$	VRP on v and v' from case $v = 0$ and $\sum_{v'}$	[138]-σ_p

[a] Note that although the respective chemical equation doesn't show any possible transition in the vibrational level (or even dissociation) of the second collision partner (for the case of this one being molecular), such consideration is implicit. The chemical equation is written in a way that illustrates the probabilities uncoupling assumption that was described in the section §2.7.4.

Table B.4: Collisional processes due to electron impact for which forward rate constants were obtained. The symbol after the reference in the column "Reference" represents the physical quantity which was extracted from it: process cross section (if σ_p), average process cross section (if $\sigma_{p,\mathrm{av}}$) or forward rate constant (if k_f).

Type	Chemical equation	Remarks	Reference
V-m-e	$\mathrm{N_2}\left(\mathrm{X}^1\Sigma_\mathrm{g}^+, v\right) + \mathrm{e}^- \rightleftharpoons \mathrm{N_2}\left(\mathrm{X}^1\Sigma_\mathrm{g}^+, v'\right) + \mathrm{e}^-$	$\forall v$ and $\forall\, v' > v$, ADV	[139]-σ_p (from [140])
VE-m-e	$\mathrm{N_2}\left(\mathrm{X}, v\right) + \mathrm{e}^- \rightleftharpoons \mathrm{N_2}\left(e', v'\right) + \mathrm{e}^-$	$e' \in \{\mathrm{A}, \mathrm{B}, \mathrm{W}, \mathrm{B}', \mathrm{a}', \mathrm{a}, \mathrm{w}, \mathrm{C}\}$, VRP on v and v' from case $v = 0$ and $\sum_{v'}$	[141]-σ_p
		$e' \in \{\mathrm{c}_3, \mathrm{o}_3\}$, VRP on v and v' from case $v = 0$ and $\sum_{v'}$	[142]-σ_p
		$e' \in \{\mathrm{b}, \mathrm{c}_4', \mathrm{b}'\}$, VRP on v and v' from case $v = 0$ and $\sum_{v'}$	[143]-σ_p
		$e' = \mathrm{A}'$, Assumption of same reference values as for $e' = \mathrm{A}$, VRP on v and v' from case $v = 0$ and $\sum_{v'}$	—
VE-m-e	$\mathrm{N_2^+}\left(\mathrm{X}, v\right) + \mathrm{e}^- \rightleftharpoons \mathrm{N_2^+}\left(e', v'\right) + \mathrm{e}^-$	$e' = \mathrm{B}$, $v = 0$ and $v' = 0$, Remainder of v and v': VRP from case $v = 0$ and $v' = 0$	[144]-σ_p
		$e' \in \{\mathrm{A}, \mathrm{D}, \mathrm{C}\}$, Assumption of same reference values as for $e' = \mathrm{B}$, $v = 0$ and $v' = 0$, Remainder of v and v': VRP from case $v = 0$ and $v' = 0$	—
E-a-e	$\mathrm{N}\left(e\right) + \mathrm{e}^- \rightleftharpoons \mathrm{N}\left(e'\right) + \mathrm{e}^-$	$(e, e') \in \{(^4\mathrm{S_u}, {}^2\mathrm{D_u}), (^4\mathrm{S_u}, {}^2\mathrm{P_u}), (^2\mathrm{D_u}, {}^2\mathrm{P_u})\}$	[81]-σ_p
		Remainder of (e, e'), with $e' > e$	[86]-k_f
E-a-e	$\mathrm{N^+}\left(e\right) + \mathrm{e}^- \rightleftharpoons \mathrm{N^+}\left(e'\right) + \mathrm{e}^-$	$\forall e$ and $\forall e' > e$	[86]-k_f
D-m-e	$\mathrm{N_2}\left(\mathrm{X}^1\Sigma_\mathrm{g}^+, v\right) + \mathrm{e}^- \rightleftharpoons \mathrm{N}\left(e_1'\right) + \mathrm{N}\left(e_2'\right) + \mathrm{e}^-$	$\forall\, v$, $(e_1', e_2') = (^4\mathrm{S_u}, {}^4\mathrm{S_u})$, ADV	[139]-σ_p (from [140])
		$\forall\, v$, $(e_1', e_2') = (^4\mathrm{S_u}, {}^2\mathrm{D_u})$, ADV	[145]-σ_p (from [140])
DR-m-e	$\mathrm{N_2^+}\left(\mathrm{X}^2\Sigma_\mathrm{g}^+, v\right) + \mathrm{e}^- \rightleftharpoons \mathrm{N}\left(e_1'\right) + \mathrm{N}\left(e_2'\right)$	$v \in \{0, 2\}$ and $(e_1', e_2') \in \{(^4\mathrm{S_u}, {}^2\mathrm{D_u}), (^4\mathrm{S_u}, {}^2\mathrm{P_u}), (^2\mathrm{D_u}, {}^2\mathrm{D_u})\}$ $v \in \{1, 3, 4\}$ and $(e_1', e_2') \in \{(^4\mathrm{S_u}, {}^2\mathrm{D_u}), (^4\mathrm{S_u}, {}^2\mathrm{P_u}), (^2\mathrm{D_u}, {}^2\mathrm{D_u}), (^2\mathrm{D_u}, {}^2\mathrm{P_u})\}$ Remainder of v with $(e_1', e_2') \in \{(^4\mathrm{S_u}, {}^2\mathrm{D_u}), (^4\mathrm{S_u}, {}^2\mathrm{P_u}), (^2\mathrm{D_u}, {}^2\mathrm{D_u}), (^2\mathrm{D_u}, {}^2\mathrm{P_u})\}$: VRP from case $v = 4$	[146]-k_f
I-m-e	$\mathrm{N_2}\left(\mathrm{X}^1\Sigma_\mathrm{g}^+, v\right) + \mathrm{e}^- \rightleftharpoons \mathrm{N_2^+}\left(e', v'\right) + 2\,\mathrm{e}^-$	$\forall\, v$ and $e' \in \{\mathrm{X}, \mathrm{A}, \mathrm{B}\}$, ADV, VRP on v' from case $\sum_{v'}$	[80]-σ_p (from [140])
I-a-e	$\mathrm{N}\left(e\right) + \mathrm{e}^- \rightleftharpoons \mathrm{N^+}\left(^3\mathrm{P}\right) + 2\,\mathrm{e}^-$	$e = {}^4\mathrm{S_u}$	[82]-σ_p
		$e \in \{^2\mathrm{D_u}, {}^2\mathrm{P_u}\}$	[83]-σ_p
		Remainder of e	[86]-k_f

Appendix C

Sensibility tests on different parameters of the simulations

In this chapter, it is presented the numerical instrumentally resolved radiative intensities $\hat{I}^l(x)$ and non-equilibrium metrics $\hat{I}_\lambda^{\mathrm{ne},l}(x)$, with $l \in \{\mathrm{VUV}, \text{“Blue”}, \text{“Red”}, \mathrm{IR}\}$, obtained from Euler one-dimensional simulations of the shots 40, 19, and 20 of the 62nd EAST campaign [39], considering changes of scale of the VUV escape factor Λ^{VUV}, the dissociation rates of $\mathrm{N_2(X)}$, and the excitation rates of N.

C.1 Dependence on the escape factor

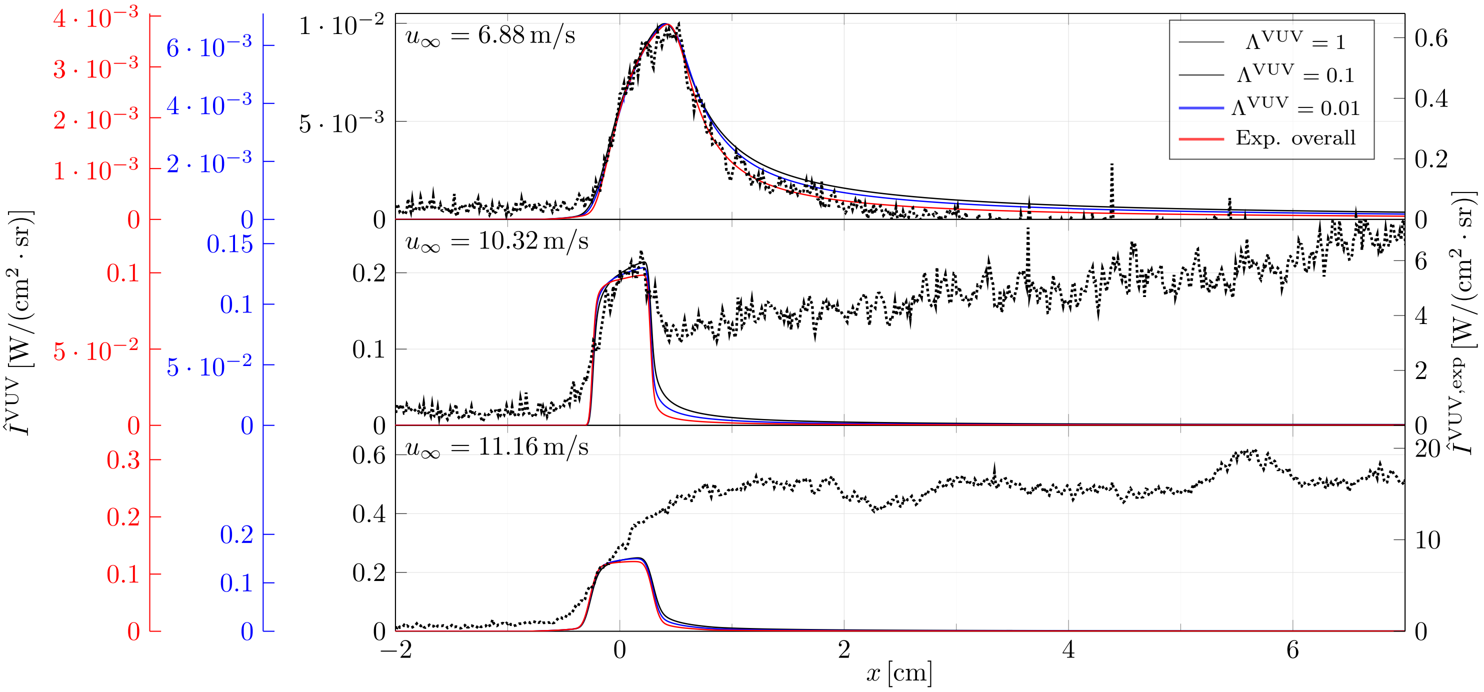

Figure C.1: Numerical instrumentally resolved radiative intensities $\hat{I}^{\mathrm{VUV}}(x)$, obtained with $\Lambda^{\mathrm{VUV}} = 1$ (solid black lines), $\Lambda^{\mathrm{VUV}} = 0.1$ (solid blue lines), and $\Lambda^{\mathrm{VUV}} = 0.01$ (solid red lines), as well as the respective experimental instrumentally resolved radiative intensities $\hat{I}^{\mathrm{VUV,exp}}(x)$ (dotted black lines).

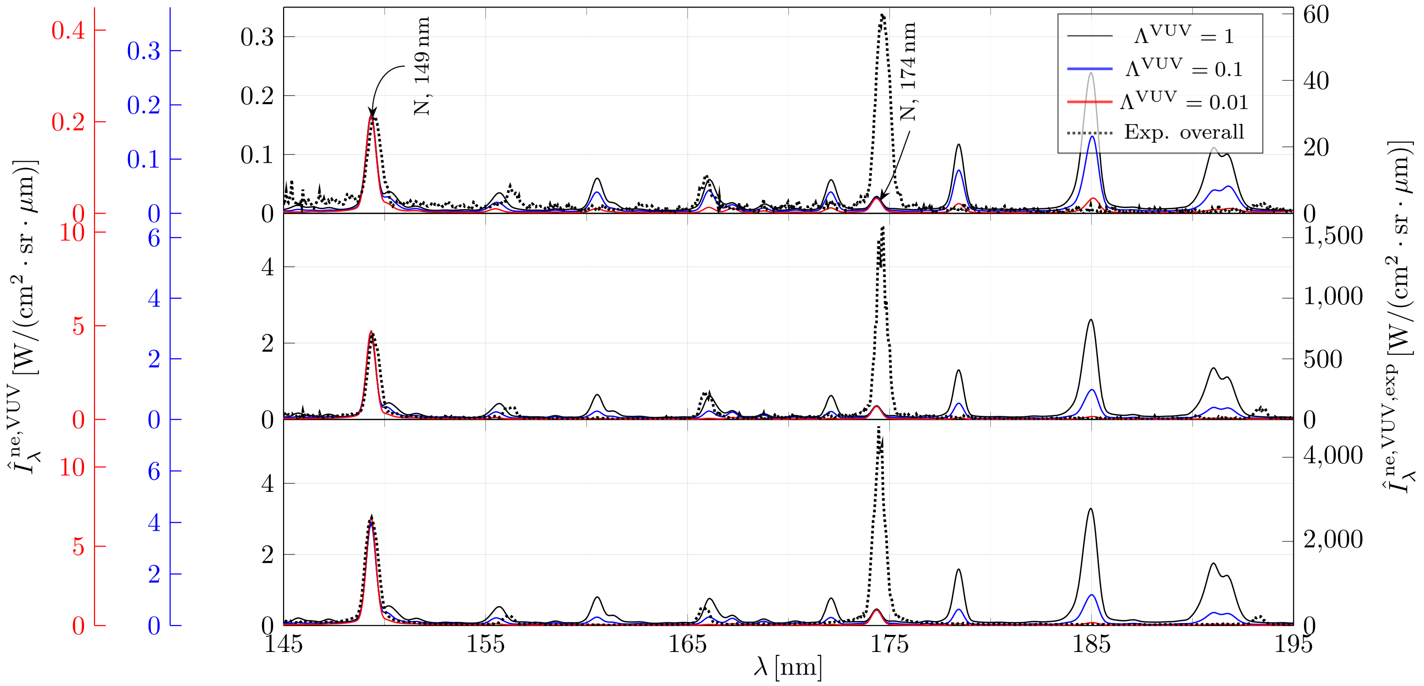

Figure C.2: Numerical instrumentally resolved non-equilibrium metrics $\hat{I}_\lambda^{\mathrm{ne,VUV}}(x)$, obtained with $\Lambda^{\mathrm{VUV}} = 1$ (solid black lines), $\Lambda^{\mathrm{VUV}} = 0.1$ (solid blue lines), and $\Lambda^{\mathrm{VUV}} = 0.01$ (solid red lines), as well as the respective experimental instrumentally resolved non-equilibrium metrics $\hat{I}_\lambda^{\mathrm{ne,VUV,exp}}(x)$ (dotted black lines).

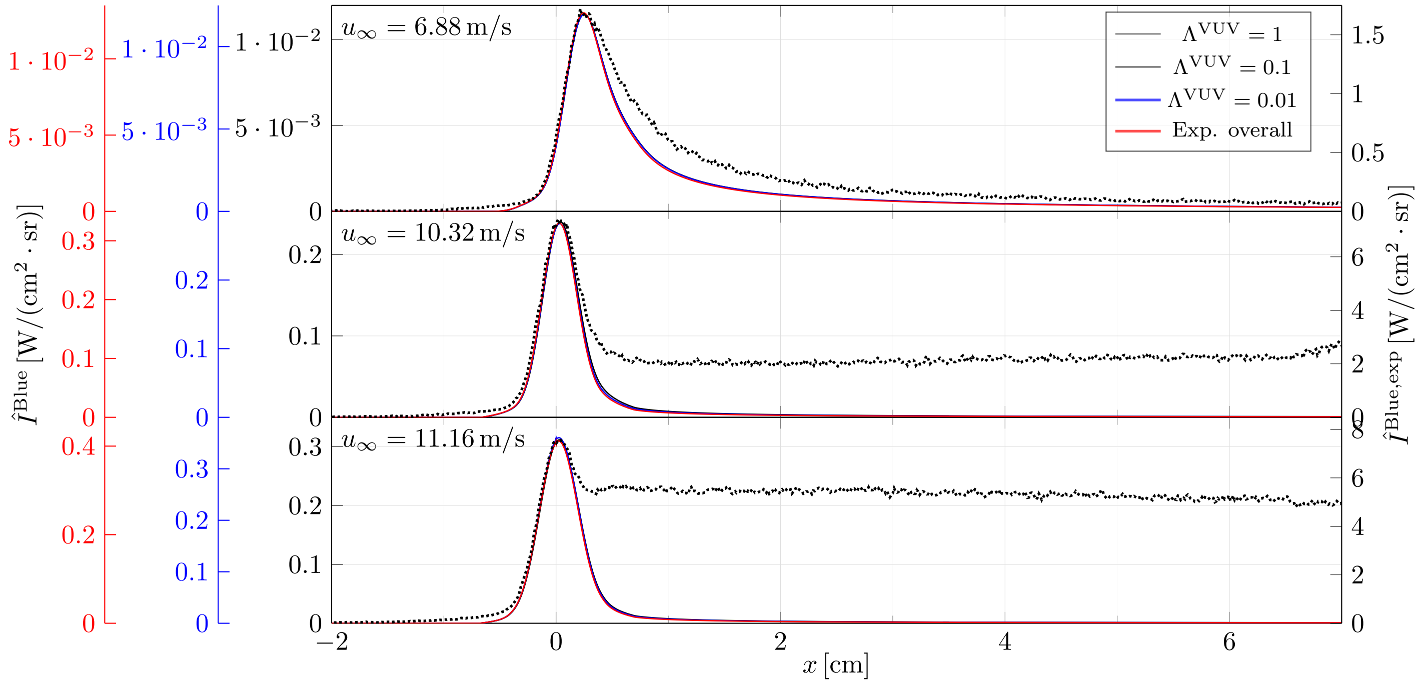

Figure C.3: Numerical instrumentally resolved radiative intensities $\hat{I}^{\mathrm{Blue}}(x)$, obtained with $\Lambda^{\mathrm{VUV}} = 1$ (solid black lines), $\Lambda^{\mathrm{VUV}} = 0.1$ (solid blue lines), and $\Lambda^{\mathrm{VUV}} = 0.01$ (solid red lines), as well as the respective experimental instrumentally resolved radiative intensities $\hat{I}^{\mathrm{Blue,exp}}(x)$ (dotted black lines).

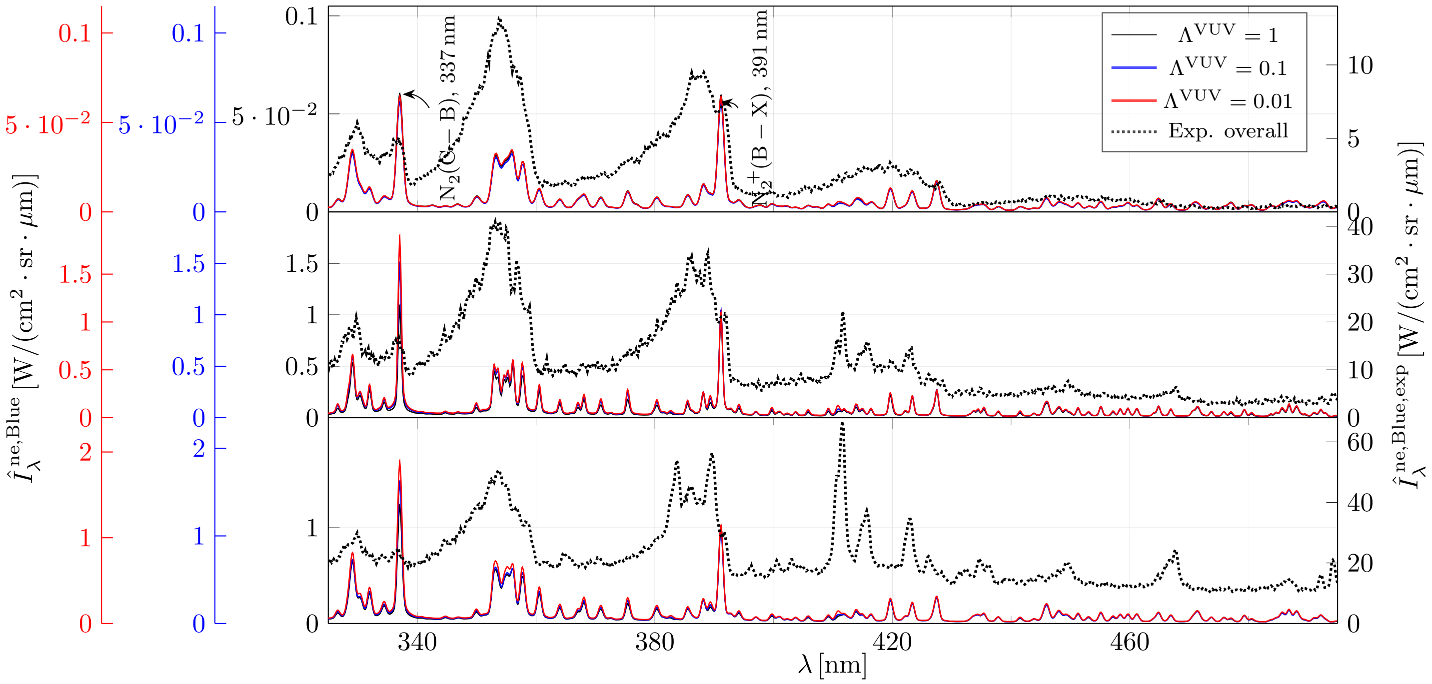

Figure C.4: Numerical instrumentally resolved non-equilibrium metrics $\hat{I}_\lambda^{\text{ne,Blue}}(x)$, obtained with $\Lambda^{\text{VUV}} = 1$ (solid black lines), $\Lambda^{\text{VUV}} = 0.1$ (solid blue lines), and $\Lambda^{\text{VUV}} = 0.01$ (solid red lines), as well as the respective experimental instrumentally resolved non-equilibrium metrics $\hat{I}_\lambda^{\text{ne,Blue,exp}}(x)$ (dotted black lines).

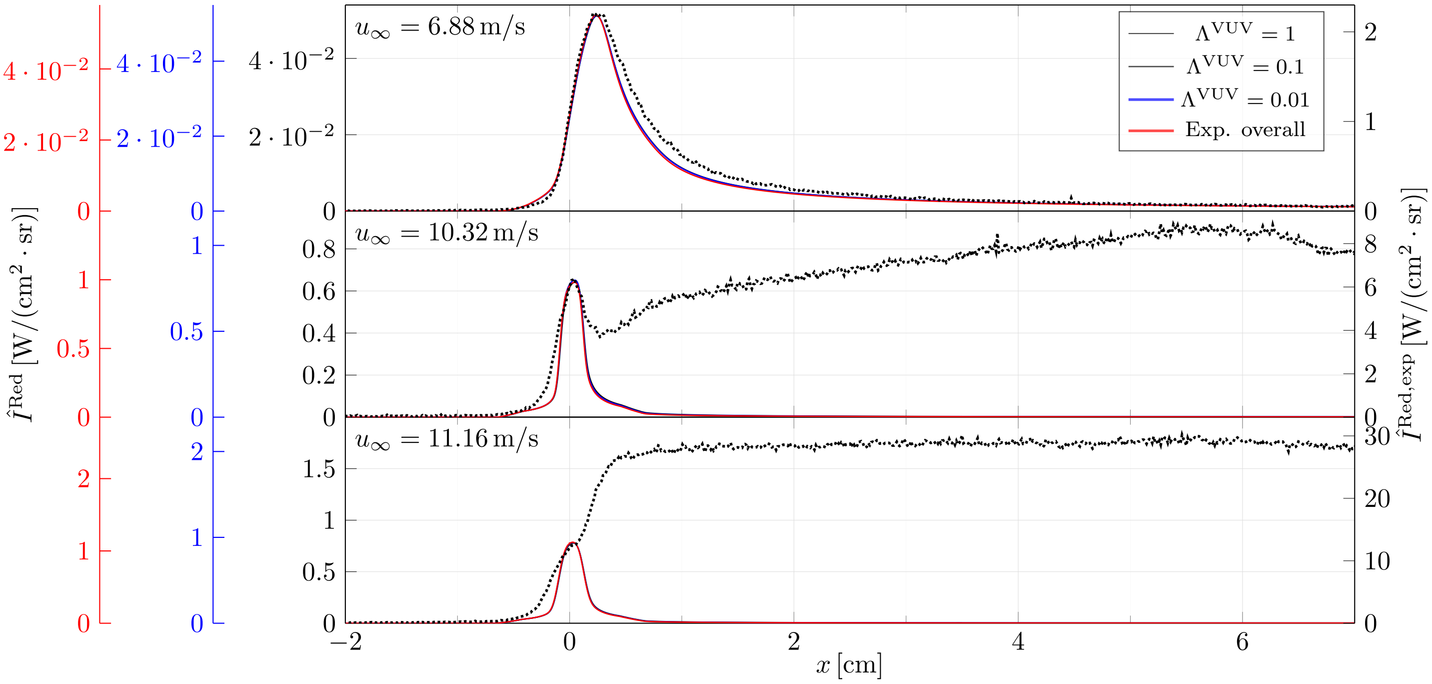

Figure C.5: Numerical instrumentally resolved radiative intensities $\hat{I}^{\text{Red}}(x)$, obtained with $\Lambda^{\text{VUV}} = 1$ (solid black lines), $\Lambda^{\text{VUV}} = 0.1$ (solid blue lines), and $\Lambda^{\text{VUV}} = 0.01$ (solid red lines), as well as the respective experimental instrumentally resolved radiative intensities $\hat{I}^{\text{Red,exp}}(x)$ (dotted black lines).

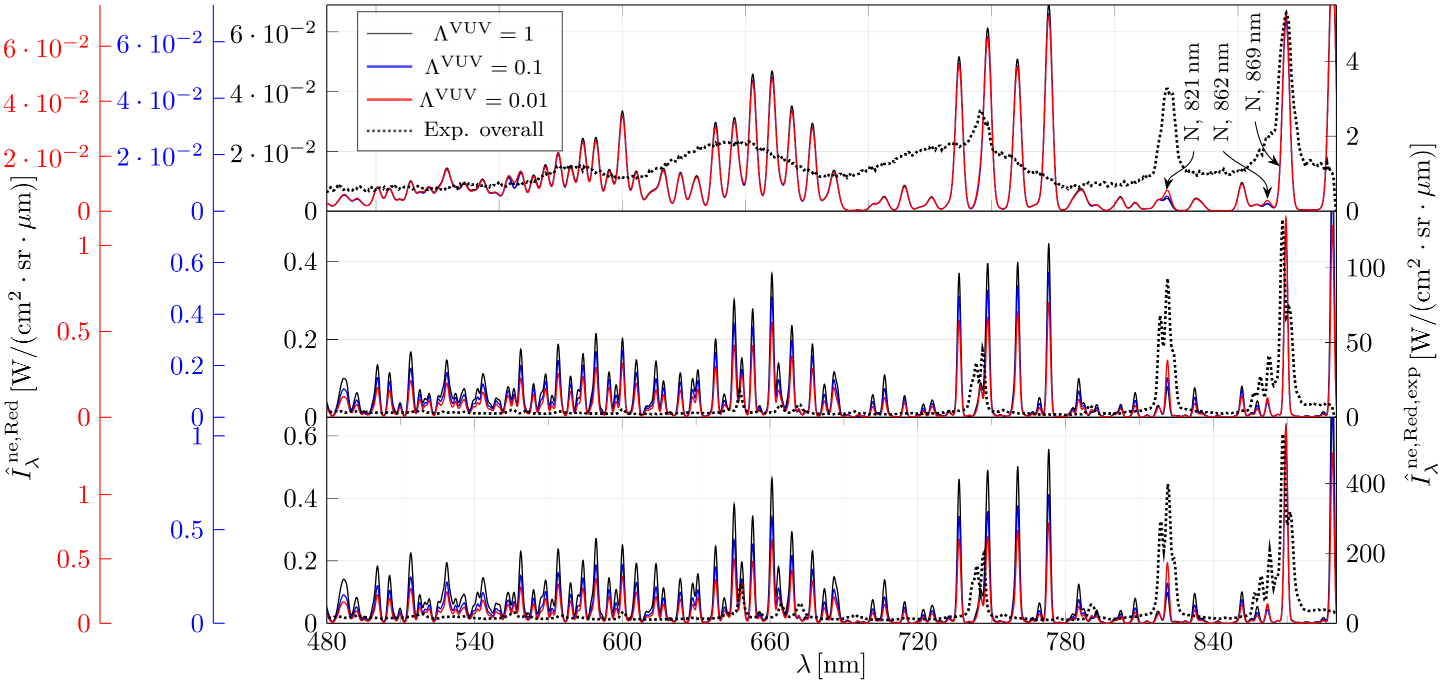

Figure C.6: Numerical instrumentally resolved non-equilibrium metrics $\hat{I}_\lambda^{\mathrm{ne,Red}}(x)$, obtained with $\Lambda^{\mathrm{VUV}} = 1$ (solid black lines), $\Lambda^{\mathrm{VUV}} = 0.1$ (solid blue lines), and $\Lambda^{\mathrm{VUV}} = 0.01$ (solid red lines), as well as the respective experimental instrumentally resolved non-equilibrium metrics $\hat{I}_\lambda^{\mathrm{ne,Red,exp}}(x)$ (dotted black lines).

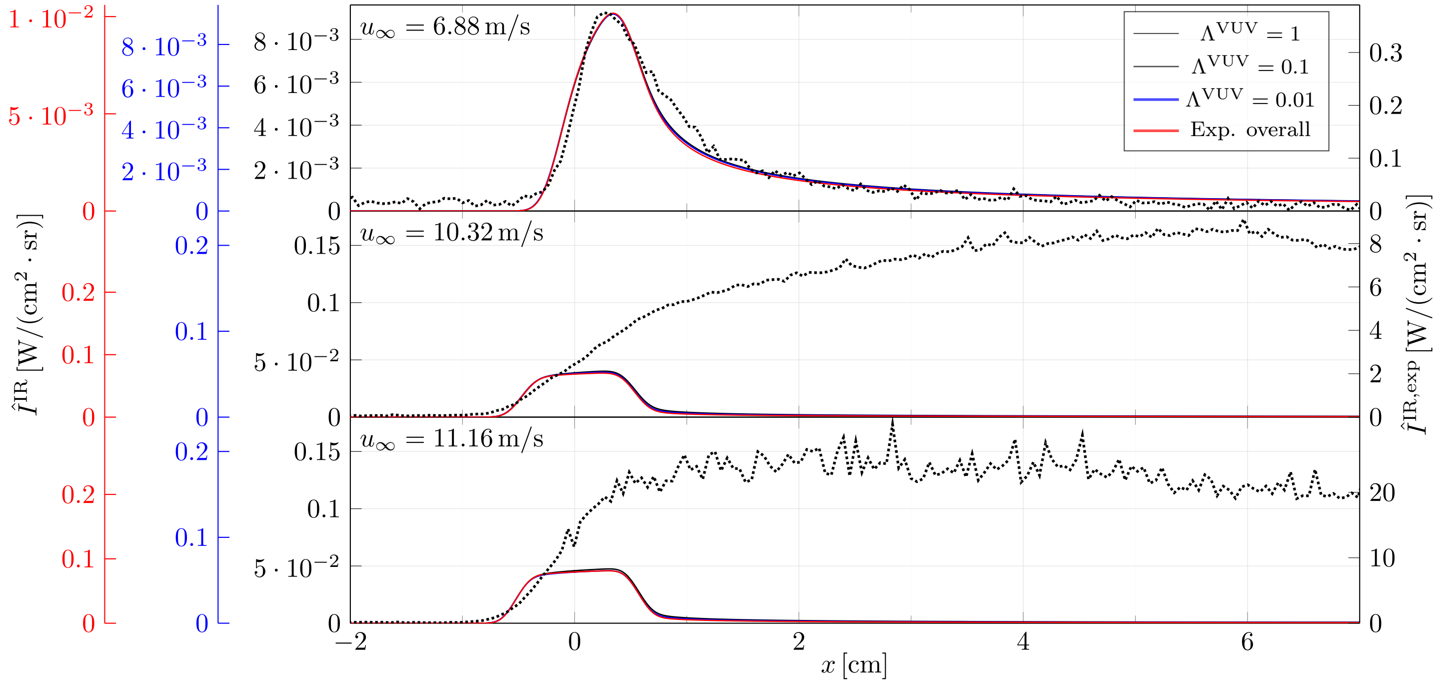

Figure C.7: Numerical instrumentally resolved radiative intensities $\hat{I}^{\mathrm{IR}}(x)$, obtained with $\Lambda^{\mathrm{VUV}} = 1$ (solid black lines), $\Lambda^{\mathrm{VUV}} = 0.1$ (solid blue lines), and $\Lambda^{\mathrm{VUV}} = 0.01$ (solid red lines), as well as the respective experimental instrumentally resolved radiative intensities $\hat{I}^{\mathrm{IR,exp}}(x)$ (dotted black lines).

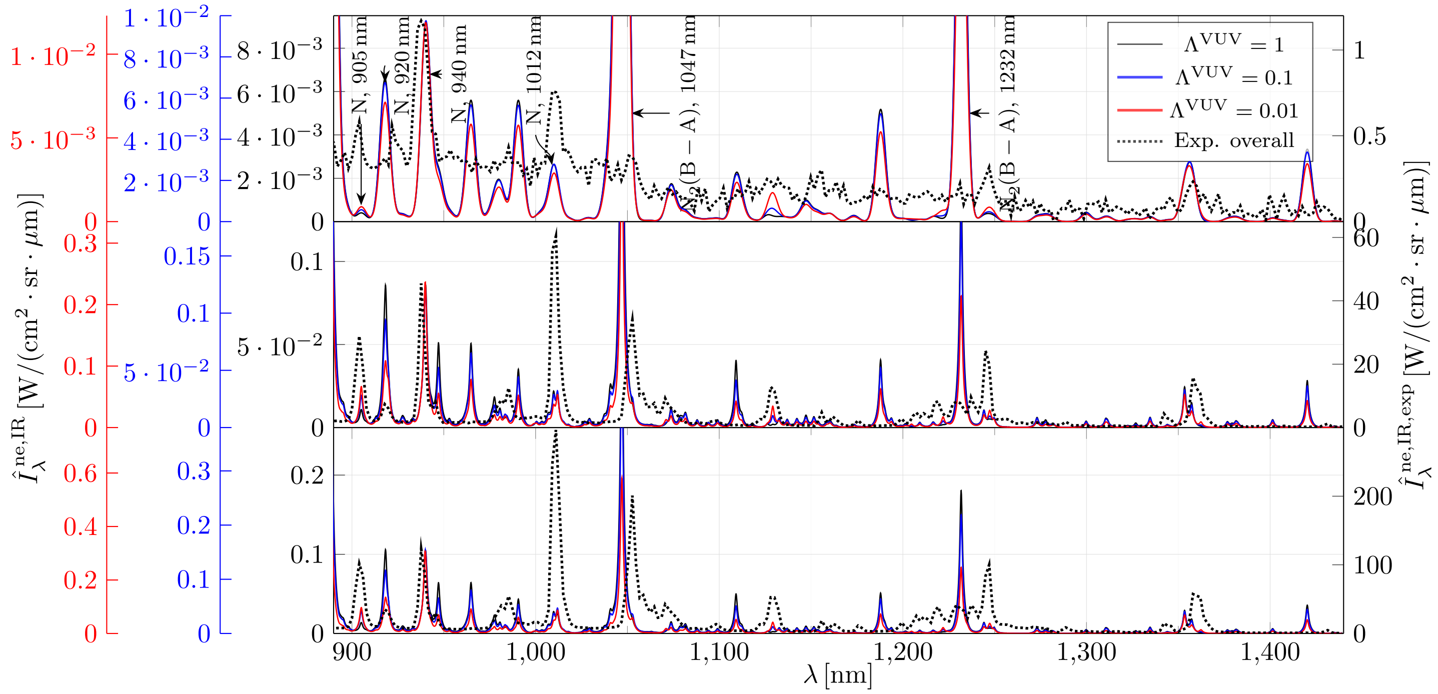

Figure C.8: Numerical instrumentally resolved non-equilibrium metrics $\hat{I}_\lambda^{\mathrm{ne,IR}}(x)$, obtained with $\Lambda^{\mathrm{VUV}} = 1$ (solid black lines), $\Lambda^{\mathrm{VUV}} = 0.1$ (solid blue lines), and $\Lambda^{\mathrm{VUV}} = 0.01$ (solid red lines), as well as the respective experimental instrumentally resolved non-equilibrium metrics $\hat{I}_\lambda^{\mathrm{ne,IR,exp}}(x)$ (dotted black lines).

C.2 Dependence on the dissociation rates of N_2

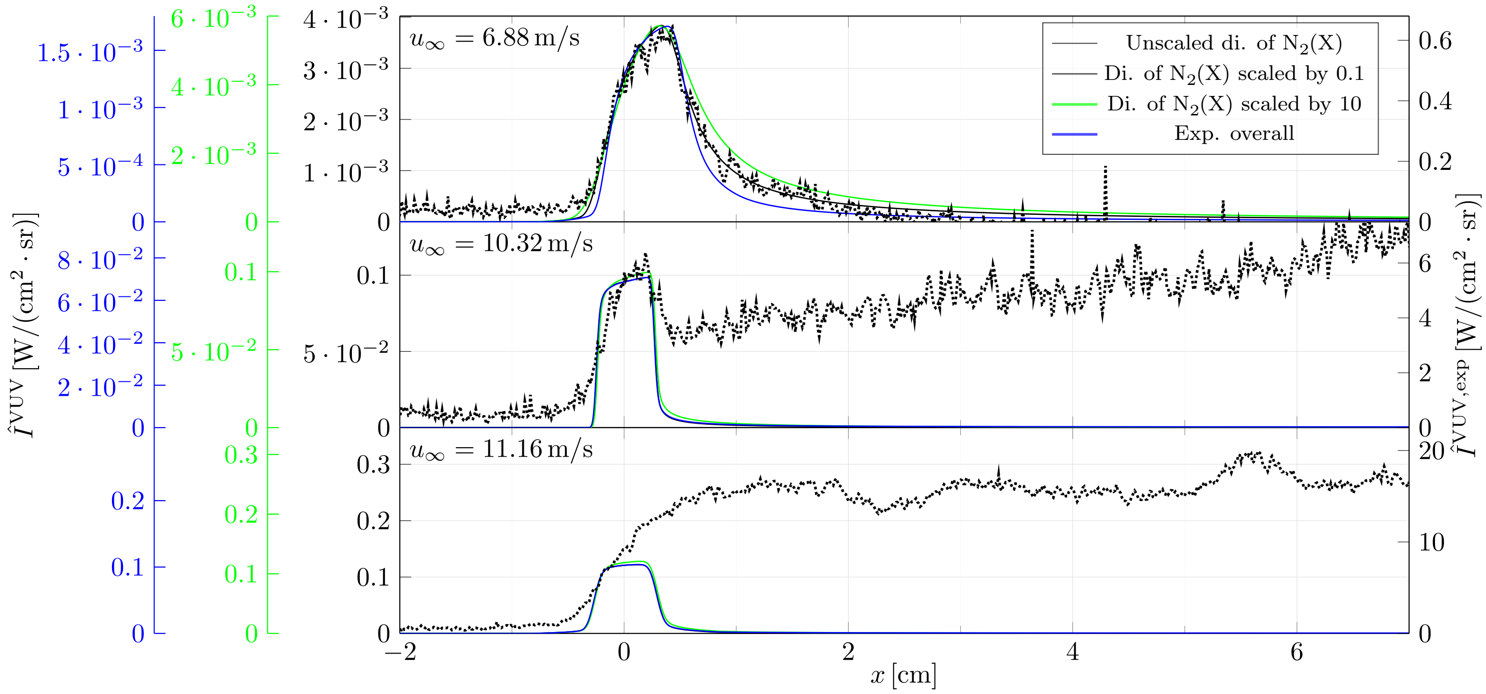

Figure C.9: Numerical instrumentally resolved radiative intensities $\hat{I}^{\mathrm{VUV}}(x)$, obtained with $\Lambda^{\mathrm{VUV}} = 0.01$, and unscaled dissociation of $N_2(X^1\Sigma_g^+)$ (solid black lines), and scaled by 0.1 (solid green lines), and by 10 (solid blue lines), as well as the respective experimental instrumentally resolved radiative intensities $\hat{I}^{\mathrm{VUV,exp}}(x)$ (dotted black lines).

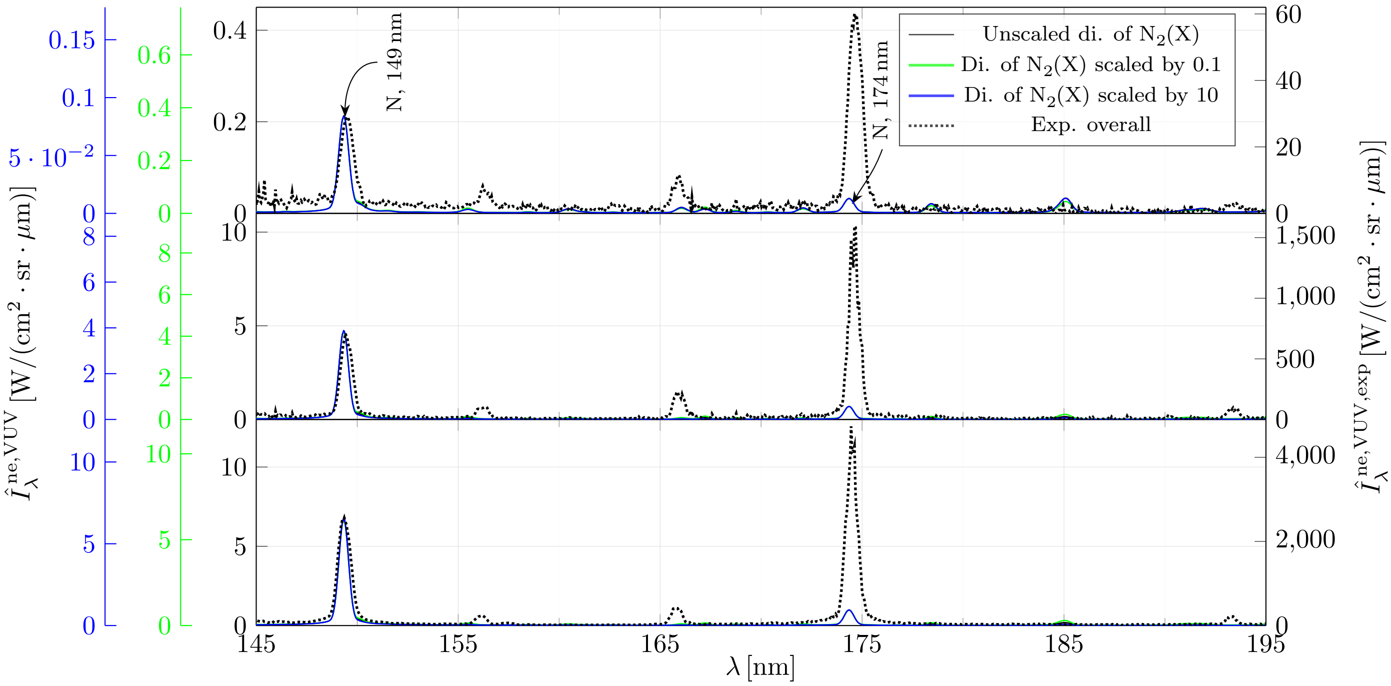

Figure C.10: Numerical instrumentally resolved non-equilibrium metrics $\hat{I}_{\lambda}^{\mathrm{ne,VUV}}(x)$, obtained with $\Lambda^{\mathrm{VUV}} = 0.01$, and unscaled dissociation of $N_2(X^1\Sigma_g^+)$ (solid black lines), and scaled by 0.1 (solid green lines), and by 10 (solid blue lines), as well as the respective experimental instrumentally resolved non-equilibrium metrics $\hat{I}_{\lambda}^{\mathrm{ne,VUV,exp}}(x)$ (dotted black lines).

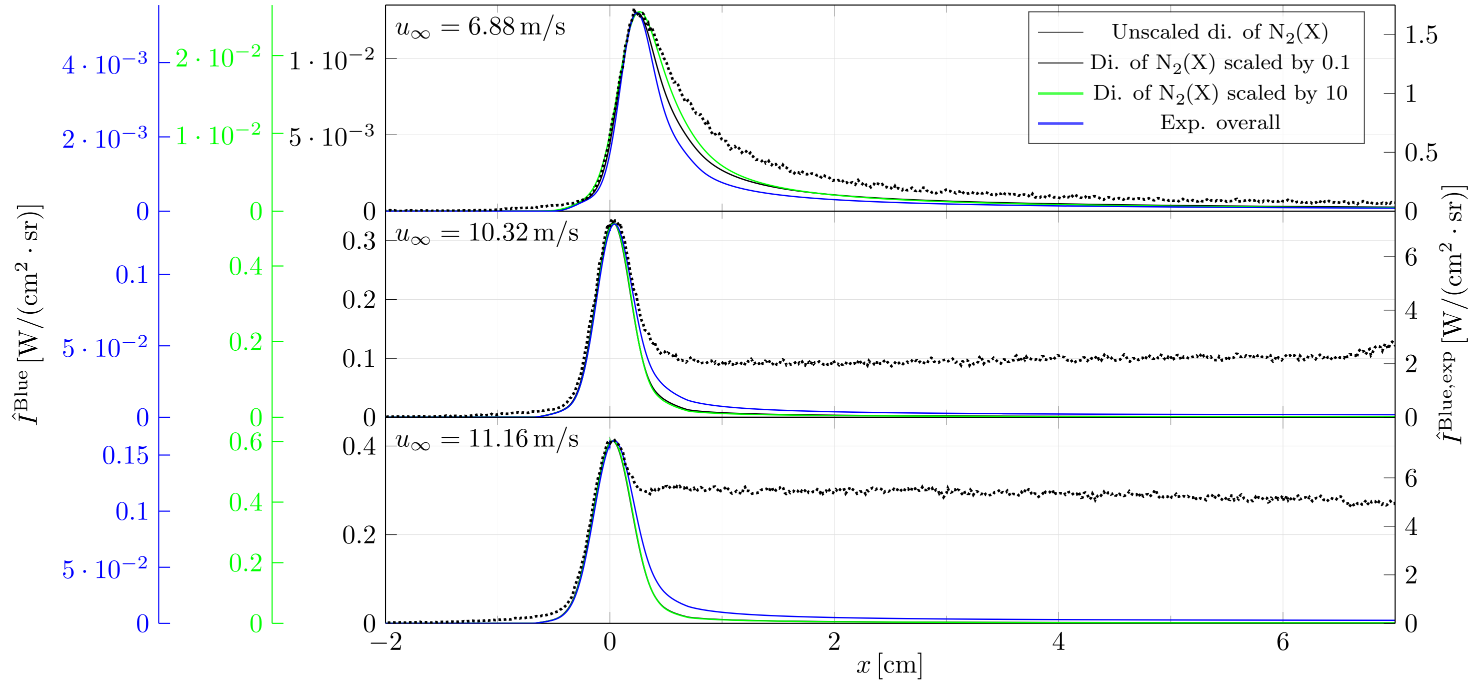

Figure C.11: Numerical instrumentally resolved radiative intensities $\hat{I}^{\mathrm{Blue}}(x)$, obtained with $\Lambda^{\mathrm{VUV}} = 0.01$, and unscaled dissociation of $N_2(X^1\Sigma_g^+)$ (solid black lines), and scaled by 0.1 (solid green lines), and by 10 (solid blue lines), as well as the respective experimental instrumentally resolved radiative intensities $\hat{I}^{\mathrm{Blue,exp}}(x)$ (dotted black lines).

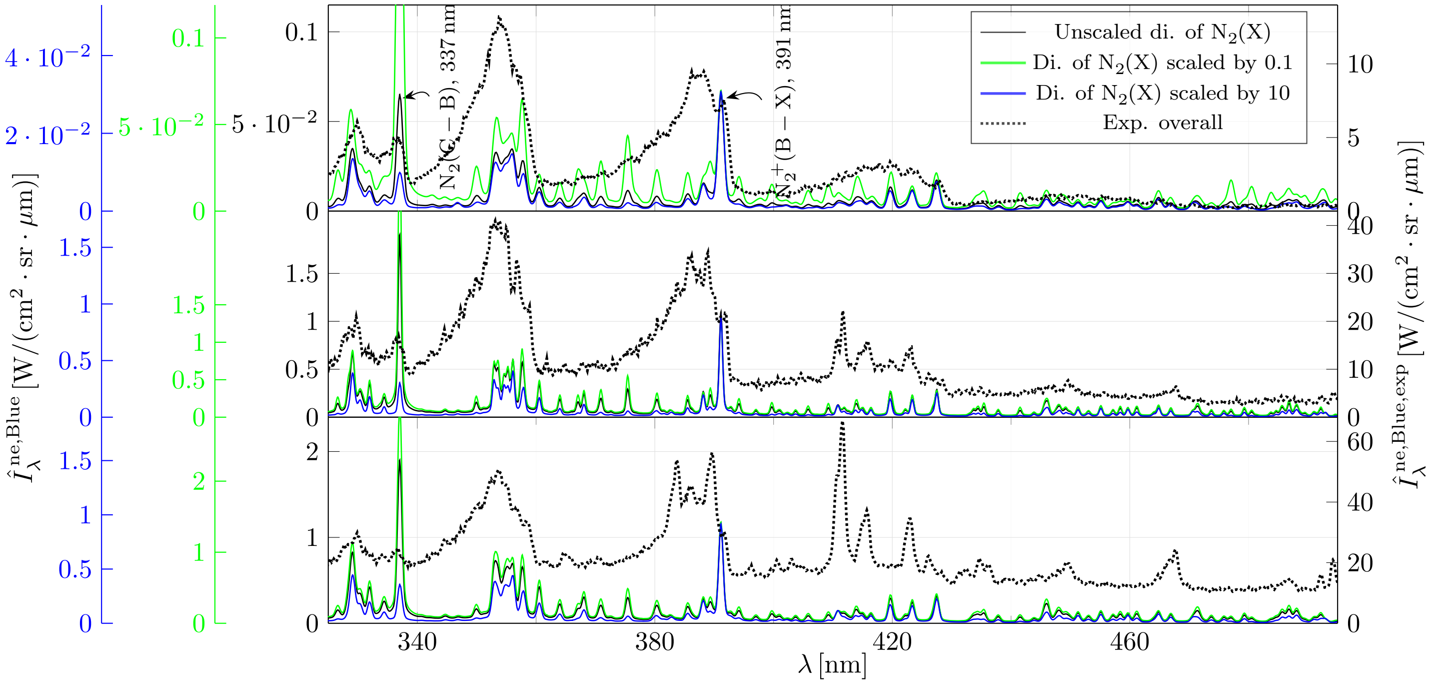

Figure C.12: Numerical instrumentally resolved non-equilibrium metrics $\hat{I}_\lambda^{\mathrm{ne,Blue}}(x)$, obtained with $\Lambda^{\mathrm{VUV}} = 0.01$, and unscaled dissociation of $\mathrm{N_2(X^1\Sigma_g^+)}$ (solid black lines), and scaled by 0.1 (solid green lines), and by 10 (solid blue lines), as well as the respective experimental instrumentally resolved non-equilibrium metrics $\hat{I}_\lambda^{\mathrm{ne,Blue,exp}}(x)$ (dotted black lines).

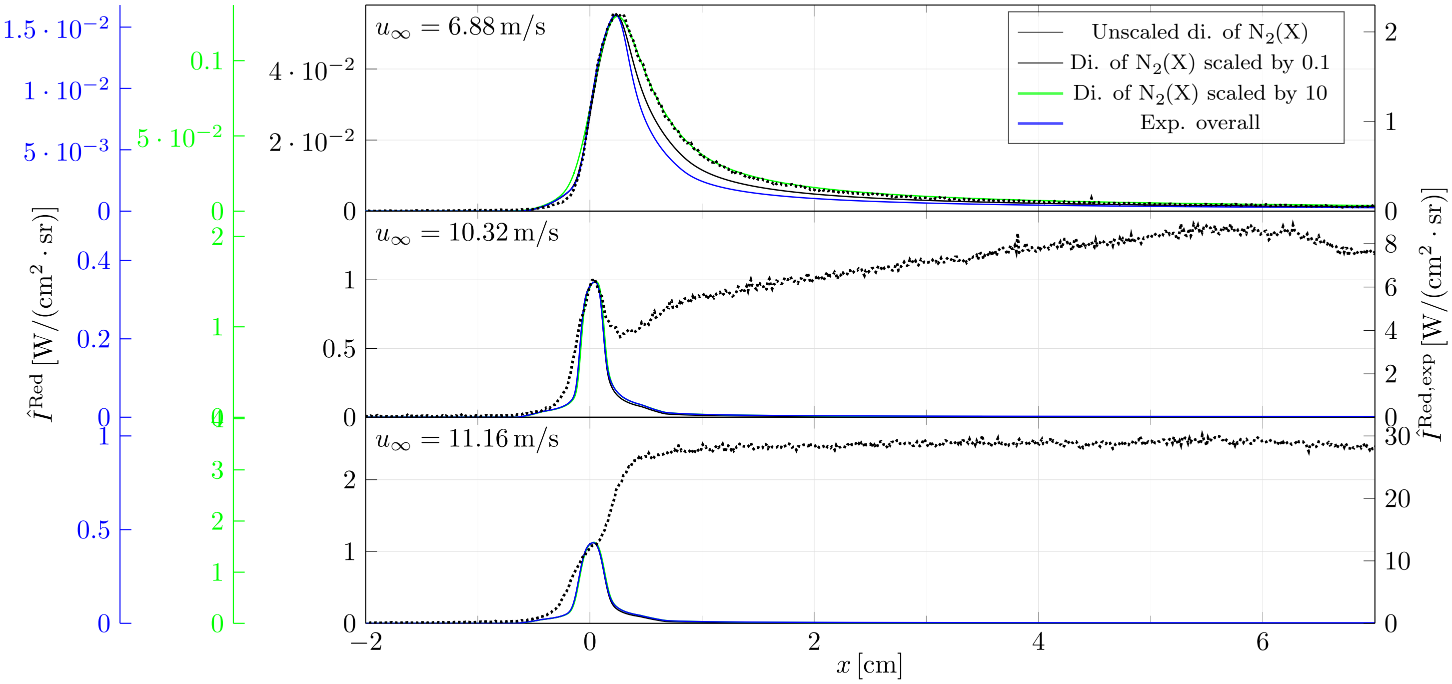

Figure C.13: Numerical instrumentally resolved radiative intensities $\hat{I}^{\mathrm{Red}}(x)$, obtained with $\Lambda^{\mathrm{VUV}} = 0.01$, and unscaled dissociation of $\mathrm{N_2(X^1\Sigma_g^+)}$ (solid black lines), and scaled by 0.1 (solid green lines), and by 10 (solid blue lines), as well as the respective experimental instrumentally resolved radiative intensities $\hat{I}^{\mathrm{Red,exp}}(x)$ (dotted black lines).

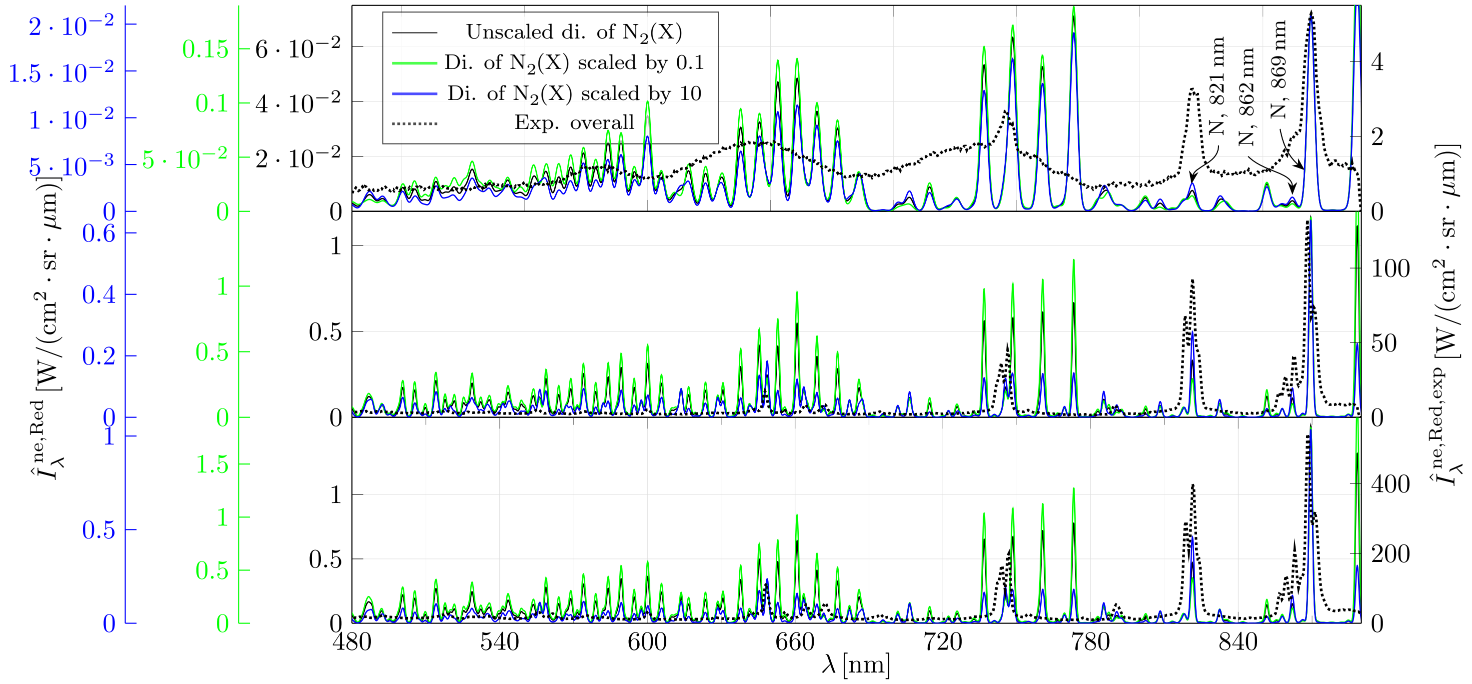

Figure C.14: Numerical instrumentally resolved non-equilibrium metrics $\hat{I}_{\lambda}^{\mathrm{ne,Red}}(x)$, obtained with $\Lambda^{\mathrm{VUV}} = 0.01$, and unscaled dissociation of $N_2(X^1\Sigma_g^+)$ (solid black lines), and scaled by 0.1 (solid green lines), and by 10 (solid blue lines), as well as the respective experimental instrumentally resolved non-equilibrium metrics $\hat{I}_{\lambda}^{\mathrm{ne,Red,exp}}(x)$ (dotted black lines).

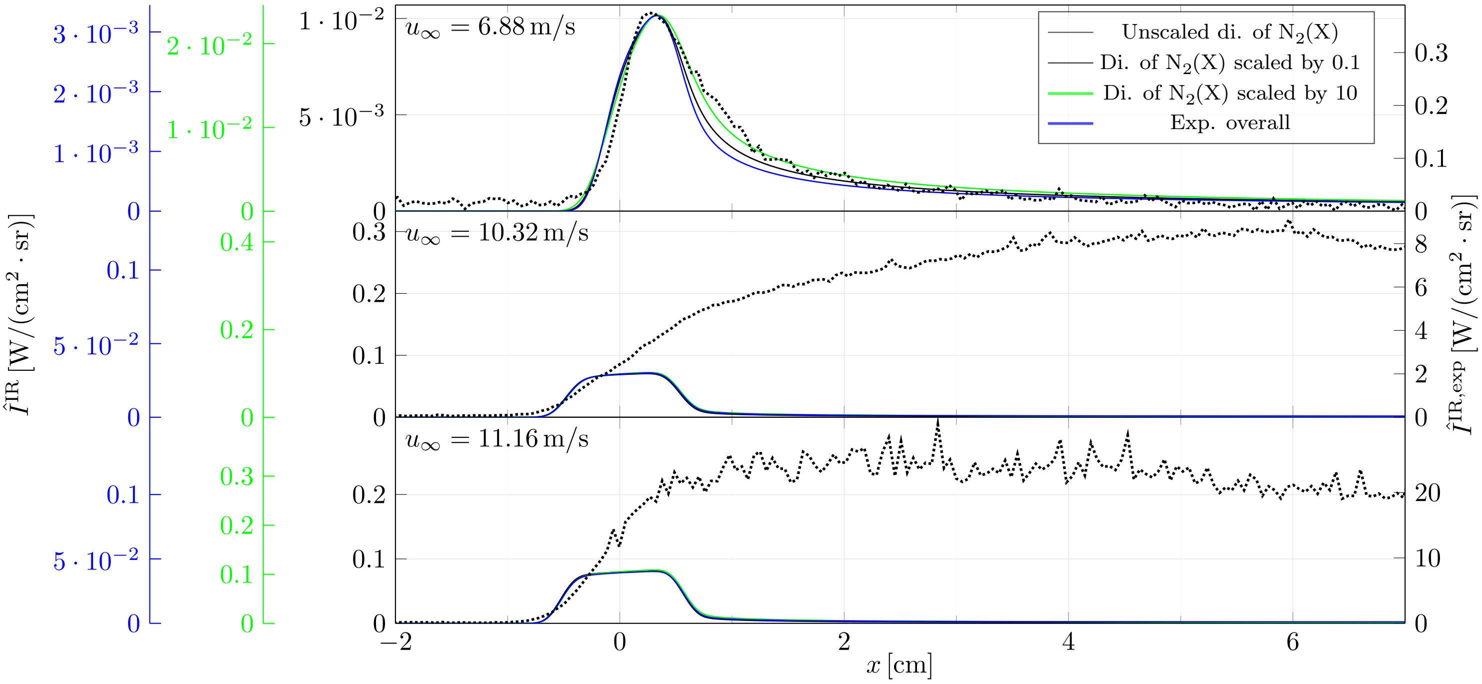

Figure C.15: Numerical instrumentally resolved radiative intensities $\hat{I}^{\mathrm{IR}}(x)$, obtained with $\Lambda^{\mathrm{VUV}} = 0.01$, and unscaled dissociation of $N_2(X^1\Sigma_g^+)$ (solid black lines), and scaled by 0.1 (solid green lines), and by 10 (solid blue lines), as well as the respective experimental instrumentally resolved radiative intensities $\hat{I}^{\mathrm{IR,exp}}(x)$ (dotted black lines).

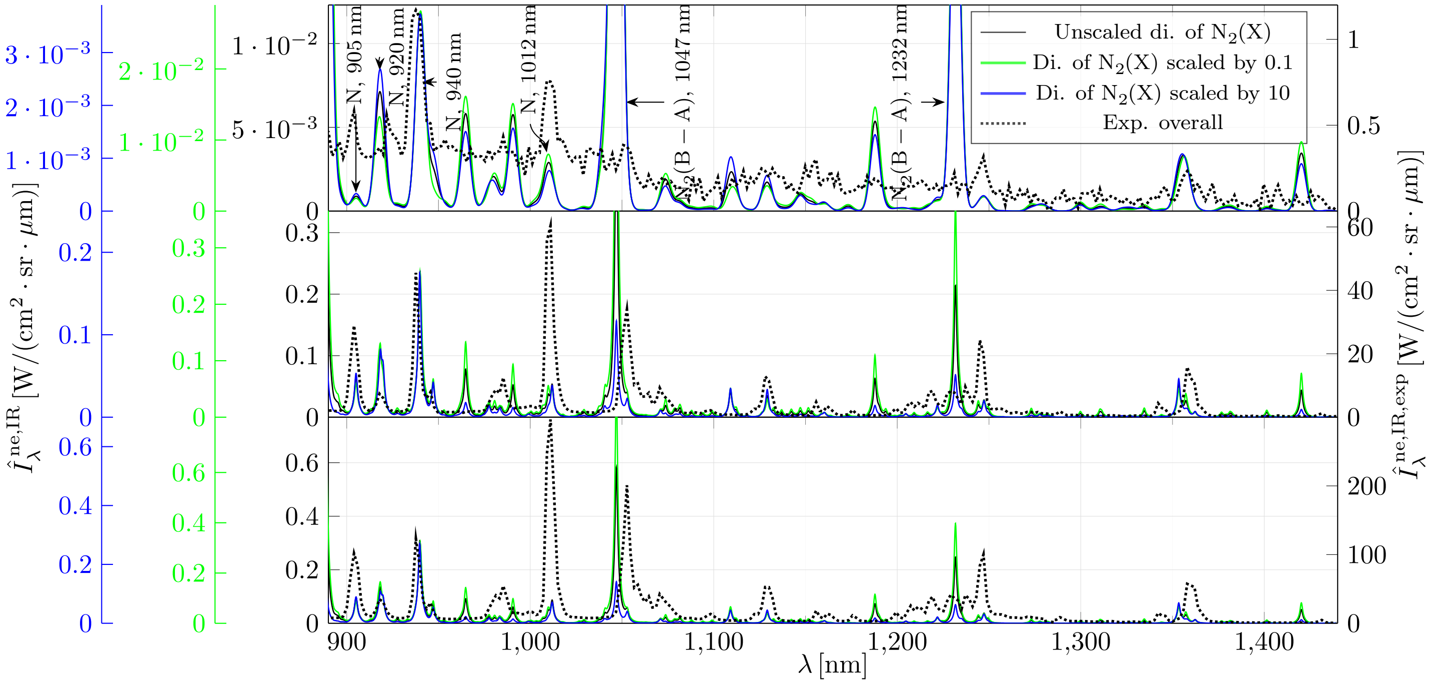

Figure C.16: Numerical instrumentally resolved non-equilibrium metrics $\hat{I}_\lambda^{\text{ne,IR}}(x)$, obtained with $\Lambda^{\text{VUV}} = 0.01$, and unscaled dissociation of $N_2(X^1\Sigma_g^+)$ (solid black lines), and scaled by 0.1 (solid green lines), and by 10 (solid blue lines), as well as the respective experimental instrumentally resolved non-equilibrium metrics $\hat{I}_\lambda^{\text{ne,IR,exp}}(x)$ (dotted black lines).

C.3 Dependence on the excitation rates of N

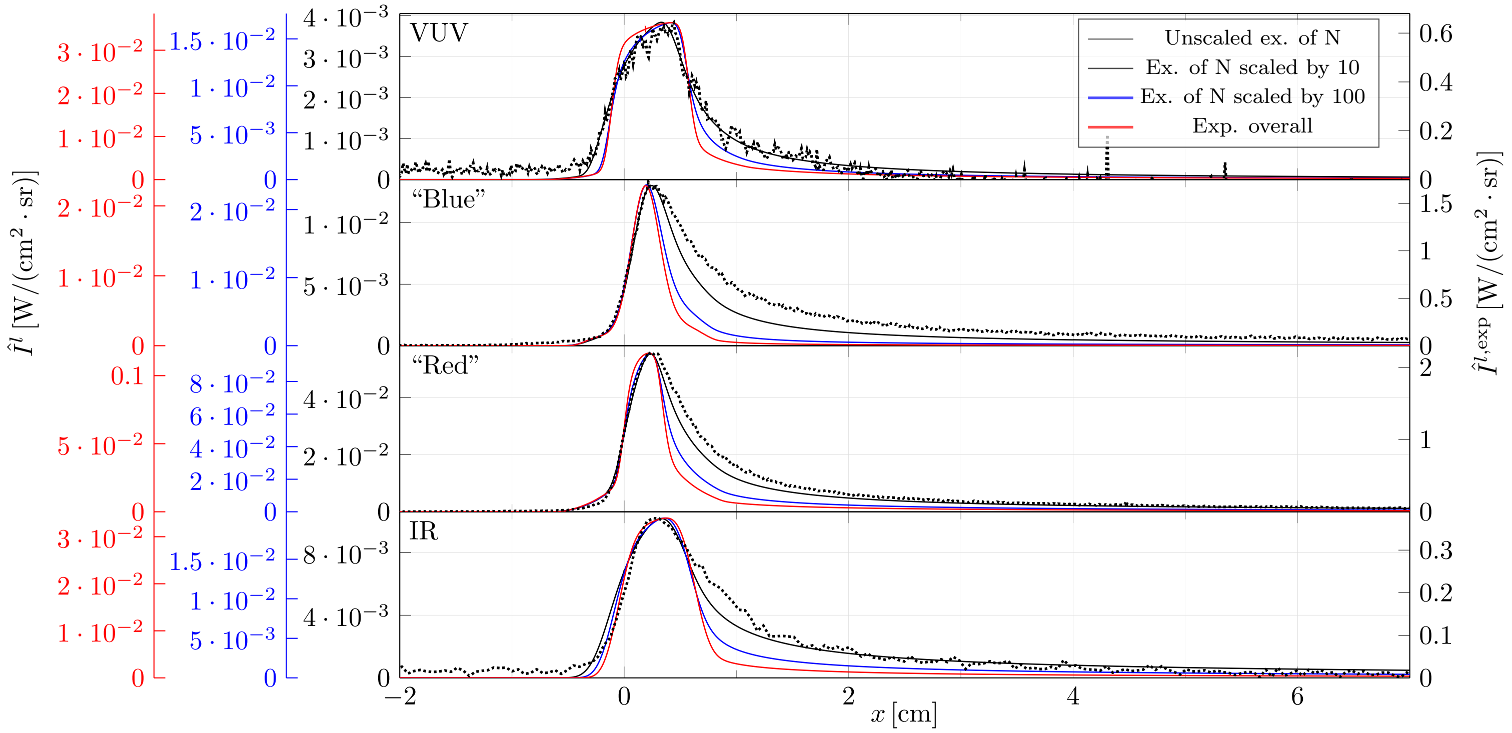

Figure C.17: Numerical instrumentally resolved radiative intensities $\hat{I}^l(x)$ obtained with $\Lambda^{\text{VUV}} = 0.01$, and unscaled excitation of N (solid black lines), and scaled by 10 (solid blue lines), and by 100 (solid red lines), as well as the respective experimental instrumentally resolved radiative intensities $\hat{I}^{l,\text{exp}}(x)$ (dotted black lines), for the case of the low speed shot.

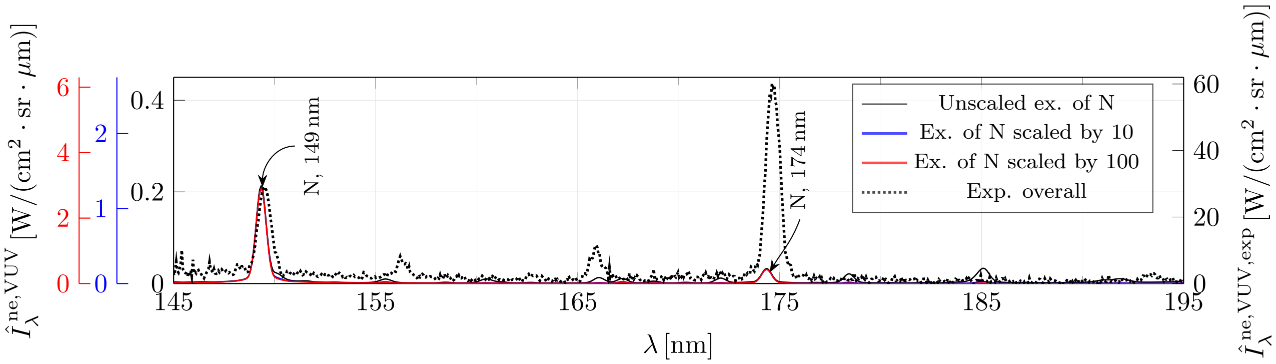

(a) For the case $l = \mathrm{VUV}$.

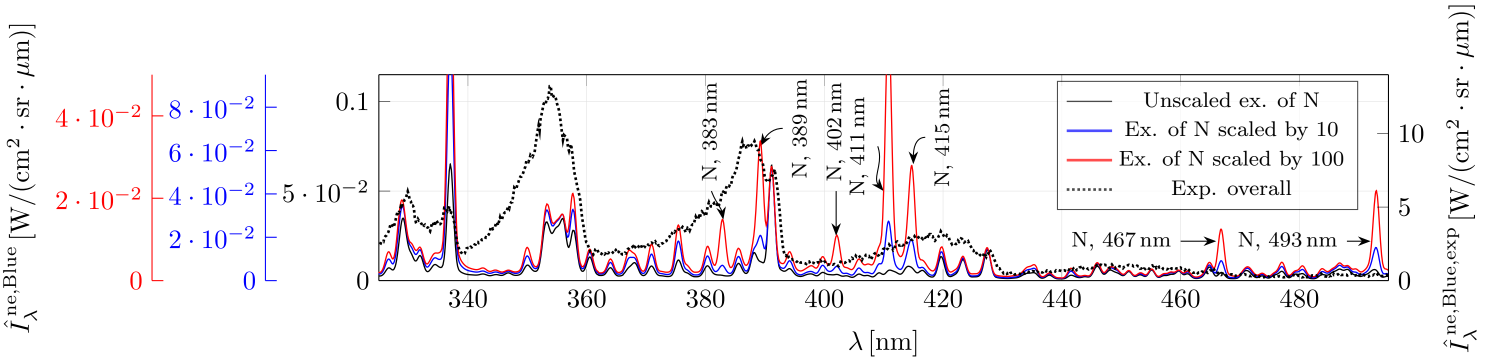

(b) For the case $l =$ "Blue".

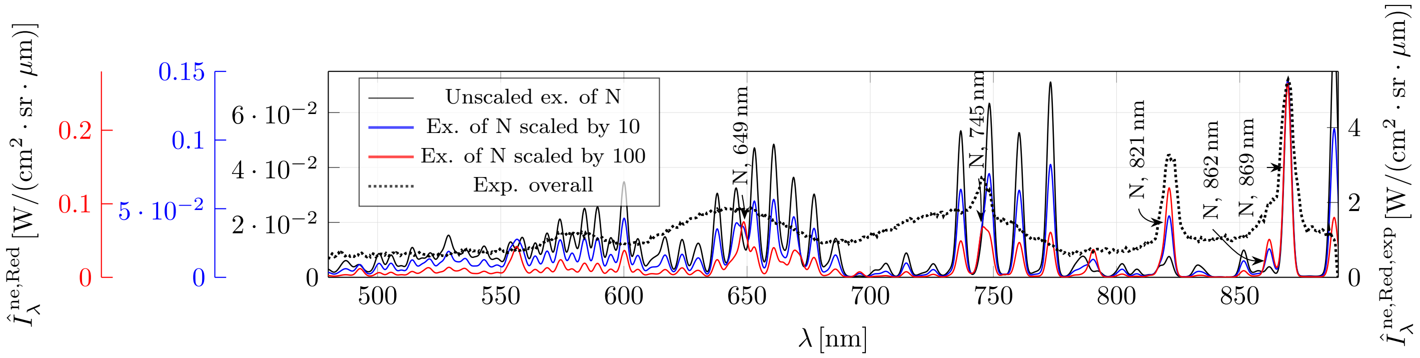

(c) For the case $l =$ "Red".

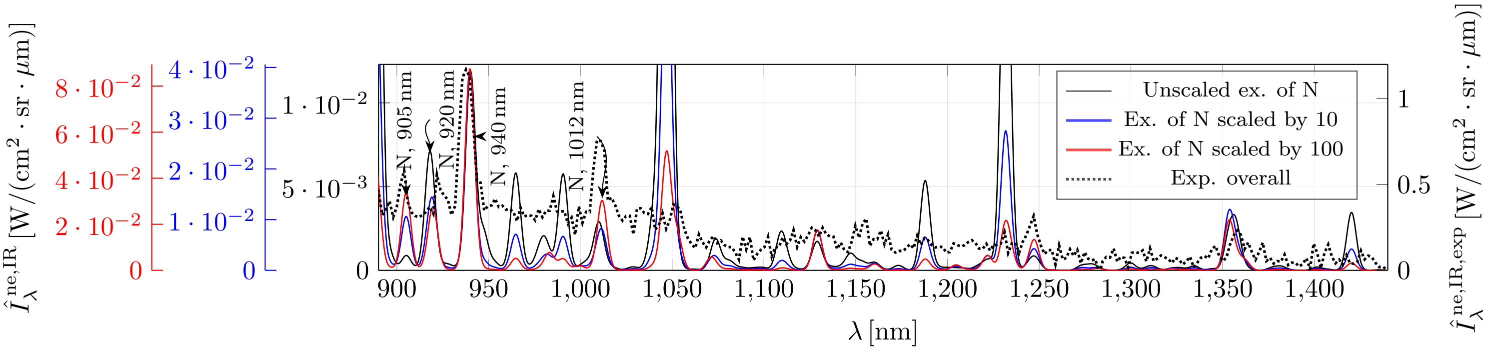

(d) For the case $l = \mathrm{IR}$.

Figure C.18: Numerical instrumentally resolved non-equilibrium metrics $\hat{I}_\lambda^{\mathrm{ne},l}(x)$, obtained with $\Lambda^{\mathrm{VUV}} = 0.01$, and unscaled excitation of N (solid black lines), and scaled by 10 (solid blue lines), and by 100 (solid red lines), as well as the respective experimental instrumentally resolved non-equilibrium metrics $\hat{I}_\lambda^{\mathrm{ne},l,\mathrm{exp}}(x)$ (dotted black lines), for the case of the low speed shot.